

# **The Connection Between Mass and Light in Galaxy Clusters**

Proefschrift

ter verkrijging van  
de graad van Doctor aan de Universiteit Leiden,  
op gezag van Rector Magnificus prof. mr. C.J.J.M. Stolker,  
volgens besluit van het College voor Promoties  
te verdedigen op woensdag 30 oktober 2013  
klokke 15:00 uur

door

Cristóbal Sifón Andalaft  
geboren te Punta Arenas, Chili  
in 1986

Promotiecommissie

Promotor: Prof. dr. Konrad Kuijken  
Co-Promotor: Dr. Henk Hockstra

Overige leden: Prof. dr. August Evrard (University of Michigan)  
Prof. dr. Marijn Franx  
Prof. dr. Huub Röttgering  
Dr. Frank van den Bosch (Yale University)

ISBN: ...

© 2016 Cristóbal Sifón,

Dit werk is gelicenseerd onder een Creative Commons Naamsvermelding-GelijkDelen 3.0 Unported licentie. Ga naar <http://creativecommons.org/licenses/by-sa/3.0/> om een kopie van de licentie te kunnen lezen.

Dit proefschrift werd ondersteund door ??? en het Leids Kerkhoven Bosscha fonds.

*Nou moe!?*  
— Guust<sup>1</sup>

---

<sup>1</sup>?



# Contents

<b>1</b>	<b>Introduction</b>	<b>1</b>
1.1	Galaxy clusters in a nutshell . . . . .	2
1.2	Mass proxies and cosmological leverage . . . . .	3
1.3	Mass and light in cluster galaxies . . . . .	4
1.3.1	Tidal effects on cluster galaxies . . . . .	6
1.4	This thesis . . . . .	7
<b>2</b>	<b>Strong lensing analysis of PLCK G004.5–19.5 at <math>z = 0.52</math></b>	<b>9</b>
2.1	Introduction . . . . .	10
2.2	Observations and data analysis . . . . .	11
2.2.1	SZ and X-ray data . . . . .	11
2.2.2	Optical imaging . . . . .	11
2.2.3	Optical spectroscopy . . . . .	12
2.3	Strong lensing analysis . . . . .	13
2.3.1	Strong lensing model . . . . .	13
2.3.2	External constraints . . . . .	15
2.4	Radio emission . . . . .	16
2.5	Conclusions . . . . .	18
<b>3</b>	<b>Dynamical masses of galaxy clusters selected through the Sunyaev-Zel'dovich effect</b>	<b>25</b>
3.1	Introduction . . . . .	26
3.2	Data and observations . . . . .	29
3.2.1	The Atacama Cosmology Telescope . . . . .	29
3.2.2	ACT SZ-selected clusters in the equator . . . . .	29
3.2.3	Gemini/GMOS spectroscopy . . . . .	30
3.2.4	SALT/RSS spectroscopy . . . . .	33
3.2.5	Archival data . . . . .	34

3.2.6	Comparison between redshift measurements . . . . .	35
3.3	Velocity Dispersions and Dynamical Masses . . . . .	35
3.3.1	Velocity dispersion measurements . . . . .	35
3.3.2	Calibrating velocity dispersions with the Multidark simulation . . . . .	36
3.3.3	From velocity dispersions to dynamical masses . . . . .	41
3.3.4	Dynamical mass estimates . . . . .	45
3.3.5	Comparison to SZ-derived masses . . . . .	47
3.3.6	Cluster substructure . . . . .	50
3.3.7	The impact of centring on the BCG . . . . .	52
3.4	Notable clusters . . . . .	54
3.4.1	Previously studied ACT clusters . . . . .	54
3.4.2	ACT-CL J0218.2–0041 . . . . .	55
3.4.3	ACT-CL J0326.8–0043 . . . . .	56
3.4.4	ACT-CL 2050.5–0055 . . . . .	57
3.4.5	ACT-CL J2055.4+0105 . . . . .	59
3.4.6	ACT-CL J2302.5+0002 . . . . .	59
3.5	Conclusions . . . . .	61
3.A	Eddington bias and selection effects . . . . .	63
3.B	Velocity histograms . . . . .	66
<b>4</b>	<b>Galaxy alignments in massive clusters from ~14,000 spectroscopic members</b>	<b>69</b>
4.1	Introduction . . . . .	70
4.2	Data . . . . .	72
4.2.1	Cluster sample and photometry . . . . .	72
4.2.2	Spectroscopic data . . . . .	74
4.3	Galaxy samples . . . . .	76
4.3.1	Spectroscopic members and dynamical masses . . . . .	76
4.3.2	Red sequence members . . . . .	85
4.3.3	Photometric redshift contamination . . . . .	87
4.3.4	Control samples . . . . .	89
4.4	Measuring intrinsic alignments . . . . .	89
4.4.1	Different alignment signals . . . . .	90
4.4.2	Shape measurements . . . . .	91
4.4.3	Systematic effects . . . . .	93
4.5	Results . . . . .	95
4.5.1	Satellite radial alignment . . . . .	95
4.5.2	Satellite-BCG alignment . . . . .	97

4.5.3	Satellite-satellite alignment . . . . .	100
4.5.4	Is there an agreement on the level of galaxy alignments in groups and clusters? . . . . .	102
4.6	Contamination to cosmic shear measurements . . . . .	103
4.6.1	Linear alignment model . . . . .	104
4.6.2	Halo model . . . . .	105
4.6.3	Impact of alignments within haloes on the power spectra .	106
4.7	Conclusions . . . . .	107
<b>5</b>	<b>Satellite galaxy-galaxy lensing in KiDS×GAMA</b>	<b>111</b>
5.1	Introduction . . . . .	112
5.2	Galaxy samples . . . . .	114
5.2.1	Lens galaxies: satellites in the GAMA galaxy group catalogue	114
5.2.2	Lensed background sources: the Kilo-Degree Survey . .	117
5.3	Galaxy-galaxy lensing of satellite galaxies . . . . .	119
5.3.1	The satellite lensing signal . . . . .	121
5.3.2	Host group contribution . . . . .	124
5.3.3	Satellite contribution . . . . .	127
5.4	Results . . . . .	128
5.4.1	Fitting procedure . . . . .	128
5.4.2	Group masses and mass-concentration relation . . . .	129
5.4.3	The masses of satellite galaxies . . . . .	130
5.4.4	The average subhalo mass . . . . .	132
5.4.5	Sensitivity to contamination in the group catalogue . .	133
5.5	Conclusions . . . . .	134
5.A	Full satellite lensing correlation matrix and the contribution from sample variance . . . . .	135
<b>Acknowledgements</b>		<b>153</b>



# 1 | Introduction

Our view of the Cosmos changed dramatically during the first third of the 20th century. The idea of a deterministic, stationary Universe governed by Newtonian dynamics with absolute measures of time and space had to be abandoned as Quantum Mechanics and the Special and General Theories of Relativity revolutionized our understanding of the very small, the very fast and the very large, respectively, along with our notions of space and time themselves.

It was not long until astronomical observations revolutionized our understanding of the Universe just a little more and, with that, our very own place in it. The year 1920 was host to one of the most famous astronomical discussions ever to take place. In what was termed “the Great Debate,” Harlow Shapley and Heber D. Curtis discussed (among other topics) the extent of the Milky Way and its place in the Universe (Shapley & Curtis 1921; a thorough review of the debate and its context is presented by Trimble 1995). Shapley argued that the Milky Way, with a size of up to 100 kpc (with 1 kpc = 3,260 light years), encompassed the entire Universe, while Curtis argued that other “spiral nebulae” were distinct galaxies much like our own Milky Way (which, he argued, was much smaller and hosted the Sun in its very centre). The issue was settled not long after, thanks to the observation of Cepheid variable stars in the Andromeda nebula by Hubble (1925). It was already known at that time that a Cepheid’s distance can be inferred by measuring the duration of its variability cycle, since they follow a tight period-luminosity relation. While Shapley was right that the Sun is not located at the centre of the Milky Way, Curtis was right about the nebulae: Hubble’s observations were definitive proof that these spiral nebulae could not be part of our Galaxy, and marked the birth of *extragalactic* astronomy.

A few years later, Hubble (1929) showed that there exists a linear relation between the distance and the velocity of galaxies other than the Milky Way (now known as Hubble’s law), which became the first solid evidence for an expanding Universe. He based this inference on measurements of i) the period of Cepheid stars (from which he inferred their luminosities and thereby their distances) and ii)

the Doppler shift of their spectra, using spectroscopic observations made by Vesto Slipher. Detailed discussions of pre-1929 observations of receding galaxies and an expanding Universe are presented by Trimble (2012, 2013).

Then, in 1933 Zwicky showed that galaxies in galaxy clusters move faster than the sum of their masses would be able to hold gravitationally, and inferred that there must be 10 to 100 times more mass hidden from us. Decades later, Rubin et al. (1980) came to the same conclusion by studying the motions of stars within spiral galaxies. Zwicky’s observations are now credited as the discovery of dark matter (e.g., Trimble 1987; Einasto 2013).

Our modern standard model of cosmology came to be complete with four additional ingredients: primordial nucleosynthesis (the theory that the lightest chemical elements formed during the big bang; Alpher et al. 1948); the discovery of the cosmic microwave background (CMB) by Penzias & Wilson (1965), predicted by the hot big bang hypothesis (Dicke et al. 1965); the development of the inflationary model, which explains the homogeneity of the CMB with a brief period of exponential growth in the very early Universe (Guth 1981); and the discovery of the Universe’s accelerated expansion (Riess et al. 1998; Perlmutter et al. 1999). We use the term ‘dark energy’ to refer to the cause of this accelerated expansion, whatever it may be. Dark energy makes up approximately 70% of the energy density of the Universe, while dark matter amounts to about 25%. Consequently, only about 5% of the Universe corresponds to ‘normal’ luminous matter (Planck Collaboration 2015a).

## 1.1 Galaxy clusters in a nutshell

The cosmological model introduced above predicts that structure grows hierarchically: small structures form first and then merge to give rise to larger structures. This continuous mass accretion and merging process has given rise to what we term the ‘Cosmic Web’. Figure 1.1 shows the local ( $z < 0.2$ ) cosmic web as seen by the 2-degree Field Galaxy Redshift Survey (Colless et al. 2001). At the intersections of this web lie galaxy clusters, the most massive gravitationally-bound structures formed so far in the Universe.

As the name suggests, galaxy clusters are objects in which galaxies abound—a massive cluster can host hundreds of bright galaxies (e.g., Abell 1958). However, this simple description was rendered insufficient early on by Zwicky (1933, discussed above). We now know that galaxy clusters, with sizes of 1–2 Mpc and masses of up to a few times  $10^{15} \text{ M}_\odot$ , are mostly made of dark matter (roughly 80% of their mass); only about 2% of their mass is in stars, while the remaining 18% is in a hot ionized gas with temperatures exceeding  $10^7 \text{ K}$  that can be observed at X-ray

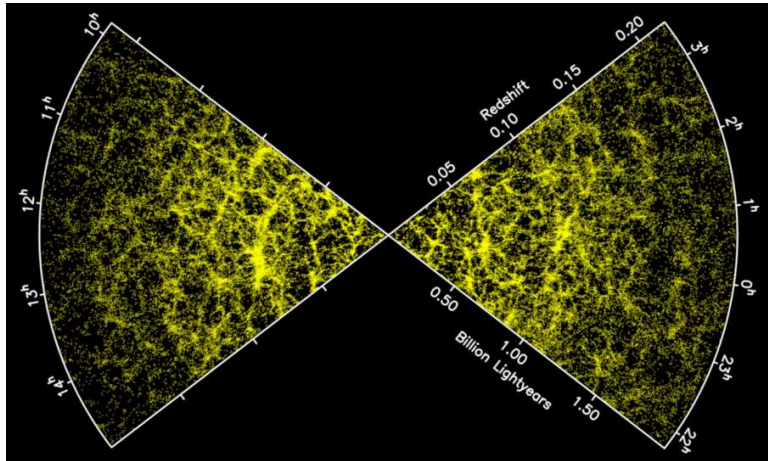


**Figure 1.1:** The local ( $z < 0.2$ ) cosmic web as seen by the 2-degree-Field Redshift Survey. Each yellow dot is a galaxy with a spectroscopic redshift.

wavelengths (e.g., Sarazin 1986).

## 1.2 Mass proxies and cosmological leverage

Galaxy clusters can be used to quantify the ability of the Universe to aggregate matter and therefore serve as powerful cosmological probes. The number of clusters in the Universe at a given time—and their masses—depends on the matter density of the Universe, usually parametrized as  $\Omega_m \equiv \rho_m/\rho_c$  (where  $\rho_c$  is the ‘critical’ density needed for the Universe to be flat), the size of density fluctuations left after the inflationary period, parametrized by  $\sigma_8$ , and the rate of expansion in the Universe, which can be quantified by the dark energy density,  $\Omega_\Lambda \equiv \rho_\Lambda/\rho_c$ .

Exploiting clusters as cosmological probes requires knowledge of their masses, which is not an easy quantity to estimate. While gravitational lensing—the deflection of light due to the mass-induced curvature of space—provides a direct measurement of the surface mass density (which can be deprojected into a total mass under some assumptions), it has not been generally available for large samples of clusters.

Because of this, considerable effort has been devoted to characterize a variety of mass *proxies*—observable quantities that, we hope, depend on mass in as simple a manner as possible, but also that are readily measurable with current capabilities. The most obvious of these is the number of galaxies, usually referred to as ‘richness’, which has received considerable attention in recent years. Although initial attempts

found that the richness was a very noisy mass proxy, recent studies have found that a properly-defined richness can be as good a proxy as any other (Rykoff et al. 2012; Andreon 2015). Also common are X-ray-derived mass proxies, including the X-ray luminosity, the gas temperature and the gas mass. Of these, the gas mass shows the least scatter (Mahdavi et al. 2013) but is the most difficult to obtain, and is currently only available for rather small samples.

A novel mass proxy, which has only been measurable in recent years thanks to new, sensitive high-resolution millimeter-wave surveys, is the Sunyaev-Zel'dovich (SZ, Sunyaev & Zel'dovich 1972) effect. The SZ effect is produced by the interaction of CMB photons with the hot electrons in galaxy clusters; this interaction increases the energy of CMB photons and creates ‘holes’ in observations at frequencies around 150 GHz in the direction of galaxy clusters. In a sense, therefore, observing the SZ effect is like seeing the shadow of a galaxy cluster. Because it is a CMB observable, the SZ surface brightness is independent of the redshift of the cluster producing it, and SZ surveys reveal the most massive clusters at all redshifts (Hasselfield et al. 2013; Bleem et al. 2015).<sup>1</sup> In contrast, X-ray or optical observations reveal flux from the clusters themselves and are therefore generally limited to rather low redshift. In addition, the relation between SZ effect and mass has been predicted to have very little scatter (at a level of 5–10%; e.g., Motl et al. 2005; Battaglia et al. 2012), although observations have shown that these predictions were rather optimistic (Benson et al. 2013; Sifón et al. 2013).

Massive galaxy clusters at high redshift have a particularly strong leverage on cosmological parameters (Vikhlinin et al. 2009), so SZ surveys are well-suited for cosmological parameter inference; the characterization of the SZ effect as a mass proxy is an active field of study. Figure 1.2 shows the constraints on cosmological parameters from galaxy clusters detected in the SZ survey by the Atacama Cosmology Telescope (ACT, Hasselfield et al. 2013) and the *Planck* satellite (Planck Collaboration 2015c). Both analyses found that the main limitation to the constraining power is given by the unknown conversion from SZ effect to cluster mass (rather than statistical uncertainties), even though the ACT analysis is based on only 15 clusters.

### 1.3 Mass and light in cluster galaxies

The galaxies we readily see in galaxy clusters tell us the story of a harsh, unforgiving environment: unlike the spiral galaxies (or ‘nebulae’) known since time immemorial

---

<sup>1</sup>This is not true for the SZ survey carried out with the *Planck* satellite, which is mostly limited to  $z < 0.6$  (Planck Collaboration 2015b). This is because high-redshift clusters have a small angular extent, so their SZ signal is diluted by the large beam of *Planck* (roughly 5').

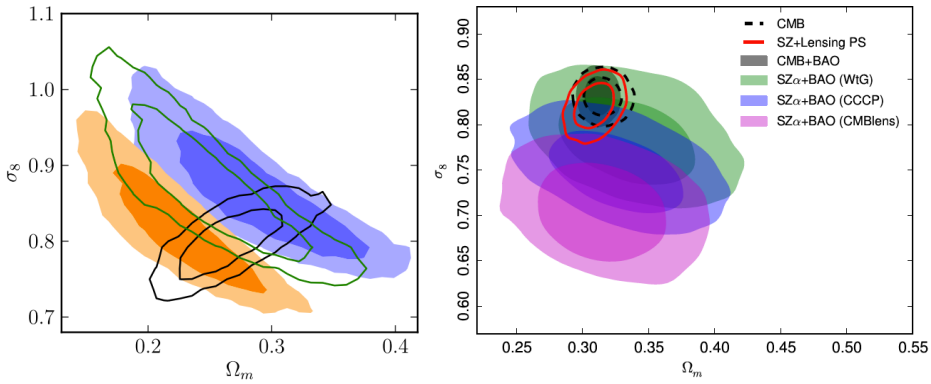


**Figure 1.2:** Constraints on cosmological parameters  $\Omega_m$  and  $\sigma_8$  from galaxy clusters detected by the Atacama Cosmology Telescope (left, from Hasselfield et al. 2013) and the *Planck* satellite (right, from Planck Collaboration 2015c) through their SZ effect. Black contours in the left and right panel show constraints from primary CMB measurements by the WMAP and *Planck* satellites, respectively. The broader, coloured contours show different assumptions about the scaling between SZ effect and mass. Clearly, this dominates the uncertainty budget on cosmological parameters.

(but whose spiral nature was discovered by William Parsons, 3rd Earl of Rosse, in 1845, and whose physical properties have only been characterized over the course of the past century), galaxies in clusters are typically of elliptical shape and a distinct reddish colour (Dressler 1980; Gladders & Yee 2000). This difference arises because galaxies entering clusters suffer the fast removal of their cold ( $\sim 10$  K) gas (which can collapse to form stars); the galaxies are then left only with old stars, which on average look redder than the bluer young stars (hence the colour of spiral galaxies).

This transformation is facilitated mainly by three distinct effects. *Galaxy harassment* is the process by which a galaxy removes the gas from another galaxy due to a high-speed encounter or fly-by (Moore et al. 1996). *Ram pressure stripping* is the removal of galactic gas by the gas in the intracluster medium, because the galaxy is traversing it at high speed (Gunn & Gott 1972; Nulsen 1982). Finally, *strangulation* refers to the process by which the strong tidal forces produced by the gravitational potential of the cluster remove the cold gas from the galaxy (Larson et al. 1980). Whatever the exact relevance of each mechanism, these effects seem to remove the star formation fuel from galaxies on relatively short timescales of about 1 billion years or less (e.g. Haines et al. 2013; Muzzin et al. 2014). Moreover, the evidence suggests that these effects are strong enough to suppress star formation even in low-mass galaxy groups (Haines et al. 2015; Balogh et al. 2016).

### 1.3.1 Tidal effects on cluster galaxies

Because galaxies do not follow radial orbits within clusters, they are subject to strong tidal torques from the cluster’s gravitational potential. These torques have an effect on both the shapes and the masses of cluster galaxies.

Regarding the shapes, the tidal torques tend to align the galaxies such that their major axes point towards the centre of the host cluster. In numerical simulations of dark matter (where gravity is the only force present), this process is very efficient, and dark matter *subhaloes* are tidally aligned with the host dark matter halo after the first pericentre passage, and remain aligned thereafter (e.g., Kuhlen et al. 2007; Pereira & Bryan 2010). However, simulations that incorporate gas and stars have shown that the case is not so clear-cut for galaxies. These simulations show that there is a degree of *misalignment* between the two components, such that the alignment of stellar light in galaxies is probably much weaker than that of the dark matter. Observational constraints on the strength of these cluster galaxy alignments, if any, can also have a strong impact on ongoing and upcoming cosmic shear surveys such as the Kilo-Degree Survey (KiDS, de Jong et al. 2015) or Euclid (Laureijs et al. 2011), as these *intrinsic* alignments are anti-correlated with the apparent alignment of background sources produced by gravitational lensing (Hirata & Seljak 2004). If not accounted for, they could introduce significant biases on cosmological parameters inferred from cosmic shear measurements.

If the visible parts of galaxies undergo such dramatic changes when they become satellites, similar effects might apply to the dark component. Just like in isolated galaxies and galaxy clusters, dark matter is expected to be the dominant mass component in cluster galaxies; exactly how much so is not well known. In fact, the same tidal forces that might cause galaxies to align also act to transfer mass from the satellite galaxy to the host cluster. Statistical measurements of this *tidal stripping* effect are particularly challenging: in addition to the difficulty of measuring the masses of galaxies in general, one must be able to identify galaxies belonging to clusters in the first place.

Measuring the total masses of cluster galaxies has implications not only for models of galaxy formation and evolution, but also for cosmology. Specifically, the energy of the postulated dark matter particle defines the amount of mass that is contained in substructures within the large scale structure (i.e., galaxies in clusters, or satellite galaxies around massive galaxies). A universe where dark matter is “warm” produces less substructure than one where dark matter is “cold” (e.g., Libeskind et al. 2013). Therefore the fraction of mass in cluster galaxies (relative to the total mass of a galaxy cluster) depends on the energy of the dark matter particle. The cold dark matter model provides a good description of large-scale structure observations and is the most widely-accepted scenario (e.g., Blumenthal

et al. 1984; Frenk & White 2012); accurate measurements of cluster galaxy masses would provide a complementary test of it.

## 1.4 This thesis

In this thesis we use a variety of observations and techniques to study the connection between the mass and light contents of galaxy clusters from different perspectives. The implications of different aspects of this connection have been briefly outlined above and are discussed in more detail in each chapter.

In **Chapter 2** we characterize PLCK G004.5–19.5, a galaxy cluster recently discovered by the *Planck* satellite through its SZ effect. We present the first optical images of this cluster, measure its redshift ( $z = 0.52$ ) and identify multiple images of a lensed background galaxy, which allows us to perform a strong lensing analysis. We also show that PLCK G004.5–19.5 hosts diffuse radio emission—the tell-tale sign of cluster mergers and, to this day, an extremely rare sight at  $z > 0.4$ .

In **Chapter 3** we use extensive spectroscopic observations of galaxy clusters detected through the Sunyaev-Zel'dovich effect to measure the velocity dispersions of their member galaxies. Taking previous results from hydrodynamical simulations, we convert these velocity dispersions into cluster masses and compare them to the strength of the SZ effect, with the aim of characterizing the latter to allow its use for cosmological parameter inference. We pay particular attention to sources of uncertainty and scatter in the determination of the velocity dispersions, and conclude that the dominant uncertainty comes from the identification of member galaxies, which poses an irreducible uncertainty on velocity dispersions as mass proxies.

In the second half of this thesis we turn our attention to the galaxies residing in clusters. In particular, in **Chapter 4** we investigate the alignment of the shapes of cluster galaxies. We base our study on a sample of 90 clusters with deep, wide-field observations devised for accurate weak lensing measurements. We first perform a thorough literature search for spectroscopic redshifts with which to select galaxies physically belonging to these clusters, resulting in a sample of more than 14,000 cluster galaxies. We then measure the orientations of cluster galaxies to see if there are any signs of alignment of galaxies within clusters.

In **Chapter 5** we exploit the overlap between the spectroscopic Galaxy And Mass Assembly survey (GAMA) and the deep photometric Kilo-Degree Survey to measure the masses of satellite galaxies in galaxy groups using weak gravitational lensing, with the aim of constraining the segregation of group galaxies by mass. The spectroscopic nature of the galaxy group catalogue ensures we can do this essentially free of contamination from both non-group galaxies and central galaxies.

Finally, in **Chapter 6** we extend the lensing measurements of **Chapter 5**

to more massive galaxy clusters using the dataset produced for **Chapter 4**. Using weak lensing measurements of the masses of cluster galaxies, we constrain the stellar-to-subhalo mass relation and study the mass segregation of cluster galaxies.

## 2 | Strong lensing analysis of PLCK G004.5–19.5 at $z = 0.52$

The recent discovery of a large number of galaxy clusters using the Sunyaev-Zel'dovich (SZ) effect has opened a new era on the study of the most massive clusters in the Universe. Multi-wavelength analyses are required to understand the properties of these new sets of clusters, which are a sensitive probe of cosmology. We aim at a multi-wavelength characterization of PLCK G004.5–19.5, one of the most massive X-ray validated SZ effect-selected galaxy clusters discovered by the *Planck* satellite. We have observed PLCK G004.5–19.5 with GMOS on the 8.1m-Gemini South Telescope for optical imaging and spectroscopy, and performed a strong lensing analysis. We also searched for associated radio emission in published catalogs. An analysis of the optical images confirms that this is a massive cluster, with a dominant central galaxy (the BCG) and an accompanying red sequence of galaxies, plus a 14''-long strong lensing arc. Longslit spectroscopy of 6 cluster members shows that the cluster is at  $z = 0.516 \pm 0.002$ . We also targeted the strongly lensed arc, and found  $z_{\text{arc}} = 1.601$ . We use LensTool to carry out a strong lensing analysis, from which we measure a median Einstein radius  $\theta_E(z_s = 1.6) \simeq 30''$  and estimate an enclosed mass  $M_E = 2.45^{+0.45}_{-0.47} \times 10^{14} M_\odot$ . By extrapolating an NFW profile we find a total mass  $M_{200}$ . Including a constraint on the mass from previous X-ray observations yields a slightly higher mass,  $M_{500}^{\text{SL+X}} = 6.7^{+2.6}_{-1.3} \times 10^{14} M_\odot$ , consistent with the value from strong lensing alone. High-resolution radio images from the TIFR GMRT Sky Survey at 150 MHz reveal that PLCK G004.5–19.5 hosts a powerful radio relic on scales  $\lesssim 500$  kpc. Emission at the same location is also detected in low resolution images at 843 MHz and 1.4 GHz. This is one of the higher redshift radio relics known to date.

## 2.1 Introduction

In the last few years, the Sunyaev-Zel'dovich (SZ) effect has proven to be an effective method to find massive galaxy clusters at all redshifts, with results from the Atacama Cosmology Telescope (ACT, e.g., Marriage et al. 2011b; Hasselfield et al. 2013), the South Pole Telescope (SPT, e.g., Williamson et al. 2011; Reichardt et al. 2013) and the *Planck* satellite (e.g., Planck Collaboration 2011a, 2014b) already yielding a few hundred newly discovered clusters up to  $z \sim 1.4$ . The SZ effect is a distortion in the Cosmic Microwave Background (CMB) spectrum in the direction of galaxy clusters caused by inverse Compton scattering of CMB photons by the hot electrons in the intracluster gas (Sunyaev & Zel'dovich 1972). Multi-wavelength follow-up observations of SZ-selected clusters have confirmed the unique potential of the SZ effect for detecting the most massive clusters in the Universe (e.g., Benson et al. 2013; Sifón et al. 2013), with the SZ-discovered El Gordo and SPT-CL J2344–4243 being two of the most extreme galaxy clusters ever known (Menanteau et al. 2012; McDonald et al. 2012). As expected, many of these clusters display strong lensing features (Menanteau et al. 2010b), a good indication that these are very massive systems.

Observations of these strongly lensed background galaxies offer one of the most robust ways of constraining the mass of a cluster, providing a direct measure of the mass within the Einstein radius (see Kneib & Natarajan 2011, for a recent review). In combination with other probes (such as X-rays and weak lensing), strong lensing analyses have provided some of the most complete mass distribution models for galaxy clusters, even allowing for the determination of the 3-dimensional configuration in some cases (e.g., Morandi et al. 2010; Limousin et al. 2013).

Here, we present a multi-wavelength analysis of PLCK G004.5–19.5, one of the most massive, hot and X-ray luminous galaxy clusters discovered by the *Planck* satellite via the SZ effect and validated with *XMM-Newton* X-ray observations (Planck Collaboration 2011b). We perform a strong lensing analysis from optical imaging and spectroscopy, and show from archival radio imaging that PLCK G004.5–19.5 hosts a powerful radio relic.

All uncertainties are quoted at the 68.3% ( $1\sigma$ ) confidence level. We assume a flat  $\Lambda$ CDM cosmology with  $\Omega_M = 0.3$  and  $H_0 = 70 \text{ km s}^{-1} \text{ Mpc}^{-1}$ . Total masses, X-ray and SZ measurements are reported within a radius  $r_{500}$ , which encloses a mean density 500 times the critical density of the Universe at the corresponding redshift. All quantities reported by Planck Collaboration (2011b) (reproduced in Sec. 3.4.1) have been corrected to the spectroscopic redshift  $z = 0.516$ . All magnitudes are in the AB system.

## 2.2 Observations and data analysis

### 2.2.1 SZ and X-ray data

PLCK G004.5–19.5 was discovered through its SZ effect by the *Planck* satellite. With a signal-to-noise ratio (S/N) of 5.9 in the Early Science release, it is just below the S/N threshold of 6.0 set for the *Planck* Early SZ sample (Planck Collaboration 2011a)<sup>1</sup>. Despite this relatively low S/N, it has a strong integrated SZ signal,  $Y_{500} = (1.90 \pm 0.19) \times 10^{-4} \text{ Mpc}^2$ , where  $Y \equiv \int y d\Omega$ . Here,  $y$  is the usual Compton parameter and the integral is over the solid angle of the cluster. We use the  $Y - M$  scaling relation of Planck Collaboration (2011c) to estimate a mass  $M_{500}^{\text{SZ}} = (10.4 \pm 0.7) \times 10^{14} \text{ M}_\odot$ .

PLCK G004.5–19.5 was subsequently validated using *XMM-Newton* (Planck Collaboration 2011b), which confirmed that it is an extended X-ray source. Moreover, the observed energy of the Fe K emission line allowed a redshift determination  $z_{\text{Fe}} = 0.54$ , making it the highest-redshift cluster of the initial *Planck-XMM-Newton* validation program. The X-ray analysis of Planck Collaboration (2011b) proves that PLCK G004.5–19.5 is a hot, massive cluster, with an X-ray luminosity<sup>2</sup> (in the [0.1-2.4] keV band) of  $L_X = 1.6 \times 10^{45} \text{ erg s}^{-1}$ , an integrated temperature  $kT_X = 10.2 \pm 0.5 \text{ keV}$  and a gas mass  $M_{\text{gas}} = 1.3 \times 10^{14} \text{ M}_\odot$ . Combined, the latter two give a pseudo-Compton parameter  $Y_X \equiv kT_X M_{\text{gas}} = (13.3 \pm 0.9) \times 10^{14} \text{ M}_\odot \text{ keV}$ . With this latter value, Planck Collaboration (2011b) estimate a total mass  $M_{500}^X = (9.6 \pm 0.5) \times 10^{14} \text{ M}_\odot$ .

### 2.2.2 Optical imaging

PLCK G004.5–19.5 was observed on UT 2012 July 19 with the *gri* filters with GMOS on the Gemini-South Telescope (ObsID:GS-2012A-C-1, PI:Menanteau), with exposure times of  $8 \times 60 \text{ s}$ ,  $8 \times 90 \text{ s}$  and  $8 \times 150 \text{ s}$  respectively. Observations were performed with photometric conditions and seeing  $\sim 0.^{\prime\prime}6$ . Images were coadded using SWarp (Bertin et al. 2002) and photometry was performed using SExtractor (Bertin & Arnouts 1996) in dual mode, using the *i*-band for detection. Figure 2.1 shows the combined *gri* image<sup>3</sup> of PLCK G004.5–19.5, which shows clearly that there is an overdensity of red elliptical galaxies with a central dominant Brightest Cluster Galaxy (BCG) close to the X-ray peak. Figure 2.1 also reveals the presence

<sup>1</sup>PLCK G004.5–19.5 has been included in the new *Planck* SZ catalog (Planck Collaboration 2014b) with a S/N of 6.15.

<sup>2</sup>The uncertainties in the X-ray values from Planck Collaboration (2011b) do not include systematic errors and have been dropped when negligible.

<sup>3</sup>Created with stiff (Bertin 2012).

of several strong lensing features, most notably a giant arc to the West of the BCG, roughly  $14''$  long.

Each galaxy is assigned a photometric redshift by fitting Spectral Energy Distributions (SEDs) to the *gri* photometry using the BPZ code (Benítez 2000) including correction for galactic extinction as described in Menanteau et al. (2010b,a). Typical uncertainties are  $\delta z/(1+z) \simeq 0.09$ . The photometric redshift of the cluster,  $z_{\text{phot}} = 0.51 \pm 0.02$ , was estimated as in Menanteau et al. (2010b,a) and is consistent with the spectroscopic redshift (Sec. 2.2.3). We consider as cluster members all galaxies within  $\Delta z = 0.03(1+z_0) = 0.045$  of  $z_0 = 0.51$  and brighter than  $m^* + 2 \simeq 22.9$  in the *i*-band, for a total 222 photometrically-selected members. (Here  $m^*$  is the characteristic luminosity of the Schechter (1976) function as found by Blanton et al. (2003), passively evolved to  $z_0$ ).<sup>4</sup>) Selecting galaxies from a color-magnitude diagram instead or imposing a brighter membership cut have no influence on the results.

### 2.2.3 Optical spectroscopy

We performed longslit spectroscopy of PLCK G004.5–19.5 on UT 2012 July 20 with GMOS, with  $0.''75$ -wide slits with three pointings, two aimed at confirming cluster members and one targeting the most prominent strongly lensed background galaxy. The data were reduced using PyGMOS<sup>5</sup> (Sifón et al. 2013), with an average wavelength calibration root-mean-square (rms) uncertainty of  $0.4\text{\AA}$ . Redshifts were measured by cross-correlating the spectra with Sloan Digital Sky Survey (Abazajian et al. 2009) template spectra using the IRAF package RVSAO (?). The six confirmed cluster members are listed in Table 2.1 and are shown in Figure 2.1 by green circles. They are all red, passive elliptical galaxies and have a rest-frame velocity dispersion  $\sigma \sim 860 \text{ km s}^{-1}$  (which is likely not representative of the cluster velocity dispersion). The median redshift of these 6 members,  $z = 0.516 \pm 0.002$ , is adopted as the cluster redshift (with uncertainties given by  $\sigma\sqrt{\pi/2N}$ ).

The left panel of Figure 2.2 shows a zoomed-in view of the brightest lensed galaxy. Two brightness peaks can be identified, which we interpret as two blended strong lensing images of a single source (see Sec. 2.3). The top-right panel shows the 2d spectrum along the arc, where a faint continuum can be distinguished between the north and south images. The red inset histogram shows the normalized counts for each row over the spectral range shown, after an iterative  $3\sigma$ -clipping rejection so that bad pixels and emission lines are not included in the counts. This histogram shows that the decrease in brightness is significant between the two peaks but that

---

<sup>4</sup>For reference, the BCG has a luminosity  $L = 9.5L^*$ .

<sup>5</sup><http://www.strw.leidenuniv.nl/~sifon/pygmos/>

**Table 2.1:** Spectroscopically confirmed cluster members.

ID	RA (hh:mm:ss)	Dec (dd:mm:ss)	<i>i</i> mag. <sup>a</sup> (AB mag)	Redshift <sup>b</sup>
1 <sup>c</sup>	19:17:05.08	-33:31:20.6	18.47	$0.5199 \pm 0.0005$
2	19:17:07.80	-33:31:31.2	19.74	$0.5126 \pm 0.0005$
3	19:17:08.98	-33:31:48.4	19.16	$0.5074 \pm 0.0004$
4	19:17:09.49	-33:31:43.5	19.70	$0.5150 \pm 0.0003$
5	19:17:10.20	-33:31:38.5	19.83	$0.5176 \pm 0.0003$
6	19:17:14.40	-33:31:57.5	20.48	$0.5187 \pm 0.0002$

<sup>a</sup>MAG\_AUTO from SExtractor. <sup>b</sup>Errors as given by RVSAC. <sup>c</sup>Brightest Cluster Galaxy.

this region is, in turn, still detected at high significance. The middle- and bottom-right panels show the 1d spectra of the two brightness peaks. Both spectra clearly show 5 redshifted FeII absorption lines with rest-frame wavelengths 2344.2, 2374.5, 2382.8, 2586.6 and 2600.2 Å. The median redshift of these 5 pairs of lines is  $z_{\text{arc}} = 1.6008 \pm 0.0002$ . The bottom spectrum also shows three emission lines (seen in the 2d spectrum as well), which correspond to H $\beta$  and [OIII] $\lambda\lambda 4958, 5007$ Å from a foreground compact star-forming galaxy at  $z = 0.203$ , for which H $\alpha$  emission is also observed but not shown in Figure 2.2. A small, bright, blue blob is indeed seen overlapping with the south knot (just West of the latter), which we interpret as this foreground galaxy.

## 2.3 Strong lensing analysis

### 2.3.1 Strong lensing model

The strong lensing analysis was performed using the Markov Chain Monte Carlo (MCMC) code LensTool (Kneib 1993; Jullo et al. 2007), as follows. The cluster is modelled with an ellipsoidal Navarro-Frenk-White (NFW, Navarro et al. 1995) profile for the main halo, plus a truncated Pseudo-Isothermal Elliptical Mass Distribution (PIEMD, Kassiola & Kovner 1993; Kneib et al. 1996) with a constant mass-to-light ratio for the 222 brightest cluster members (see Sec. 2.2.2). A PIEMD halo is modelled by three parameters: the core radius,  $r_{\text{core}}$ , the size of the halo (the cut-off radius),  $r_{\text{cut}}$ , and the velocity dispersion,  $\sigma_0$ , which scale with galaxy luminosity as (Jullo et al. 2007):

$$r_{\text{core}} = r_{\text{core}}^* (L/L^*)^{1/2} \quad (2.1\text{a})$$

$$r_{\text{cut}} = r_{\text{cut}}^* (L/L^*)^{1/2} \quad (2.1\text{b})$$

$$\sigma_0 = \sigma_0^* (L/L^*)^{1/4}, \quad (2.1\text{c})$$

where  $L^* = 6.6 \times 10^{10} L_\odot$ . The total mass of the galaxy is then given by

$$M = (\pi/G) (\sigma_0^*)^2 r_{\text{cut}}^* (L/L^*). \quad (2.2)$$

We fix  $r_{\text{core}}^* = 0.3$  kpc, and  $r_{\text{cut}}^*$  and  $\sigma_0^*$  are free parameters. The centre of the NFW halo is fixed to the peak of the X-ray emission (located at RA=19:17:04.6, Dec=−33:31:21.9; Planck Collaboration 2011b). Therefore the mass model has six free parameters: four for the main NFW halo and two for the PIEMD haloes.

As can be seen in the red inset histogram of Figure 2.2, there is a decrease in brightness in the middle of the arc in between two prominent brightness peaks. We interpret this as the merging of two images of the background galaxy and use this double-imaged arc with  $z_{\text{arc}} = 1.6$  as a constraint for the lens model, and identify a third image of the same source to the North-East of the BCG (labelled 1.3 in Figure 2.1). The positions and photometry of these three images are listed in Table 2.2.

The total mass model is therefore optimized using the 222 brightest members (including the six spectroscopic members) and the three images for the background galaxy at  $z = 1.601$ . We adopt a positional uncertainty  $\Delta\mathbf{x} = 1.^{\prime\prime}4$  for the multiple images. The goodness-of-fit for the best model is  $\chi_{\text{red}}^2/\text{d.o.f.} = 0.15$ , with a rms error on the image positions of  $0.^{\prime\prime}22$ . The total mass distribution is moderately elongated along the plane of the sky, approximately aligned with the light distribution. The best-fit values for the six free parameters plus the posterior masses and radii are listed in Table 2.3 (see also Sec. 2.3.2).

Following Meneghetti et al. (2011), the Einstein radius is estimated as the median distance of the tangential critical curves to the cluster centre. We find  $\theta_E(z_s = 1.6) = 30.^{\prime\prime}3_{-3.9}^{+1.4}$ , corresponding to a physical distance  $r_E \simeq 190$  kpc. Assuming a symmetric lens, the mass inside this region is  $M_E = 2.45_{-0.47}^{+0.45} \times 10^{14} M_\odot$ . Integrating the 3-dimensional NFW profile for the main halo, we obtain  $M_{200}$ . The corresponding radius,  $r_{500}^{\text{SL}} = 0.93_{-0.08}^{+0.16}$  Mpc, is estimated from  $M_{500}$  assuming a spherical cluster. We note that the values at  $r_{500}$  are an extrapolation of the strong lensing information.

Recently, Zitrin et al. (2012) derived a representative distribution of Einstein radii from a sample of  $\sim 10,000$  clusters from the SDSS optically-selected sample of Hao et al. (2010). They found a log-normal Einstein radius distribution with

**Table 2.2:** Images of the strongly lensed galaxy.

Source	RA (hh:mm:ss)	Dec (dd:mm:ss)	$r$ mag. <sup>a</sup> (AB mag)	$g - r$ <sup>b</sup> (AB mag)
1.1	19:17:03.14	-33:31:12.5	$21.42 \pm 0.01$	$0.40 \pm 0.03$
1.2	19:17:02.97	-33:31:19.0	$21.42 \pm 0.01$	$0.39 \pm 0.02$
1.3	19:17:06.45	-33:30:50.8	$23.75 \pm 0.03$	$0.35 \pm 0.05$

<sup>a</sup>MAG\_ISO from SExtractor. <sup>b</sup>Difference of MAG\_APER's from SExtractor.

mean and standard deviation  $\langle \log(\theta_E^{\text{eq}}/\text{arcsec}) \rangle = 0.73 \pm 0.32$  for background sources at  $z_s \sim 2$ . For comparison to Zitrin et al. (2012) and others, we estimate the equivalent Einstein radius to be  $\theta_E^{\text{eq}}(z_s = 1.6) \simeq 25''$ . PLCK G004.5–19.5 is a  $2\sigma$  outlier from this mean relation; therefore it can be said to be within the 5% strongest lensing clusters in the Universe.

### 2.3.2 External constraints

We run LensTool again including a prior in the mass, from the X-ray mass estimated by Planck Collaboration (2011b) as implemented by Verdugo et al. (2011). As mentioned in Sec. 3.4.1, however, the reported uncertainties are unrealistically small. As a more realistic estimate, we take the intrinsic scatter in the latest  $Y_X - M$  relation by Mahdavi et al. (2013) of 22%, measured by combining weak lensing and X-ray observations. Thus the additional constraint in the total mass is the following Gaussian prior:

$$M_{500}^X = (9.6 \pm 2.1) \times 10^{14} M_\odot \quad (2.3)$$

measured at  $r_{500}^X = 1245$  kpc.<sup>6</sup> The same exercise for the SZ mass, assuming an uncertainty of 18% corresponding to the central value of the intrinsic scatter in the  $Y_{\text{SZ}} - M$  measured by Sifón et al. (2013) using dynamical masses and SZ measurements from ACT, gives

$$M_{500}^{\text{SZ}} = (10.4 \pm 1.9) \times 10^{14} M_\odot \quad (2.4)$$

We only use Equation 2.3 because both measurements are very similar and because they are both measured at the same radius, determined from the X-ray scaling relation (Planck Collaboration 2011b) and are therefore not independent. The posterior distributions are shown for various combinations of parameters for the two different models in Figure 2.3, highlighting degeneracies in the strong lensing model.

<sup>6</sup>Note that in LensTool the X-ray constraint to the strong lensing model is given as a fixed mass  $M$  at a fixed radius  $r$  (with a mass uncertainty), not explicitly as the mass at a given overdensity.

**Table 2.3:** Marginalized posterior estimates of the strong lensing model with and without the X-ray mass constraint.

Parameter <sup>a</sup>	Symbol	SL	SL+X	units
Main NFW Halo				
Ellipticity	$e$	$0.40^{+0.07}_{-0.09}$	$0.37^{+0.08}_{-0.07}$	
Position Angle <sup>b</sup>	$\theta$	$52^{+7}_{-3}$	$53^{+2}_{-1}$	deg
Scale radius	$r_s$	$0.10^{+0.17}_{-0.04}$	$0.39^{+0.07}_{-0.08}$	Mpc
Concentration <sup>c</sup>	$c_{200}$	$4.0^{+5.0}_{-0.8}$	$4.1^{+1.8}_{-0.6}$	
PIEMD Halos				
Cut-off radius	$r_{\text{cut}}^*$	$47^{+13}_{-20}$	$25^{+28}_{-14}$	kpc
Velocity dispersion	$\sigma_0^*$	$225^{+42}_{-23}$	$106^{+37}_{-53}$	$\text{km s}^{-1}$
Derived Parameters				
Einstein Mass	$M_E$	$2.45^{+0.45}_{-0.47}$	$2.46^{+0.31}_{-0.59}$	$10^{14} M_\odot$
Einstein Radius	$r_E$	$30.3^{+1.4}_{-3.9}$	$30.0^{+0.6}_{-3.5}$	arcsec
Total Mass	$M_{500}$	$4.0^{+2.1}_{-1.0}$	$6.7^{+2.6}_{-1.3}$	$10^{14} M_\odot$
Radius	$r_{500}$	$0.93^{+0.16}_{-0.08}$	$1.10^{+0.14}_{-0.07}$	Mpc

<sup>a</sup>All parameters have uniform priors. <sup>b</sup>Position angle West of North. <sup>c</sup>The concentration is defined as  $c_{200} = r_{200}/r_s$ .

The X-ray constraint pushes the mass to a higher value which is marginally consistent with the strong lensing only (SL) model. Notably, the SL model allows for a low- $M_{500}$ , high- $M_E$  (through a high  $r_E$ ), high-concentration and low-ellipticity solution which is marginally excluded by the model including the X-ray constraint (SL+X). The marginalized posterior mass is  $M_{500}^{\text{SL+X}} = 6.7^{+2.6}_{-1.3} \times 10^{14} M_\odot$ . Although the contours are broader in the SL model, the maximum likelihood estimate (MLE) and marginalized 68% range of  $M_E$  (and  $r_E$ ) are mostly unaffected by the inclusion of the X-ray constraint, with a posterior estimate  $M_E^{\text{SL+X}} = 2.46^{+0.31}_{-0.59} \times 10^{14} M_\odot$ . This is expected, since  $r_E$  is directly constrained by the strongly lensed images, independently of the mass profile of the cluster.

## 2.4 Radio emission

Radio relics and radio haloes are diffuse, non-thermal emission features that have no obvious connection with individual cluster galaxies and are often associated with merging activity in massive clusters of galaxies (see Feretti et al. 2012, for a recent review). We searched for such features around PLCK G004.5–19.5 in the

high-resolution 150 MHz images of the TIFR GMRT Sky Survey (TGSS)<sup>7</sup> Data Release 5 and in VizieR<sup>8</sup> (Ochsenbein et al. 2000) for additional archival data.

Figure 2.4 shows the intensity map at 150 MHz from the TGSS with blue contours at  $(3, 5, 7, 15)\sigma$ , where  $\sigma = 11.9 \text{ mJy beam}^{-1}$  is the background rms level. Green and red contours show 1.4 GHz and 843 MHz emission from the NRAO VLA Sky Survey (NVSS; Condon et al. 1998) and the Sydney University Molonglo Sky Survey (SUMSS; Mauch et al. 2003), respectively. Both sets of contours are shown at  $(3, 5, 10, 20)\sigma$ , where  $\sigma = 0.51 \text{ mJy beam}^{-1}$  and  $2.0 \text{ mJy beam}^{-1}$  in the NVSS and SUMSS images, respectively. There is significant ( $> 5\sigma$ ) emission around PLCK G004.5–19.5 in all three frequencies at coincident locations. Moreover, this emission is extended in the TGSS and NVSS images.

We identify a tangentially extended radio relic in the TGSS image, coincident with emission at the other frequencies, although this emission is barely resolved in SUMSS and NVSS (the extent of the emission is roughly 2 beams in both low-resolution images). The multi-frequency properties of this relic are given in Table 2.4. Radio relics span a wide range of spectral indices,  $\alpha$  (where  $F_\nu \propto \nu^{-\alpha}$ ), from  $\alpha \sim 1$  up to  $\alpha \sim 3$  (Feretti et al. 2012). We give a preliminary estimate of the integrated spectral index of the relic by fitting a power-law to the 150 MHz flux combined with NVSS and SUMSS, one at a time. From both combinations we measure  $0.9 \lesssim \alpha \lesssim 1.4$  at the 68% level. Measuring the spectral index from all three frequencies gives a shallower but consistent spectral index  $\alpha \sim 0.7 - 1.1$ , suggesting that the emission at 843 MHz and/or 1.4 GHz may be contaminated by unresolved point sources, thus boosting the flux and lowering  $\alpha$ . A spectral index measured using both 843 MHz and 1.4 GHz would be more affected by this contamination since these two frequencies are closer together (in log-space) than any of them is to the TGSS frequency.

We confirm that there are no X-ray point sources associated with any of the radio emission from the *XMM-Newton* image. As with the relic, sources A, B, C and E have no counterparts in the optical images, nor in the Near Infrared (NIR) from the 2 Micron All Sky Survey (2MASS, Skrutskie et al. 2006) or the Mid Infrared (MIR) from the Wide-field Infrared Survey Explorer All Sky Survey (WISE, Wright et al. 2010), within their nominal position uncertainties. Source D has two plausible counterparts from the 2MASS and WISE (merged into one source) catalogs. Both are stars, and are also seen in our optical images. It is therefore likely that source D is a radio point source. Given its high flux and shape in the TGSS image, source A is also likely a point source, or two blended point sources.

Because the relic elongation is approximately in the same direction as the TGSS

---

<sup>7</sup><http://tgss.ncra.tifr.res.in/>

<sup>8</sup><http://vizier.u-strasbg.fr/viz-bin/VizieR>

beam and source E, we use source E (which can be regarded as noise-dominated, being much less significant and not detected at any other frequency) as a control for the significance of the relic accounting for the TGSS beam. As seen from Tables 2.4 and 2.5, both the relic and source E have similar sizes and position angles. Figure 2.4 shows however that the relic is much more significant than source E. Moreover, the following exercise shows that in the case of source E, the large size is a consequence of the background noise and the beam, whereas the source we associate to the radio relic is significantly extended over the background. We re-measured fluxes for these two sources on images in which we masked all pixels with values below  $3\sigma = 35.7 \text{ mJy beam}^{-1}$ . More than half the emission associated with source E comes from pixels with  $< 3\sigma$  emission, and the major axis is halved in this masked map. From the relic, in contrast, we still measure  $\sim 70\%$  of the total flux, and the major axis is 75% of the size measured in the original map.

## 2.5 Conclusions

We present a multi-wavelength analysis of PLCK G004.5–19.5, one of the massive galaxy clusters recently discovered by the *Planck* satellite using the SZ effect. Optical confirmation from GMOS imaging clearly shows a red sequence of galaxies with a dominant BCG, both undisputable characteristics of galaxy clusters. There is also a strongly lensed giant arc which is composed of two partially merged images of a background galaxy. Spectroscopy of 6 cluster members plus the giant arc show that the cluster is at  $z = 0.516 \pm 0.002$  and that the arc is at  $z_{\text{arc}} = 1.601$ . With these data we have performed a strong lensing analysis, confirming a third image for the source producing the arc. We use LensTool to obtain a mass model for the cluster including the contribution from cluster galaxies, and estimate an Einstein mass  $M_E = 2.45^{+0.45}_{-0.47} \times 10^{14} M_\odot$ , within a median Einstein ring  $r_E \simeq 190 \text{ kpc}$ , corresponding to an angular size  $\theta_E(z_s = 1.6) \simeq 30''$ . Compared to the universal Einstein ring distribution derived by Zitrin et al. (2012), PLCK G004.5–19.5 is among the 5% strongest gravitational lenses in the Universe. By integrating the 3-dimensional NFW profile we estimate  $M_{200}$ . We also run LensTool including a Gaussian prior for the X-ray mass estimated by Planck Collaboration (2011b) and find  $M_{500}^{\text{SL+X}} = 6.7^{+2.6}_{-1.3} \times 10^{14} M_\odot$ , marginally consistent with the mass estimated from strong lensing alone. The Einstein mass does not change significantly when including the X-ray constraint, because the latter is constrained directly by the strongly lensed galaxy. The inclusion of the X-ray mass constraint does help to exclude a high-mass, low-concentration solution which is allowed by the strong lensing-only model.

Examination of archival high-resolution radio data from the TIFR GMRT Sky

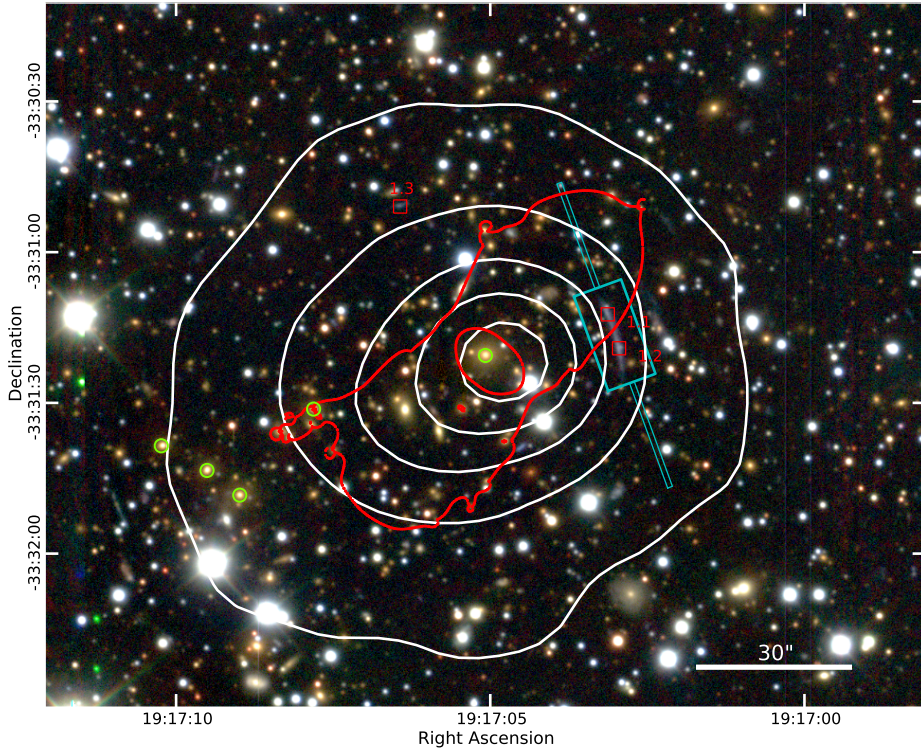


**Figure 2.1:** GMOS *gri* pseudo-color image of the central region of PLCK G004.5–19.5. North is up, east is left. X-ray surface brightness contours from *XMM-Newton* are overlaid in white. Spectroscopic cluster members are marked by green circles; only 5 out of 6 are visible in the shown region, the sixth member is  $\sim 760$  kpc to the E-SE of the BCG. Red squares mark the position of the 3 confirmed multiple images, while we show in red the critical curve for  $z_s = 1.6$ . The thin cyan box shows the slit used to get the spectrum of the arc (1'' across); the wide cyan box shows the region zoomed-in in the left panel of Figure 2.2. The thick white line in the bottom right shows a 30'' scale, corresponding to 188 kpc at  $z = 0.516$ .

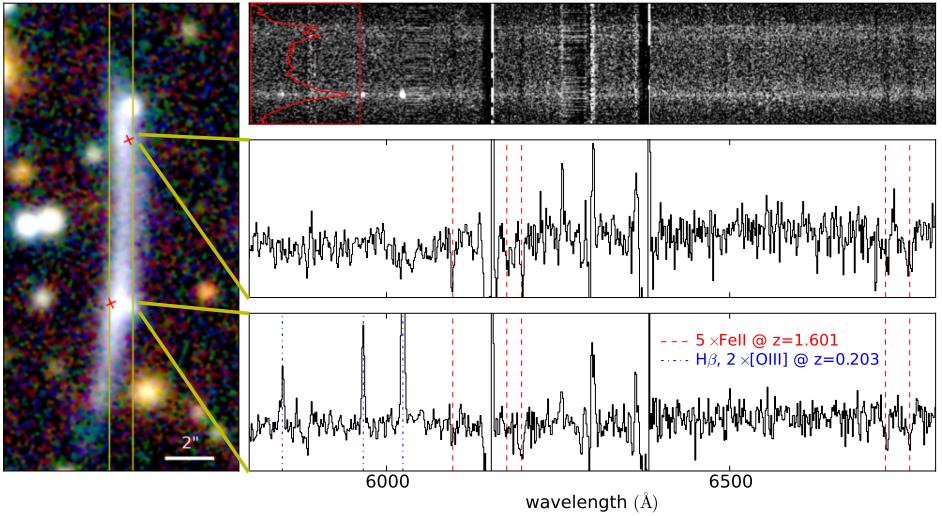


**Figure 2.2:** Strong lensing giant arc. The left panel shows a  $10'' \times 20''$  close-up *gri* image of the arc (cyan box in Figure 2.1), with the red crosses marking the location where LensTool predicts the images to be. The thin yellow lines outline the position of the slit and the thick yellow lines mark the approximate locations of the knots from where the 1D spectra are shown. The right panels show the arc spectrum in the wavelength range  $5800 - 6800$  Å. The top right panel shows the GMOS 2d spectrum. The image is 105 pixels, corresponding to  $15.''3$ , from top to bottom. The red histogram (inset) shows the total counts in each row over the shown spectral range, after an iterative  $3\sigma$ -clipping to remove bad pixels and emission lines. This highlights the decrease in brightness (and the significance of the continuum) between the two images. The middle and bottom panels show, respectively, the 1d spectra of the northern (source 1.1) and southern (source 1.2) peaks seen in the lensed arc, each marked by a yellow “wedge” in the left panel. In these, the red dashed lines mark the 5 Fell absorption lines at  $z = 1.601$  and the blue dash-dotted lines mark the emission lines from a foreground galaxy at  $z = 0.203$ , only seen in the south spectrum. The vertical axes in these two panels are in arbitrary units.

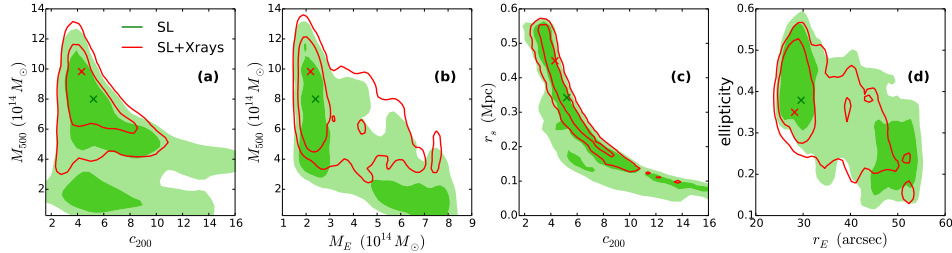


**Figure 2.3:** Joint 2D posterior distributions of  $c_{200}$  and  $M_{500}$  (panel *a*),  $M_E$  and  $M_{500}$  (panel *b*),  $c_{200}$  and  $r_s$  (panel *c*), and  $r_E$  and  $\theta$  (panel *d*). Contours are at the 68% and 95% levels. Filled green contours show constraints from strong lensing alone and red contours show the constraints when  $M_{500}^X$  is included as an independent constraint. Crosses show the corresponding maximum likelihood estimates.

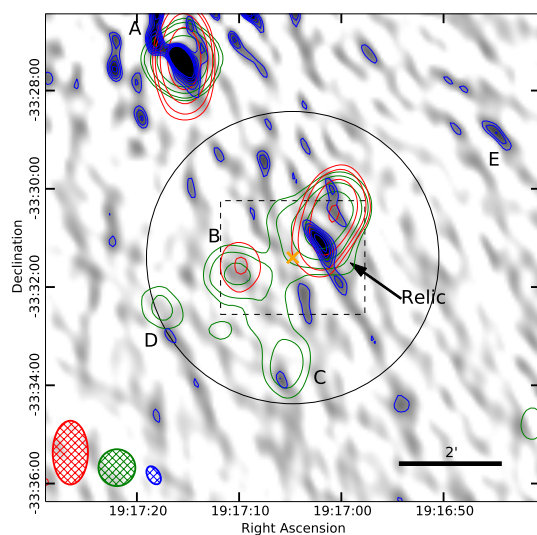


**Figure 2.4:**  $10' \times 10'$  TGSS 150 MHz intensity map around PLCK G004.5-19.5, with contours in blue. Contours are shown at 3, 5, 7 and 15 times  $\sigma$ , where  $\sigma$  is the background rms. NVSS 1.4 GHz and SUMSS 843 MHz contours are shown in green and red, respectively. Both contour sets are in units of 3, 5, 10 and 20 times each  $\sigma$ . The orange cross shows the position of the BCG. The dashed black rectangle is the region shown in Figure 2.1 and the black circle marks  $r_{500}^{SL+X} = 1.12$  Mpc. The black bar in the bottom right marks a scale of 2'. The SUMSS, NVSS and TGSS beams are shown from left to right, respectively, in the bottom left corner (hatched ellipses).

**Table 2.4:** Radio Relic

Source Name	RA <sup>a</sup> (hh:mm:ss)	Dec <sup>a</sup> (dd:mm:ss)	Freq. (MHz)	Beam (" × ")	$F_\nu$ <sup>b</sup> (mJy)	Size <sup>c</sup> (" × ")	P.A. <sup>d</sup> (deg)
GMRT173_01 <sup>e</sup>	19:17:01.94	−33:31:12.6	150	24 × 15	$382 \pm 80$	84 × 19	$28 \pm 5$
SUMSS J191701–333033	19:17:01.50(16)	−33:30:33.7(2.5)	843	51 × 43	$51 \pm 4$	70 × 62	$136 \pm 3$
NVSS 1917101–333035	19:17:01.75(08)	−33:30:35.6(1.3)	1400	45 × 45	$37 \pm 2$	74 × 50	$146 \pm 1$

<sup>a</sup>Nominal uncertainties on the last two digits in parentheses. <sup>b</sup>Integrated Flux. <sup>c</sup>Major and minor axes. <sup>d</sup>Position angle West of North. <sup>e</sup>Position uncertainties from TGSS are  $\sim 4''$ .

**Table 2.5:** Other Sources in the Radio Images.

Source	Name	RA (hh:mm:ss)	Dec (dd:mm:ss)	$F_\nu$ (mJy)	Size (" × ")	P.A. (deg)
A	GMRT243_01 <sup>a,b</sup>	19:17:16.71	−33:27:11.8	$540 \pm 75$	39 × 19	43
	NVSS J191715–332722	19:17:15.89(05)	−33:27:22.2(0.7)	$35.7 \pm 0.5$	47 × 45	176
	SUMSS J191715–332720	19:17:15.75(11)	−33:27:20.6(2.0)	$71.5 \pm 2.7$	73 × 49	165
B	NVSS J191710–333144	19:17:10.90(28)	−33:31:44.7(3.3)	$11.2 \pm 0.8$	74 × 55	102
	SUMSS J191710–333139 <sup>c</sup>	19:17:10.55(37)	−33:31:39.0(4.6)	$8.8 \pm 1.0$	57 × 52	3
C	NVSS J191705–333333	19:17:05.94(32)	−33:33:33.6(8.0)	$7.7 \pm 0.5$	81 × 49	173
D	NVSS J191717–333224	19:17:17.84(52)	−33:32:24.4(5.7)	$3.7 \pm 0.1$	57 × 42	132
E	GMRT163_01 <sup>b</sup>	19:16:45.13	−33:28:48.9	$161 \pm 41$	71 × 14	34

See Notes in Table 2.4. <sup>a</sup>Blended in the TGSS catalog. <sup>b</sup>Position uncertainties from TGSS are  $\sim 4''$ . <sup>c</sup>Not in the SUMSS catalog.

Survey at 150 MHz reveals the presence of a radio relic at approximately 250 kpc from the cluster centre. Significant emission is also detected in low-resolution images from NVSS at 1.4 GHz and SUMSS at 843 MHz. A preliminary measurement of the integrated spectral index yields  $\alpha \sim 0.9 - 1.4$ . We find no detectable point sources contributing significantly to the radio emission in the *XMM-Newton* or Gemini images, nor from archival observations in the NIR or MIR. This radio emission likely originated from recent merging activity, but the available data do not allow for a detailed study of possible merging events. The origin of the radio emission will be addressed with future observations.



# 3 | Dynamical masses of galaxy clusters selected through the Sunyaev-Zel'dovich effect

We present galaxy velocity dispersions and dynamical mass estimates for 44 galaxy clusters selected via the Sunyaev-Zel'dovich (SZ) effect by the Atacama Cosmology Telescope. Dynamical masses for 18 clusters are reported here for the first time. Using N-body simulations, we model the different observing strategies used to measure the velocity dispersions and account for systematic effects resulting from these strategies. We find that the galaxy velocity distributions may be treated as isotropic, and that an aperture correction of up to 7 per cent in the velocity dispersion is required if the spectroscopic galaxy sample is sufficiently concentrated towards the cluster centre. Accounting for the radial profile of the velocity dispersion in simulations enables consistent dynamical mass estimates regardless of the observing strategy. Cluster masses  $M_{200}$  are in the range  $(1 - 15) \times 10^{14} M_\odot$ . Comparing with masses estimated from the SZ distortion assuming a gas pressure profile derived from X-ray observations gives a mean SZ-to-dynamical mass ratio of  $1.10 \pm 0.13$ , but there is an additional 0.14 systematic uncertainty due to the unknown velocity bias; the statistical uncertainty is dominated by the scatter in the mass-velocity dispersion scaling relation. This ratio is consistent with previous determinations at these mass scales.

*Cristóbal Sifón, Nick Battaglia, Matthew Hasselfield, Felipe Menanteau, and the ACT collaboration,  
2015, arXiv:1512.00910*

### 3.1 Introduction

Galaxy clusters are a sensitive probe of cosmology. Populating the high-end of the mass function, their number density depends strongly on the matter density in the Universe,  $\Omega_m$ , and the amplitude of matter fluctuations,  $\sigma_8$  (see, e.g., the review by Allen et al. 2011). Their potential as cosmological probes, however, depends critically on our knowledge of survey selection effects and baryon physics. Survey selection effects are usually properly accounted for through analytical considerations (e.g., Vikhlinin et al. 2009), numerical simulations (e.g., Sehgal et al. 2011; Sifón et al. 2013), or modeled self-consistently with scaling relations and cosmological parameters (e.g., Pacaud et al. 2007; Mantz et al. 2010; Rozo et al. 2010; Benson et al. 2013; Hasselfield et al. 2013; Bocquet et al. 2015). In contrast, incomplete knowledge of baryonic physics poses a serious and still not well understood challenge to the accuracy with which galaxy clusters can constrain cosmological parameters, and is currently the dominant systematic effect (e.g., Benson et al. 2013; Hasselfield et al. 2013).

The Sunyaev-Zel'dovich (SZ) effect (Zel'dovich & Sunyaev 1969; Sunyaev & Zeldovich 1980) is a distortion in the cosmic microwave background (CMB) temperature produced by inverse-Compton scattering of CMB photons by free electrons in the hot ( $T > 10^7$  K) intracluster medium (ICM) of a galaxy cluster. The SZ effect has a distinct frequency dependence such that, in the direction of a massive cluster, the temperature of the sky increases at frequencies larger than 218 GHz while below this frequency the temperature decreases. The amplitude of this distortion is described by the line-of-sight-integrated Compton parameter,  $y \propto n_e T_e$ , or its solid-angle integral,  $Y = \int y d\Omega$ . Its surface brightness is independent of redshift which, to first order, means that surveying the sky at millimetre wavelengths reveals all clusters above a fixed mass to high redshift, resulting in a relatively simple selection function.

Both numerical simulations (Springel et al. 2001; da Silva et al. 2004; Motl et al. 2005; Nagai 2006; Battaglia et al. 2012) and analytical studies (Reid & Spergel 2006; Afshordi 2008; Shaw et al. 2008) predict that the SZ effect should correlate with mass with low (of order 10 per cent) intrinsic scatter, although observations correlating the SZ effect with different mass proxies from X-rays (Bonamente et al. 2008; Andersson et al. 2011; Planck Collaboration 2011c; Benson et al. 2013; Rozo et al. 2014b), optical richness (High et al. 2010; Planck Collaboration 2011d; Menanteau et al. 2013; Sehgal et al. 2013), weak lensing (Hoekstra et al. 2012; Marrone et al. 2012; Planck Collaboration 2013; Gruen et al. 2014) and galaxy velocity dispersion (Sifón et al. 2013; Ruel et al. 2014; Rines et al. 2016) find a larger intrinsic scatter between mass and  $Y$  of about 20 per cent. The effect of cluster physics

mentioned above, coupled to systematic effects arising from the use of different instruments (Mahdavi et al. 2013; Rozo et al. 2014a), dominate the uncertainties in these scaling relations. This uncertainty has been most notoriously highlighted by the tension in inferred cosmological parameters between the primary CMB and SZ cluster counts found by the Planck satellite (Planck Collaboration 2015c), and can be reduced by larger, more detailed analyses involving independent mass proxies and ICM tracers.

Velocity dispersions have been well studied as a proxy for galaxy cluster mass, dating back to the first such scaling relation reported by Evrard (1989), and are independent of the ICM properties that determine the SZ effect.<sup>1</sup> Extensive tests on numerical simulations have shown that the 3-dimensional galaxy velocity dispersion is a low-scatter mass proxy but, not surprisingly, projection effects including cluster triaxiality and large-scale structure significantly increase the scatter (White et al. 2010; Saro et al. 2013). The scatter at fixed velocity dispersion in observed samples is as large as a factor two (Old et al. 2014, 2015).<sup>2</sup> Importantly, the biases on these measurements (typically  $\lesssim 25$  per cent for  $\gtrsim 30$  observed galaxies) are much smaller than the observed scatter (Old et al. 2015), meaning that velocity dispersions remain a valuable, unbiased mass calibrator for sufficiently large cluster samples. In this paper we make use of spectroscopic data to estimate line-of-sight galaxy velocity dispersions (referred to as  $\sigma$  in the remainder of this section) and dynamical masses of galaxy clusters selected through their SZ effect using the Atacama Cosmology Telescope (ACT, Marriage et al. 2011b; Hasselfield et al. 2013).

In Sifón et al. (2013), we used the  $\sigma - M$  scaling relation of Evrard et al. (2008) to estimate dynamical masses of a subset of these clusters. Evrard et al. (2008) calibrated this scaling relation using a suite of N-body simulations, using dark matter particles to estimate velocity dispersions. They showed that the velocity dispersions of dark matter particles in N-body simulations are robust to variations in cosmology and to different simulation codes. However, galaxies, which are used as observational tracers to measure the velocity dispersion, do not necessarily sample the same velocity distribution as the dark matter particles. Both galaxies and dark matter subhaloes (the analogues of galaxies in N-body simulations) feel dynamical friction, which distorts their velocity distribution and biases their dispersion with respect to dark matter particles. Additionally, subhaloes are tidally stripped and disrupted such that they can drop below the subhalo identification limit of a parti-

---

<sup>1</sup>Some degree of correlation may still exist, however, because different observables are affected by the same large scale structure (White et al. 2010).

<sup>2</sup>In theory, the caustic technique provides a lower-scatter mass proxy than simple velocity dispersions (Gifford et al. 2013); however, it has been shown to produce similar scatter in more realistic settings (Old et al. 2014, 2015). In this respect, machine learning algorithms may become a promising alternative (Ntampaka et al. 2015b,a).

cle simulation. The lower-velocity subhaloes are more likely to be disrupted, thus the surviving subhaloes have a larger velocity dispersion which again biases the velocity dispersion of subhaloes (e.g., Faltenbacher & Diemand 2006).

The result of these effects is referred to as velocity bias, denoted  $b_v \equiv \sigma_{\text{gal}}/\sigma_{\text{DM}}$  (e.g., Carlberg 1994; Colín et al. 2000). Baryonic effects are significant when quantifying the amplitude of  $b_v$ : recent high-resolution hydrodynamical simulations show significant differences in the velocity dispersions of subhaloes versus DM particles (roughly +7 per cent, which translates to a  $\sim 20$  per cent bias in mass), but comparatively little difference between galaxies and dark matter subhaloes (e.g., Lau et al. 2010; Munari et al. 2013; Wu et al. 2013).<sup>3</sup> Additionally, the amplitude of  $b_v$  depends on the brightness of the observed galaxies: the velocity dispersion of brighter galaxies is generally biased low, but this can be counteracted by selecting a sample of ( $\gtrsim 30$ ) galaxies with a representative brightness distribution (Old et al. 2013; Wu et al. 2013). In apparent contradiction with this, Guo et al. (2015a,b) used measurements of the clustering of luminous red galaxies (LRGs) to infer a *negative* velocity bias for satellite galaxies. Moreover, they found that less luminous LRGs have a stronger velocity bias of about 90 per cent, while more luminous LRGs have velocities consistent with those of DM particles. This result can be reconciled with those of the above simulations by noting that any given cluster<sup>4</sup> typically has less than ten LRGs—both Old et al. (2013) and Wu et al. (2013) find that taking the  $N$  brightest galaxies gives rise to a velocity bias of roughly 0.9, if  $N \lesssim 10$ .

Since observationally one uses galaxies to calculate  $\sigma$ , biases may be introduced if one uses a  $\sigma - M$  scaling relation calibrated from simulations using dark matter particles, such as that of Evrard et al. (2008), but does not account for the aforementioned complexities. Therefore, in this paper we use the scaling relation of Munari et al. (2013), calibrated on simulated *galaxies* instead of dark matter particles, to relate velocity dispersions to cluster masses.

We present our SZ-selected cluster sample and describe the observations, data reduction and archival compilation in Section 3.2. In Section 5.4.3 we describe our velocity dispersion and dynamical mass estimates, including an assessment of our different observing strategies using mock observations on numerical simulations (Section 3.3.2), a comparison to SZ-derived masses (Section 3.3.5) and an investigation of cluster substructure (Section 3.3.6). We highlight interesting individual clusters in Section 3.4 and summarize the main results in Section 5.5.

We assume a flat  $\Lambda$ CDM cosmology<sup>5</sup> with  $\Omega_m = 0.3$  and  $H_0 = 70 \text{ km s}^{-1}$

---

<sup>3</sup>Selecting galaxies by stellar mass instead of total mass reduces the strength of the velocity bias (e.g., Faltenbacher & Diemand 2006; Lau et al. 2010).

<sup>4</sup>Note that both the simulations and the observations of Guo et al. (2015a,b) refer to clusters with masses well below  $10^{15} M_\odot$ .

<sup>5</sup>Assuming Planck-level uncertainties in  $\Omega_m$  and  $H_0$  (Planck Collaboration 2015a) introduces

$\text{Mpc}^{-1}$ . Throughout this work we quote measurements (e.g., masses,  $M_\Delta$ ) at a radius  $r_\Delta$ , within which the average density is  $\Delta$  times the critical density of the Universe at the corresponding redshift, where  $\Delta = \{200, 500\}$ .

## 3.2 Data and observations

In this section we detail the cluster sample, our follow-up observations and data processing, and archival data with which we supplement our observations. In summary, we study 44 SZ-selected clusters, of which 28 are in the celestial equator and are the focus of this paper, and 16 clusters are part of the southern survey and were studied in Sifón et al. (2013). We summarize our observing runs and sources of archival data in Table 3.1.

### 3.2.1 The Atacama Cosmology Telescope

The Atacama Cosmology Telescope (ACT) is a 6-meter off-axis Gregorian telescope located at an altitude of 5200 m in the Atacama desert in Chile, designed to observe the CMB at arcminute resolution. Between 2007 and 2010, ACT was equipped with three 1024-element arrays of transition edge sensors operating at 148, 218, and 277 GHz (Fowler et al. 2007; Swetz et al. 2011), although only the 148 GHz band has been used for cluster detection. In this period, ACT observed two regions of the sky, one covering 455 sq. deg. to a typical depth of  $60 \mu\text{K}$  centred around declination  $-53^\circ$  (the “southern” survey, Marriage et al. 2011b,a), and one covering 504 sq. deg. around the celestial equator, with a typical depth of  $44 \mu\text{K}$  (the “equatorial” survey, Hasselfield et al. 2013). For details on the observational strategy of ACT and map making procedure see Dünner et al. (2013).

In the remainder of this section we describe ACT detections and follow-up observations of clusters in the equatorial survey. Details about the detection and optical confirmation of clusters in the southern survey can be found in Marriage et al. (2011b) and Menanteau et al. (2010b), respectively. The spectroscopic observations are described in Sifón et al. (2013) and the latest SZ measurements are given in Hasselfield et al. (2013).

### 3.2.2 ACT SZ-selected clusters in the equator

Galaxy clusters were detected in the 148 GHz band by matched-filtering the maps with the pressure profile suggested by Arnaud et al. (2010), fit to X-ray selected local

---

a < 5 per cent difference in the reported masses, accounting for their influence on both member selection (through changes in projected physical distances) and the adopted scaling relation.

( $z < 0.2$ ) clusters, with varying cluster sizes,  $\theta_{500}$ , from  $1.^{\circ}18$  to  $27'$ . A signal-to-noise (S/N) ratio map was extracted from each of these matched-filtered maps and all pixels with  $S/N > 4$  were considered as cluster candidates. Cluster properties were extracted only from the map with  $\theta_{500} = 5.^{\circ}9$ . The properties depend weakly on the exact shape of the profile as discussed in Hasselfield et al. (2013).

Because of the complete overlap of ACT equatorial observations with Sloan Digital Sky Survey Data Release 8 (SDSS DR8, Aihara et al. 2011) imaging, *all* cluster candidates were assessed with optical data (Menanteau et al. 2013). With DR8, clusters can be confidently detected up to  $z \approx 0.5$ . Moreover, 270 sq. deg. of the ACT survey overlap with the deep, co-added SDSS Stripe82 region (S82, Annis et al. 2014), which allows the detection of the cluster red sequence up to  $z \approx 0.8$ . Confirmed clusters are all those  $S/N > 4$  candidates for which there are at least 15 galaxies within  $1 h^{-1}$  Mpc of the brightest cluster galaxy and with a photometric redshift within  $0.045(1+z)$  of the cluster redshift. We additionally targeted candidate high-redshift, high S/N candidates with near infrared  $K_s$ -band imaging with the ARC 3.5m telescope at the Apache Point Observatory, which allowed us to confirm five additional clusters at  $z \gtrsim 1$ .<sup>6</sup>

A total of 68 clusters were confirmed, of which 19 (all at  $z > 0.65$ ) were new detections. This sample has been divided into three subsamples: a complete sample of clusters within S82 at  $z < 1$  and with  $S/N > 5$  (the “cosmological” sample, containing 15 clusters), a uniform sample of 34 clusters within S82, and an incomplete sample of 19 clusters up to  $z \approx 0.7$  in the shallower DR8 region. Confirmed clusters in S82 have redshifts up to  $z \approx 1.3$  (with the aid of near infrared data for the higher redshifts). See Menanteau et al. (2013) for more details on the optical and infrared confirmation of clusters in the equatorial survey.

### 3.2.3 Gemini/GMOS spectroscopy

We observed 20 clusters from the equatorial sample with the Gemini Multi-Object Spectrograph (GMOS, Hook et al. 2004) on the Gemini-South telescope, split in semesters 2011B (ObsID:GS-2011B-C-1, PI:Barrientos/Menanteau) and 2012A (ObsID:GS-2012A-C-1, PI:Menanteau), prioritizing clusters in the cosmological sample at  $0.3 < z < 1.0$ . All observations followed our setup for the southern sample (Sifón et al. 2013). We first selected as targets those galaxies with photometric redshifts within  $\Delta z = 0.1$  of the cluster photometric redshift and prioritized bright galaxies as allowed by the multi-object spectroscopy (MOS) masks. The only major difference in strategy from Sifón et al. (2013) is that, owing to the SDSS photom-

---

<sup>6</sup>One of these clusters, ACT-CLJ0012.0–0046, associated with an overdensity of red galaxies at  $z = 1.36$  by Menanteau et al. (2013), is detected at much lower significance in new, more sensitive SZ observations performed with ACTPol (M. Hilton et al., in prep).

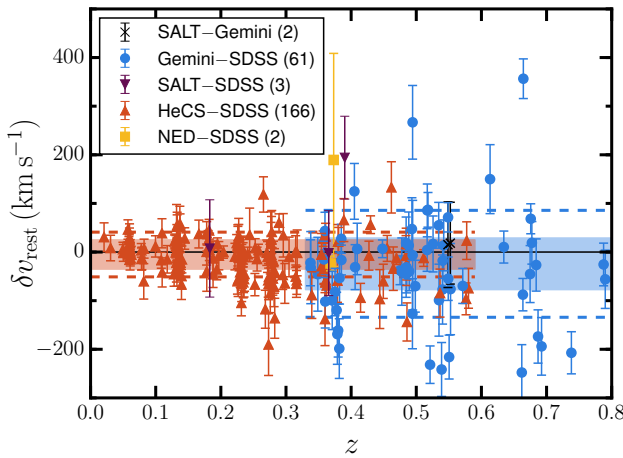


**Figure 3.1:** Comparison of redshifts from all spectroscopic datasets to SDSS measurements (for overlapping galaxies), shown as  $\delta v_{\text{rest}} = c(z_1 - z_2)/(1 + z_2)$ , where  $z_2 = z_{\text{SDSS}}$  (except for the black crosses, where  $z_2 = z_{\text{Gemini}}$ ). All redshifts are in the heliocentric frame. Red, yellow, purple and blue points correspond to redshifts from the HeCS survey (Rines et al. 2013), from NED for Abell 370, and from our SALT/RSS and Gemini/GMOS campaigns, respectively, while black crosses compare our redshift measurements between SALT/RSS and Gemini/GMOS. Individual uncertainties correspond to the quadrature sum of the uncertainties from both measurements. Red and blue shaded regions show uncertainties on the weighted means for HeCS–SDSS and Gemini–SDSS, respectively, and dashed horizontal lines show standard deviations. The number of matches per data set pair are given in parentheses in the legend.

**Table 3.1:** Summary of spectroscopic observations and sources of archival data. The last column lists the number of clusters observed in each program. Previously published data have the corresponding references. All SDSS clusters have been observed by us in one of the listed programs as well.

Instrument / Archival source	Semester	Program	PI	Data reference	Sample	N <sub>cl</sub>
VLT/FORS2	2009B	084.A-0577	Infante	Sifón et al. (2013)	South	3
	2010B	086.A-0425	Infante	Sifón et al. (2013)	South	2
Gemini/GMOS	2009B	GS-2009B-Q-2	Barrientos	Sifón et al. (2013)	South	4
	2010B	GS-2010B-C-2	Barrientos/Menanteau	Sifón et al. (2013)	South	10
	2011B	GS-2011B-C-1	Barrientos/Menanteau	this work	Equator	12
	2012A	GS-2012A-C-1	Menanteau	this work	Equator	8
SALT/RSS	2012A	2012-1-RSA_UKSC_RU-001	Hilton/Hughes	Kirk et al. (2015)	Equator	1
	2012B	2012-2-RSA_UKSC_RU-001	Hilton/Hughes	Kirk et al. (2015)	Equator	2
	2013A	2013-1-RSA_RU-001	Hilton/Hughes	Kirk et al. (2015)	Equator	1
	2013B	2013-2-RSA_RU-002	Hilton/Hughes	Kirk et al. (2015)	Equator	3
SDSS DR12	—	—	—	Alam et al. (2015)	Equator	20
HeCS	—	—	—	Rines et al. (2013)	Equator	3
NED	—	—	—	Soucail et al. (1988), Dressler et al. (1999)	Equator	1

etry, we targeted galaxies out to larger radii than in the southern observations, in which we were bound by the roughly  $5'$  fields of view of our targeted optical follow-up with 4m-class telescopes (Menanteau et al. 2010b). We followed this approach because of the indication, especially from numerical simulations, that the velocity dispersion is a decreasing function of radius; therefore an unbiased velocity dispersion estimate is predicted only if galaxies are sampled out to approximately the cluster's virial radius (e.g., Girardi et al. 1998; Biviano et al. 2006; Mamon et al. 2010). We observed 2-3 masks per cluster along the (visually identified) major axis of the galaxy distribution. In order to obtain a wide sky coverage, these masks were mostly non-overlapping in the sky, even though this meant we had fewer targets per unit area. We detail the differences with the southern strategy, and address the impact of these differences in our measurements, in Section 3.3.2.

We used `pygmos`<sup>7</sup> (Sifón et al. 2013), an automated Python/PyRAF script<sup>8</sup> that goes from raw data to one-dimensional spectra, including bias subtraction, flat field correction, wavelength calibration, cosmic ray rejection (van Dokkum 2001) and sky subtraction. Redshifts<sup>9</sup> were measured by cross-correlating the spectra with template spectra from SDSS<sup>10</sup> using `xcsao` within IRAF's `rvsao` package<sup>11</sup> (Kurtz & Mink 1998).

### 3.2.4 SALT/RSS spectroscopy

We also observed seven clusters in S82 with the Robert Stobie Spectrograph (RSS, Burgh et al. 2003) on the Southern African Large Telescope (SALT), using multi-object spectroscopy. Details of these observations are given in Kirk et al. (2015). Target selection and redshift measurements were carried in a similar, but not identical, fashion to the GMOS observations of the equatorial clusters. The data were prepared with `pysalt` (Crawford et al. 2010), after which they were reduced with standard IRAF<sup>12</sup> functions. Redshift measurements are also obtained with `xcsao`. ACT-CL J0045.2–0152 is the only cluster that was observed both with Gemini and SALT, but there are only two galaxies in our final catalogue observed with both telescopes.

---

<sup>7</sup><http://www.strw.leidenuniv.nl/~sifon/pygmos/>

<sup>8</sup>PyRAF is a product of the Space Telescope Science Institute, which is operated by AURA for NASA.

<sup>9</sup>All redshifts presented here are in the heliocentric frame.

<sup>10</sup><http://www.sdss.org/DR7/algorithms/spectemplates/index.html>

<sup>11</sup><http://tdc-www.harvard.edu/iraf/rvsao/>

<sup>12</sup><http://iraf.noao.edu/>

### 3.2.5 Archival data

In order to enlarge the sample of studied clusters and member galaxies, we also compiled archival data for the equatorial sample. Specifically, we searched the SDSS Data Release 12 (DR12, Alam et al. 2015) database<sup>13</sup>. We retrieved all galaxies with a valid redshift (that is,  $z > 0$  and  $z\text{Warning}=0$ ) within a cluster-centric distance of  $20'$  (corresponding to several times  $r_{200}$  for most clusters) and found a total of 2001 galaxies (most of which are not cluster members; see Section 5.4.3) in the direction of 25 of the ACT equatorial clusters observed with Gemini or SALT. Of the galaxies with SDSS spectra, 61 were also observed by us with Gemini, and three with SALT. We compare these repeat observations in Section 3.2.6. There are additionally four clusters in the equatorial sample with dedicated archival observations; we did not observe any of these clusters ourselves. We briefly describe these data below.

The Hectospec Cluster Survey (HeCS, Rines et al. 2013) was designed to measure the masses of galaxy clusters at  $0.1 < z < 0.3$  out to the infall regions of clusters (typically around  $4r_{200}$ ), targeting more than four hundred objects per cluster within a radius of  $30'$  (corresponding to 6 Mpc at  $z = 0.2$ ). The three clusters below  $z = 0.3$  in the cosmological sample of Hasselfield et al. (2013) were targeted by Rines et al. (2013), namely ACT-CLJ0152.7+0100 (Abell 267), ACT-CLJ2129.6+0005 (RX J2129.6+0005) and ACT-CLJ2337.6+0016 (Abell 2631). We include these three clusters in our analysis. Rines et al. (2013) also measured redshifts using xcsao; we use only galaxies with redshift quality flags 'Q' or '?', which correspond to secure redshifts for high- and medium-quality spectra, respectively (Rines et al. 2013).

Additionally, the cluster ACT-CLJ0239.8–0134 ( $z = 0.375$ ) is the well-studied, HST Frontier Fields<sup>14</sup> cluster Abell 370. Despite extensive lensing studies (e.g. Medezinski et al. 2010; Richard et al. 2010; Hoekstra et al. 2012; von der Linden et al. 2014a), there is no modern spectroscopic data on this cluster. A search in the NASA/IPAC Extragalactic Database<sup>15</sup> (NED) gives roughly 100 galaxies with redshifts in the range  $0.30 \leq z \leq 0.45$ , which safely includes all potential cluster members (we then run our membership algorithm on these galaxies, see Section 3.3.1). These galaxies go out to  $6'$  in radius. For homogeneity, we limit ourselves to redshifts measured either by Soucail et al. (1988) or Dressler et al. (1999) since these two sources make up the majority ( $\approx 90$  per cent) of galaxies returned by NED. We assign to each galaxy an uncertainty at the level of the last non-zero digit.

---

<sup>13</sup><http://skyserver.sdss9.org/public/en/home.aspx>

<sup>14</sup><http://www.stsci.edu/hst/campaigns/frontier-fields/>

<sup>15</sup><http://ned.ipac.caltech.edu>

### 3.2.6 Comparison between redshift measurements

There are many overlapping galaxies between SDSS and other data, as well as two overlapping galaxies between our SALT/RSS and Gemini/GMOS observations of ACT-CL J0045.2–0152. We compare the spectroscopic redshifts between the different measurements in Figure 3.1. There is good agreement between the different datasets. In particular, the inverse-variance-weighted average differences in rest-frame velocity (defined as  $\delta v_{\text{rest}} = c(z_1 - z_2)/(1 + z_2)$ ) are  $\delta v_{\text{rest}} = -24.2 \pm 53.1 \text{ km s}^{-1}$  (where the errorbar is the uncertainty on the mean) between GMOS and SDSS, with a standard deviation  $\sigma_{\delta v} = 110 \text{ km s}^{-1}$ , and  $\delta v_{\text{rest}} = -5.1 \pm 30.0 \text{ km s}^{-1}$  between HeCS and SDSS, with  $\sigma_{\delta v} = 46 \text{ km s}^{-1}$ . The standard deviations are 2.07 and 1.39 times the average xcsao errors, respectively. We conclude that xcsao underestimates the true cross-correlation velocity uncertainty by up to a factor two, consistent with previous determinations (e.g., Quintana et al. 2000; Boschin et al. 2004; Barrena et al. 2009). HeCS spectra have a higher S/N than GMOS spectra; therefore it is possible that the level of underestimation depends on the S/N of the spectrum.

## 3.3 Velocity Dispersions and Dynamical Masses

### 3.3.1 Velocity dispersion measurements

We use the shifting gapper method developed by Fadda et al. (1996) as implemented in Sifón et al. (2013) to select cluster members, as follows. Assuming the BCG to correspond to the cluster centre<sup>16</sup> (the impact of this assumption is assessed in Section 3.3.7), we bin galaxies by their (projected) cluster-centric distance in bins of at least 250 kpc and 10 galaxies. Therefore member selection in clusters with fewer than 20 redshifts was performed using a single bin (i.e., a standard sigma-clipping). A visual inspection of the phase-space diagrams of clusters with few members suggests that this choice is better than the 15 galaxies used in Sifón et al. (2013), where clusters had an average 65 members over a smaller area of the sky.<sup>17</sup> In each bin in projected distance we sort galaxies by the absolute value of their peculiar velocity (taken initially with respect to the median redshift of potential cluster members). In practice, this means we assume that clusters are symmetric in the radial direction. We then select a main body of galaxies having peculiar velocities  $|v_i| < |v_{i-1}| + 500 \text{ km s}^{-1}$ , where the index  $i$  runs over all galaxies in a

---

<sup>16</sup>The only exception is ACT-CL J2302.5+0002, which we discuss in Section 3.4.6.

<sup>17</sup>The difference in the dynamical masses (which are reported in Section 3.3.4) between using 10 or 15 galaxies as a minimal bin size in the shifting gapper is six per cent, well within the reported errorbars.

given radial bin. In other words, the main body is composed, in each radial bin, by the group of galaxies intersecting  $v = 0$  and bound by velocity differences of less than  $500 \text{ km s}^{-1}$ . All galaxies with peculiar velocities less than  $1000 \text{ km s}^{-1}$  away from the main body are considered cluster members. Modifying the velocity gaps does not have a noticeable impact on our results—all clusters have well defined boundaries in velocity space. This process is iterated, updating the cluster redshift and the radial binning, until the number of members converges (usually two to three iterations).

At every step in the member selection process, cluster redshifts and velocity dispersions are calculated as the biweight estimators of location and scale (i.e., the central value and dispersion, respectively, see equations 5 and 9 of Beers et al. 1990), respectively. We correct the velocity dispersion for individual redshift uncertainties (Danese et al. 1980), but this is a  $< 1$  per cent correction for  $\sigma = 1000 \text{ km s}^{-1}$ . We estimate 68 per cent uncertainties in cluster redshifts and velocity dispersions by bootstrapping over all galaxies within  $3\sigma$  of the measured velocity dispersion, which is always larger than the velocity limit defined by the shifting gapper. Therefore we include galaxies which are rejected by our member selection algorithm, and thus account for uncertainties arising from membership selection in the redshift and velocity dispersion uncertainties. We find that the membership selection process increases the statistical uncertainties in the mass by a median 2 per cent for the full sample (but by  $> 20$  per cent for nine clusters where a large number of objects are rejected by the member selection algorithm). Such a small value is dominated by the southern clusters where, since we targeted the central regions only, the number of galaxies rejected by our algorithm is small compared to the number of members (only 2 per cent, compared to 24 per cent of galaxies rejected for the equatorial clusters). For comparison, we also implement a Bayesian algorithm to estimate velocity dispersions statistically accounting for an interloper component with constant spatial density (Wojtak et al. 2007; Andreon et al. 2008). The Bayesian analysis yields velocity dispersions, as well as uncertainties, that are consistent with our analysis.

Cluster redshifts and velocity dispersions are listed in Table 3.2. We show velocity histograms of clusters in the equatorial and southern samples in Figures 3.13 and 3.14, respectively.

### 3.3.2 Calibrating velocity dispersions with the Multidark simulation

To estimate a possible bias in the velocity dispersions arising from the different optical observations, especially between our southern and equatorial campaigns, we use mock observations of dark matter haloes in the Multidark simulation (Prada et al. 2012). Here we want to understand whether there is a relative bias between

**Table 3.2:** Redshifts, velocity dispersions and dynamical masses of ACT SZ-selected clusters. The horizontal line separates equatorial and southern clusters. Clusters in the cosmological samples of Hasselfield et al. (2013) have a “Cosmo” suffix in the second column. The third and fourth columns give the total number of members,  $N_m$ , and the number of members within  $r_{200}$ ,  $N_{200}$ . We list the maximum radius at which we have spectroscopic members,  $r_{\max}$ , and the velocity dispersion of all members,  $\sigma(< r_{\max})$ , as well as the quantities calculated specifically within  $r_{200}$ . Uncertainties in the masses do not include the scatter in the  $\sigma - M$  scaling relation. Alternative cluster names are given in Menanteau et al. (2013).

Cluster	Sample	$N_m$	$N_{200}$	$z_{\text{cl}}$	$\sigma(< r_{\max})$ ( $\text{km s}^{-1}$ )	$r_{\max}$ ( $r_{200}$ )	$\sigma_{200}$ ( $\text{km s}^{-1}$ )	$r_{200}$ (Mpc)	$M_{200}$ ( $10^{14} \text{ M}_\odot$ )
ACT-CLJ0014.9–0057	S82-Cosmo	62	45	$0.5331 \pm 0.0007$	$806 \pm 91$	1.75	$850 \pm 108$	$1.31 \pm 0.16$	$4.5 \pm 1.6$
ACT-CLJ0022.2–0036	S82-Cosmo	55	44	$0.8048 \pm 0.0014$	$961 \pm 124$	1.71	$1025 \pm 164$	$1.33 \pm 0.20$	$6.6 \pm 3.0$
ACT-CLJ0045.2–0152	DR8	56	44	$0.5483 \pm 0.0010$	$930 \pm 77$	1.40	$967 \pm 88$	$1.45 \pm 0.12$	$6.3 \pm 1.6$
ACT-CLJ0059.1–0049	S82-Cosmo	44	23	$0.7870 \pm 0.0012$	$884 \pm 150$	1.82	$874 \pm 206$	$1.19 \pm 0.28$	$4.6 \pm 3.2$
ACT-CLJ0119.9+0055	S82	16	14	$0.7310 \pm 0.0011$	$725 \pm 128$	1.06	$786 \pm 149$	$1.10 \pm 0.20$	$3.4 \pm 1.9$
ACT-CLJ0127.2+0020	S82	46	46	$0.3801 \pm 0.0008$	$994 \pm 106$	0.92	$991 \pm 108$	$1.64 \pm 0.17$	$7.5 \pm 2.3$
ACT-CLJ0152.7+0100	S82-Cosmo	253	144	$0.2291 \pm 0.0004$	$931 \pm 41$	2.57	$1065 \pm 54$	$1.89 \pm 0.09$	$9.7 \pm 1.4$
ACT-CLJ0206.2–0114	S82-Cosmo	40	23	$0.6758 \pm 0.0010$	$570 \pm 105$	2.02	$625 \pm 164$	$0.94 \pm 0.25$	$2.0 \pm 1.6$
ACT-CLJ0215.4+0030	S82-Cosmo	14	11	$0.8622 \pm 0.0026$	$1386 \pm 262$	1.27	$1256 \pm 268$	$1.57 \pm 0.33$	$11.7 \pm 7.3$
ACT-CLJ0218.2–0041	S82-Cosmo	61	41	$0.6727 \pm 0.0008$	$723 \pm 76$	1.80	$790 \pm 92$	$1.12 \pm 0.12$	$3.4 \pm 1.1$
ACT-CLJ0219.9+0129	DR8	10	10	$0.3651 \pm 0.0014$	$1001 \pm 224$	0.56	$963 \pm 215$	$1.66 \pm 0.36$	$7.6 \pm 5.0$
ACT-CLJ0223.1–0056	S82-Cosmo	38	27	$0.6632 \pm 0.0011$	$829 \pm 96$	1.25	$911 \pm 165$	$1.31 \pm 0.23$	$5.3 \pm 2.8$
ACT-CLJ0239.8–0134	DR8	75	75	$0.3751 \pm 0.0009$	$1216 \pm 128$	0.64	$1183 \pm 128$	$1.94 \pm 0.19$	$12.2 \pm 3.7$
ACT-CLJ0241.2–0018	S82	36	26	$0.6872 \pm 0.0013$	$830 \pm 132$	1.70	$905 \pm 160$	$1.28 \pm 0.22$	$5.1 \pm 2.6$
ACT-CLJ0256.5+0006	S82-Cosmo	78	78	$0.3625 \pm 0.0008$	$1185 \pm 102$	0.59	$1144 \pm 102$	$1.89 \pm 0.16$	$11.2 \pm 2.8$
ACT-CLJ0320.4+0032	S82	25	25	$0.3847 \pm 0.0014$	$1284 \pm 209$	0.56	$1236 \pm 215$	$2.03 \pm 0.34$	$14.3 \pm 7.1$
ACT-CLJ0326.8–0043	S82-Cosmo	62	59	$0.4471 \pm 0.0006$	$897 \pm 96$	1.21	$927 \pm 101$	$1.49 \pm 0.15$	$6.0 \pm 1.8$
ACT-CLJ0342.7–0017	S82	19	19	$0.3072 \pm 0.0015$	$941 \pm 173$	0.80	$930 \pm 173$	$1.64 \pm 0.29$	$6.9 \pm 3.7$
ACT-CLJ0348.6–0028	S82	15	15	$0.3449 \pm 0.0010$	$642 \pm 117$	0.51	$614 \pm 112$	$1.10 \pm 0.19$	$2.2 \pm 1.1$
ACT-CLJ2050.5–0055	S82-Cosmo	33	14	$0.6226 \pm 0.0007$	$539 \pm 120$	2.32	$511 \pm 97$	$0.79 \pm 0.14$	$1.1 \pm 0.6$
ACT-CLJ2050.7+0123	DR8	47	47	$0.3339 \pm 0.0009$	$1046 \pm 104$	0.92	$1043 \pm 103$	$1.76 \pm 0.16$	$8.8 \pm 2.4$
ACT-CLJ2055.4+0105	S82	55	52	$0.4089 \pm 0.0005$	$759 \pm 77$	1.11	$778 \pm 78$	$1.29 \pm 0.12$	$3.8 \pm 1.1$

**Table 3.2:** *Continued.*

Cluster	Sample	$N_m$	$N_{200}$	$z_{\text{cl}}$	$\sigma(< r_{\text{max}})$ ( $\text{km s}^{-1}$ )	$r_{\text{max}}$ ( $r_{200}$ )	$\sigma_{200}$ ( $\text{km s}^{-1}$ )	$r_{200}$ (Mpc)	$M_{200}$ ( $10^{14} M_\odot$ )
ACT-CLJ2058.8+0123	DR8	16	16	$0.3285 \pm 0.0014$	$1109 \pm 196$	0.65	$1080 \pm 191$	$1.86 \pm 0.31$	$10.2 \pm 5.2$
ACT-CLJ2128.4+0135	DR8	59	56	$0.3856 \pm 0.0006$	$895 \pm 116$	1.12	$906 \pm 119$	$1.51 \pm 0.19$	$5.9 \pm 2.2$
ACT-CLJ2129.6+0005	S82-Cosmo	291	68	$0.2337 \pm 0.0005$	$786 \pm 39$	5.05	$859 \pm 91$	$1.56 \pm 0.15$	$5.5 \pm 1.6$
ACT-CLJ2154.5–0049	S82-Cosmo	52	42	$0.4904 \pm 0.0011$	$918 \pm 108$	1.42	$964 \pm 121$	$1.51 \pm 0.18$	$6.6 \pm 2.3$
ACT-CLJ2302.5+0002	S82	47	39	$0.5199 \pm 0.0007$	$648 \pm 67$	1.16	$671 \pm 63$	$1.06 \pm 0.11$	$2.4 \pm 0.7$
ACT-CLJ2337.6+0016	S82-Cosmo	154	51	$0.2769 \pm 0.0007$	$853 \pm 52$	4.85	$879 \pm 96$	$1.56 \pm 0.16$	$5.7 \pm 1.7$
ACT-CLJ0102–4915	South-Cosmo	86	81	$0.8700 \pm 0.0010$	$1273 \pm 114$	1.18	$1284 \pm 117$	$1.55 \pm 0.13$	$11.3 \pm 2.9$
ACT-CLJ0215–5212	South	54	54	$0.4803 \pm 0.0009$	$1027 \pm 110$	0.83	$1018 \pm 111$	$1.59 \pm 0.16$	$7.6 \pm 2.3$
ACT-CLJ0232–5257	South	63	63	$0.5561 \pm 0.0007$	$924 \pm 87$	0.66	$900 \pm 86$	$1.35 \pm 0.12$	$5.2 \pm 1.4$
ACT-CLJ0235–5121	South	80	80	$0.2775 \pm 0.0005$	$1044 \pm 93$	0.48	$994 \pm 92$	$1.74 \pm 0.15$	$8.0 \pm 2.0$
ACT-CLJ0237–4939	South	65	65	$0.3343 \pm 0.0007$	$1290 \pm 91$	0.39	$1210 \pm 91$	$2.01 \pm 0.14$	$13.1 \pm 2.7$
ACT-CLJ0304–4921	South	61	61	$0.3917 \pm 0.0007$	$1098 \pm 98$	0.51	$1050 \pm 96$	$1.71 \pm 0.15$	$8.7 \pm 2.2$
ACT-CLJ0330–5227	South-Cosmo	71	71	$0.4417 \pm 0.0008$	$1247 \pm 96$	0.46	$1182 \pm 98$	$1.85 \pm 0.14$	$11.6 \pm 2.7$
ACT-CLJ0346–5438	South	88	88	$0.5297 \pm 0.0007$	$1081 \pm 76$	0.77	$1066 \pm 75$	$1.60 \pm 0.10$	$8.3 \pm 1.6$
ACT-CLJ0438–5419	South-Cosmo	63	63	$0.4212 \pm 0.0009$	$1268 \pm 109$	0.56	$1221 \pm 108$	$1.93 \pm 0.16$	$12.9 \pm 3.2$
ACT-CLJ0509–5341	South-Cosmo	74	71	$0.4601 \pm 0.0005$	$860 \pm 79$	1.13	$865 \pm 82$	$1.38 \pm 0.12$	$4.9 \pm 1.3$
ACT-CLJ0521–5104	South	19	19	$0.6742 \pm 0.0018$	$941 \pm 194$	0.97	$940 \pm 198$	$1.35 \pm 0.28$	$5.9 \pm 3.6$
ACT-CLJ0528–5259	South	55	44	$0.7676 \pm 0.0010$	$934 \pm 114$	1.45	$984 \pm 125$	$1.30 \pm 0.16$	$5.9 \pm 2.1$
ACT-CLJ0546–5345	South-Cosmo	45	40	$1.0668 \pm 0.0013$	$1020 \pm 138$	1.20	$1018 \pm 148$	$1.13 \pm 0.15$	$5.5 \pm 2.3$
ACT-CLJ0559–5249	South-Cosmo	25	25	$0.6094 \pm 0.0016$	$1085 \pm 136$	0.86	$1078 \pm 137$	$1.55 \pm 0.19$	$8.3 \pm 3.0$
ACT-CLJ0616–5227	South-Cosmo	18	18	$0.6837 \pm 0.0015$	$1156 \pm 193$	0.75	$1139 \pm 190$	$1.58 \pm 0.25$	$9.5 \pm 4.5$
ACT-CLJ0707–5522	South	58	58	$0.2958 \pm 0.0005$	$838 \pm 82$	0.66	$816 \pm 83$	$1.44 \pm 0.14$	$4.6 \pm 1.3$

the two strategies compared to the “true” velocity dispersion. By “true” we mean the line-of-sight velocity dispersion obtained using all the subhaloes found in the simulation within  $r_{200}$ , where  $r_{200}$  is measured directly in the simulation as the distance from the centre of mass within which the density is 200 times the critical density. We begin by describing the Multidark simulation and then describe our mock observations of subhaloes that follow our real observing strategies.

We used haloes from the Multidark BDMW database (Riebe et al. 2013) constructed from the N-body Multidark MDPL simulation (Prada et al. 2012). The Multidark simulation is an N-body simulation containing  $3840^3$  dissipationless particles in a box of length  $1 h^{-1}\text{Gpc}$  and run using a variation of the Gadget2 code (Springel 2005). The halo catalog was constructed using a spherical over-density halo finder that used the bound density maxima algorithm (BDM, Klypin & Holtzman 1997) with an over-density criterion of 200 times the critical density of the Universe. The cosmology used in the simulation is a concordance  $\Lambda\text{CDM}$  model that is consistent with Planck Collaboration (2014a); the parameters are  $\Omega_\Lambda = 0.69$ ,  $\Omega_m = 0.31$ ,  $\Omega_b = 0.048$ ,  $h = 0.68$ , and  $\sigma_8 = 0.82$ . The small differences in cosmological parameters between the simulations and those adopted by us ( $\Omega_m = 0.3$ ,  $h = 0.7$ ) have no impact on our results.

We select all haloes at  $z = 0$  more massive than  $10^{14} h^{-1}\text{M}_\odot$  and containing a minimum number of 50 subhaloes more massive than  $10^{12} h^{-1}\text{M}_\odot$ . A total of 572 haloes meet these criteria. We created mock observations of the Multidark haloes by implementing distinct algorithms for the southern and equatorial strategies to mimic our observational strategies. While the southern campaign was confined to areas  $\approx 5' \times 5'$  around the BCGs, for the equatorial sample we tried to observe as far out as possible (see Section 3.2.3). First, we scaled projected distances of the subhaloes to  $z = 0.5$ , the median redshift of our sample. As our sample spans  $0.25 < z < 1.06$ , an observing field of fixed angular extent contains different fractions of  $r_{200}$ . However, as we show below, the most important parameter is the radial coverage. There is therefore no extra information in scaling distances to different redshifts.

We note that our goal in this section is not to test the membership selection algorithm, and we therefore only include subhaloes in Multidark within  $r_{200}$ . Unbound subhaloes may appear to be part of a cluster in projection, and this can bias velocity dispersion measurements. However, the same member selection and velocity dispersion algorithms used here were applied to mock catalogs including this ‘interloper’ population in Old et al. (2015), who showed that despite this our method is able to recover unbiased mass measurements. Instead, we aim to assess any intrinsic, *relative* biases introduced in our sample by having different observing strategies. We account for the impact of these projection effects as a systematic uncertainty in

our final estimate of the dynamical mass uncertainties (see Section 3.3.4).

To simulate the southern observations, we observed up to 70 galaxies in the inner  $5' \times 5'$  randomly. Given the resolution of Multidark, we were typically able to “observe” 45 subhaloes following this strategy. To recreate the equatorial observations we first identified the approximate major axis of the subhalo distribution for each cluster by taking the mean direction of the 10 largest distances between cluster members. We then created a MOS mask with slits of length  $8''$  along this major axis (axis  $x'$  as per the right panel of Figure 3.2), and observed exactly one subhalo in each slit (unless there were no subhaloes in the slit area). To define which subhalo to “observe,” we selected an object from each slit with a Gaussian distribution around the cluster major axis such that we preferentially, but not exclusively, observed subhaloes close to the line passing through the central subhalo (representing the BCG). This setup led to, on average, 25 subhaloes observed per cluster for the equatorial strategy. Figure 3.2 illustrates our southern and equatorial spectroscopic strategies applied to a halo of the Multidark simulation. Because the number of “observed” subhaloes per halo is lower than the number of observed galaxies per cluster, the statistical uncertainties in the velocity dispersions from the mock observations overestimate the measured uncertainties per cluster. This, however, does not compromise our assessment of a bias introduced by either strategy, and is compensated by the large number of simulated haloes used. We note that the strategies defined above are generalizations (e.g., some clusters in the equator have denser sampling and out to smaller radii). We apply the relevant corrections (see below) to all clusters irrespective of the sample they belong to (that is, southern or equatorial sample), solely based on their particular observational setup.

The residuals in the recovered velocity dispersions with respect to the true halo velocity dispersion (i.e., that determined using all subhaloes, typically 60) are shown in Figure 3.3 for each observational strategy. As a consistency check, we also show the residuals determined from measuring the velocity dispersion from all subhaloes within  $r_{200}$ , as determined iteratively from the mock observations following the procedure described in Section 3.3.1, which are consistent with the true velocity dispersions within the statistical uncertainty. This comparison shows that the adopted scaling relation (see Section 3.3.3) is consistent with the scaling of Multidark haloes and that, in an ideal case where we observe all subhaloes, our estimates of both  $\sigma_{200}$  and  $r_{200}$  (and thereby  $M_{200}$ ) are unbiased.

Figure 3.3 also shows the distribution of velocity dispersions recovered from the simulations for both our observing strategies. For the equatorial strategy the velocity dispersions are unbiased, meaning that the velocity distributions are well sampled within the statistical precision we require—there is no bias introduced by sampling galaxies along a particular direction (but see Skielboe et al. 2012, for

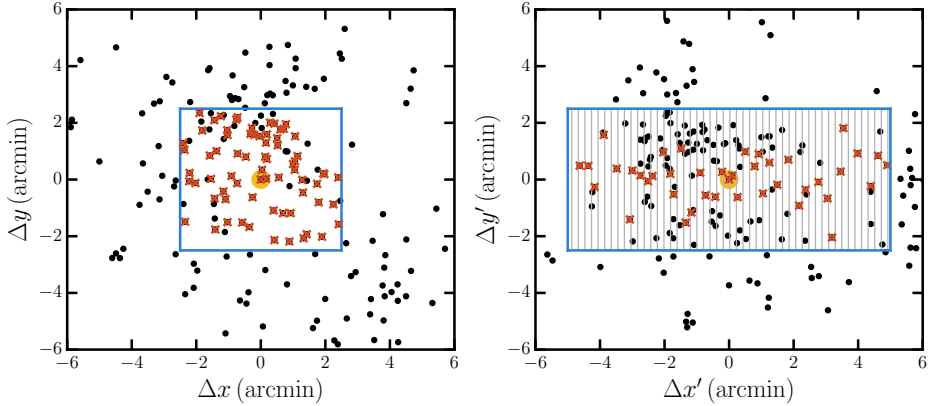


**Figure 3.2:** The two simulated observational strategies, for a Multidark halo of mass  $M_{200} = 1.76 \times 10^{15} M_\odot$ . The same halo is shown in both panels; in the right panel axes are rotated such that the slits are placed along the horizontal axis. Angular distances are scaled to  $z = 0.5$ ; at this redshift, the size  $r_{200}$  of this halo corresponds to  $7.6'$ . Black dots are all halo members, of which red crosses are used to calculate the velocity dispersion. The orange circle in the middle marks the central subhalo, which is always used to calculate the velocity dispersion, and the blue rectangle outlines the field of view. *Left:* the southern strategy, in which we observed up to 70 randomly selected members in the central  $5' \times 5'$ . *Right:* the equatorial strategy, in which we observed an average 25 members inside a  $10' \times 5'$  field of view along the major axis of the subhalo distribution. Grey vertical stripes show the mask slit boundaries, and only one galaxy is observed per slit.

evidence of a preferred direction for the velocity distribution in galaxy clusters). The velocity distribution derived from the southern strategy is, on the other hand, biased by 0.02 dex (corresponding to  $\approx 5$  per cent) on average, which is consistent with the picture of a decreasing velocity dispersion outward from the cluster centre (e.g., Mamon et al. 2010). We correct for this bias by measuring the *true* integrated velocity dispersion profiles for Multidark haloes and scaling them up to  $\sigma_{200} \equiv \sigma(r = r_{200})$ . We list the radial correction  $\sigma(< r)/\sigma_{200}$  and the associated scatter in Table 3.3, and show it in Figure 3.4. While the spread increases towards small apertures, the correction is  $< 10$  per cent at all radii. However, at small radii the scatter is large and must be included in the error estimate when measuring velocity dispersions. We apply this correction to each halo when observed with the southern strategy and are able to recover unbiased velocity dispersions (see Figure 3.3).

### 3.3.3 From velocity dispersions to dynamical masses

In Sifón et al. (2013), we used the  $\sigma - M_{200}$  scaling relation of Evrard et al. (2008) to estimate dynamical masses. As discussed in Section 3.1, the scaling relation of

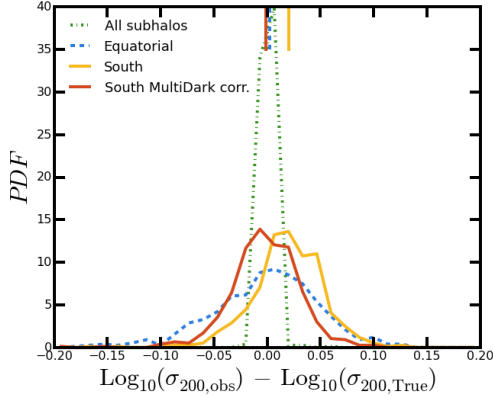


**Figure 3.3:** Probability distribution functions of the residuals between the measured and true velocity dispersions in the Multidark simulation, in logarithmic space. The dash-dotted green, dashed blue, and solid yellow lines show the differences using all subhaloes, an average of 25 subhaloes with the equatorial strategy, and an average of 45 subhaloes with the southern strategy, respectively. The red solid line shows the residuals in the southern strategy after correcting for incomplete sky coverage (see Section 3.3.2). Vertical lines at the top of the figure show the median values.

$r/r_{200}$	$\langle \sigma(<r) \rangle / \sigma_{200}$
0.2	$1.03 \pm 0.27$
0.3	$1.07 \pm 0.17$
0.4	$1.06 \pm 0.11$
0.5	$1.05 \pm 0.08$
0.6	$1.03 \pm 0.05$
0.7	$1.02 \pm 0.04$
0.8	$1.01 \pm 0.02$
0.9	$1.00 \pm 0.01$
1.0	$1.00 \pm 0.00$

**Table 3.3:** Ratio of one-dimensional velocity dispersion within an aperture  $r$ ,  $\sigma(<r)$ , to the one-dimensional velocity dispersion within  $r_{200}$ ,  $\sigma_{200}$ , estimated using subhaloes in the Multidark simulation. Uncertainties are the standard deviations. These values are plotted in Figure 3.4.

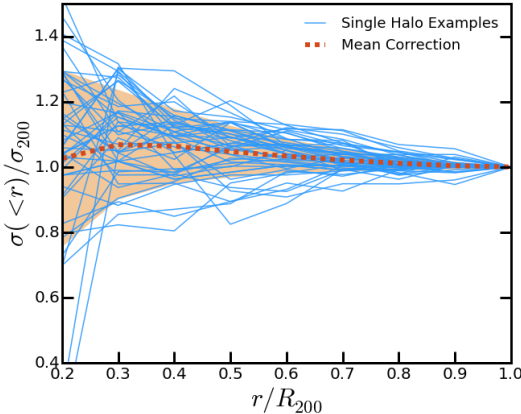


**Figure 3.4:** Enclosed one-dimensional velocity dispersion,  $\sigma(<r)$ , as a function of radius,  $r$ , for subhaloes in Multidark, normalized to  $\sigma_{200}$  and  $r_{200}$ , respectively. The red dashed line is the mean value, and the orange region encloses 68 per cent of the haloes. Blue lines are a random subset of the Multidark haloes. The data for this figure are presented in Table 3.3.

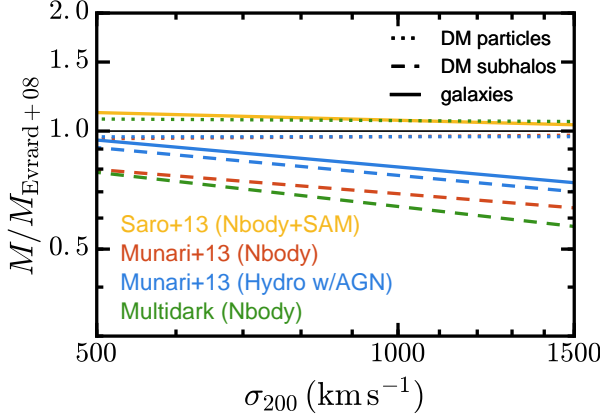


**Figure 3.5:** Comparison between different  $\sigma - M$  scaling relations, relative to the scaling relation of dark matter particles derived by Evrard et al. (2008). Dotted, dashed and solid lines show scaling relations for dark matter particles, dark matter subhaloes and galaxies, respectively. We show the scaling relation for galaxies derived from a semi-analytic model implemented in a dark matter-only simulation by Saro et al. (2013) in yellow. Red and blue lines show the scaling relations derived from dark matter-only and full hydrodynamical simulations, respectively, by Munari et al. (2013), and the green lines show scaling relations from the Multidark simulation. In this work, we calculate dynamical masses using the scaling relation given by the blue solid line.

Evrard et al. (2008) was calibrated from a suite of N-body simulations using dark matter particles to estimate velocity dispersions. However, the galaxies, from which velocity measurements are made in reality do not sample the same velocity distribution as the dark matter (hereafter DM) particles. They feel dynamical friction and some are tidally disrupted, which distorts their velocity distribution and biases their dispersion (e.g., Carlberg 1994; Colín et al. 2000). Recent high resolution hydrodynamical simulations of “zoomed” cosmological haloes have shown that there is a significant difference between the velocity distributions of DM particles and galaxies themselves; whether galaxies (i.e., overdensities of stars in hydrodynamical simulations) or dark matter subhaloes are used makes comparatively little difference (Munari et al. 2013). Results from state-of-the art numerical simulations depend on the exact definition of a galaxy and the member selection applied, but the current consensus is that galaxies are biased high (i.e., at a given mass the velocity dispersion of galaxies or subhaloes is larger than that of DM particles) by 5–10 per cent with respect to DM particles (Lau et al. 2010; Munari et al. 2013; Wu et al. 2013), translating into a positive 15–20 per cent bias in dynamical masses

when using DM particles. This is illustrated in Figure 3.5: DM particles are not significantly impacted by either dynamical friction or baryonic physics; therefore the scaling relations for DM particles are essentially the same for all simulations. In contrast, dark matter subhaloes are affected by baryons in such a way that including baryonic feedback (most importantly feedback from active galactic nuclei (AGN), but also from cooling and star formation) makes their velocity dispersions much more similar to those of simulated galaxies. This means we can rely on our analysis of the previous section, based on dark matter subhaloes, to correct the velocity dispersions measured for ACT clusters, and then estimate dynamical masses using predictions obtained either from galaxies or subhaloes. The difference between the Saro et al. (2013) and Munari et al. (2013) galaxy scaling relations depends on the details of the semi-analytic and hydrodynamical implementations used in Saro et al. (2013) and Munari et al. (2013), respectively. The different cosmologies used in the Millennium simulation (in particular,  $\sigma_8 = 0.9$ ; Springel et al. 2005) by Saro et al. (2013) and the simulations by Munari et al. (2013) ( $\sigma_8 = 0.8$ ) may also play a role.

We therefore use the scaling relation between the projected galaxy velocity dispersion and mass estimated by Munari et al. (2013), obtained from zoomed-in hydrodynamical simulations of dark matter haloes, that includes prescriptions for cooling, star formation, and AGN feedback,

$$\sigma_{200} = A_{1D} \left[ \frac{h E(z) M_{200}}{10^{15} M_\odot} \right]^\alpha \quad (3.1)$$

where  $\sigma_{200}$  is the 3-dimensional velocity dispersion of galaxies within  $r_{200}$ , divided by  $\sqrt{3}$  (i.e., the line-of-sight velocity dispersion in a spherical cluster),  $E(z) = [\Omega_\Lambda + (1+z)^3 \Omega_m]^{1/2}$ ,  $A_{1D} = 1177 \pm 4.2 \text{ km s}^{-1}$ , and  $\alpha = 0.364 \pm 0.002$ . The intrinsic scatter *at fixed mass* in Equation 3.1 is of order 5 per cent, or  $\approx 15$  per cent in mass (Munari et al. 2013), but this value does not include the effect of interlopers (that is, impurity in the member sample), which can increase the intrinsic scatter by up to a factor two (Biviano et al. 2006; Mamon et al. 2010; White et al. 2010; Saro et al. 2013). This is an irreducible uncertainty since there is always a fraction of contaminating galaxies that cannot be identified by their peculiar velocities because they overlap with the velocity distribution of actual members (see, e.g., figure 10 of White et al. 2010). Hence we adopt a figure of 30 per cent for each cluster's mass uncertainty arising from interlopers in the member sample. Note that we automatically account for the velocity bias,  $b_v$ , by adopting a scaling relation based on simulated galaxies rather than dark matter particles (see Section 3.3.4 for further discussion).

The velocity dispersion measurements were obtained for a pre-selected set of clusters, and the sample was not further refined based on these measurements. So

**Table 3.4:** Individual cluster mass uncertainty budget, given as a fraction of cluster mass. Central values are the medians of the cluster distributions and uncertainties are 16th and 84th percentiles; upper limits are 84th percentiles. The median is equal to zero for all values with upper limits. “Reported” uncertainties correspond to those in Table 3.2, which arise from the combination of the three effects preceding them, while “total” uncertainties include the 30 per cent scatter from the  $\sigma - M$  scaling relation, which is fixed for all clusters, added in quadrature. The 15% uncertainty in the velocity bias is an overall uncertainty on the average masses.

Source	Equator	South	All
Statistical	$0.31^{+0.21}_{-0.08}$	$0.25^{+0.09}_{-0.03}$	$0.28^{+0.20}_{-0.06}$
Member selection	$0.14^{+0.18}_{-0.14}$	$< 0.01$	$0.04^{+0.18}_{-0.04}$
Multidark correction	$< 0.12$	$0.07^{+0.18}_{-0.07}$	$< 0.18$
<b>Reported</b>	<b>0.36</b>	<b>0.26</b>	<b>0.31</b>
Scatter in $M(\sigma)$	0.30	0.30	0.30
<b>Total</b>	<b>0.47</b>	<b>0.40</b>	<b>0.44</b>
Velocity bias uncertainty	0.15	0.15	0.15

although the measurements are affected by noise and intrinsic scatter, we can expect positive and negative noise and scatter excursions to be equally likely. The dynamical mass measurements on this sample are thus not affected by Eddington bias; this is discussed further in Section 3.A. We therefore calculate dynamical masses by directly inverting Equation 3.1, which gives  $\sigma(M)$ , in order to obtain  $M(\sigma)$ . For this computation we take the uncertainty on  $\sigma$  to be normal, and report the mean and standard deviation of  $M(\sigma)$  after propagating the full error distribution.<sup>18</sup> We note that this procedure can yield biased dynamical masses if velocity dispersion and SZ effect measurements are correlated for individual clusters (Evrard et al. 2014). In fact, we may expect some degree of correlation between any pair of observables for a given cluster, because the same large scale structure is affecting all cluster observables (White et al. 2010). We defer a proper treatment of correlations between observables to future work.

### 3.3.4 Dynamical mass estimates

The masses thus estimated are listed in Table 3.2, along with the redshifts, velocity dispersions, number of members used and  $r_{200}$ . We also list the radius at which our spectroscopic coverage ends,  $r_{\max}$ , and the initial velocity dispersion measured within  $r_{\max}$ . Below we summarize the corrections applied with respect to our anal-

<sup>18</sup>The error distribution is normal in  $\sigma$  but not in  $M \propto \sigma^{1/\alpha}$  (with  $1/\alpha \approx 3$ ). Therefore the mean mass is not the cube of the central value of  $\sigma$ . This difference depends only on the measurement uncertainty and for our sample its median is 3 per cent, with a maximum of 16 per cent for ACT-CLJ0206.2-0114.

ysis in Sifón et al. (2013) and then present a detailed account of uncertainties entering our dynamical mass estimates, before comparing our mass estimates with masses derived from SZ measurements.

Two sources of bias are now accounted for that were not included in Sifón et al. (2013). The first is the radial coverage of spectroscopic members (which was discussed, but not corrected for, in Sifón et al. 2013) which includes (i) an iterative calculation of the velocity dispersion within  $r_{200}$  only for 24 clusters with  $r_{\max} > r_{200}$  and (ii) a correction to the velocity dispersion, based on the velocity dispersion profile of subhaloes in the Multidark simulation (see Figure 3.4), for 20 clusters with  $r_{\max} < r_{200}$ . Over the full sample these two situations produce a net correction of –5 per cent, compared to applying no correction as in Sifón et al. (2013). The second source of bias is the relation between the velocity dispersion of dark matter particles and that of galaxies. We account for this difference by using the  $\sigma - M$  scaling relation of galaxies derived by Munari et al. (2013), which gives average masses 20 per cent lower than those derived from the scaling relation of Evrard et al. (2008) used in Sifón et al. (2013). In addition, we have updated the minimum bin size in our member selection algorithm (cf. Section 3.3.1), which lowers the masses by an average 6 per cent with respect to the value adopted in Sifón et al. (2013). Because of these updates to our analysis, for the southern clusters we report masses that are, on average,  $(71 \pm 8)$  per cent of those reported in Sifón et al. (2013).

We present a breakdown of the contributions to individual cluster mass uncertainties for the equatorial and southern samples in Table 3.4. The uncertainty budget is dominated by the scatter induced by interlopers. Based on the discussion presented in Section 3.3.3, we estimate that this uncertainty amounts roughly to 30% in mass. Because this contribution corresponds to a constant uncertainty for all clusters, we do not include them in the uncertainties reported in Table 3.2. We do recommend this 30% systematic (i.e., that cannot be reduced by observing more galaxies) uncertainty to be added to the reported uncertainties in any cosmological analysis that uses these dynamical masses, and we include it in our calculation of the SZ mass bias in Section 3.3.5. Similarly, based on the discussion in Section 3.1, we adopt a 15 per cent systematic uncertainty arising from the unknown velocity bias (5% in velocity; e.g., Wu et al. 2013). This 15 per cent essentially accounts for i) the fact that our galaxy sample may not correspond to the galaxy samples used by Munari et al. (2013) to arrive at Equation 3.1 (because the velocity bias is luminosity-dependent), and ii) differences in scaling relations compared to that of Munari et al. (2013) that may arise because of different hydrodynamical implementations (each producing a different velocity bias). The unknown velocity bias therefore limits our constraints on the SZ mass bias (see Section 3.3.5).

Statistical uncertainties are the dominant contribution to the reported uncertainties, with a median contribution of 28% of the cluster mass. Uncertainties from member selection and the scatter in the correction of Table 3.3 are subdominant. We note here that by “member selection” we mean uncertainties arising from including or rejecting particular galaxies through the shifting gapper. The true uncertainty from contaminating galaxies is included in the scaling relation scatter as discussed in Section 3.3.3. We make this distinction because there is a fraction of false members which cannot be identified observationally via their peculiar velocities (e.g., Mamon et al. 2010; White et al. 2010; Saro et al. 2013). For the SZ-selected clusters of the South Pole Telescope survey, Ruel et al. (2014) found that the uncertainty from member selection, estimated by “pseudo-observing” their stacked cluster, depends on the number of galaxies observed. For the number of members we observed (which is roughly a factor two larger than the average number of members observed by Ruel et al. 2014), their estimate of the combined statistical and member selection uncertainty is consistent with ours.

### 3.3.5 Comparison to SZ-derived masses

The usefulness of clusters for constraining cosmological parameters depends on the accurate calibration of the cluster mass scale. Calibrated SZ masses are especially informative because SZ surveys yield large samples of clusters reaching to high redshifts. While our dynamical and SZ mass proxies may have non-trivial mass or redshift-dependence, the data in our study permit us to constrain the average bias between these proxies within the mass range probed in this study.

We compare the dynamical masses to the SZ-derived masses,  $M_{500}^{\text{SZ}}$ , in Figure 3.6. For the purpose of this comparison we rescale dynamical masses to  $M_{500}$  using the mass-concentration relation of Dutton & Macciò (2014). The SZ-derived masses assume a scaling relation between the SZ effect (specifically,  $Y_{500}$ ) and mass based on the pressure profile of Arnaud et al. (2010), derived from X-ray observations of local ( $z < 0.2$ ) clusters, and have been corrected for Eddington bias as detailed in Hasselfield et al. (2013), assuming a 20 per cent intrinsic scatter in  $Y_{500}$  at fixed true mass (the “UPP” masses of Hasselfield et al. 2013). We refrain from fitting a scaling relation to these data since this requires a proper calibration of the survey selection effects and accounting for the mass function and cosmological parameters; the dynamical mass–SZ scaling relation and inferred cosmological parameters will be presented in a future paper.

Beyond the assumptions used to obtain the SZ masses, any additional bias in the inferred mass relative to the true cluster mass is often parametrized in terms of the SZ mass bias,  $1 - b_{\text{SZ}}$  (e.g., Planck Collaboration 2015c), defined by the relation  $\langle M_{\text{SZ}} | M_{\text{true}} \rangle = (1 - b_{\text{SZ}})M_{\text{true}}$ . An understanding of this calibration

is essential to the cosmological interpretation of cluster counts from SZ surveys. Similarly, our dynamical masses may be biased proxies for the true cluster mass. Following Hasselfield et al. (2013), we parametrize this bias with  $\beta_{\text{dyn}}$ , defined by  $\langle M_{\text{dyn}} | M_{\text{true}} \rangle \equiv \beta_{\text{dyn}} M_{\text{true}}$ . For the remainder of this section we use the word “bias” to refer to systematic effects on the sample, such as “Eddington bias,” that do not average down to an expectation value of zero with an increasing sample size.

The SZ and dynamical mass data permit us to place limits on the ratio  $(1 - b_{\text{SZ}})/\beta_{\text{dyn}}$  by comparing the average SZ and dynamical masses of the clusters from the cosmological sample. We first combine the dynamical masses into a single characteristic mass

$$\bar{M}_{\text{dyn}} \equiv \frac{\sum_i w_i M_{i,\text{dyn}}}{\sum_i w_i}, \quad (3.2)$$

where the  $M_{i,\text{dyn}}$  represent the individual dynamical mass measurements, and the  $w_i$  are weighting factors. For this analysis we set all  $w_i = 1$ , but see below for further discussion of the choice of weights. We also compute the error, through standard error analysis.<sup>19</sup> For the SZ masses, we form the analogous sum,  $\bar{M}_{\text{SZ}} \equiv (\sum_i w_i M_{i,\text{SZ}})/(\sum_i w_i)$ . Note that the weights  $w_i$  used in this expression are the same weights used to compute  $\bar{M}_{\text{dyn}}$ ; this is essential to obtaining an unbiased answer when we later combine the two characteristic masses.

Each mass measurement is contaminated by intrinsic scatter and noise, in the sense that

$$\bar{M}_{i,\text{dyn}} = M_{i,\text{true}} e^{\xi_i} + \delta M_i, \quad (3.3)$$

where  $\delta M_{i,\text{true}} \sim \mathcal{N}(0, \epsilon_i)$  is the contribution from measurement noise, and  $\xi_i \sim \mathcal{N}(0, 0.3)$  is the contribution from intrinsic scatter. The expectation value for  $\delta M_i$  is zero, while the expectation value of  $e^{\xi_i}$  is 1.046. So when we combine our measurements into a characteristic mass we expect that

$$\langle \bar{M}_{\text{dyn}} \rangle = \frac{\sum_i w_i \langle M_{i,\text{dyn}} \rangle}{\sum_i w_i} = 1.046 \beta_{\text{dyn}} \frac{\sum_i w_i M_{i,\text{true}}}{\sum_i w_i}. \quad (3.4)$$

For the combination of the SZ masses, the expectation value is  $\langle \bar{M}_{\text{SZ}} \rangle = 1 - b_{\text{SZ}}$ , because the skewness introduced by intrinsic scatter has already been fully accounted for in the calculation of the  $M_{\text{SZ}}$  values used here by Hasselfield et al. (2013). Taking the ratio of these two characteristic masses gives

$$\frac{\langle \bar{M}_{\text{SZ}} \rangle}{\langle \bar{M}_{\text{dyn}} \rangle} = \frac{(1 - b_{\text{SZ}})}{1.046 \beta_{\text{dyn}}}. \quad (3.5)$$

---

<sup>19</sup>The error in  $\bar{M}$  is  $(\sum_i w_i^2 \epsilon_i^2)^{1/2}/(\sum_i w_i)$ , where  $\epsilon_i$  is the error in  $M_i$ .

Our measured values of  $\bar{M}_{\text{SZ}}$  and  $\bar{M}_{\text{dyn}}$  thus provide a useful measurement of  $(1 - b_{\text{SZ}})/\beta_{\text{dyn}}$ . (We show in Section 3.A that this ratio is unbiased.) For the 21 clusters in the cosmological sample, the characteristic dynamical mass under uniform weights is  $\bar{M}_{\text{dyn}} = (4.8 \pm 0.5) \times 10^{14} M_{\odot}$ , and the characteristic SZ mass is  $\bar{M}_{\text{SZ}} = (5.0 \pm 0.2) \times 10^{14} M_{\odot}$ . The ratio of calibration factors is then

$$\frac{(1 - b_{\text{SZ}})}{\beta_{\text{dyn}}} = 1.10 \pm 0.13 \text{ (stat.)} \pm 0.14 \text{ (syst.)} \quad (3.6)$$

where the 0.14 systematic uncertainty arises from the 15% fractional uncertainty on the average dynamical masses due to the unknown velocity bias discussed in Section 3.3.4. We note again that, in computing Equation 3.6, we have accounted for the 30 per cent scatter in the  $M(\sigma)$  relation (see Section 3.3.3) which is not included in the cluster mass uncertainties reported in Table 3.2 and shown in Figure 3.6. Recent estimates of the SZ mass bias combining weak lensing measurements and SZ mass estimates from Planck Collaboration (2015b) have found  $M_{\text{SZ}}/M_{\text{WL}} \approx 0.7$  (von der Linden et al. 2014b; Hoekstra et al. 2015). These measurements were then used as priors for the cosmological analysis of Planck SZ-selected clusters (under the assumption that  $\langle M_{\text{WL}} \rangle = \langle M_{\text{true}} \rangle$ , Planck Collaboration 2015c), highlighting the importance of calibrating these biases. We note that both von der Linden et al. (2014b) and Hoekstra et al. (2015) probed higher masses than we do. In fact, both works found evidence (at 95 per cent confidence) for a mass-dependent bias which, at the typical masses of ACT clusters, is consistent with our estimate. Similar to us, Rines et al. (2016) found no evidence that the mass ratio  $\langle \bar{M}_{\text{SZ}} \rangle / \langle \bar{M}_{\text{dyn}} \rangle$  is different from unity, using dynamical masses estimated with the caustic technique, in a mass regime similar to ours.

Battaglia et al. (2015) used a stacked weak lensing measurement on a subset of these clusters, which they fit using hydrodynamical simulations, and found an SZ mass bias  $1 - b_{\text{SZ}} = \bar{M}_{\text{SZ}}/\bar{M}_{\text{WL}} = 0.98 \pm 0.28$  (assuming  $\langle M_{\text{WL}} | M_{\text{true}} \rangle = M_{\text{true}}$ , as has been assumed in recent studies). This value has been computed with weights that depend on the weak lensing measurements. As a consistency check, we estimate the average dynamical mass of the nine clusters used by Battaglia et al. (2015), using the same weak lensing weights, and find  $\bar{M}_{\text{dyn-WL}} = (4.7 \pm 1.4) \times 10^{14} M_{\odot}$ , which implies a mass ratio  $\bar{M}_{\text{dyn-WL}}/\bar{M}_{\text{WL}} = 0.98 \pm 0.33$ . Therefore the dynamical masses are consistent with the weak lensing masses derived by Battaglia et al. (2015).

We have used uniform weights  $w_i = 1$  to obtain the ratio in Equation 3.6, but one might expect that more carefully chosen weights could provide a more precise answer. In fact the weights should be chosen with some care, as it is possible to introduce a bias into this ratio if one permits the weights to depend too much

on the measured data themselves. For example, if we take weights  $w_i = 1/\epsilon_{i,\text{dyn}}^2$  (where  $\epsilon_{i,\text{dyn}}$  is the measurement uncertainty on the velocity dispersion of cluster  $i$ ), we find that clusters with low dynamical mass are more strongly weighted, because the dynamical mass uncertainties are strongly correlated with the dynamical mass measurements. However, the SZ masses are limited by sample selection effects to lie above some minimum value, and the characteristic SZ mass under these weights is almost twice the characteristic dynamical mass. A somewhat weaker effect is that these weights (i.e., the  $w_i$  above) have the potential to introduce a sort of Eddington bias into the computation, even though we carefully constructed a sample for which the dynamical mass measurements were unbiased. By re-weighting the clusters in a way that is correlated with the dynamical mass measurements themselves, we are effectively sub-selecting for measurements that are more likely to have scattered below the true mass values.

To avoid such biases, one should not incorporate dynamical mass or its uncertainty into the weights. Similarly, one should be wary of using the measured SZ masses and uncertainties to set the weights. In the present data, using weights  $w_i = 1/\epsilon_{i,\text{SZ}}^2$  or  $w_i = M_{i,\text{SZ}}^2/\epsilon_{i,\text{SZ}}^2$  changes the resulting ratio by +3 or -2 per cent, respectively, without reducing the uncertainty. We discuss alternative weighting schemes in Section 3.A.

### 3.3.6 Cluster substructure

Probes of substructure within a galaxy cluster provide information on a cluster's dynamical state: for example, whether or not a recent merger event has occurred. Since the thermodynamic properties of clusters vary depending on their dynamical state, a measurement of the amount of substructure provides an important additional cluster property. Of particular interest to SZ experiments is how the integrated  $Y$  parameter fluctuates with dynamical state. Simulations have shown that  $Y$  can fluctuate by tens of percent shortly after merger events (e.g., Poole et al. 2007; Wik et al. 2008; Krause et al. 2012; Nelson et al. 2012), and that the intrinsic scatter of the  $Y - M$  scaling relation for a subsample of relaxed clusters is smaller than for the entire sample (e.g., Battaglia et al. 2012; Yu et al. 2015). The latter conclusion was also reached by Sifón et al. (2013), albeit with low statistical significance.

Because of the sparser spectroscopic sampling used for the equatorial clusters, it is more difficult to identify localized substructure than it is with our dense sampling of the southern clusters (which is, however, confined to a smaller region of the cluster). We therefore refrain from a detailed, cluster-by-cluster analysis of substructure in the equatorial sample as we did for the southern clusters in Sifón et al. (2013). However, it is still valuable to study the presence of substructure in the sample as

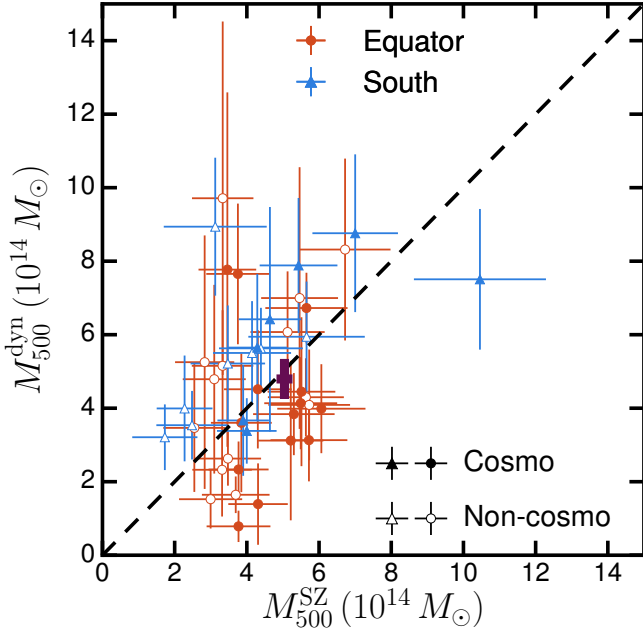


**Figure 3.6:** Comparison of dynamical and SZ-derived masses. Red circles and blue triangles show clusters in the equatorial and southern samples, respectively. Uncertainties on dynamical masses correspond to those reported in Table 3.2, and for clarity do not include the 30% scatter in the  $M(\sigma)$  relation. The dashed line shows equality and the purple cross shows the average SZ and dynamical masses of the combined southern and equatorial cosmological samples (filled symbols), calculated including the 30% intrinsic scatter in the  $M(\sigma)$  relation on the dynamical masses. There is an additional 15% overall uncertainty on dynamical masses arising from the unknown galaxy velocity bias. See Section 3.3.5 for details.

a whole, to be able to compare between our equatorial and southern samples, and whether the SZ selects different cluster populations than other techniques.

We use two quantities used by Sifón et al. (2013) to study cluster substructure. The first is the peculiar velocity of the BCG,  $v_{\text{BCG}} = c(z_{\text{BCG}} - z_{\text{cl}})/(1+z_{\text{cl}})$ , where  $z_{\text{cl}}$  is the cluster redshift listed in Table 3.2. Based on the results of Section 3.2.6, we assume an error of  $100 \text{ km s}^{-1}$  on  $v_{\text{BCG}}$ . The second estimator we use is the DS test (Dressler & Shectman 1988), which measures the deviation of the velocity distribution in localized regions of a cluster with respect to the cluster as a whole through the statistic  $\Delta = \sum_i \delta_i$ , where

$$\delta^2 = \frac{N_{\text{local}}}{\sigma^2} \left[ (\bar{v}_{\text{local}} - \bar{v})^2 + (\sigma_{\text{local}} - \sigma)^2 \right]^2 \quad (3.7)$$

is calculated for each galaxy, where  $\bar{v}_{\text{local}}$  and  $\sigma_{\text{local}}$  are the mean and dispersion of

the velocity distribution of the  $N_{\text{local}}$  nearest neighbors, where typically  $N_{\text{local}} = \sqrt{N_{200}}$ . For each cluster we compare  $\Delta$  to 1000 realizations where we shuffle the galaxy velocities, keeping their positions fixed.  $\mathcal{S}_\Delta$  is then the probability to exceed the  $\Delta$  measured for the clusters, given statistical fluctuations as determined through these realizations. We calculate 68 per cent level uncertainties on  $\mathcal{S}_\Delta$  by varying  $N_{\text{local}}$  in the range  $\sqrt{N_{200}} - 3 \leq N_{\text{local}} \leq \sqrt{N_{200}} + 3$ . Typically,  $\mathcal{S}_\Delta < 0.05$  is taken as evidence for substructure (Pinkney et al. 1996). See Sifón et al. (2013) for more details.

We compare in Figure 3.7 the distributions of (absolute values of) BCG peculiar velocities,  $|v_{\text{BCG}}|$ , and  $\mathcal{S}_\Delta$  to those found in the Multidark simulation. In general, the southern sample shows more evidence of substructure than the equatorial sample through the DS test, with 38 per cent and 22 per cent, respectively, having  $\mathcal{S}_\Delta < 0.05$ . In turn, 31 per cent of Multidark clusters fulfill this criterion. Two-sided Kolmogorov-Smirnov tests, however, show no evidence of the distributions of either  $\mathcal{S}_\Delta$  or  $|v_{\text{BCG}}|$  being different between the southern, equatorial and Multidark samples (all  $p$ -values from the KS tests are  $\gtrsim 0.20$ ). In Sifón et al. (2013), we selected clusters as non-relaxed (i.e., containing substructure) if, among other properties, they had  $|v_{\text{BCG}}| > 0$  at 95 per cent confidence. In the southern sample 50 per cent of clusters pass this test, while 41 per cent (11/27) of the clusters in the equatorial sample do. This 40–50 per cent rate of non-relaxed clusters is somewhat lower than fractions found for X-ray– and optically–selected clusters (e.g., Böhringer et al. 2010; Wen & Han 2013). Using mock cluster observations, Lin et al. (2015) showed that the SZ significance can be boosted by up to 10 per cent for cool core (i.e., relaxed) clusters depending on the redshift, cuspiness and size of the cluster. This would then lead to a preferential selection of relaxed clusters, qualitatively consistent with our results. The fact that this bias is not apparent when comparing to Multidark clusters may relate to the fact that Multidark is a dark matter only simulation, but a detailed comparison is beyond the scope of this work.

### 3.3.7 The impact of centring on the BCG

As mentioned in Section 3.3.1, we have assumed that the BCGs correspond to the centre of the cluster potential. In this section we estimate the impact of this assumption on the reported masses.

We first re-calculate the velocity dispersions for all clusters assuming that the cluster centre is the centre of light instead of the BCG. To estimate the centre of light we take the luminosity-weighted average position of photometric members using photometric redshifts estimated by Menanteau et al. (2013) using the Bayesian Photometric Redshift (BPZ) code (Benítez 2000). The average mass ratio

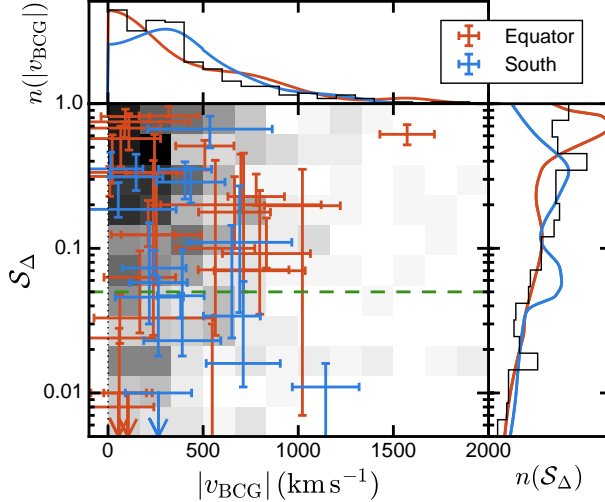


**Figure 3.7:** Comparison between BCG peculiar velocity and DS test significance level for the southern (blue) and equatorial (red) samples, and haloes in the Multidark simulation (grey scale background, where zero is white and one is black, and black histograms). The green, dashed horizontal line shows the threshold  $S_\Delta = 0.05$ , below which the DS test is usually considered to provide evidence for substructure. The *top* and *right* panels show the corresponding histogram for the Multidark simulation and the summed probability distribution functions for the southern (blue) and equatorial (red) clusters, normalized to subtend the same area as the histograms.

is  $\langle M_{\text{CoL}}/M_{\text{BCG}} \rangle = 1.01 \pm 0.09$  with a standard deviation of 0.16, which is within the quoted mass uncertainties. Note that Viola et al. (2015) have shown, using weak lensing measurements, that the centre of light is generally significantly offset from the true cluster centre while BCGs are, on average, consistent with being at the centre of the cluster potential.

We also looked for clusters whose BCG cannot be identified unambiguously because there are other similarly bright member galaxies. Three southern (ACT-CL J0215–5212, ACT-CL J0232–5257 and ACT-CL J0521–5104) and four equatorial (ACT-CL J0239.8–0134, ACT-CL J0256.5+0006, ACT-CL J2055.4+0105 and ACT-CL J2302.5+0002) clusters fall under this category (see Menanteau et al. 2010b, 2013, for optical images of ACT clusters; Section 3.4 for more detailed comments on some of these clusters). We estimate the masses of these clusters once more, taking the next most probable BCG candidate (where this is determined by visual inspection) as the cluster centre. In all cases the mass difference is well within the reported uncertainties.

From these two tests we conclude that uncertainties due to the choice of clus-

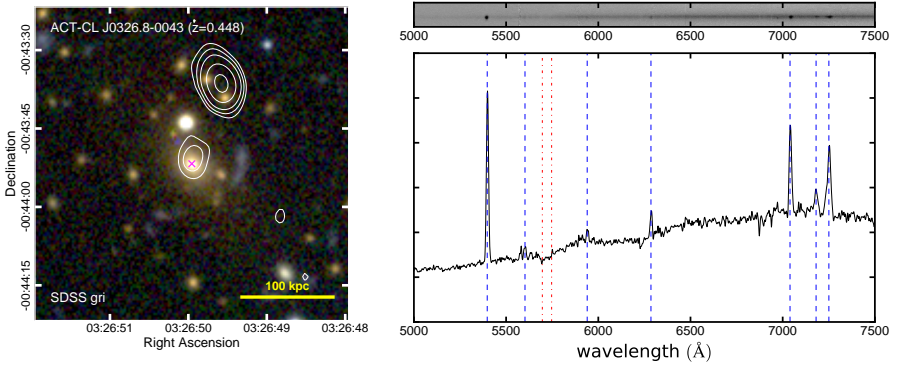


**Figure 3.8:** The BCG of ACT-CL J0326.8–0043 at  $z = 0.45$ . *Left:* Optical *gri* image from SDSS with 1.4 GHz contours from the FIRST survey overlaid in white and shown at  $(3, 5, 8, 15, 25)\sigma$  levels, where  $\sigma = 0.14 \text{ mJy beam}^{-1}$ . The BCG is marked with a magenta cross and the thick yellow line in the bottom-right corner is 100 kpc wide, corresponding to  $17.^{\prime\prime}4$  at the cluster redshift. North is up and East is left. *Right:* Optical one- (bottom) and two-dimensional (top) Gemini/GMOS spectra. The former is smoothed with a 3-pixel boxcar. In the bottom panel, detected emission lines are marked with dashed blue lines (in order of increasing wavelength: [O ii], Ne iii, H $\delta$ , H $\gamma$ , H $\beta$  and [O iii] $\lambda\lambda 4959, 5007$ ); the Ca ii K,H absorption doublet is marked with dash-dotted red lines. The asymmetric broadening of the [O iii] $\lambda 5007$  line is an artifact introduced by interpolating the GMOS chip gaps. The vertical axis is in arbitrary units.

ter centre are within the quoted errorbars and therefore cluster centring does not introduce any biases or additional uncertainties on our mass estimates.

## 3.4 Notable clusters

In this section we describe some notable clusters in the equatorial sample in more detail. Similar notes on southern clusters can be found in Sifón et al. (2013). We first summarize ACT clusters that have been studied in detail elsewhere and then discuss individual clusters.

### 3.4.1 Previously studied ACT clusters

El Gordo (ACT-CL J0102–4915,  $z = 0.87$ , Menanteau et al. 2012) is probably the most massive cluster known at  $z > 0.8$  (Jee et al. 2014b). It is a merging system composed of two roughly equal-mass subclusters colliding approximately perpendicular to the line-of-sight (Zitrin et al. 2013; Jee et al. 2014b), probably seen about 1 Gyr after core passage (Ng et al. 2015). It hosts the highest-redshift known radio relics and halo (Lindner et al. 2014). Its dynamical mass ( $M_{200} =$

$(1.13 \pm 0.29) \times 10^{15} M_{\odot}$ , cf. Table 3.2) is significantly smaller than the total mass estimated from weak lensing ( $M_{200} = (2.84 \pm 0.51) \times 10^{15} M_{\odot}$ , Jee et al. 2014b), but the former can be expected to be biased when such an extreme system is assumed to be composed of a single component (as is the case here for consistency with the rest of the sample). As a result of the major merger, the total stellar mass in El Gordo is lower than the expectation based on its SZ effect (Hilton et al. 2013).

ACT-CL J0022.2–0036 ( $z = 0.81$ ) is the highest-significance detection in the S82 sample (Hasselfield et al. 2013). The dynamical mass is consistent with independent mass estimates from weak lensing (Miyatake et al. 2013), optical richness and high-resolution SZ measurements (Reese et al. 2012), giving an inverse-variance-weighted average mass of  $M_{200} = (7.8 \pm 0.9) \times 10^{14} M_{\odot}$  (see also the discussion in Menanteau et al. 2013).

ACT-CL J0256.5+0006 ( $z = 0.36$ ) was studied in detail by Knowles et al. (2015). It is one of the lowest-mass systems known to host a giant radio halo, which is likely produced by the interaction of two systems with a mass ratio of approximately 2:1 being observed prior to the first core crossing. The merging scenario is supported by the velocity distribution (ACT-CL J0256.5+0006 has  $\mathcal{S}_{\Delta} < 0.01$  at 68 per cent confidence) and X-ray observations; there are two X-ray peaks coincident with two dominant galaxies. The velocity dispersions of the two components suggests that the reported mass, which assumes a single component, may be biased high by roughly 40 per cent, an amount comparable to the quoted uncertainty.

ACT-CL J0320.4+0032 ( $z = 0.385$ ) is one of the few clusters whose BCG is known to host a type II quasar (Kirk et al. 2015). The low number of observed members precludes a detailed analysis of the cluster structure, but we note that a maximally-predictive histogram (Knuth 2006) of the galaxy velocities shows two peaks and a somewhat asymmetric distribution (see Figure 3.14), which suggests that ACT-CL J0320.4+0032 is a dynamically young cluster.

### 3.4.2 ACT-CL J0218.2–0041

ACT-CL J0218.2–0041 ( $z = 0.673$ ) is one of the lowest-mass clusters in the sample (Table 3.2). In addition to the cluster itself, we have identified in our spectroscopic data an overdensity of eight galaxies at  $z = 0.82$ . Their velocity dispersion, while not necessarily representative of this system’s velocity dispersion, is  $\sigma_{\text{gal}} = 880 \text{ km s}^{-1}$ , which would suggest a mass  $M > 10^{14} M_{\odot}$ . We additionally identified a structure of 12 galaxies around  $z = 0.73$  which, although it only spans  $6000 \text{ km s}^{-1}$ , has  $\sigma_{\text{gal}} = 2320 \text{ km s}^{-1}$ , suggesting that the structure is probably not collapsed.

Two of the three structures have velocity dispersions that suggest cluster-sized systems. The fact that we detect these overdensities, instead of non-members be-

ing scattered in redshift space, suggests that ACT-CL J0218.2–0041 may be associated with a larger cosmic structure along the line of sight, with two relatively massive clusters at  $z = 0.67$  and  $z = 0.82$  possibly connected by a filament (the  $z = 0.73$  structure). For comparison, we also detected additional galaxy overdensities in the lines of sight of ACT-CL J0235–5121 (7 galaxies at  $z = 0.44$ ) and ACT-CL J0215.4+0030 (8 galaxies at  $z = 0.39$ ), which have  $\sigma_{\text{gal}} = 280 \text{ km s}^{-1}$  and  $\sigma_{\text{gal}} = 170 \text{ km s}^{-1}$ , respectively. This shows that low-mass groups may in fact be identified with our observations—that is, the structures detected behind ACT-CL J0218.2–0041 are not likely to be low mass groups. This large-scale scenario is also appealing given the low mass of ACT-CL J0218.2–0041. It would be interesting to explore the impact of this structure on the measured SZ effect, and similarly on X-ray emission, but this is deferred to future work.

### 3.4.3 ACT-CL J0326.8–0043

ACT-CL J0326.8–0043 ( $z = 0.447$ ) was first discovered as part of the Massive Cluster Survey (MACS J0326.8–0043, Ebeling et al. 2001). The left panel of Figure 3.8 shows a SDSS *gri* image of the centre of the cluster, with 1.4 GHz contours from the Faint Images of the Radio Sky at Twenty centimetres (FIRST, Becker et al. 1995) survey overlaid in white. The BCG (which we refer to simply as J0326 in the remainder of this section) shows strong emission lines across the optical spectrum (Figure 3.8, right panel). Because our Gemini/GMOS spectrum is not flux-calibrated we use the line measurements from the SDSS MPA/JHU Value-Added Galaxy Catalog (Brinchmann et al. 2004) throughout. We cannot distinguish whether the emission in J0326 is dominated by star formation or an AGN from the line ratio diagnostic introduced by Lamareille (2010), appropriate for high-redshift ( $z > 0.4$ ) objects for which H $\alpha$  falls outside the optical wavelength range (specifically,  $\log([\text{O ii}]\lambda\lambda 3726 + 3729/\text{H}\beta) = 0.57 \pm 0.03$  and  $\log([\text{O iii}]\lambda 5007/\text{H}\beta) = -0.23 \pm 0.03$ ).

The left panel of Figure 3.8 shows that there is additionally significant 1.4 GHz emission from a point source whose peak is offset 1. $''$ 2 (7 kpc) from the BCG (but note that the positional uncertainty in the FIRST source is  $\approx 1''$ ), but again the nature of the emission cannot be determined. In the case of star forming galaxies with no AGN contamination, the 1.4 GHz luminosity can be used as an unobscured tracer of star formation. The 1.4 GHz luminosity of the source associated to the BCG is  $\log L_{1.4}/(\text{W Hz}^{-1}) = 24.0$ , which at face value implies a star formation rate (SFR) of several hundred  $M_{\odot} \text{ yr}^{-1}$  (Hopkins et al. 2003). In contrast, the [O ii] $\lambda 3727$  doublet suggests a SFR of a few tens of  $M_{\odot} \text{ yr}^{-1}$ . Systems with such marked differences in estimated SFRs are almost always AGN hosts (J. Brinchmann, private communication). Chang et al. (2015) fitted spectral energy distri-

butions to optical SDSS data plus mid infrared data from the Wide-field Infrared Survey Explorer (WISE, Wright et al. 2010) of one million objects. For J0326 they estimated a best-fit star formation rate of  $\text{SFR} = 15^{+10}_{-5} \text{ M}_\odot \text{ yr}^{-1}$ , consistent with the radio emission being dominated by nuclear activity. If this is the case then J0326 is a new Type II AGN BCG (Type I AGNs are characterized by broad components in the [O iii] lines), similar to the case of the BCG of ACT-CL J0320.4+0032 recently reported by Kirk et al. (2015) and noted in Section 3.4.1. Therefore J0326 probably adds to the very sparse sample of Type II AGNs in BCGs (see references in Kirk et al. 2015).

Gilmour et al. (2009) analyzed a 10 ks *Chandra* observation of ACT-CL J0326.8–0043 and found no evidence for an X-ray point source in the BCG location to suggest the presence of an AGN; however, the observations are too shallow to draw any firm conclusions. While available X-ray data are not sufficient to establish the cooling rate in the cluster core, all evidence points to a fairly relaxed cluster. There is no evidence for substructure from the velocity distribution;  $v_{\text{BCG}} = 205 \pm 147 \text{ km s}^{-1}$  suggests the BCG is located at the centre of the potential; and the magnitude gap to the second-brightest member (based on photometric redshifts to avoid a bias due to spectroscopic incompleteness) is relatively large,  $\Delta m_{12} = 1.62$ , which is also an indication of a dynamically old cluster (e.g., Wen & Han 2013).

### 3.4.4 ACT-CL 2050.5–0055

The BCG of ACT-CL 2050.5–0055 ( $z = 0.623$ ; hereafter simply “the BCG”) has the highest peculiar velocity of all BCGs in the ACT sample. In fact, the BCG is rejected by our member selection algorithm, with a peculiar velocity of  $v_{\text{BCG}} = -(1572 \pm 143) \text{ km s}^{-1}$ , different from zero at  $11\sigma$ , compared with a cluster velocity dispersion  $\sigma_{200} = (511 \pm 97) \text{ km s}^{-1}$ , the lowest  $\sigma_{200}$  in the entire sample (cf. Table 3.2). The BCG also has a redshift in the SDSS catalogue,  $z_{\text{SDSS}} = 0.6133 \pm 0.0002$ , which would make  $v_{\text{BCG}}$  more negative by about  $200 \text{ km s}^{-1}$  (compared to  $z_{\text{Gemini}} = 0.6141 \pm 0.0003$ ). For the purpose of this discussion, this difference is not important and we will continue to use  $z_{\text{Gemini}}$  throughout. Such a high  $v_{\text{BCG}}$  probably originated as a result of either merging activity or strong galaxy-galaxy interactions in the centre (Martel et al. 2014). Regarding the possibility of a cluster-scale merger, the DS test does not reveal any evidence for substructure, although we do not have enough member galaxies to draw firm conclusions. As seen in Figure 3.7, there are haloes in our Multidark sample that have comparable BCG velocities but they tend to have lower values of  $\mathcal{S}_\Delta$  than ACT-CL 2050.5–0055.

Coziol et al. (2009) studied a sample of 452 BCGs in low-redshift clusters, and found that BCGs have, on average,  $|v_{\text{BCG}}| = 0.32\sigma$  (where  $\sigma$  is the cluster velocity dispersion), with only three BCGs having velocities  $|v_{\text{BCG}}| > 2\sigma$ . In comparison,

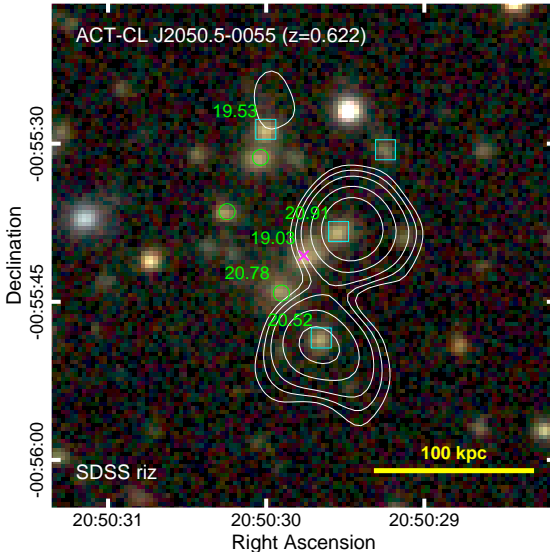


**Figure 3.9:** Optical *riz* image of the central region of ACT-CL J2050.5–0055 ( $z = 0.62$ ) from SDSS, with 1.4 GHz contours from the FIRST survey overlaid in white at  $(3, 5, 8, 15, 25)\sigma$  levels, where  $\sigma = 0.15 \text{ mJy beam}^{-1}$ . The BCG is marked with a magenta cross; cyan squares show other spectroscopically confirmed cluster members and green circles show bright photometric redshift members. Green numbers to the top-left of the five brightest cluster members correspond to dereddened  $i$ -band magnitudes from SDSS. The thick yellow line in the bottom-right corner is 100 kpc wide, corresponding to  $14.^{\circ}7$  at the cluster redshift. North is up and East is left.

the BCG of ACT-CL 2050.5–0055 has  $v_{\text{BCG}} = -(3.1 \pm 0.7) \sigma_{200}$ .<sup>20</sup> Similarly, all the BCGs studied by Coziol et al. (2009) have  $|v_{\text{BCG}}| < 1500 \text{ km s}^{-1}$ . Therefore the BCG of ACT-CL 2050.5–0055 is unique in this respect; it will be interesting to study the conditions that led to such high  $|v_{\text{BCG}}|$ . All other spectroscopic members in the cluster centre (Figure 3.9) have peculiar velocities between  $-550$  and  $350 \text{ km s}^{-1}$ , consistent with the low cluster velocity dispersion.

Figure 3.9 shows FIRST contours overlaid on an SDSS *gri* image of the central region of ACT-CL 2050.5–0055. There are two point-like sources coinciding with two galaxies within 100 kpc from the BCG. The integrated 1.4 GHz luminosities of the northern and southern sources are  $\log L_{1.4}/(\text{W Hz}^{-1}) = 25.1$  and  $25.0$ , respectively. Such high luminosities suggest that indeed these are point sources rather than extended emission originating in the ICM. All spectroscopic members

<sup>20</sup>Including the BCG in the member sample by hand increases the cluster velocity dispersion to  $\sigma_{200} = (607 \pm 107) \text{ km s}^{-1}$ , yielding  $v_{\text{BCG}} = -(2.6 \pm 0.5) \sigma_{200}$ .

shown in Figure 3.9 have spectra typical of passive, elliptical galaxies with no signs of activity, with strong Ca ii K,H absorption and no optical emission lines.

We also show in Figure 3.9 the dereddened  $i$ -band magnitudes from the SDSS catalog for the five brightest galaxies (spectroscopic and photometric members). The BCG is brighter than any other galaxy by 0.5 mag. In combination with its central location relative to the galaxy distribution, it is unlikely that the BCG is not the central galaxy of the cluster. In particular, the galaxies that coincide with radio sources are only the third and fifth brightest galaxies, making it unlikely that any of them is the central galaxy. We conclude that misidentification of the central galaxy is unlikely to explain the high  $|v_{\text{BCG}}|$  reported for this cluster.

### 3.4.5 ACT-CL J2055.4+0105

As mentioned in Section 3.3.7, the identification of the BCG is not obvious for this cluster at  $z = 0.409$ . In fact, we identify four galaxies along a straight line extending 1.2 Mpc SE of the BCG (the BCG is the one further NW of the four), the faintest of which is only 0.86 mag fainter than the BCG (all four galaxies are spectroscopically confirmed). Two of the four galaxies (the first and third brightest, and in the NW-SE line joining them, which are separated by 940 kpc) have extended light envelopes characteristic of cD galaxies. Only the fiducial BCG is clearly surrounded by a large overdensity of red galaxies, suggesting it is indeed the central galaxy. The fact that its peculiar velocity is consistent with zero also supports this scenario. The “alternative BCG” velocity (of  $-700 \text{ km s}^{-1}$ ) shown in Figure 3.14 corresponds to this secondary cD galaxy; the other two galaxies have peculiar velocities of less than  $400 \text{ km s}^{-1}$ .

Overall, this elongated configuration with multiple dominant galaxies strongly suggests that ACT-CL J2055.4+0105 is undergoing a major merger between at least two massive subclusters, and possibly more. The DS test does not reveal any evidence for substructure ( $\mathcal{S}_\Delta = 0.81 \pm 0.10$ ), but we note that this is also the case for El Gordo (Sifón et al. 2013). This is because the DS test (nor, indeed, dynamical information in general) is not sensitive to mergers happening along the plane of the sky. As with other clusters described in this section, more data would be required for a detailed assessment of this system.

### 3.4.6 ACT-CL J2302.5+0002

ACT-CL J2302.5+0002 at  $z = 0.520$  is also one of the lowest-mass clusters in the sample. We show the central 300 kpc of this cluster in Figure 3.10, which shows strong evidence that the brightest galaxy is not the *central* cluster galaxy: the second-brightest galaxy, 130 kpc away, shows strong 1.4 GHz emission and

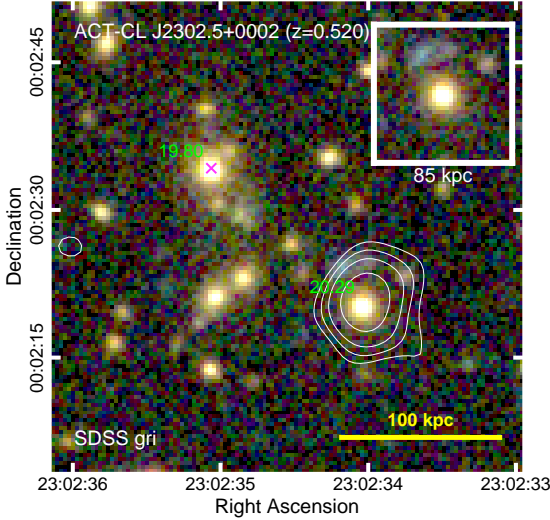


**Figure 3.10:** Optical SDSS *gri* image of the inner 300 kpc of ACT-CL J2302.5+0002. Symbols, labels and contours are as in Figure 3.9. The inset in the top-right corner is 85 kpc on a side and shows the region around the second-brightest galaxy without the radio contours, which show what appears to be a strongly lensed background image. The thick yellow line in the bottom-right corner is 100 kpc wide, corresponding to 16.<sup>''</sup>0 at the cluster redshift. North is up and East is left.

what appears to be a strongly lensed background galaxy around it. The coordinates given by Menanteau et al. (2013) indeed correspond to the brightest galaxy, but for our purposes we take the second-brightest galaxy as the cluster centre. ACT-CL J2302.5+0005 is therefore the only cluster for which we do not take the brightest galaxy as the cluster centre in Section 5.4.3. As mentioned in Section 3.3.7, adopting either galaxy as the centre gives consistent mass estimates; using the brightest galaxy instead of the central one we obtain  $M_{200} = (1.9 \pm 0.7) \times 10^{14} M_\odot$ , compared to the fiducial value of  $M_{200} = (2.4 \pm 0.7) \times 10^{14} M_\odot$ . We do not detect any optical emission lines in either galaxy.

Although such clear examples of brightest galaxies not being the central galaxy are rare, the value of the separation between the two galaxies is not uncommon (Skibba et al. 2011; Martel et al. 2014). Martel et al. (2014) have argued that the positional offset of the BCG is not as robust an indication of major mergers as the velocity offset,  $v_{\text{BCG}}/\sigma$ , where  $\sigma$  is the cluster velocity dispersion. As shown in Figure 3.14, both galaxies have large peculiar velocities, with  $v = -470 \text{ km s}^{-1}$  ( $v/\sigma_{200} = 0.70$ ) and  $v = -600 \text{ km s}^{-1}$  ( $v/\sigma_{200} = 0.89$ ) for the central and bright-

est galaxies, respectively. Similar to (but less extreme than) the BCG in ACT-CL J2050.5–0055, these peculiar velocities—especially given the small cluster velocity dispersion—strongly suggest that ACT-CL J2302.5+0002 is undergoing a major merger (Martel et al. 2014), but the available data do not allow us to perform a more detailed analysis.

### 3.5 Conclusions

We have carried out a spectroscopic follow-up effort of ACT SZ-selected clusters in the equatorial survey in the redshift range  $0.3 < z < 0.9$ . Combined with our previous follow-up program of the southern clusters and archival data, we present velocity dispersions and dynamical masses for 44 clusters at  $0.24 < z < 1.06$  with a median of 55 spectroscopic members per cluster.

We calibrate our velocity dispersion measurements using the Multidark simulation, taking into account the spectroscopic coverage of clusters which is qualitatively different for southern and equatorial clusters, owing to the different optical imaging available (namely, targeted  $5' \times 5'$  observations in the south and full SDSS coverage in the equator, Figure 3.2). We find that velocity dispersions are unbiased so long as the measurement includes galaxies out to  $r_{200}$  but the azimuthal distribution of spectroscopic targets is not important for our purposes (see Section 3.3.2 and Figure 3.3). We use the average radial velocity dispersion profile of subhaloes in Multidark to correct measurements for clusters whose coverage does not reach  $r_{200}$  and include the uncertainties from this correction (Table 3.3) in the reported velocity dispersions.

We use a scaling relation between galaxy velocity dispersion and cluster mass derived from zoomed cosmological hydrodynamical simulations to infer dynamical masses consistently for the full sample of clusters with spectroscopic observations. We make a detailed assessment of the different contributions to the reported mass uncertainties, which are dominated by a  $\approx 30$  per cent scatter in the scaling relation induced by interlopers, triaxiality and the intrinsic scatter of the relation. Because this is a constant value, we do not include this contribution in the reported cluster mass uncertainties but recommend that it be included in cosmological analyses derived from these data. Statistical uncertainties from our average 55 members per cluster are comparable to said scatter, while uncertainties from member selection and the spectroscopic aperture selection are subdominant.

The updated dynamical mass estimates of the southern clusters are, on average, 71 per cent of the masses presented in Sifón et al. (2013). This overall difference results from (i) accounting for the observing strategies used to get the galaxy redshifts when calculating cluster velocity dispersions (Section 3.3.2), and (ii) using a

$\sigma - M_{200}$  scaling relation that includes the effects of baryonic physics and dynamical friction (Section 3.3.3). We find that masses derived from the SZ effect assuming a scaling relation based on the pressure profile of Arnaud et al. (2010) are consistent with the dynamical masses and report a mass bias which results from the combination of the dynamical mass bias and the SZ bias,  $(1 - b_{\text{SZ}})/\beta_{\text{dyn}} = \bar{M}_{500}^{\text{SZ}}/\bar{M}_{500}^{\text{dyn}} = 1.10 \pm 0.13$ , with an additional 0.14 systematic uncertainty due to the unknown galaxy velocity bias (see Figure 3.6 and Section 3.3.5), consistent with previous estimates from the literature if one accounts for the different mass regimes. Hasselfield et al. (2013) used the dynamical masses of Sifón et al. (2013) as prior information on the cosmological analysis derived from the SZ cluster counts and found that dynamical masses suggested a higher  $\sigma_8$  than other cosmological probes. The new, lower dynamical masses will bring the estimate of  $\sigma_8$  down. A cosmological analysis incorporating these new dynamical mass estimates will be presented in a future paper.

We also highlight five newly-characterized clusters. ACT-CL J0218.2–0041 ( $z = 0.67$ ) appears to be part of a structure where two cluster-sized systems are connected by a filament along the line of sight. The BCG of ACT-CL J0326.8–0043 ( $z = 0.45$ ) is likely a rare Type II AGN host which also seems to be associated with strong radio emission. The BCG of ACT-CL 2050.5–0055 ( $z = 0.62$ ) has a peculiar velocity of  $v_{\text{BCG}} = 3\sigma_{200}$  and is surrounded by double-peaked (probably point-source) radio emission. ACT-CL J2055.4+0105 ( $z = 0.41$ ) has four bright, locally-dominant galaxies separated by 1.2 Mpc along a straight line. Finally, ACT-CL J2302.5+0002 ( $z = 0.52$ ) is a clear example of the brightest galaxy not being the central cluster galaxy, confirmed by the presence of a strong lensing arc around the second-brightest galaxy. Further follow-up studies will reveal more details about these intriguing systems.

The uncertainty on the average dynamical mass is dominated by the scatter in the  $\sigma - M$  relation (see Table 3.4), which cannot be significantly reduced by observing more galaxies per cluster. Ntampaka et al. (2015b) recently developed a machine learning approach to measure dynamical masses which incorporates information about the distribution of galaxies and their velocities to predict cluster masses, which has been successfully applied to mock observations that include the effects of impurity and incompleteness, reducing the errors by up to 60 per cent (Ntampaka et al. 2015a). Further tests on more realistic galaxy catalogues will assess its effectiveness in measuring galaxy cluster masses in real observations.

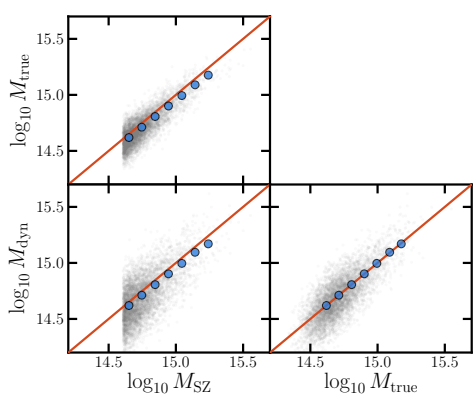


**Figure 3.11:** Comparison of SZ, dynamical, and true cluster masses for a mock catalog that incorporates a simple model for noise, scatter and selection effects. The gray points are individual mock clusters. The blue points show the mean masses for several bins in  $M_{\text{SZ}}$ . Because the binning is based on the measured  $M_{\text{SZ}}$  value, the binned  $M_{\text{SZ}}$  are consistently higher than the binned  $M_{\text{true}}$  (upper left panel). In contrast, the  $M_{\text{dyn}}$  are not affected by Eddington bias (lower right panel) and lie on the  $y = x$  (red) line.

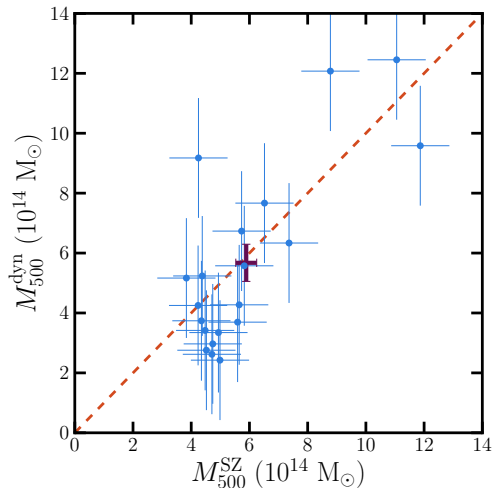


**Figure 3.12:** Masses of 20 clusters drawn from a large mock catalog that simulates noise, scatter, and selection effects. Purple cross shows the mean characteristic SZ and dynamical mass, computed under uniform weights. As in Figure 3.6, error-bars in the individual cluster masses include only the noise contribution and not intrinsic scatter.

### 3.A Eddington bias and selection effects

In this appendix we discuss the SZ and dynamical mass measurements in the context of understanding potential biases, such as Eddington bias (Eddington 1913), that might affect the comparison of the two mass proxies. We then demonstrate with a simple simulation that the method used in Section 3.3.4 to determine the ratio  $(1 - b_{\text{SZ}})/\beta_{\text{dyn}}$  is unbiased.

The SZ masses used in this work have been corrected for Eddington bias by Hasselfield et al. (2013). The calculation accounts for the fact that the underlying mass function is falling steeply as mass increases, so a direct inversion of  $y_{\text{SZ}}(M)$  gives a biased estimate of  $M(y_{\text{SZ}})$  (Evrard et al. 2014). The computation of the correction requires certain assumptions, such as the form of the cluster mass function

and the survey selection function, which is constructed assuming a particular model for the SZ signal and an assumption about the degree of intrinsic scatter. Under these assumptions the correction is then computed in a Bayesian framework, with the posterior probability of a cluster's mass given by  $P(M|y) \propto P(y|M)n(M)$ , where the likelihood  $P(y|M)$  accounts for intrinsic scatter and measurement noise and the prior  $n(M)$  is the cluster mass function (see section 3.2 of Hasselfield et al. 2013).

Aside from the modelling assumptions, it is important to note that the correction is no longer valid if we change the underlying distribution of cluster masses upon which the ACT selection is effectively acting. For example, if we were to remove objects from the sample based on some auxiliary information (such as X-ray flux, or membership in an optical cluster survey), then we would risk complicating the underlying mass function and invalidating the Eddington bias correction applied in Hasselfield et al. (2013).

However, there are many ways to sub-sample the ACT sample without changing the validity of the Eddington bias correction. Restricting the survey to a smaller region of the sky, or to a particular redshift range<sup>21</sup> does not affect the Eddington bias correction. Although less obvious, it is also true that raising the S/N threshold of the catalog does not change the correction (though of course this will change the membership of the sample). While the S/N threshold affects the survey selection function (which we take to mean the probability that a cluster of some mass and redshift would be included in the sample), it does not affect the underlying distribution of masses which we should consider when working with a particular cluster that has been detected. In a Bayesian framework, the posterior distribution for any one cluster's mass is not dependent on the overall survey selection function. The cosmological sample considered in this work satisfies the requirements above, and so we take the masses of Hasselfield et al. (2013), which have been corrected for Eddington bias, to be unbiased on average.

The dynamical masses presented in this work were obtained for all clusters passing certain redshift and S/N cuts (i.e., those in the cosmological sample of Hasselfield et al. 2013), and the present measurements were not used to refine the sample further. Though noise and scatter will certainly affect the velocity dispersion measurements, we expect positive and negative noise (or scatter) excursions to be equally likely. The dynamical mass measurements thus constitute a complete set of “follow-up” observations for the sample, and are not affected by Eddington bias.

While the descriptions above can be justified formally (see Evrard et al. 2014), we illustrate their validity using mock catalogs of SZ and dynamical mass mea-

---

<sup>21</sup>The redshift cut can in principle affect the bias correction due to uncertainty in the cluster redshifts; in practice the redshift uncertainties are small enough that this is not significant.

surements. We draw a large number of masses,  $M_{\text{true}}$ , from a realistic cluster mass function, considering a single redshift. We create SZ and dynamical mass proxy measurements by adding intrinsic scatter (at the 20 and 30 per cent levels, respectively) and measurement noise (fixed at  $10^{14} M_{\odot}$  and  $2 \times 10^{14} M_{\odot}$ , respectively) to the true masses. Then we simulate the effect of SZ selection by keeping only mock clusters with  $M_{\text{SZ}} > 4 \times 10^{14} M_{\odot}$ .

In Figure 3.11 we show these mock clusters, and demonstrate that if we bin the objects according to their  $M_{\text{SZ}}$  measurement, we see Eddington bias effects in  $M_{\text{SZ}}$  relative to the true cluster mass, but  $M_{\text{dyn}}$  is not biased. In the real observations, the Eddington bias in  $M_{\text{SZ}}$  is corrected by modeling the mass function and SZ scaling relation. For the mock study we simply fit a constant bias factor to the binned  $M_{\text{SZ}}$  and  $M_{\text{true}}$  points and use it to correct the individual mock  $M_{\text{SZ}}$  values.

We then take a random subsample consisting of 20 mock clusters, to roughly match the size of the real sample considered in this work. We compute the characteristic SZ and dynamical mass of these clusters, under uniform weights, as was done in Section 3.3.5. The resulting ratio is consistent, as expected, with unity. This subsample and the characteristic masses are plotted in Figure 3.12.

We also repeat the entire procedure for alternative weighting schemes. We find that weighting schemes that incorporate the measured dynamical masses are significantly biased. For example, if we take the weights to be the inverse square of the combined measurement error and intrinsic scatter, the characteristic dynamical mass is 10 per cent lower, on average, than the characteristic SZ mass. Such biases are also seen in weights that include the fractional measurement error (which requires the input of the measured mass), or weights that incorporate the intrinsic scatter contribution (which scales in proportion to the measured mass). The real data contain additional correlations between dynamical mass and measurement error beyond those modeled in this simple simulation, because more massive clusters also tend to have more galaxies that can be used to measure the dispersion. For these reasons it is clear that one should not incorporate the dynamical mass measurements and errors into the weights unless the impact can be fully modelled.

In contrast, for this simulation we find that weighting by the inverse square of the SZ mass error (including the contribution from intrinsic scatter) does not bias the mass comparison. This is because we have already corrected the SZ masses to make them unbiased, even under weights (or selection choices) that depend on the measured SZ mass.

### 3.B Velocity histograms

We show in Figures 3.13 and 3.14 the velocity histograms for all clusters (only member galaxies are shown). We show histograms with bins of  $400 \text{ km s}^{-1}$  and with a constant bin size that maximizes the predictive power of the histogram in a Bayesian sense (Knuth 2006)<sup>22</sup>.

---

<sup>22</sup>We use the version implemented in the `plotting` library of `astroML` (VanderPlas et al. 2012).

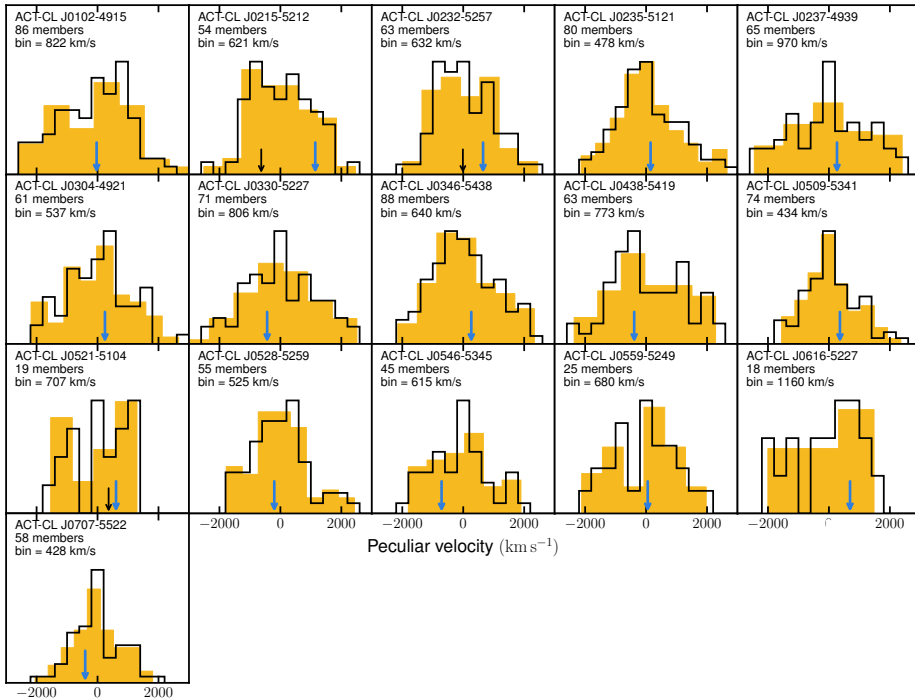


**Figure 3.13:** Velocity histograms of all clusters in the southern sample. Black empty histograms have a bin size of  $400 \text{ km s}^{-1}$  and filled yellow histograms have a bin size indicated in the legend, which is such that the predictive power of the histogram (i.e., the likelihood that the next datum will fall in a given bin) is maximized using a bayesian approach. We show normalized counts and list the number of members in each cluster in the legends (see also Table 3.2). Blue arrows mark the BCG velocities and, where applicable, smaller black arrows mark peculiar velocities of alternative choices for the BCG (see Sections 3.3.7 and 3.4). BCG velocities have a typical uncertainty of  $\approx 100 \text{ km s}^{-1}$ .

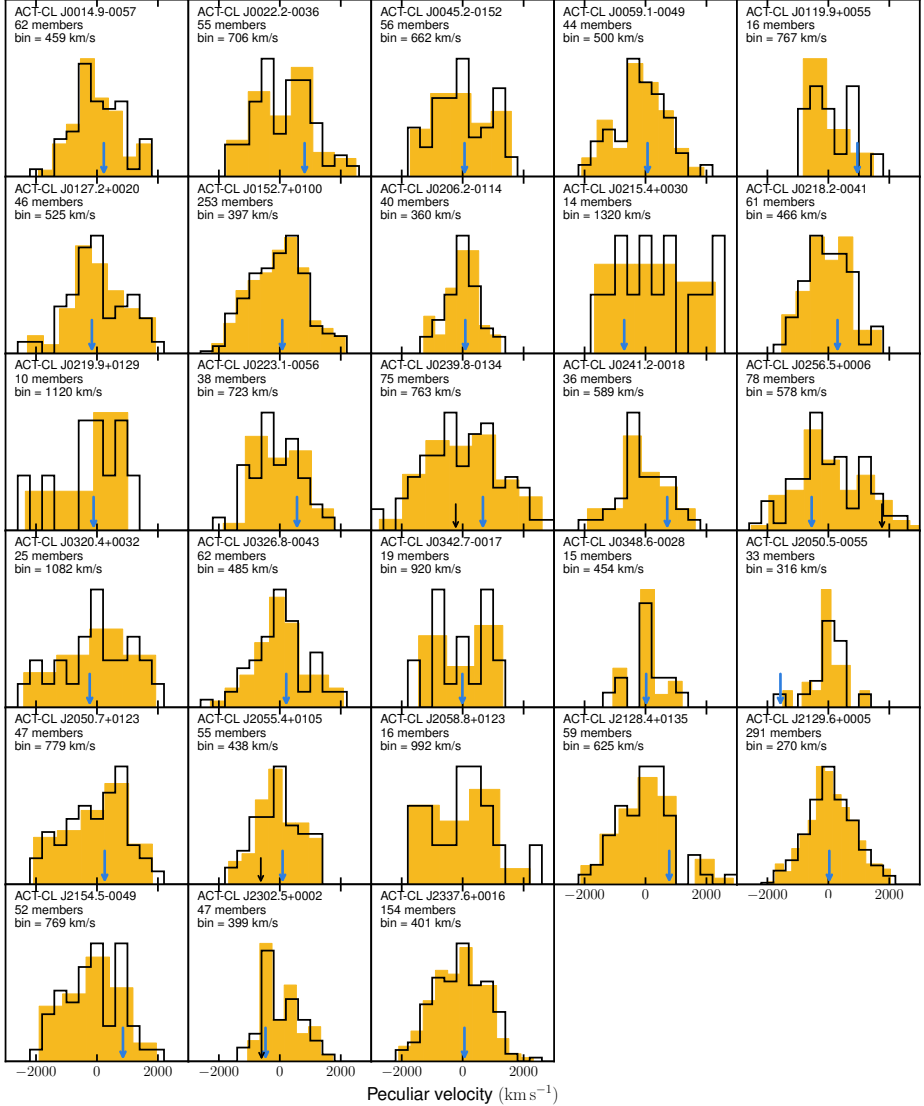


**Figure 3.14:** Rest-frame velocity histograms of all clusters in the equatorial sample. Styles are the same as Figure 3.14. We do not know the redshift of the BCG of ACT-CL J2058.8+0123.

# 4 | Galaxy alignments in massive clusters from $\sim$ 14,000 spectroscopic members

Torques acting on galaxies lead to physical alignments, but the resulting ellipticity correlations are difficult to predict. As they constitute a major contaminant for cosmic shear studies, it is important to constrain the intrinsic alignment signal observationally. We measured the alignments of satellite galaxies within 90 massive galaxy clusters in the redshift range  $0.05 < z < 0.55$  and quantified their impact on the cosmic shear signal. We combined a sample of 38,104 galaxies with spectroscopic redshifts with high-quality data from the Canada-France-Hawaii Telescope. We used phase-space information to select 14,576 cluster members, 14,250 of which have shape measurements and measured three different types of alignment: the radial alignment of satellite galaxies toward the brightest cluster galaxies (BCGs), the common orientations of satellite galaxies and BCGs, and the radial alignments of satellites with each other. Residual systematic effects are much smaller than the statistical uncertainties. We detect no galaxy alignment of any kind out to at least  $3r_{200}$ . The signal is consistent with zero for both blue and red galaxies, bright and faint ones, and also for subsamples of clusters based on redshift, dynamical mass, and dynamical state. These conclusions are unchanged if we expand the sample with bright cluster members from the red sequence. We augment our constraints with those from the literature to estimate the importance of the intrinsic alignments of satellites compared to those of central galaxies, for which the alignments are described by the linear alignment model. Comparison of the alignment signals to the expected uncertainties of current surveys such as the Kilo-Degree Survey suggests that the linear alignment model is an adequate treatment of intrinsic alignments, but it is not clear whether this will be the case for larger surveys.

*Cristóbal Sifón, Henk Hoekstra, Marcello Cacciato, Massimo Viola, Fabian Köhlinger,  
Remco F. J. van der Burg, David J. Sand, & Melissa L. Graham,  
2015, A&A, 575, A48*

## 4.1 Introduction

Tidal torques tend to align triaxial satellite galaxies toward the centre of the larger “host” gravitational potential as they orbit around its centre. This mechanism is well established in numerical simulations, where galaxies are typically locked pointing toward the centres of clusters, possibly with brief periodic misalignments depending on the specific orbit, well within a Hubble time (e.g., Ciotti & Dutta 1994; Altay et al. 2006; Faltenbacher et al. 2008; Pereira et al. 2008; Pereira & Bryan 2010). In a hierarchical clustering scenario, this effect could be coupled with alignments arising from the nonlinear evolution of structure. Therefore the patterns and evolution of galaxy alignments—if any—contain important information about the initial conditions that gave rise to the present-day cosmic web, as well as the formation history and environments of galaxies.

Additionally, these galaxy alignments (commonly referred to as “intrinsic,” as opposed to apparent, alignments) are a potential contaminant of cosmic shear, which is a measurement of the coherent distortions of galaxies in the background of a matter distribution. While the signal from these intrinsic alignments is weak enough that it is not relevant for weak lensing measurements of galaxy clusters (and in general cluster members can be identified and removed to a sufficient level), it is a concern for large-area cosmic shear surveys, which are more susceptible to this contamination, and where the requirements on precision and accuracy are more stringent. The contamination induced by these galaxy alignments into cosmic shear measurements can be divided into two effects. The first effect is the tidal alignment of galaxies with similar formation histories, so-called intrinsic-intrinsic or II signal. Since this effect is restricted to pairs with common formation or evolutionary histories, this II signal can be avoided by selecting pairs of galaxies with large angular and/or redshift separations (e.g., King & Schneider 2002; Heymans & Heavens 2003; Heymans et al. 2004). The second effect is more subtle and more difficult to control: the same gravitational field that aligns galaxies within a halo is responsible for the deflection of the light coming from background galaxies (Hirata & Seljak 2004). This effect is referred to as gravitational-intrinsic or GI signal (for consistency, the lensing signal itself is referred to as gravitational-gravitational, or GG, signal). In tomographic analyses, it is possible to account for this effect through its distinct redshift dependence (King 2005; Joachimi & Schneider 2008; Zhang 2010b,a) or, inversely, to measure it from cosmic shear data by boosting its signal while suppressing the contribution from gravitational lensing (Joachimi & Schneider 2010). This cross-correlation has recently been shown to exist also between galaxy-galaxy lensing and CMB lensing (Hall & Taylor 2014; Troxel & Ishak 2014). Intrinsic alignments can also be modeled directly in cosmic shear

data and marginalized over to extract cosmological parameters (Joachimi & Bridle 2010; Heymans et al. 2013). In an attempt to identify a consistent model for galaxy shapes and alignments, Joachimi et al. (2013a,b) have tried to match semi-analytical models to galaxies from the COSMOS survey (Scoville et al. 2007) and find that the intrinsic alignment contamination to upcoming cosmic shear surveys should be  $< 10\%$ .

Recent large photometric and spectroscopic surveys such as the 2-degree Field redshift survey (2dF, Colless et al. 2001) and the Sloan Digital Sky Survey (SDSS, York et al. 2000) have allowed the study of galaxy alignments out to several tens of Mpc exploiting cross-correlation techniques, with robust direct detections of the GI signal up to  $z \sim 0.7$  between galaxy samples with large line-of-sight separations (Mandelbaum et al. 2006; Hirata et al. 2007; Joachimi et al. 2011), although Mandelbaum et al. (2011) reported a null detection. However, the II signal is much weaker than the GI signal in nontomographic studies at intermediate redshifts typical of these surveys, and has typically eluded detection (e.g., Mandelbaum et al. 2006, 2011; Blazek et al. 2012).

On smaller scales the history of these measurements goes back further, but the issue is far from settled. Early measurements of galaxy alignments focused on galaxy clusters, trying to understand galaxy formation and (co-)evolution. Rood & Sastry (1972) were the first to claim a detection of a preferential direction of galaxies in clusters. Specifically, they found that satellite galaxies in Abell 2199 tend to point in the direction of the major axis of the BCG. However, most subsequent measurements have been consistent with random orientations of satellite galaxies in clusters (e.g., Hawley & Peebles 1975; Thompson 1976; Dekel 1985; van Kampen & Rhee 1990; Trevese et al. 1992; Panko et al. 2009; Hung & Ebeling 2012), although some authors have also claimed significant nonrandom orientations of these cluster satellites (e.g., Djorgovski 1983; Godłowski et al. 1998, 2010; Baier et al. 2003; Plionis et al. 2003).

More recent studies have focused on smaller mass galaxy groups, where the number of objects is much larger. Similar to the results summarized above, most of these measurements are consistent with no alignments (Bernstein & Norberg 2002; Hao et al. 2011; Schneider et al. 2013; Chisari et al. 2014), although there are claims of significant detections (e.g., Percira & Kuhn 2005; Faltenbacher et al. 2007b).<sup>1</sup> Interestingly, although this effect might be expected to be stronger for more massive haloes, Agustsson & Brainerd (2006) found that satellite galaxies are radially aligned in galaxy-scale haloes. However, Hao et al. (2011) and Schneider et al. (2013) have shown that the results can depend on the method used to estimate the direction of the satellite galaxies, so each result must be taken with care.

---

<sup>1</sup>We discuss sources of this discrepancy in light of recent results in Section 4.5.4.

In general, there is clear tension between observations and numerical N-body simulations, with the latter predicting much higher signals than have been observed. This discrepancy can be attributed, for instance, to a misalignment between stars and dark matter, such that stars—being more centrally concentrated than dark matter—react more slowly and less strongly to tidal torquing from the parent halo (Pereira & Bryan 2010; Tenneti et al. 2014). Whatever the physical reasons of this discrepancy, the potential impact of the choice of intrinsic alignment *model* on cosmological parameter estimation (Kirk et al. 2012) makes it imperative that we know the level of intrinsic alignments to high precision at all relevant mass and spatial scales, and this can only be achieved through detailed observations.

In this work, we study the alignments of galaxies in clusters from a sample of galaxy clusters with high-quality photometric observations and a large number of spectroscopic redshifts from archival sources. We measure different kinds of alignments, assess systematic errors, and use the halo model to characterize galaxy alignments in the context of upcoming cosmic shear analyses.

We adopt a flat  $\Lambda$ CDM cosmology with  $\Omega_\Lambda = 0.7$ ,  $\Omega_M = 0.3$  and  $H_0 = 70 \text{ km s}^{-1} \text{ Mpc}^{-1}$ . To calculate the power spectra, we use  $\sigma_8 = 0.8$ ,  $\Omega_b h^2 = 0.0245$ , and  $n_s = 1.0$ . All magnitudes are **MAG\_AUTO** from SExtractor in the AB system, and all absolute magnitudes and luminosities are in the rest frame of the corresponding cluster.

## 4.2 Data

### 4.2.1 Cluster sample and photometry

The cluster sample is drawn from two large, nonoverlapping X-ray selected cluster surveys carried out with the Canada-France-Hawaii Telescope (CFHT), namely the Multi-Epoch Nearby Cluster Survey (MENeACS; Sand et al. 2012) and the Canadian Cluster Comparison Project (CCCP; Hoekstra et al. 2012). MENeACS performed multi-epoch observations of 57 clusters in the redshift range  $0.05 < z < 0.15$ , aimed at measuring the supernova Ia rate in these clusters. For this, clusters were observed using the *g* and *r* bands with MegaCam. CCCP was designed to study the scaling relations between different tracers of mass in galaxy clusters, and includes 50 clusters in the redshift range  $0.15 < z < 0.55$ . Of these, 20 clusters had archival *B*- and *R*-band data taken with the CFH12k camera, and 30 clusters were observed with the *g* and *r* bands with MegaCam (Hoekstra 2007; Hoekstra et al. 2012).

The data were reduced using the Elixir pipeline (Magnier & Cuillandre 2004), and processed further following the method outlined in ?, which is summarized

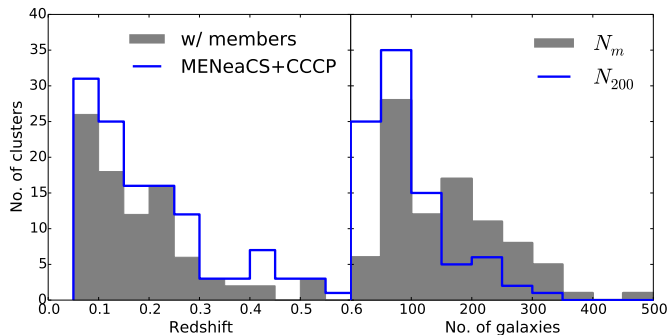


**Figure 4.1:** Left: redshift distributions of all MENeaCS+CCCP clusters (blue histogram) and clusters used in this study (gray filled histogram). Right: distributions of number of spectroscopic members,  $N_m$  (gray filled histogram), and number of spectroscopic members within  $r_{200}$ ,  $N_{200}$  (blue histogram). Abell 2142, with  $N_m = 1052$  and  $N_{200} = 731$ , is not shown.

below. In order to simplify point spread function (PSF) modeling for shape measurements, we homogenized the PSF across the entire field-of-view by finding a locally-varying convolution kernel that makes the PSF circular and Gaussian everywhere (Kuijken 2008). This PSF homogenization was done for each exposure, after which the individual exposures were co-added. By applying a Gaussian weight function to measure aperture fluxes we optimized color measurements in terms of S/N (see Kuijken 2008 and ?, Appendix A). This gaussianization process introduces correlations in pixel noise, which we do not account for. As we show in Section 4.4.3, this is not a problem for the present analysis.

We performed object detection with SExtractor (Bertin & Arnouts 1996) in dual-image mode, using the  $r$  (or  $R$ ) band as detection image. All sources were detected in the  $r$ -band image obtained by stacking the nonhomogenized images. Photometric zero points were calibrated using the stellar locus regression (SLR) software developed by Kelly et al. (2014)<sup>2</sup>. SLR uses the known colors of stars to obtain solutions for the photometric zero points of any photometric catalog, correcting for instrumental response and atmospheric and Galactic extinctions (see also High et al. 2009). We used the Two-Micron All Sky Survey (2MASS, Skrutskie et al. 2006)  $J$ -band star catalog in addition to our MegaCam  $g$  and  $r$ , or CFH12k  $B$  and  $R$ , observations as inputs to the SLR. We retrieved extinction values in the  $J$  band from the NASA/IPAC Extragalactic Database (NED)<sup>3</sup>, which use the reddening measurements of Schlafly & Finkbeiner (2011). With these two colors, plus

<sup>2</sup><https://code.google.com/p/big-macs-calibrate/>

<sup>3</sup><http://ned.ipac.caltech.edu/>

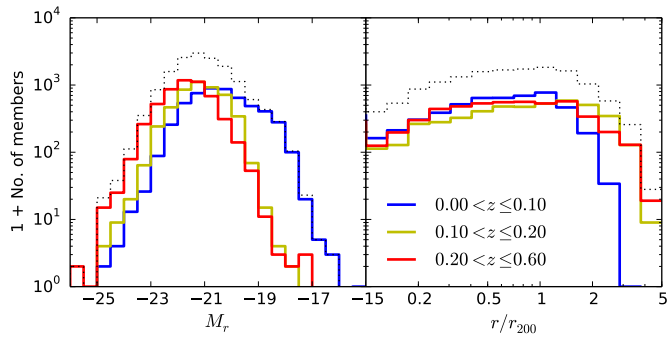


**Figure 4.2:** Distribution of spectroscopic members. Left: as a function of rest-frame absolute  $r$ -band magnitude. Right: as a function of cluster-centric distance in units of  $r_{200}$ . The dotted black lines show the distribution of the full sample; the solid lines show the distribution split into three redshift bins of approximately equal number of clusters.

the absolute photometric calibrations of 2MASS (including the extinction correction), we obtained absolute zero points for the CFHT catalogs. For clusters within the SDSS footprint we also use the SDSS *griz* photometry to check for consistency, from which we conclude that SLR-corrected zero points are calibrated to an absolute uncertainty of  $\sim 0.01$  mag. Galaxies were separated from stars by visual inspection of the magnitude-size<sup>4</sup> plane for each cluster individually. Stars occupy a well-defined region in this plane, having essentially a single size up to the saturation flux. Given that the stacks generally have a sub-arcsecond sized PSF, galaxies used here are large compared to the PSF and are therefore easily distinguishable from stars.

We computed  $r$ -band absolute magnitudes,  $M_r$ , using EzGal<sup>5</sup> (Mancone & Gonzalez 2012), using a passive evolution Charlot & Bruzual 2007 (unpublished, see Bruzual & Charlot 2003) single burst model with solar metallicity and formation redshift  $z_f = 5$ .

#### 4.2.2 Spectroscopic data

We searched for spectroscopic redshifts around all clusters in the MENeACS+CCCP sample in six archival sources: NED, the WIYN Long-Term Variability survey (WLT; Crawford et al. 2011), the Canadian Network for Observational Cosmology Survey (CNOC; Yee et al. 1996, 1998; Ellingson et al. 1997; Abraham

<sup>4</sup>Here, sizes are given by FLUX\_RADIUS from SExtractor.

<sup>5</sup><http://www.baryons.org/ezgal/>

**Table 4.1:** Spectroscopic catalogs.

Source	Total redshifts	Unique redshifts	Clusters	Avg. unique per cluster
Compilations				
NED	16,125	9,161	79	116
WLTV	1,613	1,399	2	700
CNOC	1,427	1,266	10	127
SDSS DR10	14,634	13,995	62	226
HeCS	8,470	8,368	27	310
MENeACS-spec	1,966	1,966	12	164
Single-cluster				
Geller et al. (2014)		834	1	834
Ebeling et al. (2014)		1,115	1	1,115
<b>Total</b>	<b>38,104</b>	<b>90</b>	<b>423</b>	

et al. 1998), the SDSS Data Release 10<sup>6</sup> (DR10; Ahn et al. 2014) which is part of SDSS-III (Ahn et al. 2012) and the Hectospec Cluster Survey (HeCS; Rines et al. 2013). We also include redshifts from the MENeACS spectroscopic survey (hereafter MENeACS-spec). When a galaxy was found in more than one of these catalogs, each catalog replaced the preceding as listed above and in Table 4.1. Thus we included all redshifts from MENeACS-spec. In NED and in SDSS DR10, we searchws for galaxies with spectroscopic redshifts within a radius of 1 deg. around each cluster, but only galaxies in our photometric catalogs were included in the analysis. From NED, we discarded all flagged redshifts (i.e., all those whose **Redshift Flag** field is not blank) and kept only redshifts with at least 4 significant digits to ensure that only spectroscopic redshifts with enough precision are included. From SDSS we only included galaxies with **zWarning**=0. The NED search includes redshifts obtained as part of large surveys such as the 2dF, the 2MASS spectroscopic survey (2MRS), the WIde-field Nearby Galaxy cluster Survey (WINGS), and the WiggleZ Dark Energy Survey.

Additionally, we included the redshift catalogs of Abell 383 and MACS J0717.5+3745 recently published by Geller et al. (2014) and Ebeling et al. (2014), respectively, which total 1,949 redshifts within our CFHT images. From the catalog of Ebeling et al. (2014) we used only redshifts with quality flag 1 or 2. We also highlight the redshift catalog of Abell 2142 by Owers et al. (2011), containing  $\sim 1,800$  galaxies, which is included as part of the NED catalog.

Table 4.1 lists the number of (unique) spectroscopic redshifts included from each catalog and from how many cluster fields they are taken. The largest red-

---

<sup>6</sup>[http://www.sdss3.org/dr10/data\\_access/](http://www.sdss3.org/dr10/data_access/)

shift catalog(s) for each cluster are listed in Table 4.2, including the largest catalogs within NED; for most clusters the NED redshifts come mainly from one or two large catalogs (with  $\gtrsim 90\%$  of redshifts). The final spectroscopic sample is summarized in the last row of Table 4.1: it contains 38,104 redshifts in the direction of 90 clusters, selected to have at least 30 members, at least 10 of which must be within  $r_{200}$  (see Section 4.3.1). The left panel of Fig. 4.1 shows the redshift distribution of these 90 clusters, compared to the entire MENeacs+CCCP sample. The analysis in this paper refers only to these 90 clusters, which are listed in Table 4.2.

## 4.3 Galaxy samples

### 4.3.1 Spectroscopic members and dynamical masses

Spectroscopic membership is determined using the shifting gapper method (Fadda et al. 1996), slightly adjusted from the implementation of Sifón et al. (2013). We bin galaxies in radial bins of at least 15 galaxies and 250 kpc and, for each radial bin, members are selected as those galaxies that are within  $800 \text{ km s}^{-1}$  from the main body of galaxies, which is bound by gaps of  $400 \text{ km s}^{-1}$ . The reduction in the velocity gaps compared to Sifón et al. (2013)—who used 1000 and  $500 \text{ km s}^{-1}$ , respectively—is due to the larger number of galaxies used here, producing a distribution that has less obvious gaps in velocity space. In some cases, we introduced a radial cut determined from visual inspection. The left panel of Fig. 4.2 shows that the distribution of confirmed cluster members is similar at low and high redshift for luminous ( $M_r \lesssim -21$ ) galaxies but low-luminosity galaxies used here come mainly from low redshift clusters. We iteratively measure the velocity dispersion,  $\sigma_{200}$ , as the biweight estimator of scale (Beers et al. 1990) using all galaxies within  $r_{200}$ , correcting for measurement errors (Danese et al. 1980). Since the measurement uncertainties are not available for all galaxies (most notably, they are not given in NED), we use a fiducial value of  $150 \text{ km s}^{-1}$  for the uncertainty of all redshifts, which is a conservative estimate for recent measurements, but can be representative of older or low resolution measurements listed in NED. The change in mass introduced by this correction is, in any case, at the percent level for a cluster with  $\sigma \sim 1000 \text{ km s}^{-1}$ . The cluster redshift is determined iteratively in this process as the biweight estimator of location, considering again galaxies within  $r_{200}$ . We estimate the mass within  $r_{200}$ , namely  $M_{200}$ , using the  $\sigma_{200} - M_{200}$  relation of Evrard et al. (2008), and estimate  $r_{200} = [3/(4\pi) \cdot M_{200}/(200\rho_c)]^{1/3}$ . The resulting  $\sigma_{200}$  is insensitive to uncertainties in  $r_{200}$ ; varying  $r_{200}$  by  $\pm 20\%$  from those obtained from this relation only changes  $\sigma_{200}$  by  $\lesssim 5\%$  for every cluster (in other words, velocity dispersion profiles are very close to flat near  $r_{200}$ ). The uncertainties in

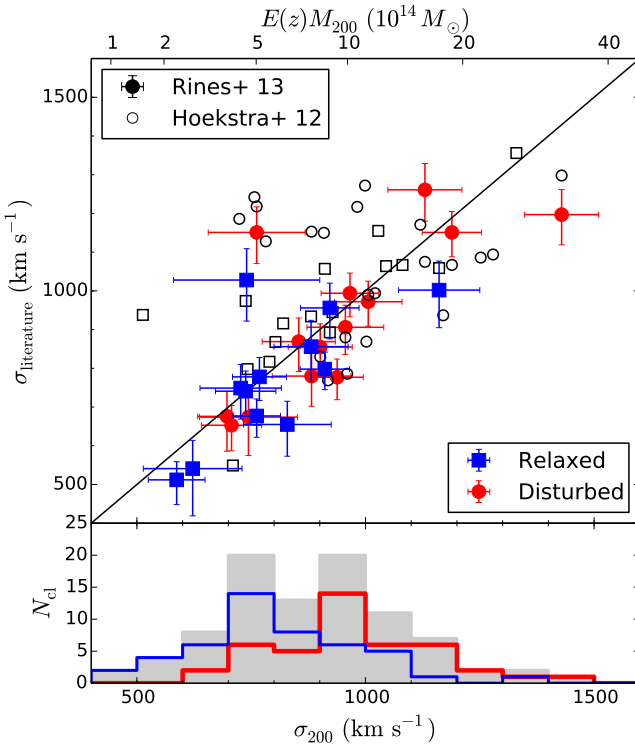


**Figure 4.3:** Top: comparison between velocity dispersions calculated from spectroscopic members in this work with those in Rines et al. (2013), and with velocity dispersions calculated by fitting a single isothermal sphere to the weak lensing profile (Hoekstra et al. 2012) for CCCP clusters used in this work. Errorbars are not shown for the latter for clarity. Squares and circles show relaxed and disturbed clusters, respectively. The black line shows the one-to-one relation, and the top axis shows  $E(z)M_{200}$  for a given  $\sigma_{200}$  from the Evrard et al. (2008) relation. Bottom: distribution of velocity dispersions of the full sample. The gray histogram shows the total distribution, with the blue and red histograms showing the distributions for relaxed and disturbed clusters, respectively.

the velocity dispersion are obtained from 1,000 jackknife samples drawn from all galaxies with peculiar velocities up to 3 times the cluster velocity dispersion; therefore quoted uncertainties include an estimate of the effect of membership selection. Uncertainties in the dynamical mass are obtained by propagating the uncertainties on the velocity dispersion. The dynamical properties described above are listed in Table 4.2, together with the number of members,  $N_m$ , and the number of members within  $r_{200}$ ,  $N_{200}$ . The right panel of Fig. 4.1 shows the distribution of  $N_{200}$

and  $N_m$ , the number of members out to arbitrary radius.

In cases where the spectroscopic members do not reach out to  $r_{200}$ , we cannot infer  $\sigma_{200}$  directly from the data. We therefore apply a correction to the measured velocity dispersion assuming the isotropic velocity dispersion profile of Mamon et al. (2010) and the mass–concentration relation of Duffy et al. (2008) to get the theoretical expectation for  $\sigma_{200}$  given  $\sigma(< r_{\max})$ . This correction is linear with  $r_{\max}$  for  $r_{\max} \gtrsim 0.2r_{200}$ , with correction factors 0.93 and 0.81 for the velocity dispersion and mass, respectively, for  $r_{\max} = 0.6r_{200}$  (i.e., the mass within  $0.6r_{200}$  is  $0.81M_{200}$ ), only weakly dependent on mass and redshift. In our sample there are 14 clusters with  $r_{\max} < r_{200}$ , with a median of  $r_{\max}/r_{200} = 0.69$  and 10th and 90th percentiles of 0.51 and 0.79, respectively. For these clusters, we list the corrected values in Table 4.2.

There are a total of 14,576 cluster members among 90 clusters, 9,054 of which are within  $r_{200}$ . The radial distribution of cluster members is shown in the right panel of Fig. 4.2. The spectroscopic members on average follow a Navarro-Frenk-White (NFW, ?) profile with concentration  $c_{200} \sim 2$  (van der Burg et al., in prep). The median redshift of the sample is  $z = 0.144$ , and the median velocity dispersion is  $\sigma_{200} = 881 \text{ km s}^{-1}$  which translates to a median dynamical mass  $M_{200} = 7.2 \times 10^{14} M_\odot$  and a median size  $r_{200} \sim 1.7 \text{ Mpc}$ . The distribution of  $\sigma_{200}$  is shown in the bottom panel of Fig. 4.3.

In Fig. 4.3, we compare the present velocity dispersions to those of Rines et al. (2013); there is a large overlap between the two data sets (see Table 4.1). The two sets of measurements are consistent, with a median ratio  $\langle \sigma_{200}/\sigma_{\text{Rines+13}} \rangle = 1.04 \pm 0.03$ . We also show, for comparison, the singular isothermal sphere velocity dispersions fit by Hoekstra et al. (2012) to the weak lensing signal of 39 overlapping clusters, which are also consistent with our measurements to within 2% on average. It is apparent from Fig. 4.3 that the agreement between  $\sigma_{200}$  and  $\sigma_{WL}$  is better for relaxed clusters than for disturbed ones, consistent with expectations. For comparison, using the velocity gaps used by Sifón et al. (2013) in our analysis, we obtain velocity dispersions larger than those of Rines et al. (2013) by  $\sim 14\%$ .

#### 4.3.1.1 Dynamical state

We can take further advantage of our large spectroscopic catalogs by studying the dynamical states of clusters. To this end we use the DS test (Dressler & Shectman 1988), which uses both the positions and velocities of galaxies. The DS test gives a measure of substructure by identifying galaxies that do not follow the cluster velocity distribution through the metric

$$\delta^2 = \frac{N_{\text{local}}}{\sigma^2} \left[ (\bar{v}_{\text{local}} - \bar{v})^2 + (\sigma_{\text{local}} - \sigma)^2 \right]^2, \quad (4.1)$$

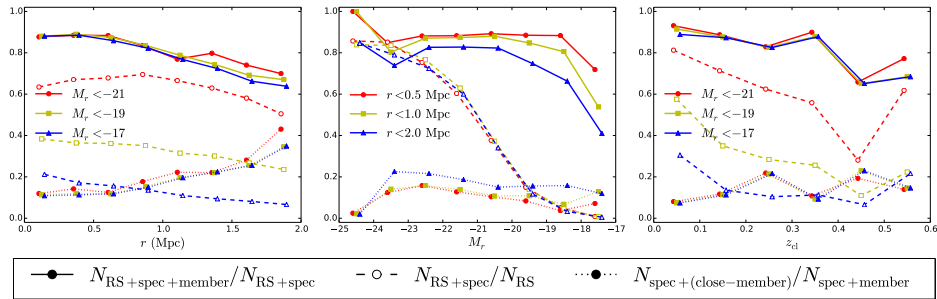


**Figure 4.4:** Purity of the red sequence (filled symbols with solid lines) and spectroscopic completeness within the red sequence (open symbols with dashed lines). Filled symbols with dotted lines show the fraction of galaxies that are not selected as members but that are within  $\Delta z = 0.03(1 + z)$  of the cluster, which represents the contamination in an unbiased photometric redshift selection. Left: as a function of cluster-centric distance, for different luminosity limits. Middle: as a function of absolute magnitude, for different radial apertures. Right: as a function of redshift for different luminosity limits, at an aperture of 1 Mpc. Note that points within a given line are independent (each line is a differential distribution), but lines of the same type are not independent from each other.

**Table 4.2:** Cluster sample, redshifts, and velocity dispersions.

Cluster	$z$	$N_m$	$N_{200}$	$\sigma_{200}$ (km s $^{-1}$ )	$M_{200}$ (10 $^{14}$ M $_{\odot}$ )	$r_{200}$ (Mpc)	$\mathcal{S}_{\Delta}$	Main sources <sup>a</sup>	Main NED sources <sup>b</sup>
Abell 85	0.0555	284	248	$967 \pm 55$	$10.0 \pm 1.7$	$2.03 \pm 0.12$	$0.01^{+0.00}_{-0.00}(\text{D})$	3	14
Abell 115	0.1930	73	73	$1028 \pm 108$	$11.2 \pm 3.5$	$2.03 \pm 0.21$	$0.24^{+0.02}_{-0.07}(\text{R})$	—	1
Abell 119	0.0443	268	255	$875 \pm 48$	$7.5 \pm 1.2$	$1.85 \pm 0.10$	$< 0.01(\text{D})$	3	7
Abell 133	0.0558	62	59	$791 \pm 79$	$5.5 \pm 1.7$	$1.66 \pm 0.17$	$0.24^{+0.03}_{-0.14}(\text{R})$	—	21
Abell 209 <sup>c</sup>	0.2090	110	110	$1170 \pm 99$	$16.4 \pm 4.1$	$2.28 \pm 0.19$	$0.01^{+0.00}_{-0.01}(\text{D})$	—	27
Abell 222 <sup>c</sup>	0.2132	76	76	$881 \pm 79$	$7.0 \pm 1.9$	$1.72 \pm 0.15$	$0.30^{+0.04}_{-0.04}(\text{R})$	—	11,33
Abell 223 <sup>c</sup>	0.2076	64	64	$910 \pm 80$	$7.8 \pm 2.1$	$1.78 \pm 0.16$	$0.05^{+0.02}_{-0.02}(\text{D})$	—	11,33
Abell 267	0.2291	219	156	$1006 \pm 74$	$10.3 \pm 2.3$	$1.95 \pm 0.14$	$< 0.01(\text{D})$	3,4	—
Abell 383	0.1885	182	134	$918 \pm 53$	$8.1 \pm 1.4$	$1.81 \pm 0.11$	$< 0.01(\text{D})$	—	18
Abell 399	0.0718	250	229	$1046 \pm 47$	$12.5 \pm 1.7$	$2.18 \pm 0.10$	$< 0.01(\text{D})$	5	20
Abell 401	0.0735	104	83	$933 \pm 81$	$8.9 \pm 2.3$	$1.94 \pm 0.17$	$0.32^{+0.19}_{-0.05}(\text{R})$	—	20
Abell 520	0.2007	153	127	$1045 \pm 73$	$11.8 \pm 2.5$	$2.05 \pm 0.14$	$0.27^{+0.04}_{-0.11}(\text{R})$	—	19

Columns are: (1) cluster name; (2): cluster redshift; (3): number of members out to arbitrary radius; (4): number of members within  $r_{200}$ ; (5): velocity dispersion of members within  $r_{200}$ ; (6): total mass within  $r_{200}$ ; (7): cluster radius  $r_{200}$ ; (8): significance level of the DS test, the letter in parenthesis shows whether a cluster is classified as disturbed (D) or relaxed (R).

<sup>a</sup>Numbers are: (1): WLTV; (2): CNOC; (3): SDSS; (4): HeCS; (5): MENeaCS-spec. See text for references. <sup>b</sup>Catalogs extracted from NED that contribute significantly to each cluster. These are: (1): Barrena et al. (2007); (2): Barrena et al. (2011); (3): Belloni & Roeser (1996); (4): Boschin et al. (2004); (5): Boschin et al. (2009); (6): Braglia et al. (2009); (7): WINGS (Cava et al. 2009); (8): Christlein & Zabludoff (2003); (9): 2dF (Colless et al. 2003); (10): Czoske et al. (2001); (11): Dietrich et al. (2002); (12): Dressler & Gunn (1992); (13): WiggleZ (Drinkwater et al. 2010); (14): Durret et al. (1998); (15): Ebeling et al. (2014); (16): Ferrari et al. (2003); (17): Fisher et al. (1998); (18): Geller et al. (2014); (19): Girardi et al. (2008); (20): Hill & Oegerle (1993); (21): 2MRS (Huchra et al. 2012); (22): Jäger et al. (2004); (23): Liang et al. (2000); (24): Martini et al. (2007); (25): Maurogordato et al. (2008); (26): Maurogordato et al. (2011); (27): Mercurio et al. (2003); (28): Miller et al. (2004); (29): Miller et al. (2006); (30): Oegerle et al. (1995); (31): Owers et al. (2011); (32): Pimbblet et al. (2006); (33): Proust et al. (2000). <sup>c</sup>Spectroscopic members extend out to less than  $0.8r_{200}$ .

**Table 4.2:** *Continued*

Cluster	$z$	$N_m$	$N_{200}$	$\sigma_{200}$ (km s $^{-1}$ )	$M_{200}$ (10 $^{14}$ M $_{\odot}$ )	$r_{200}$ (Mpc)	$S_{\Delta}$	Main sources <sup>a</sup>	Main NED sources <sup>b</sup>
Abell 521 <sup>c</sup>	0.2469	95	95	$1002 \pm 95$	$10.1 \pm 2.9$	$1.92 \pm 0.18$	$0.06_{-0.02}^{+0.02}$ (D)	—	16
Abell 545 <sup>c</sup>	0.1577	80	80	$1038 \pm 89$	$11.8 \pm 3.0$	$2.08 \pm 0.18$	$0.07_{-0.00}^{+0.02}$ (R)	—	2
Abell 553	0.0670	54	44	$665 \pm 75$	$3.3 \pm 1.1$	$1.39 \pm 0.16$	$0.01_{-0.00}^{+0.03}$ (D)	5	—
Abell 586	0.1704	33	21	$803 \pm 104$	$5.4 \pm 2.1$	$1.60 \pm 0.21$	$0.28_{-0.07}^{+0.12}$ (R)	3	—
Abell 644 <sup>c</sup>	0.0696	31	31	$625 \pm 96$	$2.7 \pm 1.2$	$1.31 \pm 0.20$	$0.67_{-0.05}^{+0.11}$ (R)	—	24
Abell 646	0.1266	259	69	$707 \pm 66$	$3.8 \pm 1.1$	$1.44 \pm 0.13$	$0.07_{-0.04}^{+0.22}$ (D)	3,4	—
Abell 655	0.1271	306	109	$938 \pm 57$	$8.8 \pm 1.6$	$1.91 \pm 0.12$	$0.03_{-0.02}^{+0.01}$ (D)	3,4	—
Abell 697	0.2821	215	106	$1161 \pm 89$	$15.4 \pm 3.6$	$2.19 \pm 0.17$	$0.44_{-0.02}^{+0.05}$ (R)	3,4	—
Abell 754	0.0546	305	300	$959 \pm 43$	$9.8 \pm 1.3$	$2.01 \pm 0.09$	$0.01_{-0.00}^{+0.00}$ (D)	—	8
Abell 780 <sup>c</sup>	0.0547	33	33	$822 \pm 113$	$6.2 \pm 2.5$	$1.73 \pm 0.24$	$0.01_{-0.00}^{+0.01}$ (D)	—	21
Abell 795	0.1385	166	117	$768 \pm 59$	$4.9 \pm 1.1$	$1.56 \pm 0.12$	$0.06_{-0.02}^{+0.07}$ (D)	3,4,5	—
Abell 851	0.4038	53	47	$999 \pm 138$	$9.3 \pm 3.8$	$1.77 \pm 0.24$	$0.01_{-0.01}^{+0.03}$ (D)	—	3,12
Abell 959	0.2882	67	67	$982 \pm 101$	$9.4 \pm 2.9$	$1.85 \pm 0.19$	$0.08_{-0.03}^{+0.04}$ (D)	—	5
Abell 961	0.1275	58	16	$740 \pm 142$	$4.4 \pm 2.5$	$1.51 \pm 0.29$	$0.84_{-0.13}^{+0.06}$ (R)	3	—
Abell 963	0.2036	165	85	$922 \pm 64$	$8.1 \pm 1.7$	$1.81 \pm 0.13$	$0.17_{-0.06}^{+0.06}$ (R)	3,4	—
Abell 990	0.1421	209	86	$829 \pm 96$	$6.1 \pm 2.1$	$1.68 \pm 0.19$	$0.74_{-0.05}^{+0.03}$ (R)	3,4,5	—
Abell 1033	0.1224	170	98	$762 \pm 52$	$4.8 \pm 1.0$	$1.56 \pm 0.11$	$0.59_{-0.21}^{+0.08}$ (R)	3,4	—
Abell 1068	0.1393	104	32	$740 \pm 160$	$4.3 \pm 2.8$	$1.50 \pm 0.32$	$0.93_{-0.04}^{+0.04}$ (R)	3,4	—
Abell 1132	0.1349	160	55	$727 \pm 89$	$4.1 \pm 1.5$	$1.48 \pm 0.18$	$0.13_{-0.05}^{+0.06}$ (R)	3,4	—
Abell 1234	0.1638	54	30	$513 \pm 86$	$1.4 \pm 0.7$	$1.03 \pm 0.17$	$0.87_{-0.07}^{+0.06}$ (R)	3,4	—
Abell 1246	0.1920	207	87	$956 \pm 84$	$9.1 \pm 2.4$	$1.89 \pm 0.17$	$0.01_{-0.00}^{+0.01}$ (D)	3,4	—
Abell 1285	0.1078	77	51	$826 \pm 90$	$6.1 \pm 2.0$	$1.70 \pm 0.19$	$0.52_{-0.18}^{+0.08}$ (R)	5	—
Abell 1361	0.1157	143	46	$587 \pm 62$	$2.2 \pm 0.7$	$1.21 \pm 0.13$	$0.39_{-0.07}^{+0.15}$ (R)	3,4	—
Abell 1413	0.1418	124	65	$881 \pm 81$	$7.3 \pm 2.0$	$1.78 \pm 0.16$	$0.72_{-0.23}^{+0.07}$ (R)	3,4	—

**Table 4.2:** *Continued*

Cluster	$z$	$N_m$	$N_{200}$	$\sigma_{200}$ ( $\text{km s}^{-1}$ )	$M_{200}$ ( $10^{14} \text{ M}_\odot$ )	$r_{200}$ (Mpc)	$\mathcal{S}_\Delta$	Main sources <sup>a</sup>	Main NED sources <sup>b</sup>
Abell 1650	0.0841	266	140	$720 \pm 48$	$4.1 \pm 0.8$	$1.50 \pm 0.10$	$0.99^{+0.00}_{-0.02}(\text{R})$	3,5	–
Abell 1651	0.0847	214	138	$903 \pm 51$	$8.0 \pm 1.4$	$1.87 \pm 0.11$	$0.65^{+0.04}_{-0.16}(\text{R})$	–	9,21
Abell 1689	0.1847	252	235	$1429 \pm 81$	$30.0 \pm 5.1$	$2.82 \pm 0.16$	$< 0.01(\text{D})$	3,4	–
Abell 1758	0.2772	133	34	$744 \pm 107$	$4.1 \pm 1.8$	$1.41 \pm 0.20$	$0.11^{+0.06}_{-0.03}(\text{R})$	3,4	–
Abell 1763	0.2323	186	103	$1130 \pm 81$	$14.6 \pm 3.1$	$2.18 \pm 0.16$	$< 0.01(\text{D})$	3,4	–
Abell 1781	0.0622	54	16	$419 \pm 93$	$0.8 \pm 0.5$	$0.88 \pm 0.19$	$0.92^{+0.02}_{-0.19}(\text{R})$	3	–
Abell 1795	0.0629	191	133	$778 \pm 51$	$5.2 \pm 1.0$	$1.63 \pm 0.11$	$0.26^{+0.04}_{-0.09}(\text{R})$	3	21
Abell 1835	0.2506	195	41	$762 \pm 106$	$4.5 \pm 1.9$	$1.46 \pm 0.20$	$0.66^{+0.06}_{-0.23}(\text{R})$	3,4	–
Abell 1914	0.1671	257	146	$911 \pm 54$	$7.9 \pm 1.4$	$1.82 \pm 0.11$	$0.86^{+0.03}_{-0.05}(\text{R})$	3,4	–
Abell 1927	0.0953	138	58	$725 \pm 58$	$4.2 \pm 1.0$	$1.50 \pm 0.12$	$0.25^{+0.02}_{-0.08}(\text{R})$	3,5	–
Abell 1942	0.2257	51	27	$820 \pm 140$	$5.6 \pm 2.9$	$1.59 \pm 0.27$	$0.04^{+0.05}_{-0.01}(\text{D})$	3	–
Abell 1991	0.0587	175	99	$553 \pm 45$	$1.9 \pm 0.5$	$1.17 \pm 0.10$	$0.12^{+0.09}_{-0.05}(\text{R})$	3,5	–
Abell 2029	0.0777	317	181	$1152 \pm 58$	$16.6 \pm 2.5$	$2.39 \pm 0.12$	$< 0.01(\text{D})$	3	21
Abell 2033	0.0796	190	88	$911 \pm 69$	$8.3 \pm 1.9$	$1.89 \pm 0.14$	$0.03^{+0.03}_{-0.01}(\text{D})$	3	21
Abell 2050	0.1202	164	82	$854 \pm 80$	$6.7 \pm 1.9$	$1.74 \pm 0.16$	$0.34^{+0.06}_{-0.03}(\text{R})$	3,4	–
Abell 2055	0.1028	154	69	$697 \pm 64$	$3.7 \pm 1.0$	$1.44 \pm 0.13$	$0.04^{+0.02}_{-0.00}(\text{D})$	3,4	21
Abell 2064	0.0734	62	32	$675 \pm 108$	$3.4 \pm 1.6$	$1.41 \pm 0.22$	$0.40^{+0.13}_{-0.05}(\text{R})$	3	–
Abell 2065	0.0725	219	164	$1095 \pm 67$	$14.3 \pm 2.6$	$2.28 \pm 0.14$	$0.03^{+0.01}_{-0.01}(\text{D})$	3	–
Abell 2069	0.1139	331	146	$966 \pm 63$	$9.7 \pm 1.9$	$1.98 \pm 0.13$	$0.01^{+0.00}_{-0.00}(\text{D})$	3,4	–
Abell 2104	0.1547	90	56	$1081 \pm 126$	$13.3 \pm 4.6$	$2.17 \pm 0.25$	$0.22^{+0.09}_{-0.09}(\text{R})$	–	23
Abell 2111	0.2281	256	83	$738 \pm 66$	$4.1 \pm 1.1$	$1.43 \pm 0.13$	$0.46^{+0.09}_{-0.04}(\text{R})$	3,4	29
Abell 2125	0.2466	141	55	$857 \pm 122$	$6.4 \pm 2.7$	$1.65 \pm 0.23$	$0.46^{+0.01}_{-0.26}(\text{R})$	–	28
Abell 2142	0.0903	1052	731	$1086 \pm 31$	$13.9 \pm 1.2$	$2.24 \pm 0.06$	$0.01^{+0.00}_{-0.00}(\text{D})$	3	31
Abell 2163	0.2004	309	290	$1279 \pm 53$	$21.5 \pm 2.7$	$2.51 \pm 0.10$	$0.03^{+0.02}_{-0.01}(\text{D})$	–	25

**Table 4.2:** *Continued*

Cluster	$z$	$N_m$	$N_{200}$	$\sigma_{200}$ (km s $^{-1}$ )	$M_{200}$ (10 $^{14}$ M $_{\odot}$ )	$r_{200}$ (Mpc)	$S_{\Delta}$	Main sources <sup>a</sup>	Main NED sources <sup>b</sup>
Abell 2204	0.1507	100	15	$782 \pm 278$	$5.1 \pm 5.4$	$1.58 \pm 0.56$	$0.35_{-0.12}^{+0.33}(R)$	—	32
Abell 2219	0.2255	364	241	$1189 \pm 65$	$17.0 \pm 2.8$	$2.30 \pm 0.13$	$< 0.01(D)$	3,4	4
Abell 2259	0.1602	158	77	$901 \pm 70$	$7.7 \pm 1.8$	$1.80 \pm 0.14$	$0.04_{-0.01}^{+0.12}(D)$	3,4	—
Abell 2261	0.2257	206	76	$882 \pm 86$	$7.0 \pm 2.0$	$1.71 \pm 0.17$	$0.03_{-0.02}^{+0.05}(D)$	3,4	—
Abell 2319 <sup>c</sup>	0.0538	83	83	$1101 \pm 99$	$14.7 \pm 4.0$	$2.31 \pm 0.21$	$0.52_{-0.16}^{+0.07}(R)$	—	30
Abell 2390	0.2287	136	92	$1120 \pm 113$	$14.3 \pm 4.3$	$2.17 \pm 0.22$	$0.23_{-0.10}^{+0.01}(R)$	2	—
Abell 2409	0.1454	101	46	$826 \pm 94$	$6.0 \pm 2.0$	$1.67 \pm 0.19$	$0.16_{-0.03}^{+0.09}(R)$	3,5	—
Abell 2440 <sup>c</sup>	0.0906	88	88	$766 \pm 61$	$4.9 \pm 1.2$	$1.59 \pm 0.13$	$0.13_{-0.02}^{+0.03}(R)$	3	26
Abell 2495	0.0790	98	46	$631 \pm 55$	$2.8 \pm 0.7$	$1.32 \pm 0.12$	$0.23_{-0.01}^{+0.06}(R)$	3,5	—
Abell 2537	0.2964	175	65	$909 \pm 85$	$7.4 \pm 2.1$	$1.70 \pm 0.16$	$0.05_{-0.01}^{+0.04}(D)$	3	6
Abell 2597	0.0829	39	17	$682 \pm 131$	$3.5 \pm 2.0$	$1.42 \pm 0.27$	$0.37_{-0.09}^{+0.15}(R)$	—	9,13
Abell 2670	0.0763	241	196	$919 \pm 46$	$8.5 \pm 1.3$	$1.91 \pm 0.10$	$< 0.01(D)$	3	21
Abell 2703	0.1140	75	13	$657 \pm 53$	$3.1 \pm 0.8$	$1.35 \pm 0.11$	$0.17_{-0.05}^{+0.18}(R)$	3	—
CL 0024.0+1652	0.3948	229	131	$757 \pm 48$	$4.1 \pm 0.8$	$1.35 \pm 0.09$	$< 0.01(D)$	—	10
MACS J0717.5+3745	0.5436	468	215	$1370 \pm 79$	$22.0 \pm 3.8$	$2.24 \pm 0.13$	$< 0.01(D)$	—	15
MKW3S	0.0444	125	82	$592 \pm 49$	$2.3 \pm 0.6$	$1.25 \pm 0.11$	$0.83_{-0.11}^{+0.06}(R)$	3	—
MS 0015.9+1609	0.5475	232	122	$1330 \pm 115$	$20.0 \pm 5.2$	$2.17 \pm 0.19$	$0.32_{-0.18}^{+0.10}(R)$	1,2	—
MS 0440.5+0204	0.1962	51	35	$742 \pm 103$	$4.3 \pm 1.8$	$1.46 \pm 0.20$	$0.26_{-0.13}^{+0.14}(R)$	2	—
MS 0451.6–0305	0.5382	247	200	$1252 \pm 55$	$16.8 \pm 2.2$	$2.05 \pm 0.09$	$< 0.01(D)$	1,2	—
MS 1008.1–1224	0.3077	86	85	$1028 \pm 92$	$10.6 \pm 2.8$	$1.91 \pm 0.17$	$0.59_{-0.11}^{+0.07}(R)$	2	22
MS 1224.7+2007	0.3258	33	29	$790 \pm 95$	$4.8 \pm 1.7$	$1.46 \pm 0.17$	$0.57_{-0.07}^{+0.23}(R)$	2,3	—
MS 1231.3+1542	0.2347	84	65	$710 \pm 57$	$3.7 \pm 0.9$	$1.38 \pm 0.11$	$0.87_{-0.03}^{+0.03}(R)$	2,3	—
MS 1358.4+6245	0.3289	189	152	$1021 \pm 56$	$10.3 \pm 1.7$	$1.88 \pm 0.10$	$0.01_{-0.00}^{+0.01}(D)$	2	17
MS 1455.0+2232	0.2565	57	57	$928 \pm 111$	$8.0 \pm 2.9$	$1.77 \pm 0.21$	$0.58_{-0.24}^{+0.07}(R)$	2,3	—

**Table 4.2:** *Continued*

Cluster	$z$	$N_m$	$N_{200}$	$\sigma_{200}$ ( $\text{km s}^{-1}$ )	$M_{200}$ ( $10^{14} \text{ M}_\odot$ )	$r_{200}$ (Mpc)	$S_\Delta$	Main sources <sup>a</sup>	Main NED sources <sup>b</sup>
MS 1512.4+3647	0.3719	30	29	$960 \pm 170$	$8.4 \pm 4.4$	$1.73 \pm 0.30$	$0.04^{+0.03}_{-0.00}(\text{D})$	2	–
MS 1621.5+2640	0.4254	70	41	$724 \pm 82$	$3.5 \pm 1.2$	$1.27 \pm 0.14$	$0.17^{+0.20}_{-0.04}(\text{R})$	2	–
RX J0736.6+3924	0.1179	62	28	$432 \pm 64$	$0.9 \pm 0.4$	$0.89 \pm 0.13$	$0.52^{+0.12}_{-0.03}(\text{R})$	3,5	–
ZwCl 0628.1+2502	0.0814	72	66	$843 \pm 96$	$6.6 \pm 2.2$	$1.75 \pm 0.20$	$0.04^{+0.02}_{-0.01}(\text{D})$	5	–
ZwCl 1023.3+1257	0.1425	84	24	$622 \pm 108$	$2.6 \pm 1.3$	$1.26 \pm 0.22$	$0.79^{+0.17}_{-0.17}(\text{R})$	3,4	–
ZwCl 1215.1+0400	0.0773	183	107	$902 \pm 65$	$8.0 \pm 1.7$	$1.88 \pm 0.14$	$0.29^{+0.02}_{-0.04}(\text{R})$	3	–

where  $\bar{v}_{\text{local}}$  and  $\sigma_{\text{local}}$  are the local velocity and velocity dispersion, measured for the  $N_{\text{local}}$  nearest neighbors around a test member, and  $\bar{v}$  and  $\sigma$  are the global values. The  $\Delta$ -statistic is the sum of  $\delta$ 's over all cluster members. This statistic is then measured 5,000 times after shuffling the velocities of cluster members, keeping positions fixed, with the same  $N_{\text{local}}$ . The substructure significance (hereafter  $S_\Delta$ ) is the fraction of random samples which have  $\Delta$  higher than that of the cluster. Errorbars are 68% ranges obtained from 5 runs for each cluster, varying the number of neighbors within  $\sqrt{N_{200}} - 2 \leq N_{\text{local}} \leq \sqrt{N_{200}} + 2$ , and the central value is their median. We run the DS test using only members within  $r_{200}$  because  $r_{200}$  is very close to the virial radius, beyond which the cluster *should not* be relaxed, by definition.

The DS test is not designed to assess the dynamical state of clusters in general but specifically to find substructure, which furthermore has to have a different spatial and velocity location from the cluster itself. It is therefore incomplete; there are indeed examples of known merging clusters from which the DS test cannot find indications of substructure, most notably mergers along the plane of the sky (e.g., Menanteau et al. 2012; Barrena et al. 2013). This is the case here with Abell 520 (e.g., Jee et al. 2014a), for example. By means of  $N$ -body simulations, Pinkney et al. (1996) showed that  $S_\Delta < 0.05$  is a reasonable condition to define a pure, but not necessarily complete, sample of dynamically disturbed clusters. We follow the results of Pinkney et al. (1996) in a conservative way, selecting as disturbed all cluster that are consistent with  $S_\Delta \leq 0.05$  within errorbars (52 clusters). All others are classified as relaxed (38 clusters). This is conservative in the sense that we aim to construct a pure sample of relaxed clusters (see Section 4.5.1). Table 4.2 lists  $S_\Delta$  together with the classification for each cluster. We find that more massive clusters tend to be classified as disturbed (D), while less massive clusters are generally relaxed (R); this can be seen in Fig. 4.3.

### 4.3.2 Red sequence members

While spectroscopy provides a clean sample of member galaxies from precise velocities, it suffers from incompleteness mainly due to two practical reasons: 1) obtaining a redshift for a galaxy is expensive; typically it takes  $\sim 30$  minutes of observations for galaxies in low-redshift ( $z \lesssim 0.5$ ) clusters, depending on the telescope and observing conditions; and 2) only a limited number of galaxies can be targeted in a single observation because of slit overlap or fiber collisions.

Being a distinct feature of clusters, the red sequence provides an ideal complement to spectroscopic members. As we show below, for luminous galaxies near the centres of clusters this also provides a clean membership selection, though not as clean as spectroscopy. Using the red sequence *in addition to* the spectroscopic selec-

tion ensures that only a small fraction of galaxies need to be included through this more uncertain method, making the purity of the sample very close to 100%.

To find the red sequence in each cluster, we first separate blue and red galaxies by fitting two one-dimensional gaussians to the color distribution of galaxies using an Error-Corrected Gaussian Mixture Model (ECGMM, Hao et al. 2009). We then fit a straight line in color-magnitude space to the red galaxies using a maximum likelihood approach that accounts for intrinsic scatter and the measurement uncertainty in color, iteratively rejecting  $2\sigma$  outliers. Details will be presented in a forthcoming paper (Sifón et al., in prep).

We assess the purity of the red sequence as a cluster member selection procedure by looking at red sequence members that have redshifts. There are in total 57,885 red sequence galaxies up to  $M_r = -17$  and within 2 Mpc, 7,224 of which have a redshift measurement ( $\sim 12\%$ ). Fig. 4.4 shows that the red sequence is a high-fidelity member selection method even to large radii. Only the sample of both low-luminosity ( $M_r \gtrsim -19$ ) and distant ( $r \gtrsim 1$  Mpc) red sequence members has a lower purity, although the latter is still  $\gtrsim 70\%$  for most of this distance-luminosity space. We include in the extended sample all red sequence galaxies more luminous than  $M_r = -19$  within 1 Mpc of the cluster centre. Within these parameter boundaries, 84% of red sequence galaxies with a spectroscopic redshift are confirmed cluster members. This level of contamination (16% of red sequence members) has no effects on our results.

The rightmost panel of Fig. 4.4 shows that up to  $z \sim 0.4$ , the purity is extremely high ( $\sim 90\%$ ) but then decreases to  $\sim 70\%$ , because above  $z \sim 0.4$  the 4000Å break is no longer bracketed by the  $g$  and  $r$  bands (similarly for the  $B$  and  $R$  bands). The completeness of the spectroscopic samples does drop noticeably with redshift because of the higher difficulty posed by spectroscopic observations of high redshift clusters.

From a lensing perspective, one other important ingredient in assessing the red sequence is the redshift distribution of the contaminating fraction, which we can quantify using red sequence galaxies that are confirmed to be outside the cluster. If they are sufficiently far behind the cluster, they could in fact be lensed, inducing a signal that we wish to avoid. If instead they are either very close behind or in front of the cluster, then they will not be lensed and will only dilute the signal. Fig. 4.5 shows the redshift distribution of red sequence galaxies that are confirmed to be nonmembers through the distance ratio,  $D_{ls}/D_s$ , where  $D_{ls}$  is the angular diameter distance between the lens (i.e., cluster) and the source galaxy, and  $D_s$  is the angular diameter distance to the source. Note that  $D_{ls} < 0$  for  $z_s < z_l$ . Galaxies behind the clusters are lensed, resulting in (apparent) tangential alignments. The

amplitude of this effect can be quantified by the “lensing efficiency,”  $\beta$ , defined as

$$\beta \equiv \left\langle \max \left( 0, \frac{D_{ls}}{D_s} \right) \right\rangle, \quad (4.2)$$

which is typically calculated using photometric redshifts or an average redshift distribution. Note that Eq. 4.2 naturally accounts for galaxies in front of the cluster, which do not contain a lensing signal (but do introduce noise), which is especially important when using a generic redshift distribution, or full photometric redshift probability distributions (in which case background galaxies have a nonzero probability of being in front of the cluster). Of the 688 confirmed nonmembers in the red sequence, 496 (72%) are behind the cluster (including those immediately behind the cluster), and the lensing efficiency of red sequence nonmembers is  $\beta = 0.085$ . It is therefore possible that the contaminating red sequence galaxies contain some lensing signal from background galaxies, but within the red sequence selection limits imposed here, this sample is only 16% of the red sequence galaxies. Therefore there is a fraction  $\sim 0.72 \times 0.16 \simeq 12\%$  of contaminating galaxies (with  $\sim 0.28 \times 0.16 \simeq 4\%$ —those in the foreground—adding noise). The lensing signal in these galaxies is  $\gamma_{+,rs} \lesssim 0.11 \cdot \beta \cdot \gamma_+ = 0.11 \cdot 0.085 \cdot 0.10 \approx 9 \times 10^{-4}$ , several times smaller than the statistical uncertainties (where  $\gamma_+ \approx 0.1$  is a typical shear amplitude in the inner regions of galaxy clusters).

In summary, the red sequence gives a high-fidelity cluster member selection. It is important, however, to restrict this selection to the inner regions of clusters and to luminous galaxies (as shown in Fig. 4.4), because the red sequence may contain some lensing signal. The purity of the red sequence as selected here is 84%, so this contamination is not expected to be significant. Adding the red sequence members to the 14,576 spectroscopically confirmed members gives a total of  $N_m + N_{rs} = 23,041$  members with an estimated contamination of  $0.16 \cdot N_{rs} / (N_m + N_{rs}) \approx 8\%$ .

### 4.3.3 Photometric redshift contamination

By taking a fixed width in velocity, we can simulate the members found by an accurate, unbiased photometric redshift criterion. The dotted lines in Fig. 4.4 show the fraction of galaxies that are within  $\Delta z = 0.03(1 + z)$  (as expected for large ongoing photometric redshifts) but are not members of the cluster,<sup>7</sup> as determined in Section 4.3.1. The contamination is roughly independent of magnitude at all radii and at a level of  $\sim 13\%$  within 1 Mpc of the BCG, rising steeply beyond this radius. In terms of apparent magnitude the curves look similar in the range

---

<sup>7</sup> $\Delta z = 0.03(1 + z)$  corresponds to  $\approx 10,000 \text{ km s}^{-1}$  at the median redshift of the sample,  $z = 0.15$ .

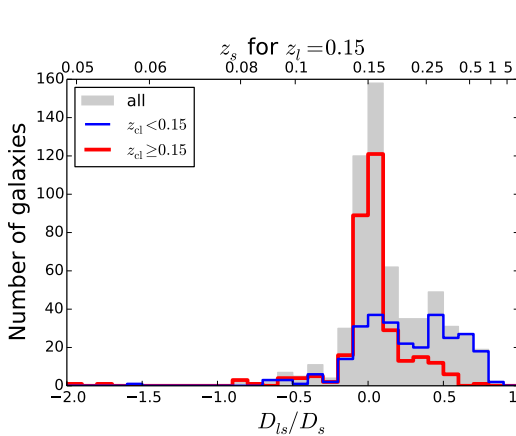


**Figure 4.5:** Distribution of the distance ratio,  $D_{ls}/D_s$ , for red sequence members that are confirmed to be nonmembers of the clusters from spectroscopic redshifts. The gray filled histogram shows red sequence galaxies from all clusters; the blue and red (empty) histograms show the distributions for clusters at low and high redshift, respectively. For illustration, the top axis shows the source redshift for a cluster at  $z = 0.15$ .

$m_r \lesssim 23$ , the range in which most of the selected red sequence galaxies are found. This contamination rises shallowly with redshift, reaching  $\sim 20\%$  at  $z \gtrsim 0.3$ .

The radial dependence in Fig. 4.4 is shown in physical units instead of in units of  $r_{200}$  because this is more generally used with photometric surveys where the physical size of each cluster is not known, and Fig. 4.4 gives an idea of the apertures that should be used to either search for clusters or characterize the cluster based on a red sequence sample.

Comparing the dotted and solid curves, it seems that there is not such a significant gain in using photo- $z$ 's versus the red sequence. A photo- $z$  selection has the advantage that it selects a more representative population of the cluster, and that the red sequence depends on a single color (at least in this implementation) and it becomes less reliable when the 4000Å break is not bracketed by the filters used. This is the case in our study for  $z \gtrsim 0.36$ . It is also apparent, as with the red sequence, that a photo- $z$  selection becomes significantly contaminated beyond  $r \sim 1$  Mpc.

Finally, we note that the galaxies we refer to here (shown with the dotted lines) are not cluster members but also do not contribute a lensing signal, because they are too close behind. They are, indeed, likely to be part of the same large-scale structure of the cluster so would probably feel tidal torque from it similar to the actual member galaxies. Thus from the perspective of galaxy alignment measurements these galaxies should not dilute the signal significantly, nor introduce a lensing signal.

### 4.3.4 Control samples

We construct two catalogs as control samples to assess spurious contributions to our measurements. The shapes of objects in these two samples are unaffected by the cluster (and are mostly unrelated between objects in each sample), so their alignment signals (see Section 4.4) should be consistent with zero. A departure from zero would mean that there is significant residual PSF ellipticity in the images, and therefore that the shape measurements are unreliable.

First, we use all stars in the magnitude range  $17 < m_r < 22$ , selected as outlined in Section 4.2.1, for a total of 443,321 stars. We choose the bright limit to avoid saturated stars, whereas the faint limit ensures that the star sample is not contaminated by faint, unresolved galaxies.

We also use all spectroscopically confirmed foreground galaxies, which are selected as all galaxies with peculiar velocities more negative than  $-10,000 \text{ km s}^{-1}$  in the rest-frame of the cluster. There are 3,666 spectroscopically confirmed foreground galaxies in the direction of 73 clusters. The clusters with the most foreground galaxies are two high-redshift clusters, namely MS 0451.6–0305 at  $z = 0.539$  and MACS J0717.5+3745 at  $z = 0.544$ , with  $N_{\text{fg}} = 306$  and  $N_{\text{fg}} = 304$ , respectively.

## 4.4 Measuring intrinsic alignments

We measure the alignment signal of galaxies within clusters by weight-averaging the ellipticity components of all galaxies within a given radial annulus,

$$\langle \epsilon_i \rangle = \frac{\sum_n w_n \epsilon_{i,n}}{\sum_n w_n}, \quad (4.3)$$

with weights equal to

$$w_n = \frac{1}{\epsilon_{\text{int}}^2 + \sigma_n^2}, \quad (4.4)$$

where  $\sigma_n$  is the measurement uncertainty on the ellipticity of the  $n$ -th galaxy. We assume an intrinsic (i.e., unlensed) galaxy ellipticity dispersion  $\epsilon_{\text{int}} = \sqrt{\langle \epsilon_i \epsilon_i \rangle} = 0.25$ . The uncertainty in Eq. 4.3 is equal for both components and is given by  $\sigma(\epsilon_i) = (\sum_n w_n)^{-1/2}$ . In this work, we use the shapes of cluster members to measure three kinds of alignment: the alignment of (satellite) galaxies toward the centre of the cluster, the alignment of galaxies with respect to the BCG orientation, and the alignment between satellite galaxies. These three quantities are detailed below.

Throughout, we refer to raw ellipticities as  $\epsilon_i$ , and to ellipticities that account for instrumental effects (i.e., PSF size in the case of gaussianized images) as  $\epsilon_i$ .

#### 4.4.1 Different alignment signals

In this section we outline the different rotations we apply to the ellipticity measurements of Section 5.2.2.2 in order to extract alignment signals within clusters.

##### 4.4.1.1 Satellite radial alignment

We measure the alignment of galaxies with respect to the centre of the cluster using ellipticity components rotated to a frame such that

$$\epsilon_+ = -(\epsilon_1 \cos 2\theta + \epsilon_2 \sin 2\theta) \quad (4.5)$$

$$\epsilon_\times = \epsilon_1 \sin 2\theta - \epsilon_2 \cos 2\theta \quad (4.6)$$

where  $\epsilon_1$  and  $\epsilon_2$  are the galaxy ellipticities in the cartesian frame, with  $\epsilon_1$  measuring the ellipticity in the  $x$  and  $y$  directions, and  $\epsilon_2$  in diagonal directions. Here  $\theta$  is the azimuthal angle with respect to the centre of the cluster. In this frame,  $\epsilon_+$  measures the distortion in the tangential and radial directions while  $\epsilon_\times$  measures the distortion at  $\pm 45^\circ$  from the radial direction (see, e.g., Figure 1 of Bernstein & Norberg 2002, for a diagram). Note that the definition of  $\epsilon_+$  in Eq. 4.5 has the opposite sign to that typically used in weak lensing analyses. For symmetry reasons the cross component,  $\langle \epsilon_\times \rangle$ , of an ensemble of clusters should be consistent with zero (although a single cluster might have a preferred nonradial alignment direction such that  $\langle \epsilon_\times \rangle \neq 0$ , the average over an ensemble of clusters must be zero), so it serves as a check for systematic effects. On the other hand,  $\langle \epsilon_+ \rangle < 0$  indicates that galaxies are preferentially aligned in the tangential direction, as is the case for gravitationally lensed background galaxies, while  $\langle \epsilon_+ \rangle > 0$  would indicate a radial alignment of the galaxies, which could be the case for cluster members. Finally,  $\langle \epsilon_+ \rangle = 0$  implies that galaxies are randomly oriented toward the centre of the cluster.

##### 4.4.1.2 Satellite-BCG alignment

To measure the alignment between satellite galaxies and the BCG, we rotate the shapes and coordinates of satellites to a frame where the direction of  $\epsilon_1 > 0$  coincides with the major axis of the BCG, namely

$$\begin{aligned} \epsilon'_1 &= \epsilon \cos [2(\phi - \phi_{\text{BCG}})] \\ \epsilon'_2 &= \epsilon \sin [2(\phi - \phi_{\text{BCG}})] , \end{aligned} \quad (4.7)$$

where  $\phi$  and  $\phi_{\text{BCG}}$  are the position angles of a satellite galaxy and the BCG, respectively, and  $\epsilon \equiv (\epsilon_1^2 + \epsilon_2^2)^{1/2}$  is the ellipticity of the galaxy. In this new frame, the BCG has ellipticity components  $\epsilon'_1 = \epsilon$  and  $\epsilon'_2 = 0$ . For the BCG position

angles we use only GALFIT measurements (see Section 4.4.2.2), since these are expected to be more reliable for galaxies as large as BCGs. Analogous to the radial alignments,  $\langle \epsilon'_1 \rangle > 0$  implies that satellite galaxies are oriented along the major axis of the BCG,  $\langle \epsilon'_1 \rangle < 0$  that satellites are oriented along the BCG minor axis, and  $\langle \epsilon'_1 \rangle = 0$  implies random orientations;  $\epsilon'_2$  measures diagonal alignments so we expect  $\langle \epsilon'_2 \rangle = 0$ .

#### 4.4.1.3 Satellite-satellite alignment

Finally, we compute the alignment between satellite galaxies within clusters by calculating Eq. 4.5 taking every satellite galaxy as a test galaxy (i.e., as the frame for  $\theta$ ). BCGs are excluded from this analysis. This probes potential alignments of galaxies in substructures within the cluster. In principle, if there are  $N$  members in a cluster, the number of pairs is equal to  $N(N - 1)/2$ . However, we only use pairs for which a full circle can be averaged, to avoid averages that include mostly objects in the corners of the images where PSF residuals may be larger. This is a concern for massive, low redshift clusters, where  $30'$  (half the side of the MegaCam image) is roughly equal to  $r_{200}$  in the worst cases. To ensure that the average remains unbiased, therefore, we only include pairs such that the sum of the distance between the test galaxy and the centre of the cluster and the separation between the two satellites is less than 90% of the distance between the cluster centre and the edge of the image.

#### 4.4.2 Shape measurements

Measuring galaxy shapes is a challenging endeavor, especially in the presence of noise and PSF anisotropies (e.g., Massey et al. 2007; Melchior & Viola 2012; Kitching et al. 2013). For large (in units of the PSF), bright objects such as those used here, this should be less of a problem. Moreover, after gaussianization the PSF ellipticity is negligible. In this work we measure the shapes of member galaxies using two different methods, which allows us to test for consistency and robustness of the results. Below we give a brief outline of each method to highlight their differences; more details can be found in the original works.

Shapes are measured from the gaussianized images (Section 4.2.1). The PSF in these images is, by construction, circular, gaussian, and constant across the image. Therefore the shape measurement methods need to account for the blurring of the ellipticity by the PSF, but there are no systematic ellipticities in the images (to a high enough precision, see Section 4.4.3).

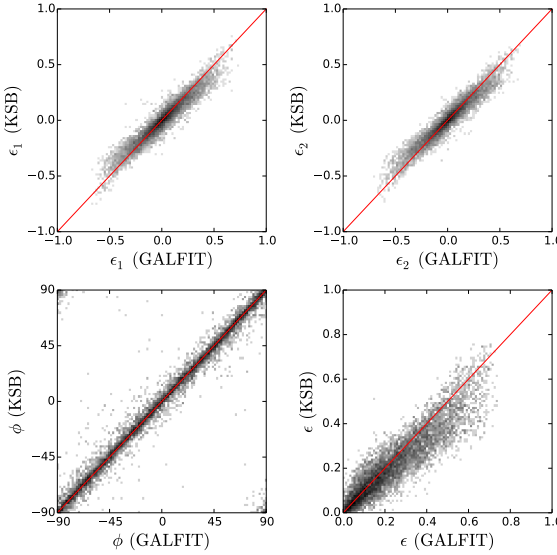


**Figure 4.6:** Comparison of shape measurements from KSB and GALFIT. Grey scales show the number of points per bin in logarithmic scale. Red lines show  $y = x$ . Top: Ellipticity components in cartesian coordinates. Bottom left: position angles,  $\phi$ , in degrees. The periodicity of  $\phi$  (of 180 deg) can be seen in the top left and bottom right corners of the plot. Bottom right: galaxy ellipticities.

#### 4.4.2.1 Kaiser-Squires-Broadhurst (KSB)

KSB was developed for weak lensing measurements by Kaiser et al. (1995) and revised by Hoekstra et al. (1998). It measures shapes by estimating the central second moments  $I_{ij}$  of the image fluxes to measure the two-component polarization

$$e_1 = \frac{I_{11} - I_{22}}{I_{11} + I_{22}}; \quad e_2 = \frac{2I_{12}}{I_{11} + I_{22}}. \quad (4.8)$$

These measurements are weighted with a circular Gaussian of width  $r_g$ , which corresponds to the radius of maximum significance measured by KSB; this weight reduces shot noise in the measurements. Blurring by the PSF is corrected by the so-called pre-seeing shear polarizability,  $P^\gamma$ , which quantifies the effect of the convolution of the PSF to the image polarization,  $e_i$  (Luppino & Kaiser 1997; Hoekstra et al. 1998). The corrected ellipticity is then  $\epsilon_i = e_i / P^\gamma$ .<sup>8</sup> Both  $e_i$  and  $P^\gamma$  are measured with the same radius,  $r_g$ , for each galaxy.

#### 4.4.2.2 GALFIT

GALFIT was developed by Peng et al. (2002), having in mind the modeling of different components of galaxies for studies of galaxy structure and evolution. It attempts to model the light of a galaxy by fitting a multi-component generalized

<sup>8</sup>Because the PSF in our images has vanishing ellipticity by construction, the PSF correction of KSB is mathematically exact. This is not the case if the PSF is significantly elliptical.

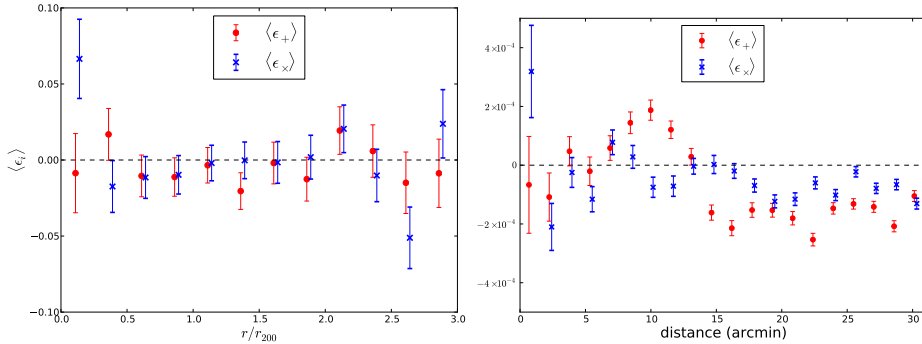


**Figure 4.7:** Alignment signal from control samples measured with KSB, with data points shifted horizontally for clarity. Left: 3,666 foreground galaxies in the direction of 73 clusters as a function of distance from the cluster, in units of  $r_{200}$ . Right: stars in the magnitude range  $17 < m_r < 22$  as a function of angular distance from the centre of each cluster. Typically,  $r_{200} \sim 10'$ . Note the different vertical scales in each plot.

ellipse given by

$$r = \left( |x|^{c+2} + \left| \frac{y}{q} \right|^{c+2} \right)^{1/(c+2)} \quad (4.9)$$

where a true ellipse has  $c = 0$ , a boxy shape  $c > 0$  and a disk-like shape  $c < 0$ ; here  $q$  is the minor-to-major axes ratio. Additionally, the position angle,  $\phi$ , is defined as the direction of the major axis. GALFIT accounts for the PSF model (in this case a single gaussian for each whole field) when measuring ellipticities. We use a simple Sérsic (1968) model for the surface brightness profile,  $\ln I(r) \propto r^{1/n}$ . Only galaxies with Sérsic index  $0.5 < n < 8$  and with axis ratio  $q > 0.15$  are included in the sample. We convert  $q$  and  $\phi$  to the same ellipticity measures of KSB through

$$\epsilon_1 = \left( \frac{1-q}{1+q} \right) \cos 2\phi; \quad \epsilon_2 = \left( \frac{1-q}{1+q} \right) \sin 2\phi. \quad (4.10)$$

#### 4.4.3 Systematic effects

Because weak lensing measurements rely on averages of a large number of small signals, they are more prone to systematic effects than photometry and require more aggressive masks. Therefore some spectroscopic members (all of which are in our photometric catalog) are not included in the shape catalogs. Moreover, the KSB and GALFIT catalogs are not the same since both have different requirements on, e.g., the size of an object and blending with nearby objects to estimate a reliable shape. Of the 14,576 spectroscopic members, 13,966 have a KSB shape

measurement and 13,360 have a GALFIT measurement, with an overlap of 12,160 galaxies and a total of 14,250 galaxies with a shape measurement. Similarly, of 23,041 spectroscopic+RS members, 20,493 have KSB measurements and 18,511 have GALFIT measurements. The smaller number of objects with GALFIT measurements comes mainly from high-redshift galaxies (compare Tables 4.3 and 4.4). This is because small, faint galaxies are harder for GALFIT to fit, while KSB is well-suited to measure the shapes of faint (background) galaxies.

We only consider galaxies with shape measurements from either method in this work, except for the assessment of the red sequence in Section 4.3.2. Fig. 4.6 compares the shape parameters for all spectroscopic members that have valid KSB and GALFIT estimates. While the measurements generally agree, there is a small but noticeable difference for large-ellipticity objects, such that KSB estimates lower ellipticities than GALFIT. This effect is present with more or less the same magnitude for all clusters; it is a genuine difference between the two methods (for our particular dataset), and there is an indication that this effect may be more pronounced for smaller objects. This difference is due to higher-order corrections that are not implemented in KSB, which become important at large ellipticities (Viola et al. 2011). As we show in Section 5.4 this has no impact on our results, so we do not explore this issue further.

As a further test, Fig. 4.7 shows the alignment signals of the control samples. As expected, foreground galaxies have a signal consistent with zero in both ellipticity components at all radii, with large errorbars due to small statistics. The average ellipticities of stars are different from zero at significant levels in most of the radial range. However, the average ellipticity is constrained to  $\langle \epsilon_i \rangle \lesssim 2 \times 10^{-4}$  at all radii, an order of magnitude smaller than the statistical errors in the alignments of cluster members. Thus any systematic effects arising from PSF uncertainty or other instrumental biases are controlled to much lower values than the statistical uncertainties, and can be neglected for the purposes of this work.

Finally, the gaussianization of the images makes the PSF round and homogeneous across an image but produces anisotropic (correlated) noise, which could introduce noise bias in our measurements. The level of anisotropy can be assessed by measuring star ellipticities as a function of magnitude: if noise is highly anisotropic then noisier measurements would show, on average, a larger anisotropy than high-S/N measurements. We test this by comparing the ellipticities of stars as a function of magnitude (for  $18 \leq m_r \leq 22$ ), and find that the average ellipticities are consistent with the levels shown in Fig. 4.7. Moreover, we use galaxies whose number density drops rapidly beyond  $m_r \sim 18$ , and are typically 8 times larger than the PSF. We conclude that anisotropic noise can be safely neglected in this study.

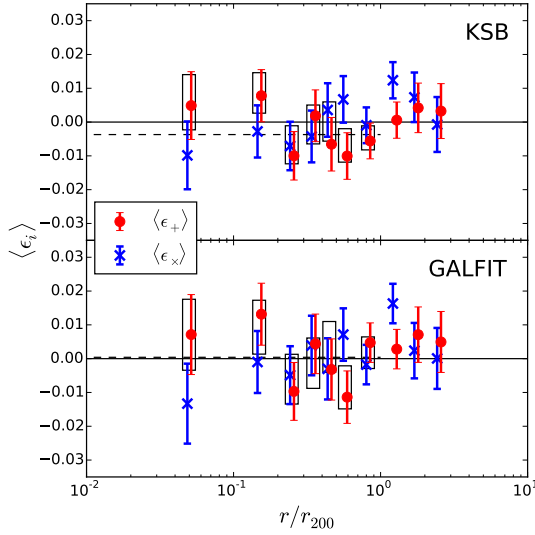


**Figure 4.8:** Average alignment of all spectroscopically confirmed members out to  $3r_{200}$ . The top panel shows the results from KSB while the bottom panel shows those from GALFIT. Shaded bands show the  $1$ ,  $2$  and  $3\sigma$  uncertainties in the overall average and white bars show the  $1\sigma$  range for  $\langle \epsilon_+ \rangle$  from the enhanced sample including red sequence members. Points are slightly shifted horizontally for clarity.

## 4.5 Results

In this section we present and discuss the main results of this paper. We refer to Section 4.4 for details on the calculations that lead to the values reported here and a discussion of systematic effects.

### 4.5.1 Satellite radial alignment

Fig. 4.8 shows the average radial alignment for all spectroscopically confirmed cluster members with good ellipticity measurements from KSB and GALFIT in annuli around the cluster centre. Both methods show that the intrinsic alignment signal of cluster members is consistent with zero across all radii. Hereafter, we choose to quote average values within  $r_{200}$  since, strictly speaking, this is the input required by the halo model (see Section 4.6). Within  $r_{200}$ , the alignment of spectroscopic members is constrained to an average of  $\langle \epsilon_+ \rangle = -0.0037 \pm 0.0027$  with KSB and  $\langle \epsilon_+ \rangle = 0.0004 \pm 0.0031$  with GALFIT at 68% confidence. The cross components are also consistent with zero. Including red sequence members roughly doubles the number of galaxies used and confirms the latter result, with  $\langle \epsilon_+ \rangle = -0.0022 \pm 0.0020$  and  $\langle \epsilon_+ \rangle = 0.0000 \pm 0.0026$  with KSB and GALFIT, respectively.

Our results are consistent with the nondetection of satellite radial alignments in massive clusters at  $z > 0.5$  (Hung & Ebeling 2012), based on  $\sim 500$  spectroscopic members in the inner  $\sim 500$  kpc of clusters, using imaging from the Hubble Space Telescope (HST), and also with measurements at smaller masses from

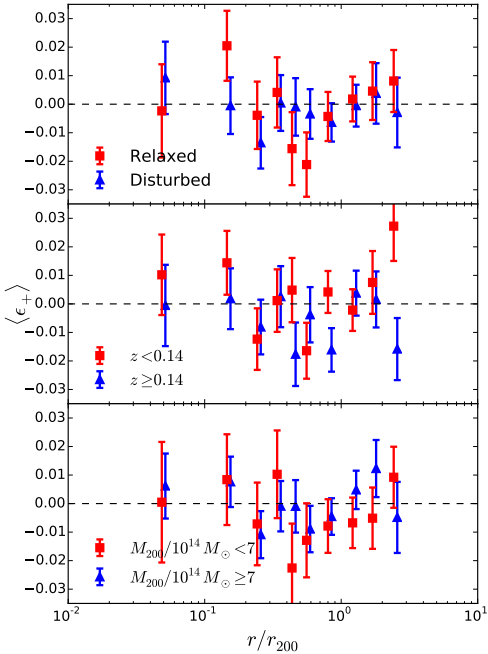


**Figure 4.9:** Average alignment  $\langle \epsilon_+ \rangle$  from KSB for spectroscopically confirmed members, divided by cluster properties: by dynamical state (top; see Section 4.3.1.1), redshift (middle), and dynamical mass (bottom). The latter two thresholds are the median values of the cluster sample.

photometrically-selected galaxy groups from SDSS (Hao et al. 2011; Chisari et al. 2014) and spectroscopically-selected galaxy groups from the Galaxy And Mass Assembly (GAMA) survey (Schneider et al. 2013). Our results suggest that the stars in galaxies within clusters do not feel a strong enough tidal torque to be aligned toward the centre of the cluster, in contrast with results from simulations which find strong alignments even when accounting for differences in the response between stars and dark matter which naturally occurs in hydrodynamical simulations (Pereira & Bryan 2010; Tenneti et al. 2014, Velliscig et al. in prep). An obvious consideration from the observational point of view is miscentring: whether the chosen cluster centre is really the minimum of the cluster potential. This effect can be measured statistically with stacked weak lensing measurements (e.g., George et al. 2012) but is otherwise hard to assess observationally. At least in very relaxed clusters, BCGs are typically very close to the peak of the gas distribution (e.g., Lin & Mohr 2004; Mahdavi et al. 2013), which is closely matched to the dark matter distribution (Faltenbacher et al. 2007a). We can therefore test, to some extent, whether miscentring could be diluting an alignment signal by isolating relaxed clusters as discussed in Section 4.3.1.1. However, as shown in the top panel of Fig. 4.9, we do not detect any alignment signal neither from relaxed nor from disturbed clusters. Thus we conclude that our results are robust to miscentring effects and that, statistically,

satellite galaxies do not align toward the centres of clusters.

As discussed by Hao et al. (2011), the redshift evolution of satellite radial alignments, if any, contains valuable information as to whether these alignments are produced during the formation of clusters or an evolving product of tidal torques within clusters. The middle panel of Fig. 4.9 shows that the alignment signal is consistent with zero across redshift, suggesting that neither of these processes is sufficient to sustain radial alignments over cosmological time. Furthermore, the bottom panel of Fig. 4.9 shows that this nondetection is also independent of cluster mass. We further tested whether any orientation bias, in the sense that we might have clusters viewed preferentially along their major axis, could have any effects on our results. To do this, we divided the cluster sample by BCG elongation, assuming that BCGs that look rounder might actually be elongated along the line-of-sight. Both cluster samples have radial alignments consistent with zero (not shown), arguing that a possible orientation bias is not a problem here.

In any of the two scenarios mentioned above (namely tidal and primordial alignments), radial alignments could show a different pattern for galaxies with different formation histories. We investigate this by splitting the galaxy sample by galaxy luminosity (as a proxy for galaxy mass) and color—since bluer galaxies have been accreted more recently. To split by galaxy color we use each cluster’s red sequence, which depends linearly on apparent magnitude, as outlined in Section 4.3.2. As seen in Fig. 4.10, we find no radial alignments consistently across galaxy colors and luminosities.

The results discussed above are summarized in Tables 4.3 and 4.4 for spectroscopic and spectroscopic plus red sequence member samples, respectively.

### 4.5.2 Satellite-BCG alignment

The second type of alignment we explore is the alignment of the satellite orientations with the BCG orientation (cf. Eq. 4.7). A large number of observations suggest that BCGs are on average oriented along the major axes of clusters themselves (e.g., Sastry 1968; Binggeli 1982; Faltenbacher et al. 2007b; Niederste-Ostholt et al. 2010; Hao et al. 2011), and there is evidence that the velocity dispersion of satellite galaxies is typically larger along the BCG major axis (Skielboe et al. 2012). It is possible, then, that the BCG orientation represents a preferred infall direction. If this is the case, it is possible that galaxies would be aligned toward this infall direction.

Fig. 4.11 shows the alignment of galaxies with the major axis of the BCGs measured with KSB as a function of radius, for the full sample of spectroscopic plus red sequence members. As in the case of radial alignments, the data are also consistent with no satellite-BCG alignments at all distances. The average KSB signal within  $r_{200}$  is  $\langle \epsilon'_1 \rangle = -0.0021 \pm 0.0022$ ; the average GALFIT signal is

**Table 4.3:** Average ellipticity components of spectroscopic members.

Sample	KSB				GALFIT			
	$N_{\text{gal}}^a$	$\langle \epsilon_+ \rangle$	$\langle \epsilon_\times \rangle$	$\sigma(\epsilon_i)^b$	$N_{\text{gal}}^a$	$\langle \epsilon_+ \rangle$	$\langle \epsilon_\times \rangle$	$\sigma(\epsilon_i)^b$
All	8,510	-0.0037	-0.0014	0.0027	8,014	0.0004	-0.0009	0.0031
$z < 0.14$	4,170	0.0002	-0.0000	0.0039	4,612	0.0029	-0.0003	0.0038
$z \geq 0.14$	4,340	-0.0074	-0.0027	0.0038	3,402	-0.0042	-0.0020	0.0053
$M_{200} < 7 \times 10^{14} M_\odot$	2,287	-0.0059	0.0051	0.0052	2,277	-0.0057	0.0041	0.0057
$M_{200} \geq 7 \times 10^{14} M_\odot$	6,223	-0.0029	-0.0038	0.0032	5,737	0.0030	-0.0030	0.0037
Relaxed	3,233	-0.0037	-0.0022	0.0044	3,058	-0.0038	-0.0025	0.0050
Disturbed	5,277	-0.0036	-0.0009	0.0034	4,956	0.0031	0.0001	0.0040
$M_r \leq -21$	4,101	-0.0031	-0.0016	0.0039	3,922	0.0009	-0.0000	0.0044
$M_r > -21$	4,409	-0.0042	-0.0012	0.0038	4,092	-0.0001	-0.0018	0.0044
RS	5,806	-0.0008	-0.0009	0.0033	5,595	0.0010	-0.0001	0.0037
Non-RS	2,704	-0.0099	-0.0025	0.0048	2,419	-0.0012	-0.0031	0.0059

<sup>a</sup>Number of galaxies used for the average, within  $r_{200}$ . <sup>b</sup>68% confidence measurement uncertainties on the average ellipticities.

**Table 4.4:** Average ellipticity components of spectroscopic plus red sequence members.

Sample	KSB				GALFIT			
	$N_{\text{gal}}$	$\langle \epsilon_+ \rangle$	$\langle \epsilon_\times \rangle$	$\sigma(\epsilon_i)$	$N_{\text{gal}}$	$\langle \epsilon_+ \rangle$	$\langle \epsilon_\times \rangle$	$\sigma(\epsilon_i)$
All	15,905	-0.0022	-0.0021	0.0020	12,930	0.0000	-0.0008	0.0026
$z < 0.14$	6,407	-0.0020	-0.0019	0.0031	6,233	0.0013	0.0002	0.0033
$z \geq 0.14$	9,498	-0.0023	-0.0022	0.0026	6,697	-0.0019	-0.0023	0.0041
$M_{200} < 7 \times 10^{14} M_\odot$	5,394	-0.0039	-0.0010	0.0034	4,345	-0.0057	0.0009	0.0044
$M_{200} \geq 7 \times 10^{14} M_\odot$	10,511	-0.0013	-0.0027	0.0024	8,585	0.0031	-0.0017	0.0032
Relaxed	7,504	-0.0034	-0.0051	0.0029	5,903	-0.0044	-0.0038	0.0038
Disturbed	8,401	-0.0011	0.0006	0.0027	7,027	0.0039	0.0018	0.0035
$M_r \leq -21$	5,394	-0.0020	-0.0011	0.0034	4,912	0.0008	0.0004	0.0040
$M_r > -21$	10,511	-0.0023	-0.0026	0.0024	8,018	-0.0005	-0.0017	0.0034

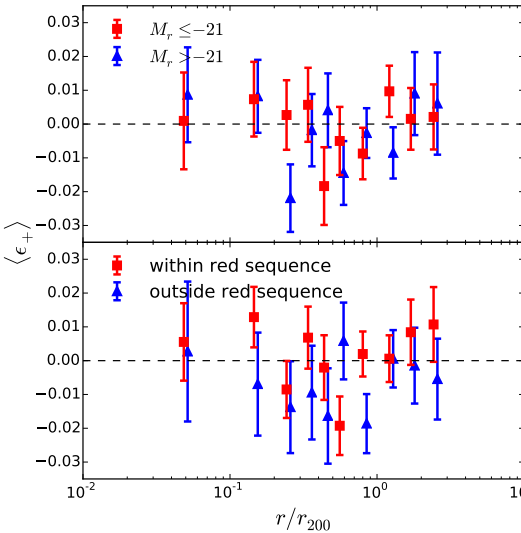


**Figure 4.10:** Average alignment  $\langle \epsilon_+ \rangle$  from KSB for spectroscopically confirmed members divided by galaxy properties: by rest-frame  $r$ -band absolute magnitude (top), and color with respect to each cluster's red sequence (bottom).

$\langle \epsilon'_1 \rangle = -0.0024 \pm 0.0029$ . We also split the sample as in the preceding section, and find no signal for all galaxy and cluster subsamples. As a consistency check, we also find that the distribution of position angles,  $|\phi - \phi_{BCG}|$ , is consistent with a random distribution.

Finally, we averaged not in annular bins but in cartesian coordinates  $\{x, y\}$ , to check if the satellite-BCG alignment could be happening only along a preferential direction, such that the azimuthal average would dilute the signal. We also found a null signal in this case (not shown).

### 4.5.3 Satellite-satellite alignment

We have shown in Section 4.5.1 that satellite galaxies are not aligned toward the centres of clusters. If galaxies reside within substructures themselves, then these substructures might have tidally aligned galaxies toward them. If the tidal torque of the cluster is not enough to overcome these substructure-scale alignments, then maybe we can observe an alignment signal at small separations, between satellite galaxies. After excluding data near the edges of the images (see Section 4.4.1.3), we use a total of  $3.93 \times 10^6$  satellite pairs. Fig. 4.12 shows the alignment signal between satellites averaged over all clusters, as a function of distance between satellites, for the full spectroscopic plus red sequence member sample. In this case we split the sample into two radial bins, namely (test) galaxies within and outside  $0.25r_{200}$ , which corresponds to the scale radius of a cluster with a concentration  $c_{200} = 4$  (roughly what is expected for massive clusters; e.g., Duffy et al. 2008), but the results

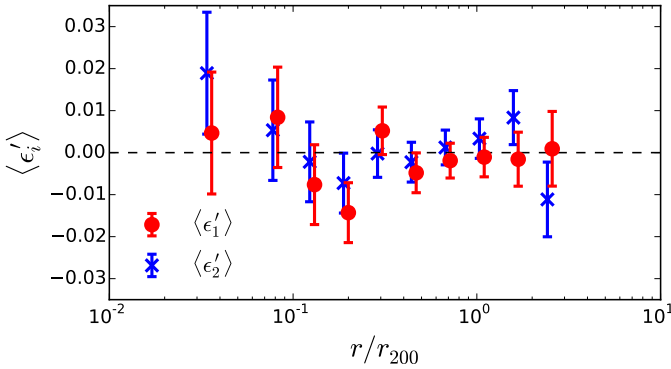


**Figure 4.11:** Mean ellipticity components of spectroscopic plus red sequence satellite galaxies in a frame rotated by the position angle of the BCG, probing the alignment of satellites with the cluster BCG. BCG position angles are measured with GALFIT, while the shapes of satellite galaxies are measured with KSB. Red circles show alignments with respect to the major ( $\epsilon'_1 > 0$ ) and minor ( $\epsilon'_1 < 0$ ) axes of the BCG, while blue crosses show alignments at  $45^\circ$  rotations.

are similar when splitting the sample at other radii.

The leftmost bins in Fig. 4.12 show the signal from substructure: outer bins probe the radial alignment between galaxies at large distances. It might be expected that substructure in the outskirts of clusters would contain an alignment signal since, presumably, they have been accreted more recently. As in the preceding sections, we do not observe any alignment signal for the full cluster sample, nor for relaxed or disturbed clusters, at any radii. We note however that the last data point in Fig. 4.12 is significantly nonzero, but so is the cross component. This suggests that at these distances measurements are affected by systematic effects, mainly because a large fraction of the pairs consist of two galaxies at the edges of the images. Moreover, this data point shows the alignments between satellites at opposite sides of the cluster; i.e., it is not a measurement of alignment within cluster substructure.

Since we do not detect any alignment signal for clusters at different redshifts and at different dynamical stages, we conclude that tidal torques in clusters, or in substructures within them, do not result in significant alignments of the stellar content of galaxies at any scale (neither toward the centre nor between galaxies). It may be possible to bring this in line with the strong alignments measured in  $N$ -body simulations by invoking a misalignment between the stellar and dark matter distributions (e.g., Okumura et al. 2009; Tenneti et al. 2014). However, such analysis is beyond the scope of this paper.

#### 4.5.4 Is there an agreement on the level of galaxy alignments in groups and clusters?

As discussed above, previous studies have reported various levels of alignment of satellite galaxies in clusters using different estimators. We expect such a lack of agreement to arise for two main reasons: the quality of the images used to measure galaxy shape parameters, and the use of shape measurements that are prone to systematic effects, e.g., isophotal measurements. The latter effect was studied by Hao et al. (2011) in detail; they found significant radial alignments only when using isophotal shape measurements, and that the strength of these alignments depends on apparent magnitude but *not* on absolute magnitude, a strong suggestion that the detection is an artifact. Specifically, isophotal measurements are subject to severe contamination from the BCG, which can extend over a few hundred kpc in the case of massive clusters. As to the first cause, the quality of imaging data used by different groups varies significantly. To our knowledge, Plionis et al. (2003) were the first to use CCD photometry to measure galaxy alignments. They found a significant anisotropy in the (isophotal) position angles of satellite galaxies of Abell 521 (though they used photographic plates for their statistical study of alignments in clusters). There are also recent studies, however, who used position angle measurements extracted from scanned photographic plates (e.g., Baier et al. 2003; Panko et al. 2009; Godłowski et al. 2010), both of which are of noticeably lower quality than present-day observations. Moreover, these works typically used single-band information to select cluster members, yielding an unknown (and likely low) sample purity.

Most recent studies have used data from SDSS because of its unmatched statistical power. These data, while of very high quality compared to photographic plate measurements, are several magnitudes shallower than our MegaCam data and taken under less ideal conditions (with seeing a factor 2 larger). Conversely, Hung & Ebeling (2012) have used deep, high-quality HST imaging to measure galaxy alignments, finding no evidence for galaxy alignments within clusters. As in our analysis, Hung & Ebeling (2012) have considered spectroscopically-confirmed cluster members, thus in addition to the superior photometry, both works have a cleaner member sample, which is key to the interpretation of the signal. Schneider et al. (2013) also used a sample of spectroscopically-confirmed group members, plus a shape measurement method that was specifically calibrated to weak lensing measurements (Mandelbaum et al. 2005), and found no significant evidence for alignments. Finally, Chisari et al. (2014) measured galaxy alignments in photometrically-selected galaxy groups and clusters in SDSS Stripe 82, fully accounting for photometric redshift uncertainties, and constrain alignments to similar values as those found here.

The fact that all recent measurements that use high-quality imaging and prop-

erly calibrated shape measurements have yielded null detections (Hao et al. 2011; Hung & Ebeling 2012; Schneider et al. 2013; Chisari et al. 2014, plus the present study) leads us to conclude that there is no evidence for intrinsic alignments of satellite galaxies in galaxy groups or clusters to the level of uncertainty achievable with current datasets (both statistical and systematic).

## 4.6 Contamination to cosmic shear measurements

In this section we explore the impact that the measured galaxy alignments in clusters can have on future cosmic shear measurements. We quantify the contribution of intrinsic alignments to cosmic shear measurements through the matter and intrinsic alignment power spectra, which can be defined as

$$\begin{aligned}\langle \tilde{\gamma}^{I*}(\mathbf{k}) \tilde{\gamma}^I(\mathbf{k}') \rangle &= (2\pi)^3 \delta_D^{(3)}(\mathbf{k} - \mathbf{k}') P_{II}(\mathbf{k}) \\ \langle \delta^*(\mathbf{k}) \tilde{\gamma}^I(\mathbf{k}') \rangle &= (2\pi)^3 \delta_D^{(3)}(\mathbf{k} - \mathbf{k}') P_{GI}(\mathbf{k}).\end{aligned}\quad (4.11)$$

Here,  $\tilde{\gamma}^I = (1 + \delta_g)\gamma^I$  is the (projected) ellipticity field weighted by the galaxy density,  $\delta_g$ , and  $P_{II}(\mathbf{k})$  and  $P_{GI}(\mathbf{k})$  are the II and GI contributions to the power spectrum including a prescription for nonlinear evolution (i.e, nonlinear power spectra, see Smith et al. 2003; Bridle & King 2007), respectively;  $\delta^*$  is the complex conjugate of the Fourier transform of the matter density contrast,  $\delta(\mathbf{r}) = (\rho(\mathbf{r}) - \bar{\rho})/\bar{\rho}$  is the matter overdensity with respect to the average density of the Universe,  $\tilde{\gamma}^{I*}$  indicates the complex conjugate of  $\tilde{\gamma}^I$ , and  $\delta_D$  is a Dirac delta function.

Additionally, we translate the 3-dimensional power spectra discussed above into (observable) angular power spectra,  $C_\ell$ , using the Limber (1953) approximation (e.g., Kaiser 1992). We use a source redshift distribution given by

$$p(z) \propto z^\alpha \exp \left[ -(z/z_0)^\beta \right], \quad (4.12)$$

where we fix the parameters  $\alpha$ ,  $\beta$ , and  $z_0$  so that the median redshift of the model distribution reproduces the median redshift of the Kilo-Degree Survey (KiDS, de Jong et al. 2013),  $z_{\text{med}} \simeq 0.7$  (Kuijken et al., in prep). We split the lens sample in redshift bins of half-width  $\Delta z = 0.1$  to illustrate the results obtained from a tomographic cosmic shear analysis (e.g., Heymans et al. 2013). We use a narrow redshift bin covering  $0.6 < z < 0.8$  for the GG and II power spectra, since this range is close to the one that maximizes the lensing signal in a KiDS-like tomographic analysis. The GI power spectrum is better captured by cross-correlating this redshift bin with one at low redshift; we choose  $0.2 < z < 0.4$  as a compromise between a high intrinsic alignment efficiency and a large enough volume observed.

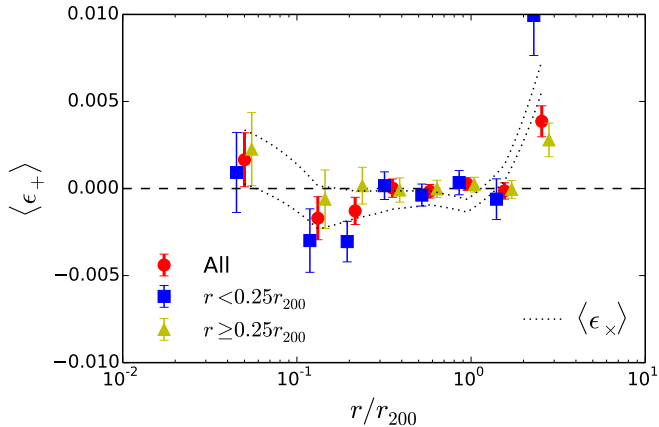


**Figure 4.12:** Satellite-satellite alignment as a function of the distance between satellites, for the full spectroscopic plus red sequence member sample. Red circles show all galaxies, while blue squares and yellow triangles show the signal with respect to galaxies inside and outside  $0.25r_{200}$ . Data points show the radial (positive) and tangential (negative) signal, while the dashed lines show the 68% range of the cross component, linearly interpolated. Uncertainties do not account for covariance between data points. Note that the vertical scale is smaller than in Figs. 4.8 to 4.11.

#### 4.6.1 Linear alignment model

The simplest models for galaxy alignments predict that elliptical galaxies are aligned with a strength that is proportional to the tidal field (Catelan et al. 2001) while spiral galaxies, which are aligned by angular momentum acquired during gravitational collapse, are aligned with a strength that is proportional to the square of the tidal field (Pen et al. 2000). On sufficiently large scales, all galaxies are predicted to experience an alignment proportional to the large scale gravitational potential (Hui & Zhang 2002). Thus a linear alignment model is usually employed to characterize large scale galaxy alignments (e.g., Kirk et al. 2010; Joachimi et al. 2011; Mandelbaum et al. 2011; Heymans et al. 2013).<sup>9</sup> We normalize the intrinsic alignment power spectra as in previous studies (Hirata & Seljak 2004; Bridle & King 2007; Schneider & Bridle 2010), matching to the SuperCOSMOS measurements of Brown et al. (2002). This normalization is also consistent with more recent observations (Heymans et al. 2004; Mandelbaum et al. 2006; Joachimi et al. 2011).

<sup>9</sup>This model is typically referred to as “nonlinear alignment model.” However, this is a misnomer, since intrinsic alignments are still modeled as depending linearly on the tidal field; instead the name arises from the use of the nonlinear power spectrum in Eq. 4.11. We therefore refer to it as linear alignment model throughout.

Solid lines in Fig. 4.13 show the angular power spectra,  $C_\ell$ , from the linear alignment model. This model includes no contribution from alignments within haloes (so-called 1-halo terms) and therefore the II and GI power spectra are subdominant to the matter power spectrum at all scales.

Fig. 4.13 also shows the expected angular power spectrum measurements of a reference cosmic shear survey with properties similar to KiDS with a redshift distribution as described above, with a sky coverage of 1,500 sq. deg. and a background source density of  $n_{\text{gal}} = 10 \text{ arcmin}^{-2}$ . We assume a coverage  $30 \leq \ell \leq 3000$ , and compute the expected  $C_\ell$  measurements and uncertainties following Cooray & Hu (2001), in logarithmic bins in  $\ell$ . The bottom panel of Fig. 4.13 shows that the II contribution remains safely subdominant to statistical uncertainties expected for KiDS, but the GI contribution cannot be ignored, contaminating the GG power spectrum at the  $\sim 10\%$  level.

## 4.6.2 Halo model

The linear alignment model aims to describe alignments at large scales and the alignments between central galaxies, because these are expected to be aligned with the host halo by the large scale gravitational potential. On smaller, nonlinear scales, galaxy formation will tend to misalign baryonic and dark matter (e.g., Pereira & Bryan 2010; Tenneti et al. 2014), so the large-scale results from  $N$ -body simulations are probably not directly applicable to galaxy alignments within haloes. Galaxy formation can also have a major impact on the power spectra (van Daalen et al. 2011; Sembolini et al. 2011), and the way these two effects interplay is unclear. We therefore require a prescription to predict the power spectra accounting for 1-halo term galaxy alignments. To this end, we employ the halo model of radial alignments introduced by Schneider & Bridle (2010).

The main assumption of the halo model is that galaxies form and reside in dark matter haloes whose masses directly influence the (observable) properties of the galaxies they host. Additionally, one can assume that satellite galaxies in a halo are radially aligned toward the centre with a strength that can in principle be a function of the galaxy position in the halo, the host halo mass, and redshift. This is known as a *satellite radial alignment model*. The total alignment can be separated into a prescription for galaxies in haloes (the 1-halo term), and one between haloes (the 2-halo term). We assume that galaxies populate haloes following the halo occupation distribution of Cacciato et al. (2013) and the halo mass and bias functions of Tinker et al. (2010). More details about the ingredients of this halo model can be found in Schneider & Bridle (2010). Given a model for radial alignments,  $\gamma^I(\mathbf{r}, M, z)$ , we calculate the power spectra through Eq. 4.11.

This model only incorporates the information about the radial alignments stud-

ied in Section 4.5.1, by definition. In principle, it would be possible to include further constraints on the alignments from measurements such as those explored in Sections 4.5.2 and 4.5.3. However, these would be second order corrections to the cluster-scale radial component. In particular, the satellite-satellite alignment constraints woud be relevant on scales smaller than what will be probed by current and upcoming experiments; we therefore choose not to include them in the present analysis.

#### 4.6.3 Impact of alignments within haloes on the power spectra

The halo model requires a prescription for the strength of small-scale radial alignments. In its simplest form this strength is constant with radius and halo mass. The power spectra derived from this model are shown as dashed lines in Fig. 4.13, for an alignment strength  $\bar{\gamma} = 0.21$  ( $\bar{\gamma}$  is the 3-dimensional alignment strength derived from a projected measurement,  $\gamma^I$ ; see Schneider & Bridle 2010). This is the fiducial value adopted by Schneider & Bridle (2010). In this work, we extend this prescription by assuming a radial alignment that depends on halo mass but not on distance within the halo. Such a model is fully consistent with our results, since we find a null signal at all radii.

We construct a mass-dependent alignment model using the present results, plus the intrinsic alignment measurements in galaxy groups from the Galaxy and Mass Assembly (GAMA) survey (Schneider et al. 2013). We assume a power law for  $\gamma^I(M)$ , such that the mean ellipticity of satellite galaxies has the  $2\sigma$  upper limits obtained in this study. We use the results for the augmented spectroscopic plus red sequence member sample, and choose to use the KSB measurement because, although the GALFIT constraint is less tight (i.e., more conservative), the contribution of each mass scale is weighted by the mass function. Since the mass function is an exponential function of mass, the overall alignment signal is dominated by lower mass objects. Since we use the constraint found for GAMA groups as a pivot, a smaller alignment strength in clusters will mean a larger overall contribution of alignments to a cosmic shear survey. Specifically, we use  $\epsilon_+ < 0.0019$  at  $M \simeq 10^{15} M_\odot$  and  $\epsilon_+ < 0.019$  at a typical mass  $M \simeq 10^{13} M_\odot$ , corresponding to the  $2\sigma$  upper limit for GAMA groups with  $N_{\text{gal}} \geq 5$  (Schneider et al. 2013). Our model is therefore  $\gamma^I(M) = (M/M_0)^\alpha$ , constant with redshift, with  $M_0 = 1.19 \times 10^9 M_\odot$  and  $\alpha = -0.5$ .<sup>10</sup> We note that the assumption of a single power law at all masses has no justification other than its simplicity. A more detailed halo model for intrinsic alignments will be presented in a forthcoming study

---

<sup>10</sup>The conversion between ellipticity and shear is given by  $\gamma = \epsilon_+/2\mathcal{R}$ , where  $\mathcal{R}$  is the shear responsivity, which we assume to be equal to 0.87.

(Cacciato et al., in prep), where we explore the impact of halo model assumptions on the predictions of the II and GI power spectra.

Dotted lines in Fig. 4.13 show the intrinsic alignment power spectra predicted by the halo model for our adopted  $\gamma^I(M)$ . Since we constructed the model using  $2\sigma$  upper limits on the measured alignments, the regions between the solid and dotted lines should be regarded as conservative estimates of the current uncertainties on the GI and II power spectra due to 1-halo term intrinsic alignments. As can be seen, both the GI and II power spectra remain subdominant to the GG power spectrum, which is not the case with the fiducial  $\bar{\gamma} = 0.21$  model used by Schneider & Bridle (2010). The GI angular power spectrum including our 1-halo term is  $\sim 70\%$  higher than that predicted by the linear alignment model at  $\ell \sim 3000$ , which translates into an excess on the total (GG+GI+II) angular power spectrum of  $\approx 10\%$ , comparable to the statistical uncertainties expected at these scales. Note that at larger scales the GI power spectrum is dominated by linear alignments and the satellite contribution is well below the statistical uncertainties of KiDS. Therefore, we do not expect that cosmic shear analyses with KiDS will need to include a contribution by satellite galaxies in the modeling of intrinsic alignments, and we conclude that the linear alignment model should be a sufficient treatment of intrinsic alignments for KiDS. We note that for a bin at  $0.2 < z < 0.4$ , the II power spectrum can be  $> 10\%$  of the lensing (GG) power spectrum at the same redshift, but the uncertainties of a KiDS-like survey are much larger than at  $z \sim 0.8$  because of the smaller volume probed. In any case, the linear alignment model captures any II contribution to sufficient accuracy. Therefore a treatment of intrinsic alignments in KiDS cosmic shear analyses can rely on the linear alignment model, similar to the cosmic shear analysis of CFHTLenS data by Heymans et al. (2013). We expect the situation to be similar for the Dark Energy Survey (DES)<sup>11</sup>, which will have three times as much area as KiDS but otherwise similar characteristics. This may not be the case for larger surveys, for which the contribution of satellite galaxies to intrinsic alignments must be characterized to higher precision.

## 4.7 Conclusions

We have compiled a large sample of galaxies with spectroscopic redshifts in the direction of 90 galaxy clusters in the redshift range  $0.05 < z < 0.55$ , selected as part of MENeACS and CCCP. We select cluster members using the shifting gapper technique, which uses phase space information, for a total 14,576 cluster members. We use these members to estimate dynamical masses using the simulation-based scaling relation between velocity dispersion and cluster mass of Evrard et al. (2008).

---

<sup>11</sup><http://www.darkenergysurvey.org>

The sample has a median redshift  $z = 0.14$  and a median mass  $M_{200} \sim 7 \times 10^{14} M_\odot$ , in good agreement with the weak lensing masses estimated by Hoekstra et al. (2012).

We quantify the alignment of galaxies within clusters using 14,250 cluster members for which we are able to measure their shapes either with KSB or GALFIT, after showing that the ellipticities measured by both methods are consistent (Fig. 4.6). Both methods take different approaches to measuring galaxy shapes and therefore provide an important consistency check. We confirm that our analysis is free of significant systematic effects by measuring the average alignment of both foreground galaxies and stars. The signal from foreground galaxies is consistent with zero; the signal from stars is significantly different from zero, but at a level of  $\langle \epsilon_+ \rangle \sim 10^{-4}$ , an order of magnitude lower than measurement uncertainties (Fig. 4.7).

We measure three different alignments: the radial alignment of satellite galaxies toward the BCG, the alignment of satellites with the BCG orientation, and the radial alignment of satellites toward each other. Each probes a different, but not necessarily independent, effect. We find no evidence for any of these alignments (Figs. 4.8 to 4.12). In particular, we constrain the average ellipticity of satellites toward BCGs to  $\langle \epsilon_+ \rangle = -0.0037 \pm 0.0027$  with KSB and  $\langle \epsilon_+ \rangle = 0.0004 \pm 0.0031$  with GALFIT, at 68% confidence, within  $r_{200}$ . Similarly, there is no evidence of galaxy alignments when splitting the sample by cluster (redshift, mass, or dynamical state) or galaxy (color or luminosity) properties. Selecting additional cluster members through the red sequence allows us to extend the sample to  $\sim 20,000$  galaxies with an estimated contamination of  $< 10\%$  from red sequence interlopers (Fig. 4.4). All signals from this enlarged sample are also consistent with zero.

We include this constraint on the radial alignment of galaxies within high-mass haloes, together with a measurement at the group scale (Schneider et al. 2013), in a halo model framework, and derive the current uncertainty on the angular power spectrum given by intrinsic alignments within haloes (a 1-halo term). We find that the total (GG+GI+II) angular power spectrum predicted from our alignment model (see Section 4.6.3) is, at most, 10% higher than the total power spectrum predicted by the linear alignment model at the smallest scales probed by KiDS,  $\ell \sim 3000$ . This level of contribution from satellite galaxies will not be relevant for cosmic shear measurements with KiDS or DES (see Fig. 4.13). We conclude that the linear alignment model is a sufficient description of intrinsic alignments for KiDS, but the situation may be different for significantly larger surveys.

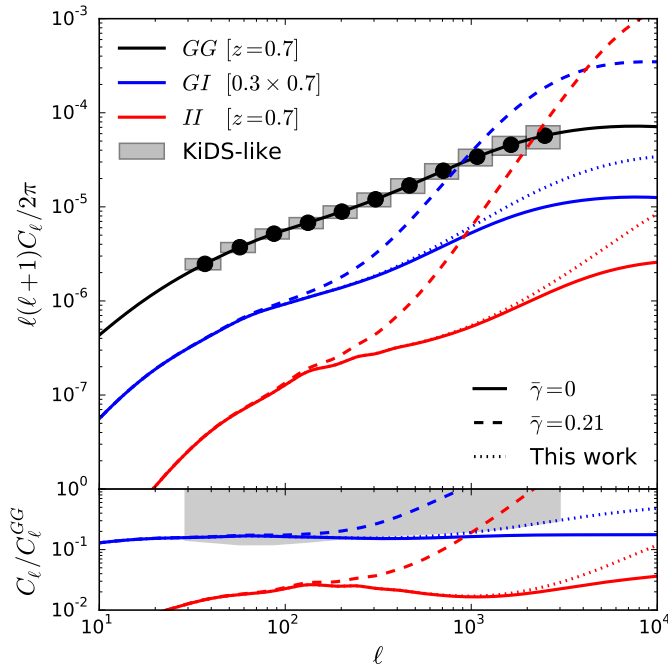


**Figure 4.13:** Effect of intrinsic alignments on the angular power spectra. *Top panel*: The black line shows the GG power spectrum, while blue and red lines show the GI and II power spectra, respectively. Solid lines show the linear alignment model with no small-scale intrinsic alignments, while dashed and dotted lines model the contribution of satellite galaxies with  $\bar{\gamma} = 0.21$  as in Schneider & Bridle (2010) and with the mass-dependent  $2\sigma$  upper limit on the alignment signal derived in this work (see Section 4.6.3), respectively. Grey boxes with black circles show the expected uncertainty levels on a KiDS-like survey covering 1,500 sq. deg. and with  $n_{\text{gal}} = 10 \text{ arcmin}^{-2}$ . The *bottom panel* shows the ratio between the GI and II power spectra and the GG power spectrum, for each model. The shaded region shows values above the  $1\sigma$  uncertainties in the angular power spectrum for a KiDS-like survey, where GI and II contributions would dominate over statistical uncertainties.



# 5 | The masses of satellites in GAMA galaxy groups from 100 square degrees of KiDS weak lensing data

We use the first  $100 \text{ deg}^2$  of overlap between the Kilo-Degree Survey (KiDS) and the Galaxy And Mass Assembly (GAMA) survey to determine the galaxy halo mass of  $\sim 10,000$  spectroscopically-confirmed satellite galaxies in massive ( $M > 10^{13} h^{-1} M_\odot$ ) galaxy groups. Separating the sample as a function of projected distance to the group centre, we jointly model the satellites and their host groups with Navarro-Frenk-White (NFW) density profiles, fully accounting for the data covariance. The probed satellite galaxies in these groups have total masses  $\log M_{\text{sub}}/(h^{-1} M_\odot) \approx 11.7 - 12.2$  consistent across group-centric distance within the errorbars. Given their typical stellar masses,  $\log M_{*,\text{sat}}/(h^{-2} M_\odot) \sim 10.5$ , such total masses imply stellar mass fractions of  $M_{*,\text{sat}}/M_{\text{sub}} \approx 0.04 h^{-1}$ . The average subhalo hosting these satellite galaxies has a mass  $M_{\text{sub}} \sim 0.015 M_{\text{host}}$  independent of host halo mass, in broad agreement with the expectations of structure formation in a  $\Lambda$ CDM universe.

*Cristóbal Sifón, Marcello Cacciato, Henk Hoekstra, et al., 2015,  
MNRAS, 454, 3938*

## 5.1 Introduction

Following a hierarchical build-up, galaxy groups grow by accretion of smaller groups and isolated galaxies. Tidal interactions tend to transfer mass from infalling galaxies to the (new) host group, with the former becoming group satellites. The favoured cosmological scenario posits that galaxies are embedded in larger dark matter haloes, with masses that largely exceed the stellar masses, a conclusion supported by a variety of observations (see, e.g., the reviews by Trimble 1987; Einasto 2013). Accordingly, satellite galaxies are hosted by ‘subhaloes,’ whose masses and distribution contain information on the properties of dark matter itself (e.g., Libeskind et al. 2013).

Because dark matter is (at least to a good approximation) dissipationless and baryons are not, it is subject to stronger tidal disruption than the baryonic component: energy losses cause baryons to sink to the centre of the potential more efficiently than dark matter, and therefore baryons are more resistant to tidal disruption (White & Rees 1978). This latter fact produces a unique prediction of the dark matter hypothesis: a satellite galaxy will be preferentially stripped of its dark, rather than stellar, matter. Thus, tidal stripping can be observed by comparing the total and stellar masses of satellite galaxies, such that galaxies accreted earlier have smaller mass-to-light ratios than galaxies accreted recently or (central) galaxies that have not been subject to tidal stripping by a larger host (e.g., Chang et al. 2013a).

Numerical simulations predict that tidal stripping is stronger within more centrally concentrated host haloes, and is more severe for more massive satellites (e.g., Tormen et al. 1998; Taffoni et al. 2003; Contini et al. 2012). Different infall timescales and concentrations induced by baryons (compared to dark matter-only simulations) can alter both the radial distribution and density profiles of subhaloes, consequently affecting tidal stripping in a radially-dependent manner (Romano-Díaz et al. 2010; Schewtschenko & Macciò 2011), although this baryon-induced radial dependence could plausibly be (partially) compensated by feedback from active galactic nuclei (AGN; Romano-Díaz et al. 2010).

Observationally, the primary difficulty lies in estimating the total masses of satellite galaxies. Weak gravitational lensing is currently the only option available to measure the total mass of statistical samples of galaxies. So-called (weak) galaxy-galaxy lensing provides a direct measure of the masses of lensing galaxies through the observation of their distortion of the images of background galaxies, without assumptions about the dynamical state of the system (e.g., Brainerd et al. 1996; Courteau et al. 2014). Weak lensing is an intrinsically statistical observational measurement: outside the strong lensing regime (typically a few tenths of arcsecond) the distortion induced in each background galaxy is much smaller than the typi-

cal galaxy ellipticity. Such measurements require high-quality multi-colour images that allow both accurate shape measurements and photometric redshift determination of faint, distant background sources. Measuring the lensing signal around satellite galaxies (hereafter ‘satellite lensing’, see, e.g., Yang et al. 2006) is particularly challenging because of i) the small relative contribution of the satellite galaxy to the lensing signal produced by the host galaxy group; ii) source blending at small separations, which hampers our ability to measure shapes reliably (and which is enhanced in high-density regions); and iii) particular sensitivity to contamination by field galaxies. This latter point is critical: since the dark matter haloes around satellite galaxies are expected to be stripped, isolated galaxies will significantly contaminate the lensing signal since they are not stripped, thus complicating a meaningful interpretation of the signal. Therefore, satellite lensing requires a clean sample of satellite galaxies to allow a proper interpretation of the signal. Satellite galaxies can usually be identified easily in massive galaxy clusters with high purity by use of, for instance, the red sequence (e.g., Rozo et al. 2015, see also Chapter 4), which in principle requires only two-band photometry. Indeed, most satellite lensing measurements so far have concentrated on massive galaxy clusters with deep Hubble Space Telescope (HST) observations in which bright cluster members can be easily identified (Natarajan et al. 2002; Limousin et al. 2007; Natarajan et al. 2009), sometimes with the aid of strong lensing measurements (Natarajan et al. 2007). Some of these studies have claimed detections of satellite truncation, but it seems likely that they are mostly attributable to the parameterization of subhalo density profiles rather than direct detections (Pastor Mira et al. 2011).

Because galaxy groups have fewer satellites than massive clusters, lensing measurements of galaxy group satellites require larger samples and have only been possible thanks to recent large optical surveys with high image quality. Furthermore, because the red sequence is generally not so well established in galaxy groups compared to galaxy clusters, accurate group membership determination requires high-completeness spectroscopic observations. Lacking such data, most measurements in galaxy groups to date have relied on more indirect means of estimating subhalo masses. Gillis et al. (2013) used an optimized density estimator on galaxies selected from Canada-France-Hawaii Telescope Lensing Survey (CFHTLenS, Heymans et al. 2012; Erben et al. 2013) and showed that the lensing signal of galaxies in high-density environments is inconsistent with the predictions of a model that does not include halo stripping, providing indirect evidence for tidal stripping in galaxy groups. Such differentiation was only possible because their high-density environment galaxies were mostly satellites, due to their carefully calibrated density estimator. Recently, Li et al. (2014) presented the first direct detection of the lensing signal from satellite galaxies in galaxy groups. They took advantage of the

overlap between deep imaging from the CFHT-Stripe82 Survey (CS82, e.g., Comparat et al. 2013) and the Sloan Digital Sky Survey (SDSS, York et al. 2000) Data Release 7 (Abazajian et al. 2009) spectroscopic catalogue. Yang et al. (2007) used this SDSS catalogue to construct a clean galaxy group catalogue with centrals and satellites identified individually; although Li et al. (2014) had only  $\sim 1,000$  lens galaxies, their sample was essentially free of contamination by central galaxies. This allowed them to use weak lensing to directly measure the masses of satellites in galaxy groups for the first time, albeit with limited constraining power.

In this paper we present a direct measurement of the lensing signal from satellite galaxies in galaxy groups by combining a sample of spectroscopically confirmed galaxy groups from the Galaxy And Mass Assembly survey (GAMA, Driver et al. 2011), and background galaxies with high-quality shape measurements from the Kilo-Degree Survey (KiDS, de Jong et al. 2013; Kuijken et al. 2015). We use these measurements to constrain the masses of satellite galaxies as a function of projected distance from the group centre. By converting, in an average sense, these projected distances into 3-dimensional distances, we can study the evolution of satellite masses as they fall into galaxy groups.

This chapter is organized as follows. In Section 5.2 we describe the galaxy samples we use as lenses and lensed background sources. In Section 5.3 we summarize the measurement of galaxy-galaxy lensing and describe our modelling of satellites and their host groups. We present our results in Section 5.4 and summarize in Section 5.5. We adopt a flat  $\Lambda$ CDM cosmology with  $\Omega_m = 0.315$ , consistent with the latest cosmic microwave background measurements (Planck Collaboration 2015a), and  $H_0 = 100h \text{ km s}^{-1}\text{Mpc}^{-1}$ . We explicitly include the dependence on  $h$  where appropriate. Throughout we use the symbol  $\langle X \rangle$  to refer to the median of distribution  $X$ .

## 5.2 Galaxy samples

### 5.2.1 Lens galaxies: satellites in the GAMA galaxy group catalogue

GAMA<sup>1</sup> is a spectroscopic survey which measured redshifts for 238,000 galaxies over a total of  $286 \text{ deg}^2$  carried out with the AAOmega spectrograph on the Anglo-Australian Telescope (AAT). GAMA is 98% spectroscopically complete down to  $m_r = 19.8$  even in the most crowded regions (Baldry et al. 2010; Driver et al. 2011; Liske et al. 2015). Here we use data over three different regions on the sky, centred at right ascensions 9h, 12h and 15h (the G09, G12 and G15 fields), which overlap with SDSS data. Below we briefly describe the GAMA galaxy group sample con-

---

<sup>1</sup><http://www.gama-survey.org/>

structed by Robotham et al. (2011), who discuss the properties, possible systematics, and limitations of the catalogue in greater detail. Galaxy photometric properties such as luminosity and stellar mass are measured from the five-band optical SDSS imaging. In particular, we use the stellar masses derived by Taylor et al. (2011) by fitting Bruzual & Charlot (2003) synthetic stellar spectra to the broadband SDSS photometry.

The GAMA galaxy group catalogue was constructed using a 3-dimensional Friends-of-Friends (FoF) algorithm, linking galaxies in projected and line-of-sight separations. We use version 7 of the group catalogue ( $G^3Cv7$ ), which contains 23,838 groups with  $N_{\text{FoF}} \geq 2$ , where  $N_{\text{FoF}}$  is the number of spectroscopic members grouped together by the FoF algorithm (each group has  $N_{\text{FoF}} - 1$  satellites). Group properties such as velocity dispersion and total luminosity<sup>2</sup> were calibrated to mock galaxy catalogues processed in the same way as the real data and were optimized for groups with  $N_{\text{FoF}} \geq 5$ . A visual inspection of the phase space (distance-velocity plane) of GAMA groups confirms that groups with  $N_{\text{FoF}} < 5$  are significantly contaminated by interlopers, while member selection for groups with  $N_{\text{FoF}} \geq 5$  is in better agreement with the expectation of a smooth distribution of galaxies with a maximum velocity that decreases with radius (e.g., Mamon et al. 2010). We therefore restrict our study to groups with  $N_{\text{FoF}} \geq 5$ , in the 68.5 deg<sup>2</sup> of unmasked area overlapping with the first release of KiDS lensing data (see Section 5.2.2). In all, we use 9683 satellites hosted by 1467 different groups<sup>3</sup>. These are the same groups used by Viola et al. (2015).

Robotham et al. (2011) identified the central galaxy in each group using three definitions of group centre: the weighted centre of light, an iterative method rejecting the galaxy farthest away from the center of light until one galaxy remained (the ‘iterative’ centre), and the brightest cluster galaxy (hereafter BCG). All galaxies that are not centrals are classified as satellites. In most cases ( $\sim 90\%$ ) the iterative central galaxy coincides with the BCG, while the centre of light is more discrepant. Viola et al. (2015) performed a detailed analysis of the lensing signal of GAMA groups comparing the different centre definitions and confirm the results of Robotham et al. (2011): the BCG and the iterative centre both represent the group centre of mass to a good degree, while the centre of light is a very poor indicator of the group centre. In this work we use the central-satellite classification that uses the BCG as the central, and therefore measure the lensing signal around all group members

---

<sup>2</sup>The total luminosity of a group is the sum of the luminosities of its member galaxies, corrected for spectroscopic incompleteness at the low-mass end (see Robotham et al. 2011).

<sup>3</sup>This is the total number of satellites considered in this work, and includes satellites that do not fall within the currently available KiDS data but reside in a group which is less than  $2 h^{-1} \text{Mpc}$  away from the center of the closest KiDS field. 9357 (97%) of these satellites fall within the KiDS footprint (see Table 5.1).

**Table 5.1:** Median properties of satellite galaxies binned by projected distance to the group centre,  $R_{\text{sat}}$ .  $N_{\text{sat}}$  is the total number of satellites considered while  $N_{\text{sat}}^{\text{KiDS}}$  is the number of satellites that fall within the  $100 \text{ deg}^2$  of KiDS imaging used in this work. Errorbars are 16th and 84th percentiles.

Bin	$R_{\text{sat}}$ range ( $h^{-1}\text{Mpc}$ )	$N_{\text{host}}$	$N_{\text{sat}}$	$N_{\text{sat}}^{\text{KiDS}}$	$\langle N_{\text{FoF}} \rangle$	$\langle R_{\text{sat}} \rangle$ ( $h^{-1}\text{Mpc}$ )	$\langle z_{\text{sat}} \rangle$	$\log \langle M_{*,\text{sat}} \rangle$ ( $h^{-2}\text{M}_\odot$ )	$\log \langle L_{\text{host}} \rangle$ ( $h^{-2}\text{L}_\odot$ )
1	$0.05 - 0.20$	1263	3714	3541	$7^{+5}_{-2}$	$0.12^{+0.05}_{-0.05}$	$0.17^{+0.09}_{-0.09}$	$10.45^{+0.26}_{-0.09}$	$11.10^{+0.17}_{-0.23}$
2	$0.20 - 0.35$	1235	3152	3042	$7^{+5}_{-2}$	$0.25^{+0.05}_{-0.04}$	$0.19^{+0.10}_{-0.09}$	$10.51^{+0.22}_{-0.10}$	$11.15^{+0.14}_{-0.26}$
3	$0.35 - 1.00$	785	2817	2773	$8^{+7}_{-3}$	$0.43^{+0.16}_{-0.08}$	$0.21^{+0.10}_{-0.07}$	$10.66^{+0.15}_{-0.14}$	$11.33^{+0.10}_{-0.25}$

except the BCGs.

### 5.2.2 Lensed background sources: the Kilo-Degree Survey

KiDS<sup>4</sup> is an ESO Public Survey being conducted with the 2.6 m VLT Survey Telescope (VST) in Cerro Paranal, Chile, which surveys the sky in the *ugri* bands. Each 1 deg<sup>2</sup> pointing is observed four times ('exposures') in the *u*-band and five times in the other bands. Upon completion, KiDS will cover 1,500 deg<sup>2</sup>: half of the survey area will be on a 9°-wide patch around the celestial equator and the other half on a similarly-shaped region around a declination of −31° (de Jong et al. 2013). In total, KiDS overlaps with four GAMA patches: three in the equator (the three used in this work) and one in the south (G23), for a total of 240 deg<sup>2</sup>. In this work, we use an unmasked area of 68.5 deg<sup>2</sup> over ∼100 deg<sup>2</sup> of overlap currently available (de Jong et al. 2015).

KiDS data were reduced using two different pipelines: a reduction based on Astro-WISE (McFarland et al. 2013) used to measure Gaussian-weighted aperture photometry (Kuijken 2008) and photometric redshifts with the Bayesian Photometric Redshift (BPZ) code (Benítez 2000), and a theli reduction (Erben et al. 2013) used to measure galaxy shapes with *lensfit* (Miller et al. 2007, 2013; Kitching et al. 2008). We briefly describe each in the following and refer to de Jong et al. (2015) and Kuijken et al. (2015) for details, including tests of systematic effects on shape measurements and photometric redshifts.

#### 5.2.2.1 Photometric redshifts

Photometric redshifts use the coadded images from the KiDS public data releases DR1 and DR2 (de Jong et al. 2015) as input. These were processed using a pipeline largely based on the Astro-WISE optical pipeline (McFarland et al. 2013) which includes crosstalk and overscan corrections, flat fielding, illumination correction, satellite track removal and background subtraction, plus masking for bad pixels, saturation spikes and stellar haloes. A common astrometric solution was calculated per filter using a second-order polynomial. Individual exposures were regridded and co-added using a weighted mean procedure. Photometric zero-points were first derived per CCD by comparing nightly standard star observations to SDSS DR8 (Aihara et al. 2011) and zero-point offsets were subsequently applied to the *gri* data, based on a comparison of the photometry between the CCDs in the five exposures. This yields a homogeneous photometry over 1 deg<sup>2</sup>.

The point spread function (PSF) of the stacked images was homogenized by convolving them with a Gaussian kernel with varying width, such that each re-

---

<sup>4</sup><http://kids.strw.leidenuniv.nl/>

sulting image has a circular, Gaussian PSF with constant width across the field of view. A ‘Gaussian Aperture and PSF’ (GAaP, Kuijken 2008) photometry can be obtained such that the resulting aperture photometry is independent of seeing (see Appendix A of Kuijken et al. 2015). The flux of a galaxy can then be measured consistently within the same physical aperture in all bands, which is necessary for unbiased galaxy colour estimates.

GAaP photometry was finally compared to SDSS photometry in order to obtain an absolute photometric calibration. Photometric redshifts were estimated using GAaP magnitudes with BPZ, following Hildebrandt et al. (2012). Kuijken et al. (2015) compared the photometric redshifts to  $\sim 17,000$  spectroscopic redshifts in the zCOSMOS (Lilly et al. 2007) and ESO/GOODS (Vanzella et al. 2008; Balestra et al. 2010) surveys. They found that the peak of the posterior distribution,  $z_B$ , is biased by less than 2% in the range  $0.005 < z_B < 1.0$ . However, for lenses at  $z_l \lesssim 0.3$ , as in our case, the lensing efficiency (cf. Equation 5.2) does not vary significantly for sources beyond  $z_s = 0.5$ . In order to have a larger number of sources for which to measure shapes, we therefore use all galaxies in the range  $0.005 < z_B < 1.2$ . In the context of the CFHTLenS survey, Benjamin et al. (2013) have shown that the stacked photometric redshift posterior distribution,  $p(z)$ , estimated by Hildebrandt et al. (2012) in this  $z_B$  range is a fair representation of the true (i.e., spectroscopic) redshift distribution. We therefore use the full  $p(z)$  in our lensing analysis (see Section 5.3).

### 5.2.2.2 Shape measurements

The  $r$ -band data were also reduced with the theli pipeline (Erben et al. 2013), independently of the Astro-WISE pipeline, in order to measure the shapes of galaxies. We used only the  $r$ -band data for shape measurements, since the  $r$ -band observing conditions are significantly better than in the other three bands (see de Jong et al. 2013); combining different bands is not expected to result in a useful improvement in shape measurements. We used SExtractor (Bertin & Arnouts 1996) to detect objects on the stacked  $r$ -band image, and used the resulting catalogue as input to *lensfit*, which is used to simultaneously analyze the single exposures. *Lensfit* is a Bayesian method that returns for each object an ellipticity and an associated weight,  $w_s$ , which quantifies the measurement uncertainty after marginalizing over galaxy position, size, brightness, and bulge-to-disk ratio. It interpolates the PSF over a 2-dimensional polynomial across the image in order to estimate the PSF at the location of each galaxy. The number density of galaxies in the unmasked region that pass the photometric redshift cuts having  $w_s > 0$  is  $n_{\text{gal}} = 8.88 \text{ gal arcmin}^{-2}$  and the effective number of galaxies is  $n_{\text{eff}} = (\sigma_\epsilon/A) \sum_i w_{s,i} = 4.48 \text{ gal arcmin}^{-2}$  (see Chang et al. 2013b; Kuijken

et al. 2015); the root-mean-square (rms) ellipticity of galaxies is  $\sigma_\epsilon = 0.279$ . We correct for *noise bias*, which produces a signal-to-noise ratio (S/N)-dependent correction factor,  $m$ , between the mean ellipticity measurements and the shear (e.g., Melchior & Viola 2012; Refregier et al. 2012; Viola et al. 2014, see Section 5.3), using the correction calculated for CFHTLenS using extensive image simulations by Miller et al. (2013), which Kuijken et al. (2015) demonstrate is appropriate for the current KiDS catalogue. We also correct the galaxy shapes for an additive bias,  $c$ , introduced by imperfect PSF modelling following Heymans et al. (2012). See Kuijken et al. (2015) for details.

In performing the lensing analysis we have decided to blind ourselves to the final results. By doing this we ensure that the analysis does not depend on the results, and minimize the risk of confirmation bias. This is an especially important concern in this era of precision cosmology. At the start of the project we contacted an external person (unknown to all members of the KiDS collaboration except for the contact person), who generated three additional catalogues by rescaling the galaxy ellipticities by factors unknown to us. We carried out the full analysis four times, one for each ellipticity catalogue. Only when the team was convinced about the analysis *carried out with the four ellipticity catalogues*, the analysis was frozen *with no further changes to the results* and we contacted the external person again to reveal the true catalogue. A detailed description of the shape analysis and catalogue blinding of KiDS data is given in Kuijken et al. (2015).

### 5.3 Galaxy-galaxy lensing of satellite galaxies

Gravitational lensing produces a differential deflection of light coming from background galaxies when it passes through an inhomogeneous mass distribution, and most strongly along a mass concentration. The observable effect is a coherent distortion on both the shape and the size of background sources around the lens. The shape distortion,  $\gamma_t$ , is referred to as *shear*, and in the weak lensing limit is much smaller than the typical ellipticities of galaxies and can only be measured statistically by averaging over many background sources. The average tangential shear relates to the excess surface mass density (ESD) at a projected distance<sup>5</sup>  $R$  of the lens,  $\Delta\Sigma(R)$ , through

$$\Delta\Sigma(R) \equiv \bar{\Sigma}(< R) - \bar{\Sigma}(R) = \Sigma_c \gamma_t(R), \quad (5.1)$$

where  $\bar{\Sigma}(< R)$  is the average surface density within  $R$ ,  $\bar{\Sigma}(R)$  is the average surface density at  $R$  (more precisely, within a thin shell  $R + \delta R$ ) and the critical density,

---

<sup>5</sup>As a convention, we list 3-dimensional distances in groups with lower case  $r$ , and distances projected in the plane of the sky with capital  $R$ .

$\Sigma_c$ , is as a geometrical factor that accounts for the lensing efficiency,

$$\Sigma_c = \frac{c^2}{4\pi G} \frac{D(z_s)}{D(z_l)D(z_l, z_s)}. \quad (5.2)$$

Here,  $D(z_l)$ ,  $D(z_s)$ , and  $D(z_l, z_s)$  are the angular diameter distances to the lens, to the source and between the lens and the source, respectively. Therefore the redshifts of the lenses and sources are essential to relate the tangential distortions of the sources to the projected mass density of the lens.

We calculate  $D(z_l)$  for each lens galaxy using its spectroscopic redshift from GAMA and marginalize over the full probability distribution of the photometric redshift of each background source,  $p(z_s)$ . Specifically, for every lens-source pair we calculate

$$\tilde{\Sigma}_{c,ls}^{-1} = \frac{4\pi G}{c^2} D(z_l) \int_{z_l}^{\infty} dz_s p(z_s) \frac{D(z_l, z_s)}{D(z_s)}. \quad (5.3)$$

Each lens-source pair is then assigned a weight that combines the *lensfit* weight and the lensing efficiency,

$$w_{ls} = w_s \tilde{\Sigma}_{c,ls}^{-2}. \quad (5.4)$$

The ESD in a bin centred on a projected distance  $R$  is then calculated as

$$\Delta\Sigma(R) = \left( \frac{\sum_{ls} w_{ls} \epsilon_t \tilde{\Sigma}_{c,ls}}{\sum_{ls} w_{ls}} \right) \frac{1}{1 + K(R)} \quad (5.5)$$

where the sum is over all lens-source pairs in the radial bin,  $\epsilon_t$  is the tangential component of the ellipticity of each source around each lens, and

$$K(R) = \frac{\sum_{ls} w_{ls} m_s}{\sum_{ls} w_{ls}} \simeq 0.1, \quad (5.6)$$

where  $m$  is the multiplicative correction for noise bias (Miller et al. 2013; Kuijken et al. 2015).

The ESD around a satellite galaxy at a projected distance  $R_{\text{sat}}$  from the group centre,  $\Delta\Sigma_{\text{sat}}(R|R_{\text{sat}})$ , is given by

$$\Delta\Sigma_{\text{sat}}(R|R_{\text{sat}}) = \Delta\Sigma_{\text{sub}}(R) + \Delta\Sigma_{\text{host}}(R|R_{\text{sat}}), \quad (5.7)$$

where  $\Delta\Sigma_{\text{sub}}$  is the ESD of the subhalo in which the satellite galaxy resides and  $\Delta\Sigma_{\text{host}}$  is the ESD of the host galaxy group, measured around the satellite galaxy. We describe the measured satellite lensing signal in Section 5.3.1 before discussing our modelling of both terms of Equation 5.7 in Sections 5.3.2 and 5.3.3. In doing this, we follow the discussion by Yang et al. (2006).

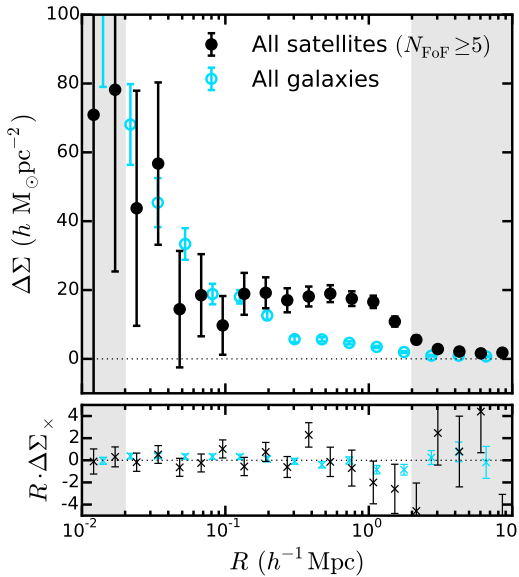


**Figure 5.1:** Top: Excess surface density around all satellites residing in groups with  $N_{\text{FoF}} \geq 5$  (black points) and around all galaxies in the GAMA catalogue (cyan circles). Bottom: corresponding cross signals, multiplied by projected separation,  $R$ , to make the errorbars of comparable size throughout the radial range (units are omitted for clarity). Dotted horizontal lines in both panels show  $\Delta\Sigma = 0$ . We used different bins to measure the signal of each sample for clarity. The grey bands show projected separations that are not used in our analysis.

### 5.3.1 The satellite lensing signal

We show in Figure 5.1 the stacked ESD of all 9683 satellites residing in groups with  $N_{\text{FoF}} \geq 5$ . We also show the ESD around all galaxies in the GAMA catalogue, which is dominated by (central) field galaxies (Robotham et al. 2011). The lensing signal around the two samples is qualitatively different. In terms of Equation 5.7, the ESD of central galaxies can be described by  $\Delta\Sigma_{\text{host}}(R|R_{\text{sat}} = 0)$  alone (see ? for a detailed comparison of the lensing signal of different lens samples). The bottom panel of Figure 5.1 shows  $\Delta\Sigma_x$ , which is defined analogously to Equation 5.1 using the shear measured at  $45^\circ$  rotations from the direction tangential to the lens.  $\Delta\Sigma_x$  should be consistent with zero because of parity symmetry (Schneider 2003), and therefore serves as a check for systematic effects. As shown in Figure 5.1,  $\Delta\Sigma_x$  is consistent with zero for both samples at all lens-source separations.

Although in Figure 5.1 we show the lensing signal for separations  $0.01 \leq R/(h^{-1}\text{Mpc}) \leq 10$ , we only use measurements of  $\Delta\Sigma$  in the range  $0.02 \leq R/(h^{-1}\text{Mpc}) \leq 2$  in our analysis. Separations outside this range are marked in Figure 5.1 by grey bands. At smaller separations, blending with and obscuration by group members become significant and therefore the S/N is very low; at larger separations the coverage is highly incomplete due to the patchiness of the current KiDS data, making measurements less reliable. We assess the effect of the patchy coverage by measuring the lensing signal around random locations on the images, which should be consistent with zero. The signal is indeed consistent with zero for

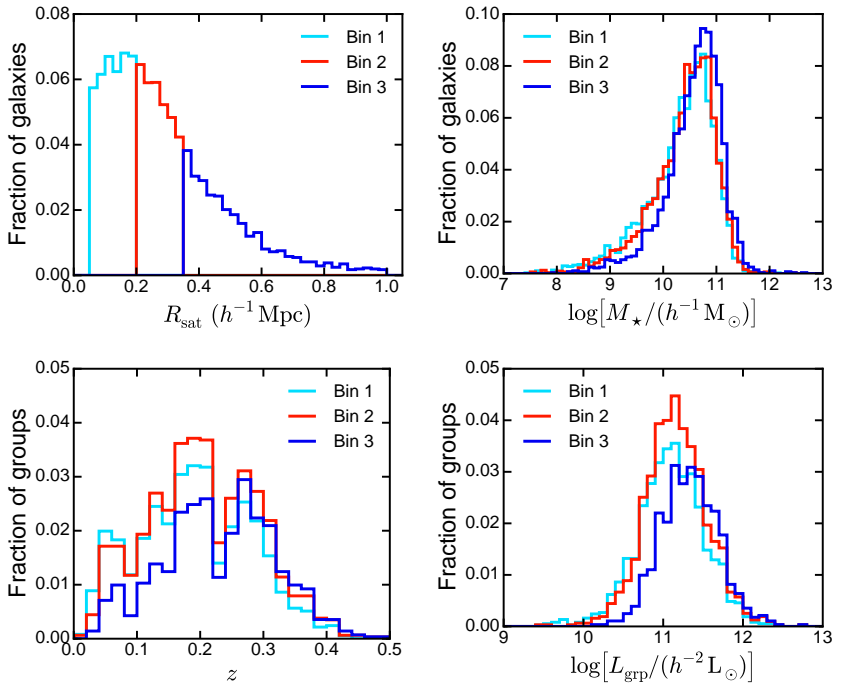


**Figure 5.2:** Top: Satellite distributions of distance to the BCG (left) and stellar mass (right); bottom: Group distributions of redshift (left) and total luminosity (right); for the radial bins defined in Table 5.1. Note that each group can contribute to more than one bin in the lower panels.

separations  $R \lesssim 5 h^{-1} \text{Mpc}$ , but at separations  $R \gtrsim 5 h^{-1} \text{Mpc}$  the lensing signal around random points deviates significantly from zero (see Viola et al. 2015). This indicates that systematic effects are affecting the shear estimation at such distances. We do not try to correct for such effects and instead conservatively discard measurements at separations  $R > 2 h^{-1} \text{Mpc}$ .

The errorbars in Figure 5.1 correspond to the square root of the diagonal elements of the covariance matrix, described in Section 5.A. In principle, the lensing covariance matrix includes contributions from shape noise and sample ('cosmic') variance. Shape noise arises because galaxies are intrinsically elliptic and because noise in the images introduces additional uncertainties in the shape measurements (see, e.g., Hoekstra et al. 2000), while sample variance accounts for the finite fraction of the sky observed. As we show in Section 5.A, the contribution from sample variance can be safely neglected for our purposes and we therefore include only the contribution from shape noise, which can be calculated directly from the data

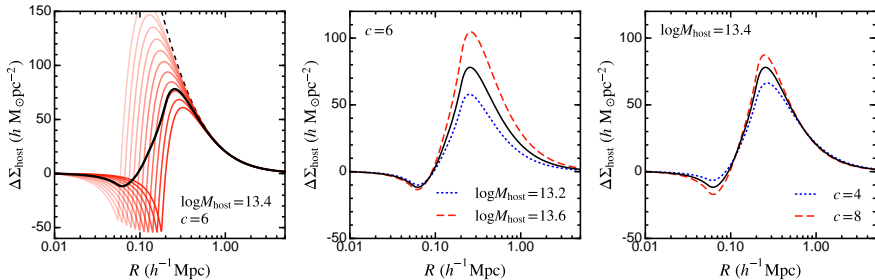


**Figure 5.3:** Illustration of the contribution from the host group,  $\Delta\Sigma_{\text{host}}(R|n(R_{\text{sat}}))$ , to Equation 5.7. Left: Red lines show the contribution to the signal around satellites at different distances from the group centre in logarithmic bins, with opacity scaling with the number density of objects in each bin,  $n(R_{\text{sat}})$ , corresponding to the cyan histogram in the top-left panel of Figure 5.2. The thick black line is the weighted average of the red lines (cf. Equation 5.12) and represents the group contribution to the lensing signal around our sample of satellites with  $0.05 \leq R_{\text{sat}}/(h^{-1} \text{ Mpc}) \leq 0.20$  in a group with  $\log M_{200} = 13.4$  and  $c = 6$ , and is reproduced in the middle and right panels. The black dashed line shows the excess surface density of the same group when measured around the group centre. Middle: Varying group mass at fixed concentration. Right: Varying group concentration at fixed mass. Note that the vertical scale in the middle and right panels is zoomed in with respect to the left panel. All masses are in units of  $h^{-1} \text{ M}_\odot$ .

(see Section 3.4 of Viola et al. 2015). In addition to the covariance between data points (as in the case of Figure 5.1), we also compute the covariance between data points around lenses in different bins of projected distance from the group centre,  $R_{\text{sat}}$  (see Figure 5.8).

The signal shown in Figure 5.1 has a high S/N, but its interpretation is complicated by the mixing of satellites with a wide range of properties. van Uitert et al. (2016) use this satellite sample to study the stellar-to-halo mass relation by binning the sample in stellar mass and redshift. Here, we bin the sample by projected distance to the group centre; this binning is shown in the top-left panel of Figure 5.2 (see also Table 5.1). We find that this particular binning allows us to study each bin with high enough S/N. We take the distance from the group centre as a proxy for time since infall to the group (e.g., Gao et al. 2004; Chang et al. 2013a) and study the evolution of the mass in satellites as these galaxies interact with their host groups. As shown in Figure 5.2 (top right), the three radial bins have similar stellar mass distributions, their medians differing by only 0.2 dex (Table 5.1). In contrast, the group redshift and luminosity distributions of bin 3 are different from the other two bins. Because we separate groups by satellite distance, we essentially split groups by size. Only the most massive (i.e., the most luminous) groups in the sample have satellites at  $R_{\text{sat}} > 0.35 h^{-1} \text{ Mpc}$ . Additionally, because GAMA is a

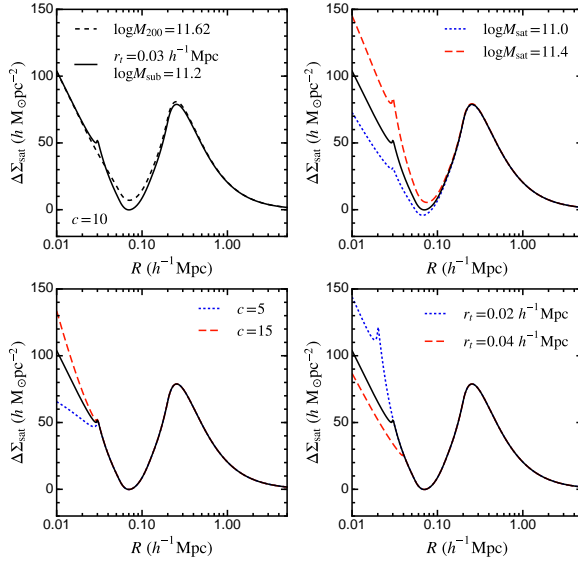


**Figure 5.4:** The satellite lensing signal,  $\Delta\Sigma_{\text{sat}}$ , for different satellite properties. The group contribution is kept fixed at the fiducial value (i.e., the thick solid line) from Figure 5.3. Top left: The dashed line shows the excess surface density of a NFW profile with  $c = 10$  and  $\log M_{200} = 11.62$ . Truncating this profile through Equation 5.15 at  $r_t = 0.03 h^{-1} \text{Mpc} \approx 2.6r_s$  produces the solid line, with a total mass  $\log M_{\text{sub}} = 11.2$ , which is reproduced in all other panels. The glitch in the solid line is produced by the sharp truncation of the density profile and is continuous but non-differentiable. Top right: Varying  $M_{\text{sub}}$ , keeping both  $c = 10$  and  $r_t = 0.03 h^{-1} \text{Mpc}$  fixed. Bottom left: Varying the concentration, keeping both  $\log M_{\text{sub}} = 11.2$  and  $r_t = 0.03 h^{-1} \text{Mpc}$  fixed. Bottom right: Varying the truncation radius, keeping both  $c = 10$  and  $\log M_{\text{sub}} = 11.2$  fixed. Note that the normalization of the inner profile changes because we fix the mass *within the truncation radius*, which is itself changing. All masses are in units of  $h^{-1} M_\odot$ .

magnitude-limited survey, groups at high redshift are on average more luminous (i.e., more massive), which causes the different redshift distributions.

### 5.3.2 Host group contribution

The average density profile of galaxy groups is well described by a Navarro-Frenk-White (NFW, Navarro et al. 1995) profile,

$$\rho_{\text{NFW}}(r) = \frac{\delta_c \rho_m}{(r/r_s)(1+r/r_s)^2}, \quad (5.8)$$

where  $\rho_m(z) = 3H_0^2(1+z)^3\Omega_M/(8\pi G)$  is the mean density of the Universe at redshift  $z$  and

$$\delta_c = \frac{200}{3} \frac{c^3}{\ln(1+c) - c/(1+c)}. \quad (5.9)$$

The two free parameters,  $r_s$  and  $c \equiv r_{200}/r_s$ , are the scale radius and concentration of the profile, respectively. However, we use the concentration and the mass<sup>6</sup>,  $M_{200}$ , as the free parameters for convenience. We further assume the mass-concentration relation,  $c(M, z)$ , of Duffy et al. (2008), allowing for a free normalization,  $f_c^{\text{host}}$ . That is,

$$c(M_{200}, z) = f_c^{\text{host}} \left[ 10.14 \left( \frac{M_{200}}{2 \times 10^{12} h^{-1} M_\odot} \right)^{-0.089} (1+z)^{-1.01} \right]. \quad (5.10)$$

The average surface density of the host group measured at a projected distance  $R_{\text{sat}}$  from the group centre is simply the azimuthal average of  $\Sigma_{\text{host}}$  around the satellite,

$$\bar{\Sigma}_{\text{host}}(R|R_{\text{sat}}) = \frac{1}{2\pi} \int_0^{2\pi} d\theta \Sigma_{\text{NFW}} \left( \sqrt{R_{\text{sat}}^2 + R^2 + 2RR_{\text{sat}} \cos \theta} \right), \quad (5.11)$$

and the contribution to the satellite ESD follows from Equation 5.1. We use the analytical expression for the projected surface density of an NFW profile,  $\Sigma_{\text{NFW}}(R)$ , derived by Wright & Brainerd (2000).

In reality we observe a sample of satellites at different distances to their respective group centres; therefore the total group contribution is

$$\Delta\Sigma_{\text{host}}(R|n(R_{\text{sat}})) = \frac{\int_{R_{\text{sat}}^{\min}}^{R_{\text{sat}}^{\max}} dR_{\text{sat}} n(R_{\text{sat}}) \Delta\Sigma_{\text{host}}(R|R_{\text{sat}})}{\int_{R_{\text{sat}}^{\min}}^{R_{\text{sat}}^{\max}} dR_{\text{sat}} n(R_{\text{sat}})}, \quad (5.12)$$

where  $n(R_{\text{sat}})$  is the number density of satellites at  $R_{\text{sat}}$ . We use Equation 5.12 to model the host group contribution to Equation 5.7 throughout. Our implementation differs from that introduced by Yang et al. (2006) and applied by Li et al. (2014) in that they fit for  $R_{\text{sat}}$ , whereas we use the measured separations to fix  $n(R_{\text{sat}})$ .

We illustrate the difference between  $\Delta\Sigma_{\text{host}}(R|R_{\text{sat}})$  and  $\Delta\Sigma_{\text{host}}(R|n(R_{\text{sat}}))$  in the left panel of Figure 5.3, for the innermost bin considered in this work (see Table 5.1 and the top left panel of Figure 5.2). The left panel of Figure 5.3 shows that  $\Delta\Sigma_{\text{host}}(R|R_{\text{sat}})$  of a single group-satellite pair has a sharp minimum at  $R = R_{\text{sat}}$  where  $\Sigma(R)$  is maximal and therefore  $\Delta\Sigma < 0$ ;  $\Delta\Sigma_{\text{host}}(R|R_{\text{sat}})$  increases

---

<sup>6</sup>Here  $M_{200}$  is the mass within a radius  $r_{200}$ , which encloses a density  $\rho(< r_{200}) = 200\rho_m(z)$ .

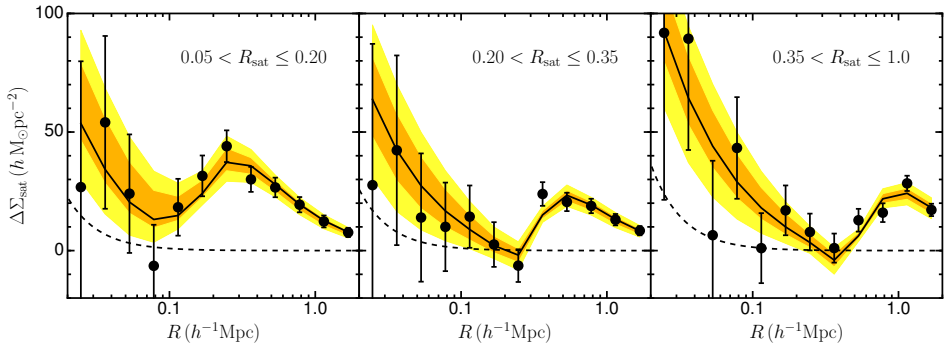


**Figure 5.5:** Excess surface density around satellite galaxies in the three radial bins summarized in Table 5.1 and shown in the legends in units of  $h^{-1}\text{Mpc}$ . Black points show lensing measurements around GAMA group satellites using KiDS data; errorbars correspond to the square root of the diagonal elements of the covariance matrix. The solid black line is the best-fit model where subhaloes are modelled as having NFW density profiles, and orange and yellow shaded regions mark 68% and 95% credible intervals, respectively. Dashed lines show the contribution of a point mass with a mass equal to the median stellar mass of each bin, which is included in the model.

abruptly further out and then drops back to the group’s outer profile, matching the group profile measured around the group centre. Accounting for the distribution of group-centric distances shifts this minimum to  $R < \langle R_{\text{sat}} \rangle$ , and makes both the peak and the dip significantly less pronounced; including the distribution of projected distances is critical to properly model the statistical properties of the lensing signal which cannot be captured by fitting for an average value. Similarly, the middle and right panels of Figure 5.3 show the effect of different host masses and concentrations on  $\Delta\Sigma_{\text{host}}(R|n(R_{\text{sat}}))$ . A higher mass increases its amplitude at all scales where the host contribution dominates, whereas a higher concentration mostly enhances the ESD signal around the peak and produces a more pronounced dip.

Our model ignores the contribution from baryons in the central group galaxy, which are noticeable at scales  $R < 0.05 h^{-1}\text{Mpc}$  (Viola et al. 2015). Because baryons are more concentrated than dark matter, they can make the total density profile steeper than a pure NFW. Viola et al. (2015) have shown, however, that the amplitude of the baryonic contribution (modelled as a point mass) is not degenerate with any other group parameter in their halo model. Therefore we expect baryons in the BCG to have no impact on our results.

### 5.3.3 Satellite contribution

Pastor Mira et al. (2011) studied the density profiles of subhaloes in the Millenium simulation (Springel et al. 2005) and found that they are well fit by an NFW profile, with no evidence for truncation at any separation from the group centre. As discussed by Hayashi et al. (2003), while tidal disruption removes mass preferentially from the outskirts, tidal heating causes the subhalo to expand after every orbit. The two effects compensate in terms of the density distribution such that a defined truncation radius cannot be discerned in subhaloes. We therefore model subhaloes as NFW profiles (Equation 5.8). We assume the  $c(M, z)$  relation of Duffy et al. (2008); in analogy to Equation 5.10, we set  $f_c^{\text{sub}} = 1$ . To account for the baryonic contribution to the subhalo mass, we include a point mass in the centre with a mass equal to the median stellar mass for each bin (Table 5.1). Our model for the satellites therefore has a single free parameter per radial bin, namely  $M_{\text{sub}}(< r_{200})$ .

For comparison, we also implement a theoretically-motivated model where subhaloes are tidally stripped by the host potential. In this model, a subhalo in a circular orbit is truncated at the radius at which the accelerations due to the tidal force from the host halo equals that arising from the gravitational force of the subhalo itself. This radius is given by

$$r_t = \left[ \frac{M_{\text{sub}}(< r_t)}{(3 - \partial \ln M / \partial \ln r) M_{\text{host}}(< r_{\text{sat}})} \right]^{1/3} r_{\text{sat}} \quad (5.13)$$

(King 1962; Binney & Tremaine 1987; Mo et al. 2010), where, for an NFW profile,

$$\frac{\partial \ln M_{\text{NFW}}}{\partial \ln r} = \frac{r^2}{(r_s + r)^2} \left[ \ln \left( \frac{r_s + r}{r_s} \right) - \frac{r}{r_s + r} \right]^{-1} \quad (5.14)$$

and  $r_s$  is the scale radius of the host halo. Note that in Equation 5.13 the truncation radius,  $r_t$ , depends on the 3-dimensional distance to the group centre,  $r_{\text{sat}}$ , which is not an observable. We draw 3-dimensional radii randomly from an NFW profile given the distribution of projected separations,  $R_{\text{sat}}$ , for each bin. We additionally force  $r_t \leq r_{200}$ , although the opposite rarely happens.

We model the truncation itself in a simple fashion, with an NFW profile instantaneously and completely stripped beyond  $r_t$ ,

$$\rho_t(r) = \begin{cases} \rho_{\text{NFW}}(r) & r \leq r_t \\ 0 & r > r_t. \end{cases} \quad (5.15)$$

Note that, in addition to  $r_t$ , this profile is defined *mathematically* by the same parameters,  $c$  and  $M_{200}$ , as a regular NFW, even though they are not well-defined physically; when referring to truncated models we report the proper physical masses,

$M_{\text{sub}} \equiv M_{\text{sub}}(< r_t)$ . We use the analytical expression for the ESD of the density profile given by Equation 5.15 derived by Baltz et al. (2009). In the leftmost panel of Figure 5.4 we show the ESD corresponding to such profile, compared with the ESD obtained assuming our fiducial NFW profile. The sharp truncation of the profile creates a glitch in the ESD around satellite galaxies at the radius of truncation which is continuous but non-differentiable and which, given our errorbars (cf. Figure 5.1), has no impact on our results. The other panels show the effect of the three parameters describing the truncated subhalo density profile, Equation 5.15 (the full NFW profile follows the same description but without the sharp cut at  $r_t$ ): as for the group profile, the mass and concentration affect the normalization and slope of the profile, respectively; the rightmost panel shows changes in  $r_t$  for the same subhalo mass *within*  $r_t$ , which is why the normalization of the different curves is different.

## 5.4 Results

We show the ESD around satellites in each of the three radial bins in Figure 5.5. Qualitatively, the signal looks similar to that of Figure 5.1, and the features described in Section 5.3 are clearly seen in each of the panels. The dip in the signal close to the typical  $R_{\text{sat}}$  is smooth, as anticipated in Section 5.3.2, and moves to higher  $R$  with increasing  $R_{\text{sat}}$ , as expected. As in Figure 5.1, the errorbars correspond to the square root of the diagonal elements of the covariance matrix (see Section 5.A).

After describing the fitting procedure in Section 5.4.1, we summarize our constraints on group properties in Section 5.4.2 and on the satellite masses in Section 5.4.3. In Section 5.4.4 we carry out a proof-of-concept comparison of our results to predictions from semi-analytical models of subhalo statistics and we discuss the effect of contamination in the group sample in Section 5.4.5.

### 5.4.1 Fitting procedure

We fit the data in Figure 5.5 with the model described in Section 5.3 for each of the radial bins, using the median redshift of each galaxy sample,  $\langle z_{\text{sat}} \rangle$ , as listed in Table 5.1. We use a single normalization  $f_c^{\text{host}}$  for the  $c(M, z)$  relation of groups in the three bins. Our model therefore has seven free parameters: the three (weighted average) masses of the satellites, the three group masses, and a normalization to the  $c(M, z)$  relation of Duffy et al. (2008) which applies to all groups across satellite radial bins.

We implement the model described above in a Markov Chain Monte Carlo

(MCMC) using `emcee`<sup>7</sup> (Foreman-Mackey et al. 2013), which is based on an affine-invariant ensemble sampler. This sampler works by using a number of ‘walkers’ (in our case, a few hundred), each of which starts at a slightly different position in parameter space. Each step is drawn for each walker from a Metropolis-Hastings proposal based on the positions of all other walkers at the previous step (see Goodman & Weare 2010, for details about the algorithm). The likelihood  $\mathcal{L}$  is given by

$$\mathcal{L} = \frac{1}{(2\pi)^{9/2}} \prod_{m=1}^3 \prod_{n=1}^3 \frac{1}{\sqrt{|C_{mn}|}} \exp \left[ -\frac{1}{2} (\mathbf{O}_m - \mathbf{E}_m)^T C_{mn}^{-1} (\mathbf{O}_n - \mathbf{E}_n) \right], \quad (5.16)$$

where  $\mathbf{O}_m$  and  $\mathbf{E}_m$  are the measurements and model predictions in radial bin  $m$ , respectively;  $C_{mn}^{-1}$  is the element of the inverse covariance matrix that accounts for the correlation between radial bins  $m$  and  $n$ ; and  $|C_{mn}|$  is the corresponding determinant. We therefore account for covariance both within and between radial bins in our MCMC. We assume flat, broad priors for all parameters, as listed in Table 5.2.

The data are well fit by the model of Section 5.3. The best-fit model is shown in Figure 5.5 and gives  $\chi^2 = 24.7$  with 28 degrees of freedom, with a probability to exceed PTE = 0.64. Joint 2-dimensional posterior distributions for the seven free parameters are shown<sup>8</sup>. Marginalized posterior estimates for all seven parameters, together with 68% credible intervals, are reported in Table 5.2, which also lists the stellar mass fractions, fractional satellite masses, and group mass-to-light ratios derived from the posterior mass estimates.

### 5.4.2 Group masses and mass-concentration relation

Before discussing the results for the satellite galaxies, we explore the constraints on group masses and the group  $c(M, z)$  relation. The masses of the same galaxy groups have been directly measured by Viola et al. (2015), which provides a valuable sanity check of our estimates.

We find that the normalization of the  $c(M, z)$  relation is significantly lower than the fiducial Duffy et al. (2008) relation,  $f_c^{\text{host}} = 0.53^{+0.19}_{-0.14}$  (where the fiducial value is  $f_c^{\text{host}} = 1$ ). This normalization implies concentrations  $c \approx 3$  for these groups. For comparison, using the same parameterization as we do, Viola et al. (2015) measured  $f_c^{\text{host}} = 0.84^{+0.42}_{-0.23}$ . Our smaller errorbars are due to the fact that

---

<sup>7</sup><http://dan.iel.fm/emcee/current/>

<sup>8</sup>We show and list the results in logarithmic space for convenience, but the analysis has been carried out in linear space and the reported uncertainties correspond to the uncertainties in linear space expressed on a logarithmic scale.

we do not account for several nuisance parameters considered by Viola et al. (2015) in their halo model implementation. Most notably, accounting for miscentring significantly increases the uncertainty on the concentration, since both affect  $\Delta\Sigma$  at similar scales (Viola et al. 2015). Indeed, when they do not account for miscentring, Viola et al. (2015) measure  $f_c^{\text{host}} = 0.59_{-0.11}^{+0.13}$ , consistent with our measurement both in the central value and the size of the errorbars. While this means that our estimate of  $f_c^{\text{host}}$  is biased, accounting for extra nuisance parameters such as miscentring is beyond the scope of this work; our aim is to constrain satellite masses and not galaxy group properties. As shown in Figure 5.6,  $f_c^{\text{host}}$  is not correlated with any of the other model parameters and therefore this bias in  $f_c^{\text{host}}$  does not affect our estimates of the satellite masses.

Group masses are consistent with the results from Viola et al. (2015) (with the same caveat that the small errorbars are an artifact produced by our simplistic modelling of the host groups). Specifically, our average mass-to-light ratios follow the mass-luminosity relation found by Viola et al. (2015),  $M_{200} \propto L_{200}^{1.16 \pm 0.13}$ . As shown in Figure 5.6, group masses are slightly correlated because they are forced to follow the same mass-concentration relation determined by Equation 5.10. Groups in the third bin are on average  $\sim 3.4 \pm 0.8$  times more massive than groups in the first radial bin. This is a selection effect, arising because groups in each bin must be big enough to host a significant number of satellites at the characteristic radius of each bin. For example, groups in the first radial bin have<sup>9</sup> in Figure 5.6  $\log\langle M_{\text{host},1}/(h^{-1}\text{M}_\odot) \rangle = 13.46_{-0.06}^{+0.06}$  and  $\langle c_1 \rangle \approx 3.3$ , which implies a scale radius  $\langle r_{s,1} \rangle = 0.19 h^{-1}\text{Mpc}$ , beyond which the density drops as  $\rho \propto r^{-3}$  (cf. Equation 5.8). The average 3-dimensional distance of satellites to the group centre (see Section 5.3.3) in the third radial bin is  $\langle r_{\text{sat},3} \rangle = 0.46 h^{-1}\text{Mpc}$ . At this radius, the average density in groups in the first radial bin is seven times smaller than at  $\langle r_{s,1} \rangle$ .

As mentioned above, our simplistic modelling of groups does not affect the posterior satellite masses significantly. Therefore it is sufficient that our group masses are consistent with the results of Viola et al. (2015), and we do not explore more complex models for the group signal. For a more thorough modelling of the lensing signal of groups in the KiDS-GAMA overlap region, see Viola et al. (2015).

#### 5.4.3 The masses of satellite galaxies

We detect the signal from satellites with significances  $>99\%$  in all three radial bins. Satellite masses are consistent across radial bins. We show the marginalized posterior estimates and 68% credible intervals in Figure 5.7 as a function of 3-dimensional group-centric distance,  $r_{\text{sat}}$  (in units of the group radius  $r_{200}$ ).

---

<sup>9</sup>Throughout, we quote masses and radii for a given radial bin by adding an index from 1 to 3 to the subscript of each value.

**Table 5.2:** Priors, marginalized posterior estimates and derived parameters of the satellites and host groups in the three radial bins. All priors are uniform in linear space in the quoted range. We use medians as central values and all uncertainties are 68% credible intervals. The normalization of the group  $c(M, z)$  relation,  $f_c^{\text{host}}$ , is the same for the three radial bins. The best-fit model has  $\chi^2 = 24.7$  with 28 degrees of freedom (PTE = 0.64).

Parameter	Units	Prior	Bin 1	Bin 2	Bin 3
$\log M_{\text{sub}}$	$h^{-1} M_\odot$	[7, 13]	$11.84^{+0.24}_{-0.34}$	$11.84^{+0.24}_{-0.35}$	$12.18^{+0.19}_{-0.24}$
$f_c^{\text{host}}$	1	[0, 2]	$0.53^{+0.19}_{-0.14}$	✓	✓
$\log M_{\text{host}}$	$h^{-1} M_\odot$	[10, 15]	$13.58^{+0.07}_{-0.07}$	$13.62^{+0.07}_{-0.08}$	$14.11^{+0.07}_{-0.07}$
Derived Parameters					
$\langle M_{*,\text{sat}} \rangle / \langle M_{\text{sub}} \rangle$	$h^{-1}$	—	$0.04^{+0.02}_{-0.03}$	$0.04^{+0.02}_{-0.03}$	$0.03^{+0.01}_{-0.02}$
$\langle M_{\text{sub}} / M_{\text{host}} \rangle$	1	—	$0.018^{+0.014}_{-0.010}$	$0.016^{+0.013}_{-0.009}$	$0.012^{+0.007}_{-0.005}$
$\langle M_{\text{host}} \rangle / \langle L_{\text{host}} \rangle$	$h M_\odot / L_\odot$	—	$300^{+49}_{-45}$	$265^{+46}_{-42}$	$386^{+66}_{-61}$

Figure 5.7 also shows the subhalo mass as a function of 3-dimensional separation from the group centre found in numerical simulations by Gao et al. (2004). Note that we compare here only the trend with radius, not the normalization. Fitting a power law,  $M_{\text{sub}} \propto (r_{\text{sat}}/r_{200})^a$ , to the data in Figure 5.7 we find  $a = 0.3 \pm 0.5$  (ignoring horizontal errorbars), consistent with the trend predicted by Gao et al. (2004) but also with no dependence on group-centric distance. The bottom panel shows the average stellar mass fractions, which are also consistent with each other,  $\langle M_{*,\text{sat}} / M_{\text{sub}} \rangle \sim 0.04 h^{-1}$ .

We also show in Figure 5.7 the results obtained for the truncated theoretical model. The difference between each pair of points depends on the posterior  $r_t$  estimated in each bin through Equation 5.13. Specifically, we find  $\langle r_t \rangle = \{0.04^{+0.02}_{-0.01}, 0.06^{+0.03}_{-0.02}, 0.09^{+0.04}_{-0.02}\} h^{-1} \text{Mpc}$ . We remind the reader that these are theoretical predictions from Equation 5.13 rather than observational results. For comparison, we also show in Figure 5.7 the masses obtained by integrating the posterior NFW models up to said truncation radii, shown by the dashed line. These masses are fully consistent with the truncated model, implying that the difference between the black and grey points (which show  $M_{\text{sub}}(< r_{200})$  and  $M_{\text{sub}}(< r_t)$ , respectively) in Figure 5.7 is only a matter of presentation; the data cannot distinguish between these two models.

After we submitted this work, Li et al. (2016) presented similar, independent satellite lensing measurements. They used  $\sim 7,000$  satellites in the redMaPPer galaxy group catalogue (Rykoff et al. 2014) with background sources from CS82 and also measured the lensing signal in three bins in projected radius. They find comparable constraints that are consistent with ours.

#### 5.4.4 The average subhalo mass

We can link the results presented in Section 5.4.3 to predictions from numerical simulations. Comparisons of the satellite populations of observed galaxies (or groups) provide valuable insights as to the relevant physical processes that dominate galaxy formation, as highlighted by the well known ‘missing satellites’ (Klypin et al. 1999; Moore et al. 1999) and ‘too big to fail’ (Boylan-Kolchin et al. 2011) problems, which suggest either that our Universe is not well described by a  $\Lambda$ CDM cosmology, or that using numerical simulations to predict observations is more complicated than anticipated. While the former may in fact be true, the latter is now well established, as the formation of galaxies inside dark matter haloes depends strongly on baryonic physics not included in  $N$ -body simulations, and the influence of baryons tends to alleviate these problems (Zolotov et al. 2012).

Here we specifically compare the average subhalo-to-host mass ratio,  $\psi \equiv M_{\text{sub}}/M_{\text{host}}$ , to  $\Lambda$ CDM predictions through the subhalo mass function, which describes the mass distributions of subhaloes for a given dark matter halo mass. In numerical simulations, the resulting subhalo mass function is a function only of  $\psi$  (e.g., van den Bosch et al. 2005; Jiang & van den Bosch 2016). As summarized in Table 5.2, we find typical subhalo-to-host mass ratios in the range  $\langle \psi \rangle \sim 0.015$ , statistically consistent across group-centric distance. We obtain these values by taking the ratio  $M_{\text{sub}}/M_{\text{host}}$  at every evaluation in the MCMC. For comparison, the values we obtain using the truncated model are  $\langle \psi_{\text{tNFW}} \rangle \approx 0.005$ , also consistent across radial bins.

We compare our results to the analytical *evolved* (that is, measured after the subhaloes have become satellites of the host halo, as opposed to one measured at the time of infall) subhalo mass function proposed by van den Bosch et al. (2005),

$$\frac{dN}{d\psi} \propto \frac{1}{\psi} (\beta/\psi)^\alpha \exp(-\psi/\beta), \quad (5.17)$$

where  $\alpha = 0.9$  and  $\beta = 0.13$ , and calculate the average subhalo-to-host mass ratio,

$$\langle \psi \rangle = \left[ \int_{\psi_{\min}}^{\psi_{\max}} \frac{dN}{d\psi} d\psi \right]^{-1} \int_{\psi_{\min}}^{\psi_{\max}} \psi \frac{dN}{d\psi} d\psi, \quad (5.18)$$

where  $\psi_{\min} \approx 10^{-3}$  is approximately the minimum fractional satellite mass we observe given the results of Section 5.4.3, and  $\psi_{\max} = 1$  is the maximum fractional satellite mass by definition. Integrating in this range gives  $\langle \psi \rangle = 0.0052$ .

There are many uncertainties involved in choosing a  $\psi_{\min}$  representative of our sample, such as survey incompleteness and the conversion between stellar and total mass; we defer a proper modelling of these uncertainties to future work. For

reference, changing  $\psi_{\min}$  by a factor 5 modifies the predicted  $\langle \psi \rangle$  by a factor  $\sim 3$ . Considering the uncertainties involved, all we can say at present is that our results are consistent with  $\Lambda$ CDM predictions.

### 5.4.5 Sensitivity to contamination in the group catalogue

Two sources of contamination in the group catalogue have been neglected in this analysis. The spectroscopic group satellite catalogue used in this work has a high, but not 100%, purity. For groups with  $N_{\text{FoF}} \geq 5$  the purity approaches 90%; groups with fewer members have significantly lower purity (Robotham et al. 2011). Li et al. (2013) have shown that a contamination fraction of 10% in the satellite sample would lead to a +15% bias in the inferred satellite masses, well within the reported uncertainties (which amount to up to a factor two).

The second source of contamination is the misidentification of the central galaxy in a group, such that the true central galaxy would be included in our satellite sample. This effect is similar to that explained above, except that contaminating galaxies now reside in particularly massive halos (namely, the groups themselves). Based on comparisons to GAMA mock galaxy catalogues, Robotham et al. (2011) found that the fraction of BCGs correctly identified with the central galaxy of dark matter halos is around 70 – 75% for groups with  $N_{\text{FoF}} \geq 5$ . Viola et al. (2015) have directly measured the offset probability of BCGs from the true minimum of the potential well. They found that the BCG is as good a proxy for the centre as the iterative centre of Robotham et al. (2011), which according to mock group catalogues are well centred in  $\sim 90\%$  of the groups. There are very few groups with  $N_{\text{FoF}} \gg 5$  (Robotham et al. 2011), and therefore the lensing signal of a central galaxy in our sample would probably have  $\Delta\Sigma(R \approx 0.05 h^{-1}\text{Mpc}) \approx 100 h M_\odot \text{pc}^{-2}$  (see Figure 7 of Viola et al. 2015). If we assume (conservatively) that 20% of the BCGs do not correspond to the central galaxy in their groups, then  $0.20/7 = 3\%$  (where  $\langle N_{\text{FoF}} \rangle \sim 7$ , cf. Table 5.1) of our satellites would be central galaxies. Therefore the total signal in the inner regions ( $R \approx 0.05 h^{-1}\text{Mpc}$ ) would be  $\Delta\Sigma_{\text{tot}} = 0.03 \times 100 + 0.97 \times \Delta\Sigma_{\text{sub}}^{\text{true}} \simeq 40 h M_\odot \text{pc}^{-2}$ , which yields  $\Delta\Sigma_{\text{sub}}^{\text{true}} = 38 h M_\odot \text{pc}^{-2}$ . Therefore central galaxy misidentification induces a +5% bias on the signal, which implies roughly a +15% bias on the mass.

Together, these two effects add up to a  $\sim 20 - 25\%$  bias in our satellite mass estimates. Such a bias is safely within our statistical uncertainties. Therefore our results are insensitive to plausible levels of contamination in the group catalogue, both from satellites that are not really group members and from misidentified central galaxies.

## 5.5 Conclusions

We used the first 100 deg<sup>2</sup> of optical imaging from KiDS to measure the excess surface mass density around spectroscopically confirmed satellite galaxies from the GAMA galaxy group catalogue. We model the signal assuming NFW profiles for both host groups and satellite galaxies, including the contribution from the stellar mass for the latter in the form of a point source. Taking advantage of the combination of statistical power and high image quality, we split the satellite population into three bins in projected separation from the group centre, which serves as a (high-scatter) proxy for the time since infall. We fit the data with a model that includes the satellite and group contributions using an MCMC (see Section 5.3 and Figure 5.5), fully accounting for the data covariance. As a consistency check, we find group masses in good agreement with the weak lensing study of GAMA galaxy groups by Viola et al. (2015), even though we do not account for effects such as miscentring or the contribution from stars in the BCG.

This model fits the data well, with  $\chi^2/\text{d.o.f.} = 0.88$  (PTE = 0.64). We are able to constrain total satellite masses to within  $\sim 0.3$  dex or better. Given these uncertainties, the estimated masses are insensitive to the levels of contamination expected in the group catalogue. Satellite galaxies have similar masses across group-centric distance, consistent with what is found in numerical simulations (accounting for the measured uncertainties). Satellite masses as a function of group-centric distance are influenced by a number of effects. Tidal stripping acts more efficiently closer to the group centre, while dynamical friction makes massive galaxies sink to the centre more efficiently, an effect referred to as mass segregation (e.g., Frenk et al. 1996). In addition, by binning the sample in (projected) group-centric distance we are introducing a selection effect such that outer bins include generally more massive groups, which will then host more massive satellites on average. Future studies with increased precision may be able to shed light on the interplay between these effects by, for instance, selecting samples residing in the same host groups or in bins of stellar mass.

As a proof of concept, we compare our results to predictions from  $N$ -body simulations. These predict that the subhalo mass function is a function only of the fractional subhalo mass,  $\psi \equiv M_{\text{sub}}/M_{\text{host}}$ . Our binning in satellite group-centric distance produces a selection effect on host groups, such that each bin probes a (slightly) different group population, which allows us to test such prediction. The average fractional mass in all three bins is consistent with a single value (within large errorbars),  $\langle \psi \rangle \sim 0.015$ . This is broadly consistent with the predictions of numerical simulations. We anticipate that weak lensing of satellite galaxies will become an important tool to constrain the physical processes incorporated in semi-analytic

models of galaxy formation and, ultimately, hydrodynamical simulations.

## 5.A Full satellite lensing correlation matrix and the contribution from sample variance

As mentioned in Section 5.3.1, we calculate the covariance matrix directly from the data including only the contribution from shape noise (see Section 3.4 of Viola et al. 2015). In Figure 5.8 we show the corresponding correlation matrix, defined as

$$\mathbf{C}'_{mnij} = \frac{C_{mnij}}{\sqrt{C_{mmii}C_{nnjj}}}, \quad (5.19)$$

where  $C_{mnij}$  is the covariance between the  $i$ -th and  $j$ -th elements of radial bins  $m$  and  $n$ , respectively (where  $m, n = 1, 2, 3$ ). In reality the lensing covariance also includes a contribution from sample ('cosmic') variance, but we have ignored it in our analysis. Below we justify this decision.

The contribution from sample variance can in principle be estimated by bootstrapping the lensing signal over individual KiDS fields. However, there are two caveats to this approach. First, the 101 KiDS fields used here do not produce enough independent bootstrap samples to properly estimate the full covariance matrix for our satellite samples, which is a symmetric  $36 \times 36$  matrix (containing 648 independent elements) including sample variance for the three radial bins. Second, using single KiDS fields as bootstrap elements means that the elements are not truly independent from each other, because lenses in one field do contribute to signal in neighbouring fields. In fact, we calculate the lensing signal of each galaxy including background galaxies in neighbouring fields.

The latter point is not crucial for our analysis since, as shown in Figure 5.5, the signal produced by satellite subhaloes is confined to the smallest scales,  $R \lesssim 0.3 h^{-1}\text{Mpc}$ . Therefore, we can estimate the relative contribution from sample variance to the covariance matrix by comparing the diagonal sub-panels of the covariance matrices estimated directly from the data (the 'analytical' covariance) and by bootstrapping over KiDS fields. Note that the bootstrap covariance also accounts for shape noise in addition to sample variance. Therefore the ratio between the bootstrap and analytical covariances is a measure of the relative contribution of sample variance to the satellite lensing covariance. It should be noted, however, that the bootstrap covariance can be biased high by as much as 40% (Norberg et al. 2009).

We show this comparison in Figure 5.9 for each of the three radial bins, where we compare  $\sqrt{C_{mmii}}$  estimated from the analytic (i.e., data) and bootstrap covariances. Both methods lead to similar values up to the largest angular separa-

tions. There is a hint of a nonzero contribution from sample variance at scales  $R > 0.3 h^{-1}\text{Mpc}$ , where the bootstrap variance is  $\sim 10\%$  larger than the analytical variance. As stated above, the satellite contribution to  $\Delta\Sigma$  is confined to scales smaller than these. We conclude that, for the purpose of this work, we can safely ignore sample variance.

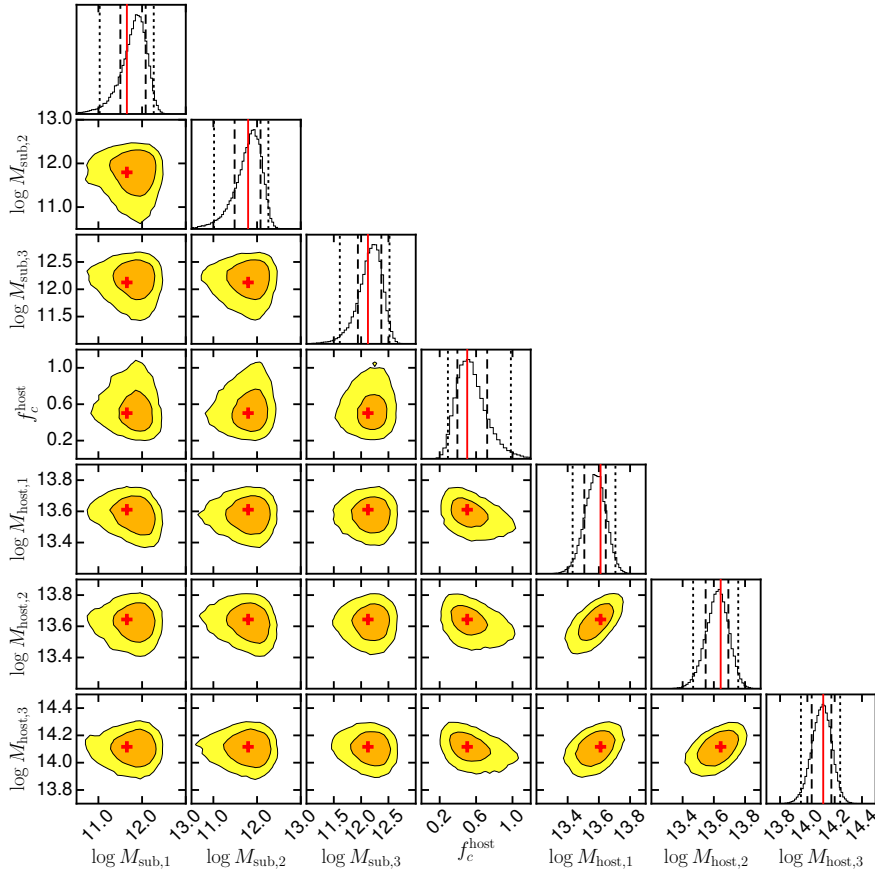


**Figure 5.6:** Joint 2-dimensional (lower off-diagonal panels, with contours at 68% and 95% joint credible regions) and marginalized 1-dimensional (diagonal panels) posterior distributions of free parameters of the model described in Section 5.3, with subhaloes modelled with NFW density profiles. In the diagonal panels, black dashed and dotted lines mark marginalized 68% and 95% credible intervals, respectively, and vertical red solid lines mark the maximum likelihood estimate. Red crosses in off-diagonal panels show the joint best-fit values. All masses are in units of  $h^{-1}M_{\odot}$  and are numbered according to the radial bin to which they correspond.

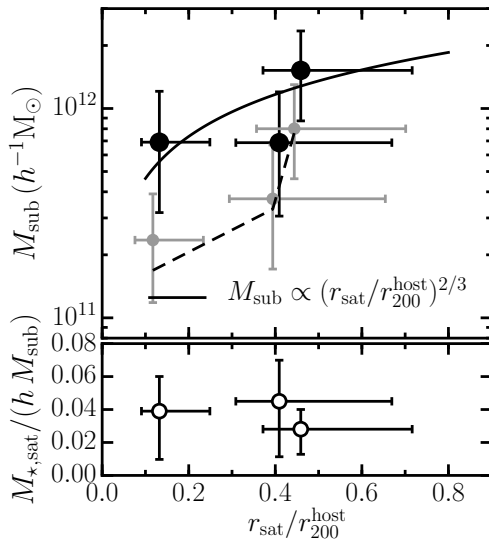


**Figure 5.7:** Top: Marginalized posterior mass estimates of satellite galaxies from the full NFW (black, large points) and truncated NFW (grey, small points) models, and the dashed black line shows the NFW masses within the same truncation radii for comparison. Horizontal errorbars are 68% ranges in (3-dimensional)  $r_{\text{sat}}/r_{200}$  per bin. The black solid line shows the radial dependence of subhalo mass predicted by the numerical simulations of Gao et al. (2004) with an arbitrary normalization. Bottom: Stellar-to-total mass ratios in each bin.

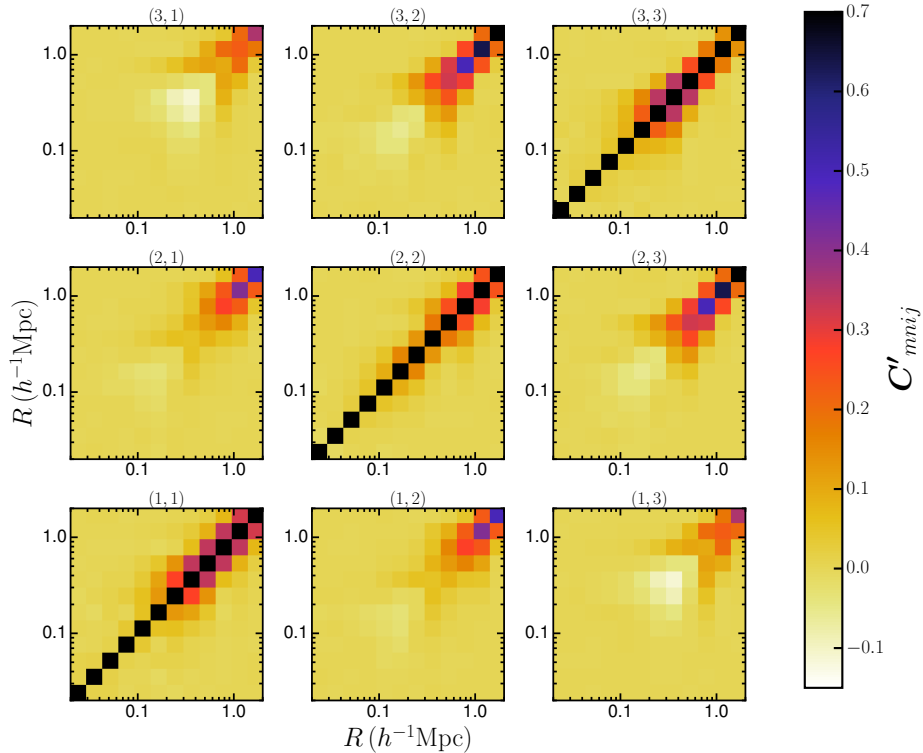


**Figure 5.8:** Full satellite lensing correlation matrix within and between radial bins as shown by the label at the top of each plot.

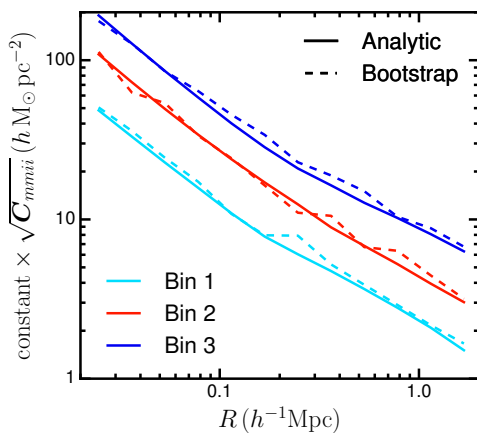


**Figure 5.9:** Comparison of the variances calculated analytically (solid), which account only for shape noise, and by bootstrapping (dashed), which also account for sample variance, for the diagonal sub-panels of the covariance matrix as per Figure 5.8. The red and blue lines have been offset vertically for clarity.



# Bibliography

- Abazajian K. N., et al., 2009, ApJS, 182, 543  
Abell G. O., 1958, ApJS, 3, 211  
Abraham R. G., Yee H. K. C., Ellingson E., Carlberg R. G., Gravel P., 1998, ApJS, 116, 231  
Afshordi N., 2008, ApJ, 686, 201  
Agustsson I., Brainerd T. G., 2006, ApJL, 644, L25  
Ahn C. P., et al., 2012, ApJS, 203, 21  
Ahn C. P., et al., 2014, ApJS, 211, 17  
Aihara H., et al., 2011, ApJS, 193, 29  
Alam S., et al., 2015, ApJS, 219, 12  
Allen S. W., Evrard A. E., Mantz A. B., 2011, ARA&A, 49, 409  
Alpher R. A., Bethe H., Gamow G., 1948, Physical Review, 73, 803  
Altay G., Colberg J. M., Croft R. A. C., 2006, MNRAS, 370, 1422  
Andersson K., et al., 2011, ApJ, 738, 48  
Andreon S., 2015, A&A, 582, A100  
Andreon S., de Propris R., Puddu E., Giordano L., Quintana H., 2008, MNRAS, 383, 102  
Annis J., et al., 2014, ApJ, 794, 120  
Arnaud M., Pratt G. W., Piffaretti R., Böhringer H., Croston J. H., Pointecouteau E., 2010, A&A, 517, A92  
Baier F. W., Godłowski W., MacGillivray H. T., 2003, A&A, 403, 847  
Baldry I. K., et al., 2010, MNRAS, 404, 86  
Balestra I., et al., 2010, A&A, 512, A12  
Balogh M. L., et al., 2016, MNRAS, 456, 4364  
Baltz E. A., Marshall P., Oguri M., 2009, JCAP, 1, 015  
Barrena R., Boschin W., Girardi M., Spolaor M., 2007, A&A, 469, 861  
Barrena R., Girardi M., Boschin W., Dasí M., 2009, A&A, 503, 357  
Barrena R., Girardi M., Boschin W., de Grandi S., Eckert D., Rossetti M., 2011, A&A, 529, A128  
Barrena R., Girardi M., Boschin W., 2013, MNRAS, 430, 3453  
Battaglia N., Bond J. R., Pfrommer C., Sievers J. L., 2012, ApJ, 758, 74

- Battaglia N., et al., 2015, preprint, ([arXiv:1509.08930](https://arxiv.org/abs/1509.08930))
- Becker R. H., White R. L., Helfand D. J., 1995, *ApJ*, 450, 559
- Beers T. C., Flynn K., Gebhardt K., 1990, *AJ*, 100, 32
- Belloni P., Roeser H.-J., 1996, *A&AS*, 118, 65
- Benítez N., 2000, *ApJ*, 536, 571
- Benjamin J., et al., 2013, *MNRAS*, 431, 1547
- Benson B. A., et al., 2013, *ApJ*, 763, 147
- Bernstein G. M., Norberg P., 2002, *AJ*, 124, 733
- Bertin E., 2012, in Ballester P., Egret D., Lorente N. P. F., eds, Astronomical Society of the Pacific Conference Series Vol. 461, Astronomical Data Analysis Software and Systems XXI. p. 263
- Bertin E., Arnouts S., 1996, *A&AS*, 117, 393
- Bertin E., Mellier Y., Radovich M., Missonnier G., Didelon P., Morin B., 2002, in Bohlander D. A., Durand D., Handley T. H., eds, Astronomical Society of the Pacific Conference Series Vol. 281, Astronomical Data Analysis Software and Systems XI. p. 228
- Binggeli B., 1982, *A&A*, 107, 338
- Binney J., Tremaine S., 1987, Galactic dynamics
- Biviano A., Murante G., Borgani S., Diaferio A., Dolag K., Girardi M., 2006, *A&A*, 456, 23
- Blanton M. R., et al., 2003, *ApJ*, 592, 819
- Blazek J., Mandelbaum R., Seljak U., Nakajima R., 2012, *JCAP*, 5, 041
- Bleem L. E., et al., 2015, *ApJS*, 216, 27
- Blumenthal G. R., Faber S. M., Primack J. R., Rees M. J., 1984, *Nature*, 311, 517
- Bocquet S., et al., 2015, *ApJ*, 799, 214
- Böhringer H., et al., 2010, *A&A*, 514, A32
- Bonamente M., Joy M., LaRoque S. J., Carlstrom J. E., Nagai D., Marrone D. P., 2008, *ApJ*, 675, 106
- Boschin W., Girardi M., Barrena R., Biviano A., Feretti L., Ramella M., 2004, *A&A*, 416, 839
- Boschin W., Barrena R., Girardi M., 2009, *A&A*, 495, 15
- Boylan-Kolchin M., Bullock J. S., Kaplinghat M., 2011, *MNRAS*, 415, L40
- Braglia F. G., Pierini D., Biviano A., Böhringer H., 2009, *A&A*, 500, 947
- Brainerd T. G., Blandford R. D., Smail I., 1996, *ApJ*, 466, 623
- Bridle S., King L., 2007, *New Journal of Physics*, 9, 444
- Brinchmann J., Charlot S., White S. D. M., Tremonti C., Kauffmann G., Heckman T., Brinkmann J., 2004, *MNRAS*, 351, 1151
- Brown M. L., Taylor A. N., Hambly N. C., Dye S., 2002, *MNRAS*, 333, 501
- Bruzual G., Charlot S., 2003, *MNRAS*, 344, 1000
- Burgh E. B., Nordsieck K. H., Kobulnicky H. A., Williams T. B., O'Donoghue D., Smith M. P., Percival J. W., 2003, in Iye M., Moorwood A. F. M., eds, SPIE Vol. 4841, Instrument Design and Performance for Optical/Infrared Ground-based Telescopes. pp 1463–1471, doi:10.1117/12.460312

- Cacciato M., van den Bosch F. C., More S., Mo H., Yang X., 2013, MNRAS, 430, 767  
Carlberg R. G., 1994, ApJ, 433, 468  
Catelan P., Kamionkowski M., Blandford R. D., 2001, MNRAS, 320, L7  
Cava A., et al., 2009, A&A, 495, 707  
Chang J., Macciò A. V., Kang X., 2013a, MNRAS, 431, 3533  
Chang C., et al., 2013b, MNRAS, 434, 2121  
Chang Y.-Y., van der Wel A., da Cunha E., Rix H.-W., 2015, ApJS, 219, 8  
Chisari N. E., Mandelbaum R., Strauss M. A., Huff E. M., Bahcall N. A., 2014, MNRAS, 445, 726  
Christlein D., Zabludoff A. I., 2003, ApJ, 591, 764  
Ciotti L., Dutta S. N., 1994, MNRAS, 270, 390  
Colín P., Klypin A. A., Kravtsov A. V., 2000, ApJ, 539, 561  
Colless M., et al., 2001, MNRAS, 328, 1039  
Colless M., et al., 2003, ArXiv Astrophysics e-prints,  
Comparat J., et al., 2013, MNRAS, 433, 1146  
Condon J. J., Cotton W. D., Greisen E. W., Yin Q. F., Perley R. A., Taylor G. B., Broderick J. J., 1998, AJ, 115, 1693  
Contini E., De Lucia G., Borgani S., 2012, MNRAS, 420, 2978  
Cooray A., Hu W., 2001, ApJ, 554, 56  
Courteau S., et al., 2014, Reviews of Modern Physics, 86, 47  
Coziol R., Andernach H., Caretta C. A., Alamo-Martínez K. A., Tago E., 2009, AJ, 137, 4795  
Crawford S. M., et al., 2010, in Observatory Operations: Strategies, Processes, and Systems III. p. 773725, doi:10.11117/12.857000  
Crawford S. M., Wirth G. D., Bershadsky M. A., Hon K., 2011, ApJ, 741, 98  
Czoske O., Kneib J.-P., Soucail G., Bridges T. J., Mellier Y., Cuillandre J.-C., 2001, A&A, 372, 391  
Danese L., de Zotti G., di Tullio G., 1980, A&A, 82, 322  
Dekel A., 1985, ApJ, 298, 461  
Dicke R. H., Peebles P. J. E., Roll P. G., Wilkinson D. T., 1965, ApJ, 142, 414  
Dietrich J. P., Clowe D. I., Soucail G., 2002, A&A, 394, 395  
Djorgovski S., 1983, ApJL, 274, L7  
Dressler A., 1980, ApJ, 236, 351  
Dressler A., Gunn J. E., 1992, ApJS, 78, 1  
Dressler A., Shectman S. A., 1988, AJ, 95, 985  
Dressler A., Smail I., Poggianti B. M., Butcher H., Couch W. J., Ellis R. S., Oemler Jr. A., 1999, ApJS, 122, 51  
Drinkwater M. J., et al., 2010, MNRAS, 401, 1429  
Driver S. P., et al., 2011, MNRAS, 413, 971  
Duffy A. R., Schaye J., Kay S. T., Dalla Vecchia C., 2008, MNRAS, 390, L64  
Dünner R., et al., 2013, ApJ, 762, 10  
Durret F., Felenbok P., Lobo C., Slezak E., 1998, A&AS, 129, 281

- Dutton A. A., Macciò A. V., 2014, MNRAS, 441, 3359
- Ebeling H., Edge A. C., Henry J. P., 2001, ApJ, 553, 668
- Ebeling H., Ma C.-J., Barrett E., 2014, ApJS, 211, 21
- Eddington A. S., 1913, MNRAS, 73, 359
- Einasto J., 2013, Brazilian Journal of Physics, 43, 369
- Ellingson E., Yee H. K. C., Abraham R. G., Morris S. L., Carlberg R. G., Smecker-Hane T. A., 1997, ApJS, 113, 1
- Erben T., et al., 2013, MNRAS, 433, 2545
- Evrard A. E., 1989, ApJL, 341, L71
- Evrard A. E., et al., 2008, ApJ, 672, 122
- Evrard A. E., Arnault P., Huterer D., Farahi A., 2014, MNRAS, 441, 3562
- Fadda D., Girardi M., Giuricin G., Mardirossian F., Mezzetti M., 1996, ApJ, 473, 670
- Faltenbacher A., Diemand J., 2006, MNRAS, 369, 1698
- Faltenbacher A., Hoffman Y., Gottlöber S., Yepes G., 2007a, MNRAS, 376, 1327
- Faltenbacher A., Li C., Mao S., van den Bosch F. C., Yang X., Jing Y. P., Pasquali A., Mo H. J., 2007b, ApJL, 662, L71
- Faltenbacher A., Jing Y. P., Li C., Mao S., Mo H. J., Pasquali A., van den Bosch F. C., 2008, ApJ, 675, 146
- Feretti L., Giovannini G., Govoni F., Murgia M., 2012, A&ARv, 20, 54
- Ferrari C., Maurogordato S., Cappi A., Benoist C., 2003, A&A, 399, 813
- Fisher D., Fabricant D., Franx M., van Dokkum P., 1998, ApJ, 498, 195
- Foreman-Mackey D., Hogg D. W., Lang D., Goodman J., 2013, PASP, 125, 306
- Fowler J. W., et al., 2007, ApOpt, 46, 3444
- Frenk C. S., White S. D. M., 2012, Annalen der Physik, 524, 507
- Frenk C. S., Evrard A. E., White S. D. M., Summers F. J., 1996, ApJ, 472, 460
- Gao L., White S. D. M., Jenkins A., Stoehr F., Springel V., 2004, MNRAS, 355, 819
- Geller M. J., Hwang H. S., Diaferio A., Kurtz M. J., Coe D., Rines K. J., 2014, ApJ, 783, 52
- George M. R., et al., 2012, ApJ, 757, 2
- Gifford D., Miller C., Kern N., 2013, ApJ, 773, 116
- Gillis B. R., et al., 2013, MNRAS, 431, 1439
- Gilmour R., Best P., Almaini O., 2009, MNRAS, 392, 1509
- Girardi M., Giuricin G., Mardirossian F., Mezzetti M., Boschin W., 1998, ApJ, 505, 74
- Girardi M., Barrena R., Boschin W., Ellingson E., 2008, A&A, 491, 379
- Gladders M. D., Yee H. K. C., 2000, AJ, 120, 2148
- Godłowski W., Baier F. W., MacGillivray H. T., 1998, A&A, 339, 709
- Godłowski W., Piwowarska P., Panko E., Flin P., 2010, ApJ, 723, 985
- Goodman J., Weare J., 2010, Communications in Applied Mathematics and Computational Science, 5, 65
- Gruen D., et al., 2014, MNRAS, 442, 1507
- Gunn J. E., Gott III J. R., 1972, ApJ, 176, 1

- Guo H., et al., 2015a, MNRAS, 446, 578  
Guo H., et al., 2015b, MNRAS, 453, 4368  
Guth A. H., 1981, PhRvD, 23, 347  
Haines C. P., et al., 2013, ApJ, 775, 126  
Haines C. P., et al., 2015, ApJ, 806, 101  
Hall A., Taylor A., 2014, MNRAS, 443, L119  
Hao J., et al., 2009, ApJ, 702, 745  
Hao J., et al., 2010, ApJS, 191, 254  
Hao J., Kubo J. M., Feldmann R., Annis J., Johnston D. E., Lin H., McKay T. A., 2011, ApJ, 740, 39  
Hasselfield M., et al., 2013, JCAP, 7, 008  
Hawley D. L., Peebles P. J. E., 1975, AJ, 80, 477  
Hayashi E., Navarro J. F., Taylor J. E., Stadel J., Quinn T., 2003, ApJ, 584, 541  
Heymans C., Heavens A., 2003, MNRAS, 339, 711  
Heymans C., Brown M., Heavens A., Meisenheimer K., Taylor A., Wolf C., 2004, MNRAS, 347, 895  
Heymans C., et al., 2012, MNRAS, 427, 146  
Heymans C., et al., 2013, MNRAS, 432, 2433  
High F. W., Stubbs C. W., Rest A., Stalder B., Challis P., 2009, AJ, 138, 110  
High F. W., et al., 2010, ApJ, 723, 1736  
Hildebrandt H., et al., 2012, MNRAS, 421, 2355  
Hill J. M., Oegerle W. R., 1993, AJ, 106, 831  
Hilton M., et al., 2013, MNRAS, 435, 3469  
Hirata C. M., Seljak U., 2004, PhRvD, 70, 063526  
Hirata C. M., Mandelbaum R., Ishak M., Seljak U., Nichol R., Pimbblet K. A., Ross N. P., Wake D., 2007, MNRAS, 381, 1197  
Hoekstra H., 2007, MNRAS, 379, 317  
Hoekstra H., Franx M., Kuijken K., Squires G., 1998, ApJ, 504, 636  
Hoekstra H., Franx M., Kuijken K., 2000, ApJ, 532, 88  
Hoekstra H., Mahdavi A., Babul A., Bildfell C., 2012, MNRAS, 427, 1298  
Hoekstra H., Herbonnet R., Muzzin A., Babul A., Mahdavi A., Viola M., Cacciato M., 2015, MNRAS, 449, 685  
Hook I. M., Jørgensen I., Allington-Smith J. R., Davies R. L., Metcalfe N., Murowinski R. G., Crampton D., 2004, PASP, 116, 425  
Hopkins A. M., et al., 2003, ApJ, 599, 971  
Hubble E. P., 1925, Popular Astronomy, 33  
Hubble E. P., 1929, Proceedings of the National Academy of Science, 15, 168  
Huchra J. P., et al., 2012, ApJS, 199, 26  
Hui L., Zhang J., 2002, ArXiv Astrophysics e-prints,  
Hung C.-L., Ebeling H., 2012, MNRAS, 421, 3229  
Jäger K., Ziegler B. L., Böhm A., Heidt J., Möllenhoff C., Hopp U., Mendez R. H., Wagner S., 2004, A&A, 422, 907

- Jee M. J., Hoekstra H., Mahdavi A., Babul A., 2014a, *ApJ*, 783, 78
- Jee M. J., Hughes J. P., Menanteau F., Sifón C., Mandelbaum R., Barrientos L. F., Infante L., Ng K. Y., 2014b, *ApJ*, 785, 20
- Jiang F., van den Bosch F. C., 2016, *MNRAS*, 458, 2848
- Joachimi B., Bridle S. L., 2010, *A&A*, 523, A1
- Joachimi B., Schneider P., 2008, *A&A*, 488, 829
- Joachimi B., Schneider P., 2010, *A&A*, 517, A4
- Joachimi B., Mandelbaum R., Abdalla F. B., Bridle S. L., 2011, *A&A*, 527, A26
- Joachimi B., Semboloni E., Bett P. E., Hartlap J., Hilbert S., Hoekstra H., Schneider P., Schrabback T., 2013a, *MNRAS*, 431, 477
- Joachimi B., Semboloni E., Hilbert S., Bett P. E., Hartlap J., Hoekstra H., Schneider P., 2013b, *MNRAS*, 436, 819
- Jullo E., Kneib J.-P., Limousin M., Elíasdóttir Á., Marshall P. J., Verdugo T., 2007, *New Journal of Physics*, 9, 447
- Kaiser N., 1992, *ApJ*, 388, 272
- Kaiser N., Squires G., Broadhurst T., 1995, *ApJ*, 449, 460
- Kassiola A., Kovner I., 1993, *ApJ*, 417, 450
- Kelly P. L., et al., 2014, *MNRAS*, 439, 28
- King I., 1962, *AJ*, 67, 471
- King L. J., 2005, *A&A*, 441, 47
- King L., Schneider P., 2002, *A&A*, 396, 411
- Kirk D., Bridle S., Schneider M., 2010, *MNRAS*, 408, 1502
- Kirk D., Rassat A., Host O., Bridle S., 2012, *MNRAS*, 424, 1647
- Kirk B., et al., 2015, *MNRAS*, 449, 4010
- Kitching T. D., Miller L., Heymans C. E., van Waerbeke L., Heavens A. F., 2008, *MNRAS*, 390, 149
- Kitching T. D., et al., 2013, *ApJS*, 205, 12
- Klypin A., Holtzman J., 1997, ArXiv Astrophysics e-prints,
- Klypin A., Gottlöber S., Kravtsov A. V., Khokhlov A. M., 1999, *ApJ*, 516, 530
- Kneib J.-P., 1993, PhD thesis, Ph. D. thesis, Université Paul Sabatier, Toulouse, (1993)
- Kneib J.-P., Natarajan P., 2011, *A&ARv*, 19, 47
- Kneib J.-P., Ellis R. S., Smail I., Couch W. J., Sharples R. M., 1996, *ApJ*, 471, 643
- Knowles K., et al., 2015, preprint, ([arXiv:1506.01547](https://arxiv.org/abs/1506.01547))
- Knuth K. H., 2006, ArXiv Physics e-prints,
- Krause E., Pierpaoli E., Dolag K., Borgani S., 2012, *MNRAS*, 419, 1766
- Kuhlen M., Diemand J., Madau P., 2007, *ApJ*, 671, 1135
- Kuijken K., 2008, *A&A*, 482, 1053
- Kuijken K., et al., 2015, *MNRAS*, 454, 3500
- Kurtz M. J., Mink D. J., 1998, *PASP*, 110, 934
- Lamareille F., 2010, *A&A*, 509, A53
- Larson R. B., Tinsley B. M., Caldwell C. N., 1980, *ApJ*, 237, 692

- Lau E. T., Nagai D., Kravtsov A. V., 2010, ApJ, 708, 1419
- Laureijs R., et al., 2011, preprint, ([arXiv:1110.3193](https://arxiv.org/abs/1110.3193))
- Li R., Mo H. J., Fan Z., Yang X., Bosch F. C. v. d., 2013, MNRAS, 430, 3359
- Li R., et al., 2014, MNRAS, 438, 2864
- Li R., et al., 2016, MNRAS, 458, 2573
- Liang H., Lémonon L., Valtchanov I., Pierre M., Soucail G., 2000, A&A, 363, 440
- Libeskind N. I., Di Cintio A., Knebe A., Yepes G., Gottlöber S., Steinmetz M., Hoffman Y., Martinez-Vaquero L. A., 2013, PASA, 30, e039
- Lilly S. J., et al., 2007, ApJS, 172, 70
- Limber D. N., 1953, ApJ, 117, 134
- Limousin M., Kneib J. P., Bardeau S., Natarajan P., Czoske O., Smail I., Ebeling H., Smith G. P., 2007, A&A, 461, 881
- Limousin M., Morandi A., Sereno M., Meneghetti M., Ettori S., Bartelmann M., Verdugo T., 2013, Space Sci. Rev., 177, 155
- Lin Y.-T., Mohr J. J., 2004, ApJ, 617, 879
- Lin H. W., McDonald M., Benson B., Miller E., 2015, ApJ, 802, 34
- Lindner R. R., et al., 2014, ApJ, 786, 49
- Liske J., et al., 2015, MNRAS, 452, 2087
- Luppino G. A., Kaiser N., 1997, ApJ, 475, 20
- Magnier E. A., Cuillandre J.-C., 2004, PASP, 116, 449
- Mahdavi A., Hoekstra H., Babul A., Bildfell C., Jeltema T., Henry J. P., 2013, ApJ, 767, 116
- Mamon G. A., Biviano A., Murante G., 2010, A&A, 520, A30
- Mancone C. L., Gonzalez A. H., 2012, PASP, 124, 606
- Mandelbaum R., et al., 2005, MNRAS, 361, 1287
- Mandelbaum R., Hirata C. M., Ishak M., Seljak U., Brinkmann J., 2006, MNRAS, 367, 611
- Mandelbaum R., et al., 2011, MNRAS, 410, 844
- Mantz A., Allen S. W., Rapetti D., Ebeling H., 2010, MNRAS, 406, 1759
- Marriage T. A., et al., 2011a, ApJ, 731, 100
- Marriage T. A., et al., 2011b, ApJ, 737, 61
- Marrone D. P., et al., 2012, ApJ, 754, 119
- Martel H., Robichaud F., Barai P., 2014, ApJ, 786, 79
- Martini P., Mulchaey J. S., Kelson D. D., 2007, ApJ, 664, 761
- Massey R., et al., 2007, MNRAS, 376, 13
- Mauch T., Murphy T., Buttery H. J., Curran J., Hunstead R. W., Piestrzynski B., Robertson J. G., Sadler E. M., 2003, MNRAS, 342, 1117
- Maurogordato S., et al., 2008, A&A, 481, 593
- Maurogordato S., Sauvageot J. L., Bourdin H., Cappi A., Benoist C., Ferrari C., Mars G., Houairi K., 2011, A&A, 525, A79
- McDonald M., et al., 2012, Nature, 488, 349
- McFarland J. P., Verdoes-Kleijn G., Sikkema G., Helmich E. M., Boxhoorn D. R., Valentijn

- E. A., 2013, Experimental Astronomy, 35, 45
- Medezinski E., Broadhurst T., Umetsu K., Oguri M., Rephaeli Y., Benítez N., 2010, MNRAS, 405, 257
- Melchior P., Viola M., 2012, MNRAS, 424, 2757
- Menanteau F., et al., 2010a, ApJS, 191, 340
- Menanteau F., et al., 2010b, ApJ, 723, 1523
- Menanteau F., et al., 2012, ApJ, 748, 7
- Menanteau F., et al., 2013, ApJ, 765, 67
- Meneghetti M., Fedeli C., Zitrin A., Bartelmann M., Broadhurst T., Gottlöber S., Moscardini L., Yepes G., 2011, A&A, 530, A17
- Mercurio A., Girardi M., Boschin W., Merluzzi P., Busarello G., 2003, A&A, 397, 431
- Miller N. A., Owen F. N., Hill J. M., Keel W. C., Ledlow M. J., Oegerle W. R., 2004, ApJ, 613, 841
- Miller N. A., Oegerle W. R., Hill J. M., 2006, AJ, 131, 2426
- Miller L., Kitching T. D., Heymans C., Heavens A. F., van Waerbeke L., 2007, MNRAS, 382, 315
- Miller L., et al., 2013, MNRAS, 429, 2858
- Miyatake H., et al., 2013, MNRAS, 429, 3627
- Mo H., van den Bosch F. C., White S., 2010, Galaxy Formation and Evolution
- Moore B., Katz N., Lake G., Dressler A., Oemler A., 1996, Nature, 379, 613
- Moore B., Ghigna S., Governato F., Lake G., Quinn T., Stadel J., Tozzi P., 1999, ApJL, 524, L19
- Morandi A., Pedersen K., Limousin M., 2010, ApJ, 713, 491
- Motl P. M., Hallman E. J., Burns J. O., Norman M. L., 2005, ApJL, 623, L63
- Munari E., Biviano A., Borgani S., Murante G., Fabjan D., 2013, MNRAS, 430, 2638
- Muzzin A., et al., 2014, ApJ, 796, 65
- Nagai D., 2006, ApJ, 650, 538
- Natarajan P., Kneib J.-P., Smail I., 2002, ApJL, 580, L11
- Natarajan P., De Lucia G., Springel V., 2007, MNRAS, 376, 180
- Natarajan P., Kneib J.-P., Smail I., Treu T., Ellis R., Moran S., Limousin M., Czoske O., 2009, ApJ, 693, 970
- Navarro J. F., Frenk C. S., White S. D. M., 1995, MNRAS, 275, 720
- Nelson K., Rudd D. H., Shaw L., Nagai D., 2012, ApJ, 751, 121
- Ng K. Y., Dawson W. A., Wittman D., Jee M. J., Hughes J. P., Menanteau F., Sifón C., 2015, MNRAS, 453, 1531
- Niederste-Ostholt M., Strauss M. A., Dong F., Koester B. P., McKay T. A., 2010, MNRAS, 405, 2023
- Norberg P., Baugh C. M., Gaztañaga E., Croton D. J., 2009, MNRAS, 396, 19
- Ntampaka M., Trac H., Sutherland D. J., Fromenteau S., Poczos B., Schneider J., 2015a, preprint, ([arXiv:1509.05409](https://arxiv.org/abs/1509.05409))
- Ntampaka M., Trac H., Sutherland D. J., Battaglia N., Póczos B., Schneider J., 2015b, ApJ, 803, 50

- Nulsen P. E. J., 1982, MNRAS, 198, 1007
- Ochsenbein F., Bauer P., Marcout J., 2000, A&AS, 143, 23
- Oegerle W. R., Hill J. M., Fitchett M. J., 1995, AJ, 110, 32
- Okumura T., Jing Y. P., Li C., 2009, ApJ, 694, 214
- Old L., Gray M. E., Pearce F. R., 2013, MNRAS, 434, 2606
- Old L., et al., 2014, MNRAS, 441, 1513
- Old L., et al., 2015, MNRAS, 449, 1897
- Owers M. S., Nulsen P. E. J., Couch W. J., 2011, ApJ, 741, 122
- Pacaud F., et al., 2007, MNRAS, 382, 1289
- Panko E., Juszczyk T., Flin P., 2009, AJ, 138, 1709
- Pastor Mira E., Hilbert S., Hartlap J., Schneider P., 2011, A&A, 531, A169
- Pen U.-L., Lee J., Seljak U., 2000, ApJL, 543, L107
- Peng C. Y., Ho L. C., Impey C. D., Rix H.-W., 2002, AJ, 124, 266
- Penzias A. A., Wilson R. W., 1965, ApJ, 142, 419
- Pereira M. J., Bryan G. L., 2010, ApJ, 721, 939
- Pereira M. J., Kuhn J. R., 2005, ApJL, 627, L21
- Pereira M. J., Bryan G. L., Gill S. P. D., 2008, ApJ, 672, 825
- Perlmutter S., et al., 1999, ApJ, 517, 565
- Pimbblet K. A., Smail I., Edge A. C., O'Hely E., Couch W. J., Zabludoff A. I., 2006, MNRAS, 366, 645
- Pinkney J., Roettiger K., Burns J. O., Bird C. M., 1996, ApJS, 104, 1
- Planck Collaboration 2011a, A&A, 536, A8
- Planck Collaboration 2011b, A&A, 536, A9
- Planck Collaboration 2011c, A&A, 536, A11
- Planck Collaboration 2011d, A&A, 536, A12
- Planck Collaboration 2013, A&A, 550, A129
- Planck Collaboration 2014a, A&A, 571, A16
- Planck Collaboration 2014b, A&A, 571, A29
- Planck Collaboration 2015a, preprint, ([arXiv:1502.01589](https://arxiv.org/abs/1502.01589))
- Planck Collaboration 2015c, preprint, ([arXiv:1502.01597](https://arxiv.org/abs/1502.01597))
- Planck Collaboration 2015b, preprint, ([arXiv:1502.01598](https://arxiv.org/abs/1502.01598))
- Plionis M., Benoist C., Maurogordato S., Ferrari C., Basilakos S., 2003, ApJ, 594, 144
- Poole G. B., Babul A., McCarthy I. G., Fardal M. A., Bildfell C. J., Quinn T., Mahdavi A., 2007, MNRAS, 380, 437
- Prada F., Klypin A. A., Cuesta A. J., Betancort-Rijo J. E., Primack J., 2012, MNRAS, 423, 3018
- Proust D., Cuevas H., Capelato H. V., Sodré Jr. L., Tomé Lehodey B., Le Fèvre O., Mazure A., 2000, A&A, 355, 443
- Quintana H., Carrasco E. R., Reisenegger A., 2000, AJ, 120, 511
- Reese E. D., et al., 2012, ApJ, 751, 12
- Refregier A., Kacprzak T., Amara A., Bridle S., Rowe B., 2012, MNRAS, 425, 1951

- Reichardt C. L., et al., 2013, ApJ, 763, 127
- Reid B. A., Spergel D. N., 2006, ApJ, 651, 643
- Richard J., Kneib J.-P., Limousin M., Edge A., Jullo E., 2010, MNRAS, 402, L44
- Riebe K., et al., 2013, Astronomische Nachrichten, 334, 691
- Riess A. G., et al., 1998, AJ, 116, 1009
- Rines K., Geller M. J., Diaferio A., Kurtz M. J., 2013, ApJ, 767, 15
- Rines K. J., Geller M. J., Diaferio A., Hwang H. S., 2016, ApJ, 819, 63
- Robotham A. S. G., et al., 2011, MNRAS, 416, 2640
- Romano-Díaz E., Shlosman I., Heller C., Hoffman Y., 2010, ApJ, 716, 1095
- Rood H. J., Sastry G. N., 1972, AJ, 77, 451
- Rozo E., et al., 2010, ApJ, 708, 645
- Rozo E., Rykoff E. S., Bartlett J. G., Evrard A., 2014a, MNRAS, 438, 49
- Rozo E., Evrard A. E., Rykoff E. S., Bartlett J. G., 2014b, MNRAS, 438, 62
- Rozo E., Rykoff E. S., Becker M., Reddick R. M., Wechsler R. H., 2015, MNRAS, 453, 38
- Rubin V. C., Ford W. K. J., Thonnard N., 1980, ApJ, 238, 471
- Ruel J., et al., 2014, ApJ, 792, 45
- Rykoff E. S., et al., 2012, ApJ, 746, 178
- Rykoff E. S., et al., 2014, ApJ, 785, 104
- Sand D. J., et al., 2012, ApJ, 746, 163
- Sarazin C. L., 1986, Reviews of Modern Physics, 58, 1
- Saro A., Mohr J. J., Bazin G., Dolag K., 2013, ApJ, 772, 47
- Sastry G. N., 1968, PASP, 80, 252
- Schechter P., 1976, ApJ, 203, 297
- Schewtschenko J. A., Macciò A. V., 2011, MNRAS, 413, 878
- Schlafly E. F., Finkbeiner D. P., 2011, ApJ, 737, 103
- Schneider P., 2003, A&A, 408, 829
- Schneider M. D., Bridle S., 2010, MNRAS, 402, 2127
- Schneider M. D., et al., 2013, MNRAS, 433, 2727
- Scoville N., et al., 2007, ApJS, 172, 38
- Sehgal N., et al., 2011, ApJ, 732, 44
- Sehgal N., et al., 2013, ApJ, 767, 38
- Semboloni E., Hoekstra H., Schaye J., van Daalen M. P., McCarthy I. G., 2011, MNRAS, 417, 2020
- Sérsic J. L., 1968, Atlas de galaxias australes
- Shapley H., Curtis H. D., 1921, Bulletin of the National Research Council, Vol. 2, Part 3, No. 11, p. 171-217, 2, 171
- Shaw L. D., Holder G. P., Bode P., 2008, ApJ, 686, 206
- Sifón C., et al., 2013, ApJ, 772, 25
- Skibba R. A., van den Bosch F. C., Yang X., More S., Mo H., Fontanot F., 2011, MNRAS, 410, 417

- Skielboe A., Wojtak R., Pedersen K., Rozo E., Rykoff E. S., 2012, ApJL, 758, L16
- Skrutskie M. F., et al., 2006, AJ, 131, 1163
- Smith R. E., et al., 2003, MNRAS, 341, 1311
- Soucail G., Mellier Y., Fort B., Cailloux M., 1988, A&AS, 73, 471
- Springel V., 2005, MNRAS, 364, 1105
- Springel V., White M., Hernquist L., 2001, ApJ, 549, 681
- Springel V., et al., 2005, Nature, 435, 629
- Sunyaev R. A., Zel'dovich Y. B., 1972, Comments on Astrophysics and Space Physics, 4, 173
- Sunyaev R. A., Zeldovich I. B., 1980, ARA&A, 18, 537
- Swetz D. S., et al., 2011, ApJS, 194, 41
- Taffoni G., Mayer L., Colpi M., Governato F., 2003, MNRAS, 341, 434
- Taylor E. N., et al., 2011, MNRAS, 418, 1587
- Tenneti A., Mandelbaum R., Di Matteo T., Feng Y., Khandai N., 2014, MNRAS, 441, 470
- Thompson L. A., 1976, ApJ, 209, 22
- Tinker J. L., Robertson B. E., Kravtsov A. V., Klypin A., Warren M. S., Yepes G., Gottlöber S., 2010, ApJ, 724, 878
- Tormen G., Diaferio A., Syer D., 1998, MNRAS, 299, 728
- Trevese D., Cirimele G., Flin P., 1992, AJ, 104, 935
- Trimble V., 1987, ARA&A, 25, 425
- Trimble V., 1995, PASP, 107, 1133
- Trimble V., 2012, The Observatory, 132, 33
- Trimble V., 2013, preprint, ([arXiv:1307.2289](https://arxiv.org/abs/1307.2289))
- Troxel M. A., Ishak M., 2014, PhRvD, 89, 063528
- VanderPlas J., Connolly A. J., Ivezić Z., Gray A., 2012, in Proceedings of Conference on Intelligent Data Understanding (CIDU), pp. 47-54, 2012.. pp 47–54 ([arXiv:1411.5039](https://arxiv.org/abs/1411.5039)), doi:10.1109/CIDU.2012.6382200
- Vanzella E., et al., 2008, A&A, 478, 83
- Verdugo T., Motta V., Muñoz R. P., Limousin M., Cabanac R., Richard J., 2011, A&A, 527, A124
- Vikhlinin A., et al., 2009, ApJ, 692, 1060
- Viola M., Melchior P., Bartelmann M., 2011, MNRAS, 410, 2156
- Viola M., Kitching T. D., Joachimi B., 2014, MNRAS, 439, 1909
- Viola M., et al., 2015, MNRAS, 452, 3529
- Wen Z. L., Han J. L., 2013, MNRAS, 436, 275
- White S. D. M., Rees M. J., 1978, MNRAS, 183, 341
- White M., Cohn J. D., Smit R., 2010, MNRAS, 408, 1818
- Wik D. R., Sarazin C. L., Ricker P. M., Randall S. W., 2008, ApJ, 680, 17
- Williamson R., et al., 2011, ApJ, 738, 139
- Wojtak R., Łokas E. L., Mamon G. A., Gottlöber S., Prada F., Moles M., 2007, A&A, 466, 437

- Wright C. O., Brainerd T. G., 2000, *ApJ*, 534, 34  
 Wright E. L., et al., 2010, *AJ*, 140, 1868  
 Wu H.-Y., Hahn O., Evrard A. E., Wechsler R. H., Dolag K., 2013, *MNRAS*, 436, 460  
 Yang X., Mo H. J., van den Bosch F. C., Jing Y. P., Weinmann S. M., Meneghetti M., 2006, *MNRAS*, 373, 1159  
 Yang X., Mo H. J., van den Bosch F. C., Pasquali A., Li C., Barden M., 2007, *ApJ*, 671, 153  
 Yee H. K. C., Ellingson E., Carlberg R. G., 1996, *ApJS*, 102, 269  
 Yee H. K. C., Ellingson E., Morris S. L., Abraham R. G., Carlberg R. G., 1998, *ApJS*, 116, 211  
 York D. G., et al., 2000, *AJ*, 120, 1579  
 Yu L., Nelson K., Nagai D., 2015, *ApJ*, 807, 12  
 Zel'dovich Y. B., Sunyaev R. A., 1969, *Ap&SS*, 4, 301  
 Zhang P., 2010a, *MNRAS*, 406, L95  
 Zhang P., 2010b, *ApJ*, 720, 1090  
 Zitrin A., Broadhurst T., Bartelmann M., Rephaeli Y., Oguri M., Benítez N., Hao J., Umetsu K., 2012, *MNRAS*, 423, 2308  
 Zitrin A., Menanteau F., Hughes J. P., Coe D., Barrientos L. F., Infante L., Mandelbaum R., 2013, *ApJL*, 770, L15  
 Zolotov A., et al., 2012, *ApJ*, 761, 71  
 Zwicky F., 1933, *Helvetica Physica Acta*, 6, 110  
 da Silva A. C., Kay S. T., Liddle A. R., Thomas P. A., 2004, *MNRAS*, 348, 1401  
 de Jong J. T. A., et al., 2013, *The Messenger*, 154, 44  
 de Jong J. T. A., et al., 2015, *A&A*, 582, A62  
 van Daalen M. P., Schaye J., Booth C. M., Dalla Vecchia C., 2011, *MNRAS*, 415, 3649  
 van Dokkum P. G., 2001, *PASP*, 113, 1420  
 van Kampen E., Rhee G. F. R. N., 1990, *A&A*, 237, 283  
 van Uitert E., et al., 2016, *MNRAS*,  
 van den Bosch F. C., Tormen G., Giocoli C., 2005, *MNRAS*, 359, 1029  
 von der Linden A., et al., 2014a, *MNRAS*, 439, 2  
 von der Linden A., et al., 2014b, *MNRAS*, 443, 1973

## Acknowledgements

Done. Thank you all!